The Interaction of Alkali Metals with Oxide Surfaces

Axel Forssberg
St. Cross College
University of Oxford

A thesis submitted for the degree of

Doctor of Philosophy

Hilary Term 2025

Abstract

Solid-state batteries (SSBs) have the potential to significantly improve key battery properties such as energy density. Their performance is currently limited largely by issues that originate at the electrolyte-electrode interfaces, such as dendrite formation, resulting in a requirement for an atomic-level understanding of interface interactions. This thesis aims to contribute to that understanding by describing Li and Na interactions with $SrTiO_3$ (STO) surfaces via STM, DFT, and XPS. It is therefore relevant chiefly to SSBs with alkali metal anodes and oxide electrolytes.

Li and Na on STO(001) at coverages below 0.3 monolayers (ML) substantially increase step edge density after 400 ^oC annealing. In the case of Na adsorption, this coincides with the induction of a $(\sqrt{5}\times\sqrt{5})-R26.6^o$ reconstruction. In the case of Li, this reconstruction is observed after 700 ^oC annealing. The increase in step edge density is proposed to result from preferential Li and Na step edge decoration. The $(\sqrt{5}\times\sqrt{5})-R26.6^o$ surface is proposed to form due to alkali metal reduction of the surface region. At coverages of $1.0 <$ 2.0 ML, both alkali metals produce wetting monolayers. Na appears to form a completely covering monolayer, while Li forms monolayer islands up to 30 nm in diameter with islands separated by areas of $(\sqrt{5}\times\sqrt{5})-R26.6^o$. On STO(111), Na does not noticeably alter the structure of the (4×4), (5×5), nor (6×6) reconstructions at coverages below 0.3 ML. Li at these coverages, on the other hand, transforms all three reconstructions after 400 ^{o}C annealing, where each new reconstruction maintains the original periodicity. Remarkably, when this system is annealed to 600 ^{o}C, areas that are flat within ±0.04 nm and up to 50 nm in diameter are revealed, which are assigned to a Li-based overlayer on a (1×1) bulk termination. At $1.0 <$ 2.0 ML coverage, both alkali adsorbates form non-wetting, amorphous films on (111). Band gap states were, furthermore, detected in XPS after annealing above 600 ^oC, which were predicted by DFT to have mainly Ti 3d character.

This thesis demonstrates that Li and Na interactions with STO surfaces depend on oxide crystal termination and reconstruction. It also proposes mechanisms by which alkali metals change the structure of oxide surfaces. This may aid the development of SSBs with desirable interface properties, such as high adhesion of Li.

Preface

The work contained in this thesis was carried out by its author from October 2019 to March 2025 at the Department of Materials, University of Oxford. The thesis was supervised by Prof. Martin Castell. No part of this thesis has been previously submitted for a degree at this or any other university. All data was produced by the author. The thesis was suspended between February and October 2022 due to external circumstances.

Acknowledgements

This thesis was made possible by the support of many individuals and institutions. First and foremost, I thank my supervisor, Prof. Martin Castell, for his guidance throughout the project. He has given me invaluable training particularly in surface science, but also in general scientific thinking, and I hope to one day match his epistemic rigour. Prof. Castell's support was especially appreciated in light of the circumstances relating to the 2022 suspension. I would also like to thank Prof. Christopher Patrick, who generously supported the modelling side of the project and gave indispensable advice on the setup and interpretation of calculations, as well as insight into density functional theory.

My fellow group members have also played crucial roles in enabling the project: Dr. Peiyu Chen, who trained me in using the scanning tunnelling microscope, Sparsh Tyagi, my steadfast lab partner, as well as Yingrui Zhao, Merel Lefferts, Tairu Ge, and Michael Furlan, who have been fantastic colleagues. It was also always a pleasure to work with Chris Spencer, whose technical skill borders on magic. Sparsh deserves special thanks for the hours of discussion about all things pertaining to this project, from instrument operation to experimental setup, results, and theory.

The project was funded by the Faraday Institution, to whom I express my gratitude for enabling my research. I would, in particular, like to thank Francesca Long and Dominic Grantley-Smith for their support in all matters pertaining to the suspension, where Dominic Grantley-Smith played a particularly important role in the final stages of the project. St. Cross College and Pusey House Chapel have also provided important support in numerous ways throughout this DPhil, for which I am highly appreciative. Among institutions, The University of Oxford in general and its Materials Department in particular deserve very special thanks for providing the entirety of my university education.

On a more personal note, I would like to thank Dominic Melvin, Marco Siniscalchi, and Michael Fraser for their friendship, and my mother Anitha, father Johan, and sister Ebba for everything.

List of Abbreviations

ASE	Atomic simulation environment
BCC	Body centred cubic
BVS	Bond valence sum
CPS	Counts per second
DOS	Density of states
DFT	Density functional theory
FCC	Face centred cubic
FFT	Fast Fourier transform
GGA	Generalized gradient approximation
IMFP	Inelastic mean free path
LCAO	Linear combination of atomic orbitals
LDA	Local density approximations
ML	Monolayer (coverage)
MTP	Multiply twinned particle
PAW	Projector augmented-waves
PW	Plane wave
QCM	Quartz crystal microbalance
SCF	Self-consistent field
SNR	Signal-to-noise ratio
STM	Scanning tunnelling microscopy
UHV	Ultra-high vacuum
XPS	X-ray photoelectron spectroscopy

Contents

1 Introduction

1.1 Background

The surface of a solid may be defined as its outermost atomic layer[1,2]. Materials thus interact with their surroundings through their surfaces[3], making surface properties essential for determining the influence a material exerts on the external world and vice versa. Interactions at solid surfaces have typically been researched on the format of some well-characterised surface interacting with an adsorbate, which has been applied to e.g. noble metal adsorbates on oxide surfaces[4–6] and alkali metal adsorbates on semiconductor surfaces[7–9]. This thesis aims to contribute to this body of work by characterising an interaction that presently is not well-understood, namely the one between oxide surfaces and alkali metals. The surface systems that result from this interaction are scientifically interesting in their own right since they provide an opportunity to study oxide surface physics in the most extreme reductive environment any element may produce. There is, however, also a technological significance to this interaction, primarily due to its importance for electrolyte-anode interfaces in solid-state batteries. The oxide used for this investigation is $SrTiO_3$, an archetypal perovskite oxide and thus suitable representative of oxide surface physics in general. The alkali metals employed were Li and Na, to which $SrTiO_3$ reconstructions on the (001) and (111) terminations were exposed. The resultant surfaces were studied by scanning tunnelling microscopy (STM), X-ray photoelectron spectroscopy (XPS), and density functional theory (DFT), which together produced a data set containing structural, chemical, and quantum mechanical information of how the character of this interaction is shaped by oxide surface properties.

To understand the properties of a surface, one must first understand its structure[10]. This principle has made the relationship between structure and properties a central focus of surface science[11]. Surfaces inherit significant structural attributes from the bulk, which in the case of oxides is exemplified by surfaces, like the bulk, consisting of cation-anion coordination polyhedra[10,12] that are arranged in accordance with Pauling's rules[10]. Surface atoms do, however, necessarily have different atomic environments due to the lack of neighbours in the surface normal direction[13]. This produces surface-specific equilibrium positions, which means all surfaces must experience some degree of relaxation[11,13,14].

Surfaces may, additionally, generate non-bulk like phases such as reconstructions[15,16]. A similar line of reasoning can be applied to surface electronic structure, because states in the surface experience a potential landscape different from the bulk[17], which alters electronic states in the surface with respect to their bulk counterparts[16,17]. Surfaces may also see the formation of electronic states that are not allowed in the bulk, which are known as surface states[18]. The structure of a surface is thus associated with characteristic coordination environments and electronic states, which together have considerable explanatory power for many surface properties. Surface energy, for example, is generally minimised when under-coordination and the number of dangling bonds in the surface are minimised[19]. If one gains a grasp of how changes in surface structure modify a desired property, one may then prepare the surface to tailor this property towards the intended application.

There is good reason to employ surface science in support of solid-state battery development. This battery technology has the potential to significantly improve key battery properties compared to conventional liquid-electrolyte batteries, including energy density[20–22], power density[20,21], and cycle life[21–23]. The wide-scale implementation of solid-state batteries is, however, currently limited largely by issues originating at electrolyte-electrode interfaces[24–27]. One may broadly group interface failure mechanisms into two interdependent categories[21,22]; chemical, such as the formation of continuously growing interphases that consume the electrolyte[21,28], and morphological, such as voiding[21,29] and the growth of alkali metal dendrites into the electrolyte[21,30–33]. To prevent chemical failure by uncontrolled interphase growth, the interface must be electrochemically stable[26,27,30], and any interphase that forms must be electronically insulating and ionically conducting[21,26,27]. To prevent voiding and dendrite formation, the interface must be morphologically stable, which means that a homogenous contact between electrolyte and anode is maintained during battery operation[21,29,30,34] and requires a high interface adhesion[21,27,30]. A fundamental study of the interaction between oxide surfaces and alkali metals could reveal oxide features that are conducive to these desirable interface properties. This could then inform the preparation of oxide electrolytes as to make their interaction with alkali metals better suited for mitigating interface failure mechanisms.

1.2 Thesis Outline

Chapter 2 provides a literature review of the central topics pertaining to alkali metal interactions with $SrTiO_3$. This chapter presents a theoretical background of oxide surface physics, an overview of $SrTiO_3$ surfaces, and finally a review of the current state of research on alkali metal interactions with surfaces in general and oxides in particular.

Chapter 3 explains the methods used in this thesis, including the experimental and computational setups, sample preparation conditions, as well as a brief theoretical background of STM, XPS and DFT. An important aspect of this project was the construction and calibration of an alkali metal evaporator which could deposit Li and Na with sub-monolayer control in ultra-high vacuum (UHV), which is presented in Chapter 4.

The chapters presenting alkali metal interactions with $SrTiO_3$ surfaces are divided into four, where Na on $SrTiO_3$(001), Li on $SrTiO_3$(001), Na on $SrTiO_3$(111), and Li on $SrTiO_3$(111) are presented in Chapters 5, 6, 7, and 8, respectively. These chapters all include STM images and DFT calculations, with Chapters 5, 7, and 8 also including XPS data. STM results are presented in order of deposition quantity (from low coverage to high coverage) and annealing temperature (from low temperature to high temperature). DFT calculations present adsorption site preference and correlations between adsorption energy and surface bonding characteristics. XPS is used to complement the characterisation of structures observed in STM with chemical data, in particular to determine how chemical environments change as a function of effective annealing temperature.

Chapter 9 summarises the key findings from Chapters 5-8 to give an overview how $SrTiO_3$ surfaces respond to alkali metal exposure. This chapter proposes how surface properties, such as alkali metal adhesion and surface chemical stability, can be explained by surface structure, specifically by the underlying termination and pre-alkali metal exposure reconstruction. The thesis is concluded with a few notes of potential future work, where the applicability of its findings to solid-state battery research is discussed.

2 Literature Review

2.1 Introduction

This thesis explores the atomic scale interaction of alkali metals with oxide surfaces using Li and Na adsorption on $SrTiO_3$ as the model system. The present chapter aims to provide the necessary background to this research. It will first give a general treatment of oxide surfaces in terms of their structure (Section 2.2) and bonding (Section 2.3). These sections introduce concepts central to explaining the observations discussed later in the chapter. This is followed by an account of $SrTiO_3$ surfaces (Section 2.4), including a review of metal deposition where $SrTiO_3$ is used as the substrate. The chapter then concludes with alkali metal deposition, starting with a brief overview of how surfaces respond to alkali metals in general, followed by a focused review of alkali metal deposition on $SrTiO_3$ and TiO_2 (Section 2.5). TiO_2 was included as the wealth of research on its interactions with alkali metals is vastly greater than that of $SrTiO_3$, which together with the similarity between $SrTiO_3$ and TiO_2 surfaces makes this research highly relevant.

2.2 Structure of Oxide Surfaces

A theoretical framework that describes the structure of solid surfaces with predictive capacity has long been sought but has not yet been adequately formulated[10,35]. Despite this, there are principles that have proven sufficiently powerful as to be generally applicable. These principles can be divided into two categories; those pertaining to stability, and those pertaining to geometry. Two principles predicting stability are commonly invoked as particularly powerful in the literature[10,11,35,36], namely electrostatic convergence and dangling bond minimisation. The principles predicting surface geometry are taken from solid-state chemistry[36] and are very effectively captured by Pauling's rules[10]. These rules have proven remarkably insightful for explaining the atomic structure of oxide surfaces, including those of $SrTiO_3$[10,37]. This section concludes with a presentation of concepts pertaining to supported structures on oxide surfaces in Section 2.2.4. This is a vast and well-researched topic, for which reason emphasis will be given to those concepts that are of importance to the findings of this thesis. Alkali metals were, for example, not observed to grow as crystallographically well-defined, homogeneous and evenly distributed crystals on $SrTiO_3$, but rather as clusters and monolayers. Concepts pertaining to supported

crystals, such as the Winterbottom constructions, will therefore not be treated in detail.

2.2.1 Surface Stability

2.2.1.1 Electrostatic Convergence

The crystal termination that meets the environment exerts great influence on surface structure. Some crystal bulk terminations have low enough surface energy to produce stable surfaces, for example rutile $TiO_2(110)-(1\times1)$[11]. Bulk terminations are, however, often unstable, which is especially pertinent when polar planes terminate the crystal because such planes produce an uncompensated surface dipole moment[37–39]. Polar bulk terminations, including e.g. $SrTiO_3(110)$ and (111)[40], must consequently be altered to cancel this dipole moment to generate a viable surface[37,38]. Four primary mechanisms have been identified for achieving this dipole moment cancellation[38,40–43]; change of stoichiometry, electronic charge redistribution, adsorption, and faceting. Stoichiometry changes produce a different phase in the surface layers, which when stable has a charge distribution that cancels the dipole[40,41]. This often drives the formation of reconstructions[15], as a reconstruction may be described as an ordered surface phase[41]. Electronic charge redistribution occurs through modification of bonding at the surface, such as changing the degree of covalency or filling surface states until dipole cancellation ensues[38,44]. Adsorbates may similarly cancel the dipole moment by exchanging electrons with the surface as to compensate for the unbalanced surface charge[38]. Faceting changes termination, thus enabling crystals to exchange a surface terminated by polar planes for one terminated by non-polar planes[42]. The preferred mechanism will be the one that yields to lowest surface energy[38].

2.2.1.2 Dangling Bond Minimisation

One may in general say that surfaces with fewer dangling bonds and more close-packed structure have lower surface energy[19]. Dangling bonds emerge when valence orbitals fail to form bonds due to lacking neighbouring atoms[14,45]. They are thus highly reactive[46] and may substantially increase the surface energy[19], leading to a driving force to modify the surface electronic structure to minimise their presence[47]. They are typically associated with semiconductors[48] but must also be considered in the case of oxides[11,17], where they come in the form of occupied cationic states and unoccupied anionic states[11]. Dangling bond minimisation in oxides specifically entails that the excess charge of cation dangling

bonds should transfer to anion dangling bonds[11,35]. An analogous case is presented in Figure 1 using GaAs as the example, which is appropriate as As is more electronegative than Ga, energetically incentivising dangling bond charge transfer[45]. An ideal oxide surface would thus have empty cation dangling bonds and filled anion dangling bonds[11]. In real oxide surfaces, however, the transfer is incomplete and the excess charge is shared between anion and cation, which contributes to oxide surfaces typically having more covalent bonding than their bulk structures[11]. An oxide that clearly displays the importance of surface dangling bonds is rutile $TiO_2(110) - (1 \times 1)$[11]. For this surface to be stable, the same number of Ti-to-O bonds as O-to-Ti bonds must be broken such that cation and anion dangling bonds are balanced. The filled Ti dangling bonds transfer electrons to the unfilled O dangling bonds, which stabilises the surface and contributes to it existing without the need for reconstructing, albeit with significant relaxation[11].

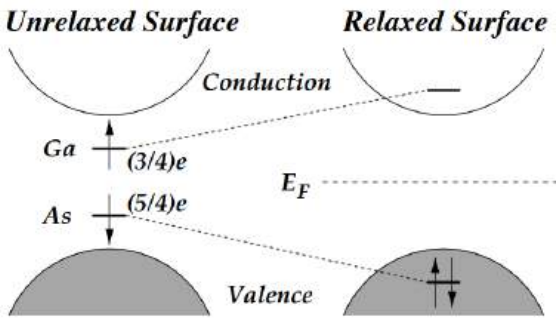

Figure 1: Schematic of GaAs(110) before (left) and after (right) relaxation and the associated charge transfer between dangling bonds. The notation (3/4)e and (4/5)e refers to the number of electrons per dangling bond in surface Ga and As atom, respectively, derived from Ga having valence 3, As having valence 5, and both forming 4 bonds in bulk GaAs[45]. E_F is the Fermi level. As is more electronegative, incentivising electrons to move from the Ga dangling bond to the As dangling bond. Once this transfer is complete, the As state is occupied and the Ga state is unoccupied, and both have moved from positions in the band gap to ones spanned by bulk bands. Reproduced from [45].

2.2.2 Surface Geometry

2.2.2.1 Polyhedral Units

Many of the same principles that dictate the formation of oxide bulk structures also apply to surfaces[12]. Crucially, both bulk and surface are generated by the same type of fundamental structural units[10], namely coordination polyhedra composed of a central cation coordinated by O[10,12,13]. The ubiquitous nature of these polyhedral units is perhaps to be expected, as their geometries result from fundamental electrostatic and quantum

mechanical principles such as electrostatic repulsion and orbital symmetry[10]. See Figure 2 for representations of three common polyhedra. An example pertinent to this project is the ABO_3 perovskites, to which $SrTiO_3$ belongs, where bulk A and B cations are 12-fold and 6-fold coordinated, respectively[13]. As such, the 12-fold O coordination of Sr in bulk $SrTiO_3$ corresponds to SrO_{12} icosahedra units, and the 6-fold O coordination of Ti corresponds to TiO_6 octahedra units. When reconstructions form, they do so by arranging polyhedral units into patterns that when repeated produce the surface unit cell[10]. The set of polyhedra employed, their arrangement, as well as the bulk-like layer on which they are arranged, are characteristic of the reconstruction in question[10]. The geometries and arrangements of polyhedral units, both in bulk and surface, are effectively predicted by Pauling's rules[10,49]. In fact, Pauling's rules have demonstrated such potency for predicting the atomic structure of oxide reconstructions that to date, no atomic level reconstruction has been proposed that violates them[10]. On a somewhat less formal note, the polyhedral units so essential to the structure of oxides remarkably often have the geometry of one of the Platonic solids described by Plato in the Timaeus[50]. One could, for example, generate an entire $SrTiO_3(110) - (n \times 1)$ material using only SrO_{12}, TiO_6 and TiO_4 units, which are icosahedral, octahedral and tetrahedral, respectively, all Platonic solids. See Figure 3 for an example of the $SrTiO_3(110) - (3 \times 1)$ reconstruction. Plato postulated that his solids were the fundamental building blocks of all matter[50], which might have been over-ambitious, but he would perhaps have been pleased to learn that they at least are the building blocks of one level in the ontology of minerals.

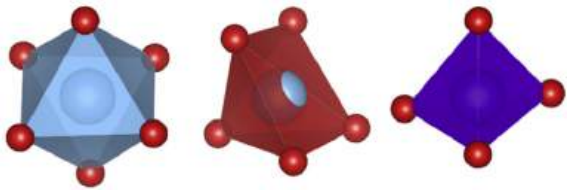

Figure 2: Idealised coordination environment for a AB_x compound where A is displayed as the central blue ball and B is the coordinating red ball, which could represent e.g. Ti and O, respectively. From left to right, the octahedral AB_6, octahedral $AB_5[]$, and tetrahedral AB_4 are shown. The "[]" in $AB_5[]$ represents a B vacancy. Reproduced from [10].

2.2.2.2 Surface Coordination

The lack of neighbours in the direction of the surface normal makes replicating the exact coordinations and symmetries of the bulk impossible[13,51]. This destabilises surface atoms as they become under-coordinated[10,35,52], but opens up a positional degree of freedom

that allows for atomic displacement along the surface normal[36,53]. Since the atomic environments in the surface differ from those in the bulk, so do equilibrium atomic positions, meaning all surfaces must at least experience some degree of relaxation[11,13,14]. The destabilising effect of under-coordination on atomic positions in the surface can be quantified via metrics like bond valence sum (BVS), which measures the valence of an atom given the lengths of its bonds[35]. For example, if an O atom has a BVS closer to -1 than its expected value of -2, this indicates insufficient bonding and hence under-coordination[35]. If the surface is unstable and a structural rearrangement is thermodynamically favoured, the increased positional degree of freedom in the surface allows for polyhedral unit geometries and arrangements impossible in the bulk[10]. When a reconstruction has formed, it may contain atomic sites that are over-coordinated if this minimises the total surface energy[35].

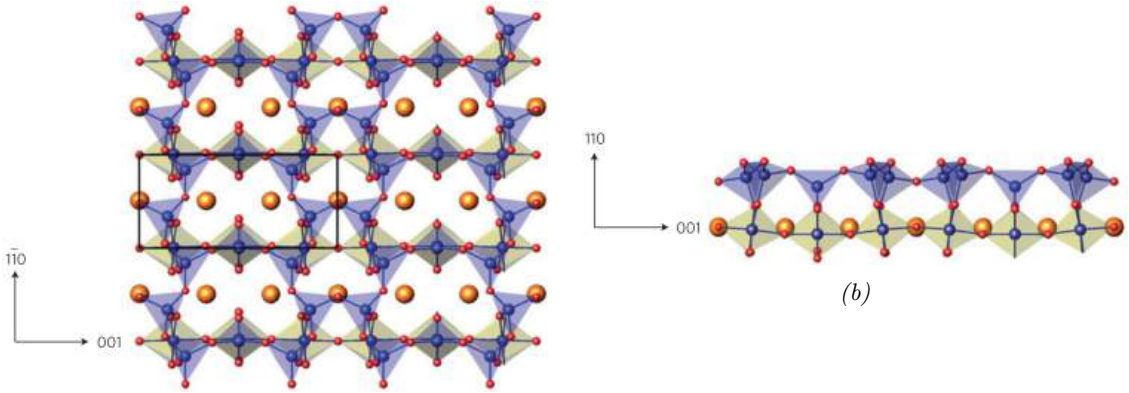

Figure 3: Schematic of the $SrTiO_3(110)-(3\times1)$ reconstruction showing a) the top view perpendicular to the surface plane with the surface unit cell indicated in black and b) the side view parallel to the surface plane. Orange, blue and red balls represents Sr, Ti, and O, respectively. Blue polyhedra represent bulk-like TiO_4 and gray polyhedra represent bulk-like TiO_6.

2.2.3 Adsorption Sites

When an adsorbate atom meets a surface, the most preferred adsorption site will be the one that minimises the free energy of the surface-adsorbate system[54,55]. In order to predict the adsorption strength of a particular site, one must consider how the adsorbate will respond to both its geometry and electronic structure[54,56]. In general, one can expect that low energy adsorption sites allow adsorbates to saturate dangling bonds and/or increase coordination[57]. There are some adsorption sites that are so common that they have attained standard names, namely the atop, bridge, and hollow (or void) sites[58–60]. In the

atop site, the adsorbate bonds a single surface atom. In the bridging sites, the adsorbate bonds two adjacent surface atoms. In hollow sites, adatoms sit in cavities between a group of at least three surface atoms. The atop site is preferred when a strong bond is possible between adatoms and substrate and the hollow is preferred when the adatom aims to maximise its coordination[59]. See Figure 4 for examples of top and hollow site adsorption.

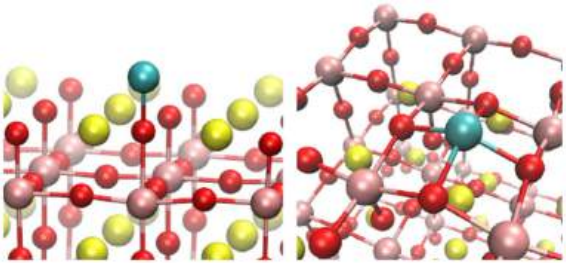

Figure 4: The minimal energy adsorption sites for Co on SrO-terminated (left) and TiO_2-terminated (right) $SrTiO_3$(001), where an atop and a hollow site are preferred, respectively. Reproduced from [61].

Real adsorption sites can be experimentally challenging to unambiguously determine[60], however, it is well established that metals have a strong tendency to bond surface O[11,62,63]. The adsorption strength of a metal adatom to an oxide surface is therefore strongly influenced by the local O coordination[35,56] and chemical potential[64]. This makes defects important to consider as probable adsorption sites[17,30,52,57,65]. Step edges are of particular interest as they offer common and well-defined sites with different coordination and bonding configurations to terraces[14,30]. Not only do step edges host under-coordinated O at their edges and corners[14,17], but may also provide environments where the adsorbate may attain higher coordination by bonding to O in the plane protruding from the surface[11].

2.2.4 Supported Structures

2.2.4.1 Equilibrium Morphology

As adsorbate atoms grow in number on a surface, they may congregate to form supported structures such as crystals and monolayers. The total energy of a supported structure has three general contributions; formation energy, surface and interface energies, and strain energy[6,66]. Assuming a supported structure has formed with no strain, its equilibrium morphology can be predicted by minimising the total energy of its surface, the substrate's

surface, and their interface, then applying the Winterbottom construction[66–68] or Young's equation[62,69,70]. Crucially, as the equilibrium morphology is the lowest energy configuration of the adsorbate-substrate system, it is also the morphology with the strongest adhesion to the substrate[62]. Adhesion strength can be calculated by the work of adhesion (W_a), which for a substrate surface energy γ_{sub}, supported structure surface energy γ_{ads}, and interface energy γ_{int} is given by $W_a = \gamma_{sub} + \gamma_{ads} - \gamma_{int}$[70]. The greater the work of adhesion, the flatter the morphology of the supported structure[62,70–72], with a wetting monolayer being produced if $\gamma_{sub} > \gamma_{ads} + \gamma_{int}$[6]. In order to study the lowest energy structure that corresponds to the equilibrium morphology, one may need to supply heat energy through annealing[73,74]. Raising the temperature reduces kinetic restrictions, e.g. O diffusion[75], and provides energy to overcome barriers, e.g. nucleation, allowing for a thermodynamically more stable structure to obtain[5,76]. See Figure 5 for an example of Li islands dewetting on Mo(001)-supported MgO due to annealing, indicating they were metastable.

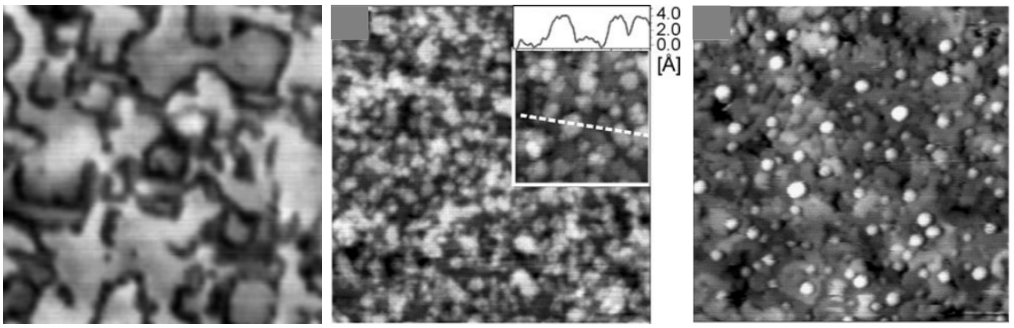

Figure 5: STM images of Li deposited on Mo(001)-supported MgO. a) The clean MgO surface, where dark lines are dislocations ($60\times60nm^2$). b) Circa 1 ML Li deposited onto the surface shown in a) ($70\times70nm^2$). c) After annealing of the surface shown in b) at 700 K for 10 min ($75\times75nm^2$). The unannealed area in b) forms islands, 0.35-0.4 nm in height and 3-6 nm in width, as can be seen in the inset image and associated height profile. This height corresponds to circa two layers[77]. After annealing in c), Li dewets and instead forms particles 1.5 nm in height and 2.5 nm in diameter, which nucleate at dislocations. Reproduced from [77].

2.2.4.2 Interface Interactions

The interface energy γ_{int} originates from the bonds at the interface, and may at first approximation be indicated by the adsorbate-O binding energy at the interface multiplied by the number of bonds per unit area[62]. The stronger the bonds and the greater their concentration, the stronger the interface interaction and the lower γ_{int}. One may, in general, expect that the greater the oxygen affinity of the adsorbate metal compared to that

of the oxide metal, the greater the bond strength and thus the work of adhesion[55,62,70,78]. To understand epitaxy at the interface, one must account for the strain produced by lattice mismatch[62]. This strain originates from differences in the supported structure and substrate surface unit cells, incentivising supported structures to adapt an epitaxial relation that minimises this mismatch[79,80]. This often leads to supported structures facing the surface with plane that has the most commensurate unit cell to the substrate[6,66]. If, however, the adsorbate-O bond is sufficiently strong, the interface may instead favour a epitaxial relationship that maximises the number of bonds[62]. The interface interaction may vary across the surface and be enhanced at defects for reasons explained in Section 2.2.3, which is why they often act as nucleation sites. For example, Li on Mo(001)-supported MgO nucleates on dislocations[77], as can be seen in Figure 5.

2.3 Bonding in Oxide Surfaces

Bonding in an oxide surface may be understood by examining the similarities and differences of its electronic structure to that of its bulk. This section will, for this reason, begin with a brief account of the general behaviour of electrons in bulk oxides before considering surface-specific effects and adsorbates. A particular focus is given to transition metal oxide surfaces, as $SrTiO_3$ belongs to this class.

2.3.1 Bulk Electronic Structure

Oxides have a valence band dominated by O 2p states and a conduction band dominated by d states for transition metals and s or p states for non-transition metals[52,81,82] (see Figure 6a). An important consideration for the electronic structure of oxides is their degree of covalency, resulting from hybridisation of O 2p and the metal valence orbitals[52,83]. Increased covalency, for example, increases the directionality of the metal-O bond[84] and reduces the magnitude of real charge around an ion with respect to its formal charge[17,82]. The hybridised metal-O state splits into bonding and anti-bonding orbitals, with bonding orbitals forming part of the valence band and anti-bonding orbitals forming part of the conduction band[52,81]. Typically, bonding orbitals are located in the lower region of the valence band, and anti-bonding states in the upper region of the conduction band[52,81]. Transition metal-O bonds typically have a considerable degree of covalency[17,82] due to d orbitals hybridising with O 2p[82], which is the case for $SrTiO_3$[40,82,85]. The electronic

properties of transition metal oxides are to a significant extent dependent on the bonding behaviour of their d orbitals, the variability of which makes their electronic structure more diverse than that non-transition metal oxides[82]. This makes d orbital energy, symmetry and occupation important to consider when analysing e.g. reactivity.

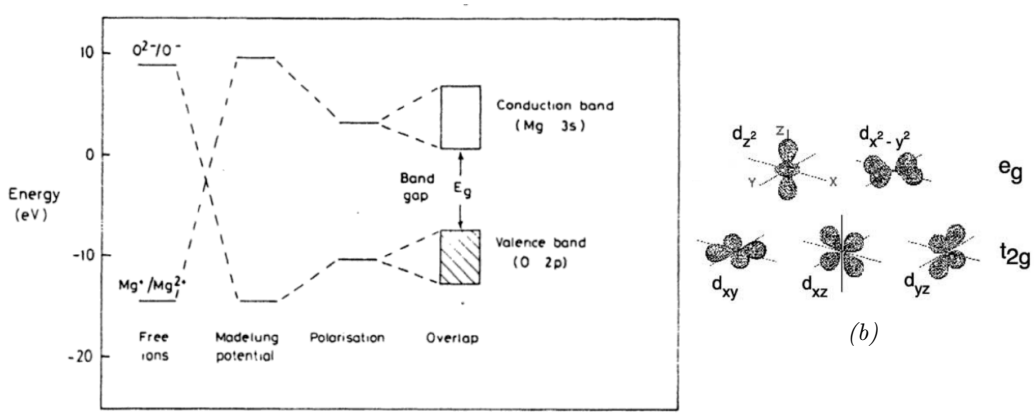

Figure 6: Left: Emergence of valence and conduction bands in MgO showing, left to right, the electronic energy levels in free ions followed by three effects in the MgO lattice. First, the Madelung potential, which gives the electrostatic energy in a lattice of point charges. This will be treated in Section 2.3.2. Second, polarisation, which allows electrons to relax their spatial distribution in response to local electric fields, attracting them towards cations while repelling anions. Third, orbital overlap, allowing electronic wavefunctions to overlap and hence broaden from flat atomic levels to acquire bandwidth. Right: Schematic of the t_{2g} orbitals comprising d_{xy}, d_{xz}, and d_{yz}, and e_g orbitals comprising d^{z^2} and $d^{x^2-y^2}$, defined with coordinating ligands along the x, y and z axes. Reproduced from [52] and [11].

The energy difference between d orbital configurations is typically small, meaning e.g. d^{n-1} and d^{n+1} may be close in energy to d^n, allowing for variations in transition metal oxidation state[82]. This makes d orbitals particularly important for interactions with foreign species[17]. The d orbitals are also sensitive to coordination due to crystal field splitting[81]. In the case of octahedral coordination, this lifts d orbital degeneracy and divides them into 2-fold e_g and 3-fold t_{2g} levels, where e_g orbitals point in the direction of the O ligands and t_{2g} orbitals point between[81,82] (see Figure 6b). The π-like t_{2g} and σ-like e_g orbitals interact with O orbitals of the same symmetry[81], which together with the repulsion from O anions make them attain different energy levels[81], splitting the d band into two[81,82]. Compared to s and p orbitals, d orbitals are spatially localised[82]. Since bandwidth arises due to orbital overlap[82], this leads to the d orbital dominated conduction band of transition metal oxides normally having a rather narrow bandwidth[81,82]. The localised character of d orbitals, in addition, make them sensitive to local electronic factors

such as electron-electron interactions and coordination geometry[81,82]. This is why much of the bandwidth of the d-band in transition metal oxides often is due to indirect bonding interactions mediated by the ligands via metal-oxygen-metal linkages[82].

2.3.2 Surface Electronic Structure

The electronic structure of a material's surface necessarily differs from that of its bulk due to the different potential landscape of the surface[17]. The very existence of a surface means that the periodic potential of the bulk crystal is terminated and replaced by the vacuum potential, leading to an asymmetric potential landscape for surface atoms[17,18,81,86,87]. The surface wave function spills out into the vacuum, giving surface atoms increased positive charge due to reduced electron density[88], which is balanced by a space charge region beneath[47]. Surface layers thus acquire different charges from the bulk[14,18,38], introducing an electric field that modifies the work function of the material[18,88,89] (see Figure 7). If a surface, in addition, differs structurally from the bulk, as in the case of reconstructions, this introduces further changes to its electronic structure[17,44]. Reconstructions may, for example, offer different coordination geometries than the bulk[17,81], which may allow for new bonding symmetries that produce states of non-bulk-like character[47,81]. Much of the difference between bulk and surface electronic structures is effectively captured by considering the Madelung potential, which shall be given a brief treatment below[52,81,90].

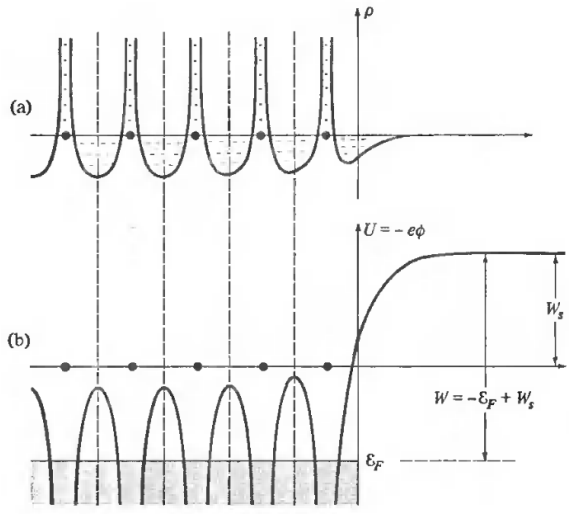

Figure 7: Schematic of electron density, ρ (a), as a function of crystal potential, U (b), displaying its change going from the periodic bulk into a vacuum. ϕ is electrostatic potential, e is electronic charge, and ϵ_F is the Fermi level. The work done by the electric field due to charges in the surface layers, W_s, modifies the work function, W. Reproduced from [18].

2.3.2.1 The Madelung Potential

The Madelung potential on an ion i is the potential energy U_i due to all the other ions j in the lattice[52,90], given by $U_i = \sum_{j,j\neq i} U_{ij}$[90]. This electrostatic energy is the chief contribution to binding energy in predominantly ionic crystals[90]. The Madelung potential decreases electron energy at anion sites and increases electron energy at cation sites, as the former has positively charged nearest neighbours while the nearest neighbours of the latter are negatively charged[52] (see Figure 6a). The lower coordination at surface sites reduces the Madelung potential magnitude at anion as well as cation sites, generally leading O 2p states above the bulk valence band and metal states below the bulk conduction band[52,81]. Hence, the surface band gap is typically narrower than the bulk[52,81,91]. The reduced Madelung potential also decreases the separation between O 2p and metal valence orbitals, facilitating mixing between these orbitals and thus contributing to strengthen covalency in the surface[17,81].

2.3.2.2 Character of Surface Electronic States

The atoms in the surface experience a potential landscape unlike that of the bulk, which gives electronic states in the surface a different character. Most states in the surface, however, remain similar to their bulk equivalents, and may as such be called bulk-like states. Bulk-like states are modified versions of bulk states[17,52,87], with spatial distributions and energy eigenvalues that are perturbed with respect to their bulk counterparts[17,19,52]. The reduced band gap and strengthened covalency mentioned previously in this section are consequences of bulk-like states[52]. In transition metal oxides, bulk-like states of predominantly metal d orbital character can differ from their equivalents in the bulk e.g. by enhanced mixing with metal s and p orbitals and changed magnitude of crystal field splitting[17]. It is often difficult to separate bulk-like states states from bulk states[9,92], as they are often found in the energy range spanned by the bulk valence or conduction bands[9]. The surface may, however, also see the creation of new states without equivalents in the bulk, which are known as surface states. Surface states are not merely perturbed bulk states and only exist in the surface[14,18,47,52,81,86,87]. They are unique solutions to the Schrödinger equation not allowed for the bulk, describing states that are spatially localised in the surface region[18,19]. Their wavefunctions must as such decay exponentially into the vacuum and are damped exponentially in the crystal[14,45] (see Figure 8a). Surface states

are important for alkali metal adsorption on Ti-based transition metal oxides and will hence be given a brief treatment in Section 2.3.2 below. An intermediate between bulk-like and surface states also exists in the form of resonant surface states, which are hybrids between discrete, localised surface states and continuous bands[93]. A resonant surface state emerges when the energy of a surface state lies within the energy range of a band, allowing for hybridisation between the two[93,94]. This hybridisation mixes band-like character into surface states, which broadens their bandwidths and makes them more delocalised[54].

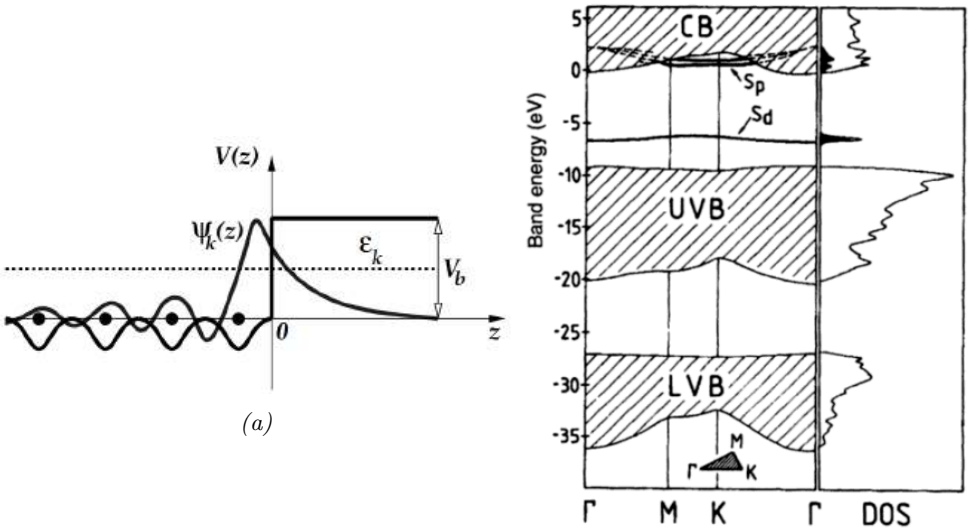

Figure 8: Left: Schematic of a surface state $\Psi_k(z)$ emerging in the surface region with an energy eigenvalue of ϵ_k. $V(z)$ is the potential as a function of position along the surface normal, z, and V_b is the vacuum potential barrier. Right: Calculated band structure and DOS for $Al_2O_3(0001)$, showing the lower (LVB) and upper (UVB) valence as well as conduction (CB) bands. S_p and S_d are surface states. Reproduced from [45] and [52].

2.3.2.3 Surface States

Historically, surface states have often been categorised as either Tamm or Shockley states, where the former is analogous to a state described by the tight binding model and the latter to a state described by the nearly-free electron model[47]. A variety of causes may give rise to surface states[86], which have in common that they significantly alter the potential landscape with respect to the bulk[47]. Surface states can arise even at non-relaxed, non-defective surfaces, simply from the loss of the translational periodicity of the bulk[81,86], which yields different boundary conditions for the wave function at the surface[18]. Other sources include dangling bonds[9,14,17,48,89], defects[17,62,92] and adsorbates[11,92,95,96]. Surface states in oxides typically emerge in the band gap between valence and conduction bands[14,19] from orbitals

at the band edges[47] (see Figure 8b). Depending on their position relative to the Fermi level, band gap surface states may act as electron donors when occupied and electron acceptors when unoccupied[17,47,54,57,97]. Oxides that form dangling bond surfaces states, for example, often have both donor (occupied) and acceptor (unoccupied) surface states[17,62], where the former is concentrated around anions and the latter around cations[17]. A particularly important source of surface states in many oxides are O vacancies[11,82], which produce n-type doping by creating shallow donor states in the band gap[17,92]. Such O vacancy-generated surface states have been observed for many types of oxide surfaces, including transition metal oxides such as $SrTiO_3$ and TiO_2 (see Figure 9), but also pre-transition metal oxides like MgO[92] and filled d-band transition metal oxides like Fe_2O_3[92].

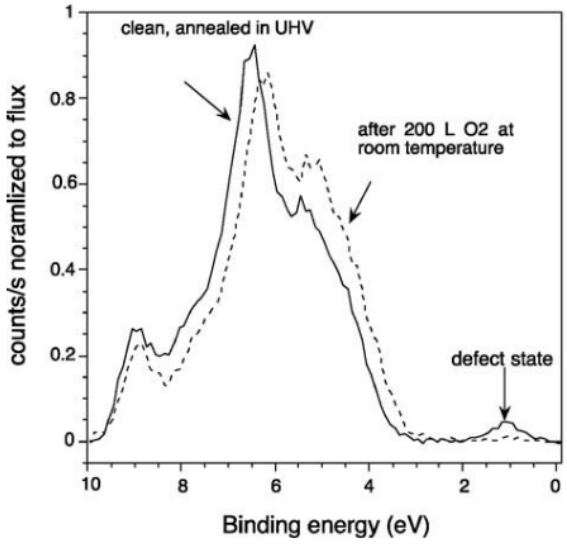

Figure 9: Photoemission spectra for more and less O vacancy rich rutile TiO_2(110), showing the O vacancy-induced band gap surface state. This surface state is produced by filling unoccupied Ti 3d orbitals, and has also been reported to emerge in $SrTiO_3$[17,92] Reproduced from [11].

2.3.3 Adsorbates

When an adsorbate comes into contact with a surface, Fermi level equalisation leads to charge transfer from the the party with the higher Fermi level to the one with lower[21,47,55,63,98]. The more ionic the adsorption bond, the more charge is exchanged with the surface[54]. The more covalent the adsorption bonds, the more the adsorption complex forms hybridised bonding states that are a mixture of surface and adsorbate orbitals[54]. The degree of covalency is thus significant for adsorption site preferences, as covalent bonding favours sites with suitable bonding geometry, whereas ionic bonding favours sites that maximise the amount of charge transfer. When there is a significant degree of hybridisation between

a localised adsorbate orbital and a band-like state in the surface, band-like character is mixed into the adsorbate orbital, yielding a resonant state[54]. When there is significant charge transfer, surface states may arise as a mechanism to accommodate electrons donated by the adsorbate[17,95], similar to the O vacancy-induced surface states described in Section 2.3.2. Such adsorbate-induced surface states are well-documented in the literature on alkali-TiO_2 surfaces systems, which will be treated in detail in Section 2.5.3.

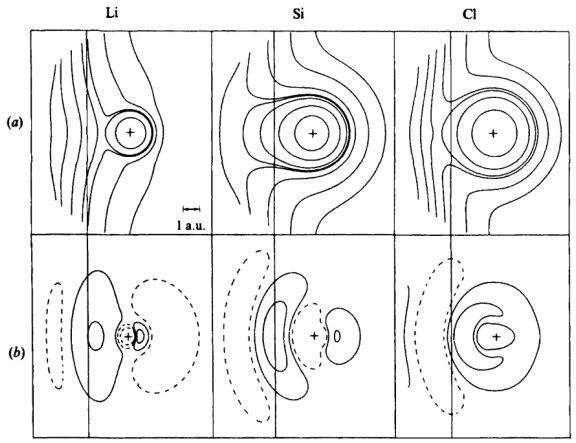

Figure 10: LDA calculation of Li, Si and Cs on jellium showing total charge density (left) and adsorption induced change in charge density. Solid lines in the right-hand-side image indicate electron density decrease, dashed lines electron density increase. Reproduced from [99].

As charge is exchanged, one side of the adsorbate-surface bond acquires positive charge and the other negative charge[22,55,100] (see Figure 10). The surface thus acquires space charges[40,63] and dipoles are produced at the point of contact with the adsorbates[63,71,86]. The strength of the adsorbate dipole moment increases with the ionicity of the adsorbate-surface bond and hence so does charge transfer magnitude[99]. The transferred charge establishes an electric field along the surface normal[63], which in the case of electropositive adsorbates like alkali metals reduces the work function[54,83,95]. This electric field may also reduce the activation energy for O diffusion, increasing the availability of O with which the adsorbate can react[63].

2.4 $SrTiO_3$ Surfaces

This section gives an account of $SrTiO_3$ surfaces, including their reconstructions and electronic structure, after which it concludes with a selection of STM studies where $SrTiO_3$ is used as a substrate for metal deposition. $SrTiO_3$ has a cubic perovskite crystal with

formal charges Sr^{2+}, Ti^{4+}, and O^{2-}, and a lattice parameter of 0.3905 nm[101]. It is an insulator with a band gap of 3.2 eV[101], but can be made sufficiency conducting for techniques like STM and XPS via doping, for example substitutional doping of Nb^{5+} on Ti sites, where Nb acts as an n-type donor[102]. All solved $SrTiO_3$ reconstructions are TiO_2-rich[10,53], meaning they can be represented as some factor of TiO_2 being added to the surface per unit cell area[10,103].

2.4.1 Reconstructions of $SrTiO_3$(001)

Along the [001] direction, $SrTiO_3$ is composed of alternating, charge neutral layers of TiO_2 and SrO[102], making $SrTiO_3$(001) non-polar[101]. (001) reconstructions are generated by the same structural unit, TiO_5[], arranged on the same bulk-like layer consisting of TiO_6 units[10,104]. The top layer TiO_5[] units connect to their neighbouring units by corner- or edge-sharing, with edge-sharing being is more common. Reconstructions observed on $SrTiO_3$(001) include (2×1)[5,105,106], (2×2)[107,108], $c(4\times2)$[79,108–110], (4×4)[111], $c(4\times4)$[112], $(\sqrt{5}\times\sqrt{5})-R26.6^o$[51,113,114] and $(\sqrt{13}\times\sqrt{13})-R33.7^o$[115], where two variations of (2×2) have been observed[10,107]. (2×1) stands out from a chemical point of view as it forms by water chemisorption and is thus hydroxylated[10,105]. It has also been proposed that $c(4\times4)$ is partially hydroxylated[116]. To the author's knowledge, the reconstructions that have to date been solved are (2×1), $c(4\times2)$, $(\sqrt{13}\times\sqrt{13})-R33.7$[10,107], as well as (2×2)[10]. The reconstruction studied in this thesis is $c(4\times2)$, but $(\sqrt{5}\times\sqrt{5})-R26.6^o$ was also observed, for which reason these two reconstructions are shown in Figure 11. $(\sqrt{5}\times\sqrt{5})-R26.6^o$ has previously been reported in reductive environments without alkali metal exposure[113,114].

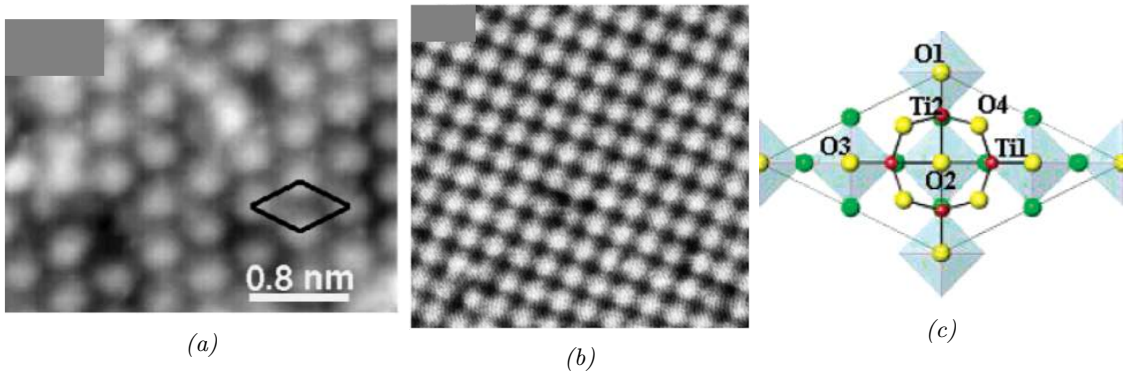

(a) *(b)* *(c)*

Figure 11: Selected $SrTiO_3$(001) reconstructions, where a) shows an STM image of $c(4\times2)$ (scale given in image), b) shows an STM image of $(\sqrt{5}\times\sqrt{5})-R26.6^o$ ($12.4\times12.4\,nm^2$), and c) shows an atomic model of $c(4\times2)$ viewed perpendicular to the surface plane. Reproduced from [101], [113], and [109].

There are two bonding requirements for the outmost TiO_2 layer of non-hydroxylated (001) reconstructions, namely that each Ti in the top layer must bond an O in the base layer, and that each O atom in the top layer must bond two or more Ti atoms[51]. These structural principles hold also for nanostructures that exist on $SrTiO_3$(001), which are closely related to reconstructions[101,102,117] but differ in that they have extra TiO_x surface layers[102] and thus enhanced TiO_2 richness. They do, like reconstructions, form ordered, periodic domains on the surface and thus also have well-defined surface unit cells, typically larger than normal reconstructions, e.g. (12×2) or (6×8)[102].

2.4.2 Reconstructions of $SrTiO_3$(110)

Along [110], $SrTiO_3$ is composed of alternating polar planes of $SrTiO^{4+}$ and O_2^{4-}[12]. This produces a macroscopic dipole moment which $SrTiO_3$(110) reconstructions must remove in order to create stable, charge compensated surface structures[10]. This may be achieved by terminating the crystal at a $SrTiO^{4+}$ plane, upon which TiO_4 structural units are arranged such that charge balance ensues[53,104]. These units attach to the surface by sharing one or two O with the Ti in the $SrTiO^{4+}$ layer beneath, producing a bulk-like O_2^{4-} layer between the two outmost Ti-containing layers[10]. Observed (110) reconstructions include $(n\times1)$[12,118,119], $(5\times1)A$[119], $c(2\times6)$[120], as well as a variety of $(n\times m)$-ordered reconstructions, including[121] (2×5), (3×4), (4×4), (4×7) and (6×4). In addition, similar to (12×2) and $c(6\times2)$ on $SrTiO_3$(001), $SrTiO_3$(110) hosts two known families of TiO_2-rich nanostructures, $(2\times n)A$ and $(2\times n)B$[53]. The atomic structure is considered solved in the case of $n\times1$, $(5\times1)A$, $(2\times n)A$ and $(2\times n)B$[10]. Figure 12 shows the $(n\times1)$-type reconstructions for n=2,4,5, which were studied by DFT in this thesis. These $(n\times1)$ reconstructions constitute a homologous series and were the first (110) reconstructions to be solved[53]. They are generated by TiO_4 units that are corner-sharing with each other and either corner- or edge-sharing with the TiO_6 beneath[12] (see Figure 12). DFT suggests that $(n\times1)$ reconstructions are thermodynamically stable for $3 < n < 6$[12] and that $n = 4$ gives the BVS values closest to expected values, closely followed by $n = 3$[35].

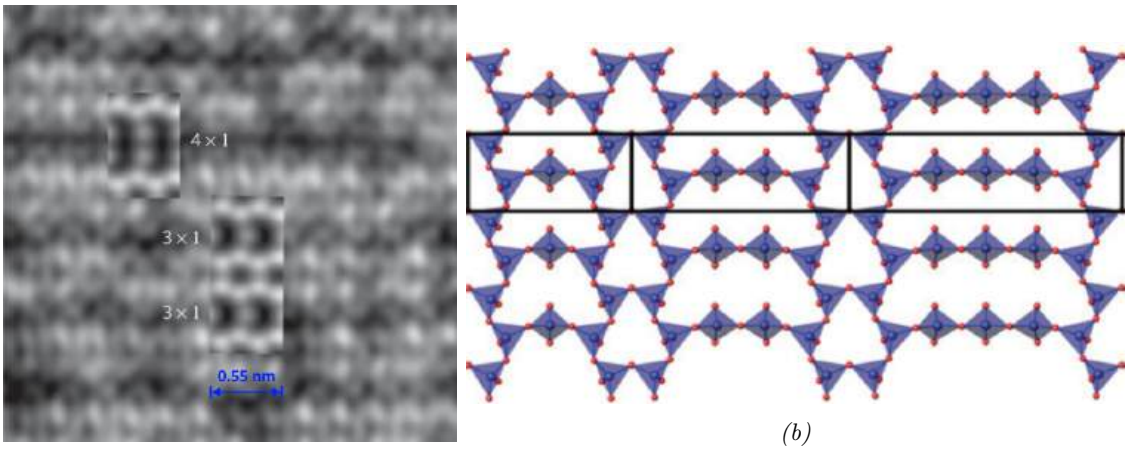

(a) (b)

Figure 12: (n×1) *reconstructions of* $SrTiO_3$. *a) shows an STM image of an area containing* (3×1) *and* (4×1) *with simulated images overlaid. The blue scale bar is not in the original image and was added by the author. b) shows, left to right, models of* (3×1), (4×1), *and* (5×1) *based on their* TiO_4 *unit arrangement in the outermost surface layer.* TiO_4 *units are organised into two rings, one smaller made from six* TiO_4 *units for all reconstructions, and one larger, in which the number of* TiO_4 *units is* $2(n+1)$ *where n the same as in the reconstruction periodicity* (n×1). *For example,* $n = 3$ *for* (3×1), *thus the number of* TiO_4 *in the larger ring is* $2(n+1) = 8$, *as can be seen in b). Reproduced from [12].*

2.4.3 Reconstructions of $SrTiO_3$(111)

(111) is the most complex[104] and least extensively studied $SrTiO_3$ termination[10]. Like (110), it is polar, consisting of alternating layers of SrO_3^{4-} and Ti^{4+}[41]. The bulk-like layer on which (111) reconstructions form is SrO_3^{4-}, on top of which all three TiO_x polyhedra are used as structural units, i.e. TiO_6, TiO_5[] and TiO_4,[104]. Observed $SrTiO_3$ reconstructions include $(\sqrt{7}\times\sqrt{7})-R19.1^o$[41,104], $(\sqrt{13}\times\sqrt{13})-R13.9^o$[41,104], $(2\times2)A$[103], $(2\times2)B$[103], (3×3)[43,103], (4×4)[103], (5×5)[42], and (6×6)[42,43]. The $SrTiO_3$(111) reconstructions that have been solved are (2×2)A, (2×2)B, (3×3)B and (4×4)B[104], as well as $(\sqrt{7}\times\sqrt{7})-R19.1^o$ and $(\sqrt{13}\times\sqrt{13})-R13.9^o$[10]. Figure 13 shows examples of the (111) reconstructions studied in this thesis, where (4×4), (5×5), and (6×6) were studied in STM, and (2×2)A and (3×3) were studied in DFT. Units of TiO_5[] and TiO_6 are placed on the bulk-like SrO_3^{4-}, and if TiO_4 also participate, they are put atop this TiO_5[]/TiO_6 layer. Double-layer (111) reconstructions thus contain all three TiO_x units, whereas single-layer ones, e.g. (2×2)A, lack TiO_4[10]. (111) is unique among terminations in that its reconstructions can add Sr to or remove Sr from the surface, which is done in order to ensure compliance with $nSrTiO_3\times mTiO_2$ stoichiometry[10]. When the reconstruction is single-layer, Sr is removed from the outermost bulk-like layer, and when it is double-layer, Sr is instead added to sites

as similar as possible to the bulk[10]. Commonly observed on $SrTiO_3$(111) are a multitude of reconstructions co-existing as neighbouring domains on the same surface[103] (see Figure 13), meaning these reconstructions have similar surface energies[10]. Domains can eventually become so small as to dissolve into their consistent structural units, producing a glass with short-range order only[10,103].

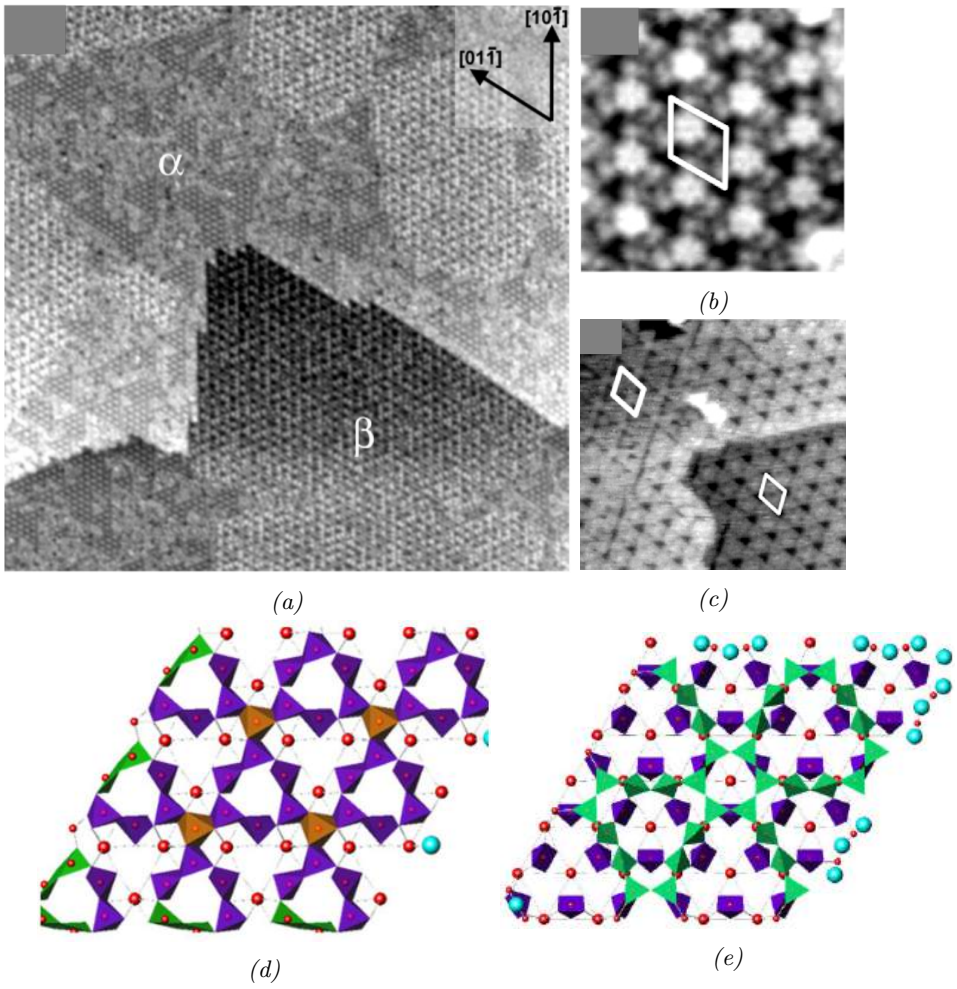

Figure 13: Selected $SrTiO_3$(111) reconstructions. a): Mixed region with a (4×4) domain (α) and a (6×6) domain (β) (160×160 nm^2). b): Close-up of (4×4) (9×9 nm^2). c): Mixed region with a (5×5) domain (bottom right) and a (6×6) domain (top left) (25×26 nm^2). d) and e) models of the (2×2)A and (3×3) reconstructions, respectively. Brown, purple and green polyhedra represent TiO_6, TiO_5[], and TiO_4, respectively. Reproduced from [42] and [103].

2.4.4 Electronic Structure of $SrTiO_3$ Surfaces

The electronic structure of $SrTiO_3$ surfaces will here be given a general treatment relying on $SrTiO_3$(001) as the primary example. First, it is instructive to note that bulk $SrTiO_3$ exhibits many typical traits of empty d-band transition metal oxides[82]. Its valence band is dominated by O 2p and conduction band by Ti 3d[17,82,92,122] (see Figure 14). It has

a significant degree of covalency that arises from the hybridisation between O 2p and Ti 3d[11,17,40,82,85], illustrated by one DFT study finding that the charge around Ti in bulk $SrTiO_3$ is +2.17, compared to its formal charge of +4[85]. The valence band splits into a lower bonding and upper non-boding region, and the conduction band splits into e_g and t_{2g}[82]. The empty d band makes $SrTiO_3$ an insulator when stoichiometric while transferring electrons into d levels when reduced or excited[82,92]. The differences that arise between bulk and surface electronic structure is rooted in the different coordination environments of the surface[17], which perturb orbitals with respect to the bulk as discussed in Section 2.3.2.

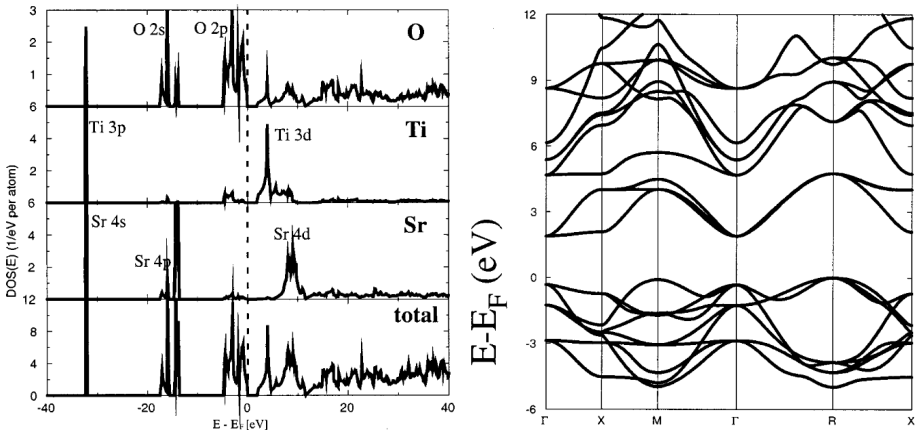

(a) *(b)*

Figure 14: Electronic structure of bulk $SrTiO_3$ displaying a) DOS including core levels and b) band structure around the Fermi level. Reproduced from [122]

As is typical for oxides, $SrTiO_3(001)$ surfaces experience enhanced covalency and decreased band gaps[82]. In the $SrTiO_3(001) - (2\times1)$ surface, for example, the average change in charge with respect to the bulk for the top surface layer Ti and O has been calculated to be -0.11 and 0.23, respectively, indicating reduced ionicity[85]. Band gap narrowing occurs by both O 2p levels shifting up in energy and Ti 3d levels shifting down[82]. One may expect the 2-fold coordinated O in the surface to have particularly high energy levels compared to the 3-fold coordinated O of the bulk[17]. The surface also sees the emergence of non-bulk-like hybridisations, e.g. an increased mixing of Ti 4s with O 2p, indicating lower symmetry coordination environments that allow orbitals to mix more freely[82]. No intrinsic surface states exist in $SrTiO_3(001)$ surfaces[82,92]. This may be understood partially by the enhanced surface covalency stabilising dangling bonds, and

partially by Coulomb repulsion between 3d electrons raising the energy of unoccupied orbitals away from the band gap[82,92]. $SrTiO_3(001)$ does, however, form a surface state in response to O vacancies[81,82], which results from reduction of Ti^{4+} to Ti^{3+} by filling a 3d orbital and is located in the band gap[17,82]. $SrTiO_3(111)$ also lacks intrinsic surface states[92] but creates this same band gap state due to O vacancies[82]. DFT calculations on $SrTiO_3(001) - (1\times1)$ predict that Ti plays an important role in adsorption also when no surface state is formed, as Ti-O hybridisation allows Ti to accept some of the charge transferred when metal adsorbates bond with O[40,123].

2.4.5 STM Studies of Metals on $SrTiO_3$

There are, to the best knowledge of the author, no published STM studies of alkali metals on $SrTiO_3$. Comparing other metals across $SrTiO_3$ reconstructions may, however, identify adsorbate behaviour so general that it should apply also to alkali metals. The selection considered for this purpose includes Au[5,66], Ag[106], Pd[76], and Cu[124] on $SrTiO_3(001) - (2\times1)$, Au[6,66], Ag[6], Pd[76], Ni[73], and Fe[79] on $SrTiO_3(001) - c(4\times2)$, Pd[74] on $SrTiO_3(001) - (6\times2) + (9\times2)$, Co[80] on $SrTiO_3(001) - (2\times2)$, as well as Au[6,66] and Ag[6] on $SrTiO_3(111) - (4\times4) + (6\times6)$. In these studies, three variables were commonly invoked to explain the observed morphologies; the underlying reconstruction, coverage and temperature, as well as epitaxy.

Considering first the underlying reconstruction, one notes that there is a rather high degree of homogeneity in crystal morphology for different metal adsorbates across different reconstructions of $SrTiO_3$. For example, FCC truncated pyramidal single crystals have been observed for Ni[73], Fe[79], and Pd[76] on $c(4\times2)$, for Co on (2×2)[80] and Cu on (2×1)[124]. The resulting epitaxy for truncated pyramidal Ni crystals on $c(4\times2)$ is $SrTiO_3(001)||Ni(001)$, $SrTiO_3[100]||Ni[100]$[73], which is a common epitaxy for metals on $SrTiO_3(001)$ surfaces[73] and has also been observed for Fe on $c(4\times2)$[79]. The reconstruction does, however, in some cases play a central role in determining morphology due to its surface energy and epitaxy with supported crystals. One example is provided by Pd, as it forms different crystal morphologies on $SrTiO_3(001)$ depending on if the underlying reconstruction is (2×1) or $c(4\times2)$, namely hut-shaped crystals with a rectangular base on the former and a variety of crystal morphologies on the latter[76]. A striking example is given by comparing Au on

(2×1) and $c(4\times2)$. On $c(4\times2)$, Au forms FCC truncated triangle single crystals, however, on (2×1), Au forms flat, irregular monolayer islands[5]. This difference was attributed to the higher surface energy of the (2×1) reconstruction, producing sufficient adhesion with Au to yield wetting, which is only possible if $\gamma_{sub} > \gamma_{ads} + \gamma_{int}$[6], as explained in Section 2.2.4.

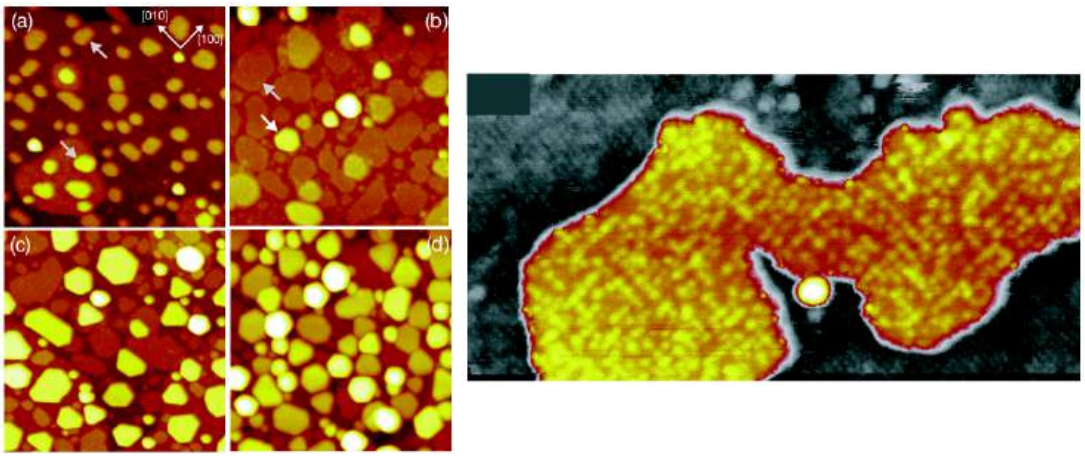

Figure 15: STM images of Au morphologies on $SrTiO_3(001)-(1\times2)$. Left: a), b), c) and d) show 0.25, 0.75, 1.25, and 1.5 ML Au deposited onto a $SrTiO_3$ substrate heated to 210°C ($80\times80\,nm^2$). 2D monolayer islands form in a), with arrows indicating typical examples. Crystals nucleate on monolayer islands in b) and grow in c). At 1.5 ML in d), nanocrystals dominate the substrate. Right: close-up of monolayer island ($60\times30nm^2$). Reproduced from [5]

The Au-on-(2×1) study mentioned above serves as an apt example also for the influence of coverage and temperature. Au forms monolayer islands only at coverage below 0.75 ML at a substrate temperature of 210 ^oC during deposition[5]. If the coverage exceeds 0.75 ML at this substrate temperature, FCC truncated triangle single crystals nucleate[5,66] (see Figure 15). This transformation is attributed to the monolayer having lower interface energy due to its greater epitaxy, but becoming metastable beyond a critical size, giving way to the single crystals[5]. Additionally, if the (2×1) substrate is held at 400 ^oC during deposition, single crystals are produced without first growing the monolayer islands[5]. The Au monolayer should, as such, constitute a metastable phase, with the single crystals being thermodynamically more stable[5].

The importance of epitaxy is demonstrated in number of metal-on-$SrTiO_3$ studies where the adsorbate adopts a crystallography that minimises lattice mismatch at the interface. Fe on $c(4\times2)$[79] and Co on (2×2)[80] are two examples, where the former adopts

BCC and the latter FCC crystallography, both of which are attributed to minimising lattice misfit strain. A study that nicely brings together the interplay between reconstruction, coverage, and epitaxy is given by Ag and Au deposited on $c(4\times2)$ and $(4\times4)+(6\times6)$[6]. On these two surfaces, Ag and Au nucleate as 5-fold symmetric MTPs, but as coverage increases, they are transformed into single crystals as they grow beyond a certain critical volume, FCC truncated triangles in the case of Ag and FCC truncated hexagons in the case of Au[6]. This MTP-to-single-crystal transformation occurs due to strain. MTPs have lower surface energy as they only have low energy {111} facets[6,66,124], but at the cost of greater strain and twin boundary energies[6,66,124], making them favoured at smaller sizes but unstable beyond a certain size[6,66,124]. Crucially, the size of the crystals at this critical volume differ between these two reconstructions, being significantly greater on $c(4\times2)$ than $(4\times4)+(6\times6)$ for both metals[6] (see Figure 16). The authors propose that possible causes for this include greater $c(4\times2)$ surface energy, as well as a higher degree of epitaxy of the FCC single crystals to $(4\times4)+(6\times6)$, as the substrate and adsorbate crystal face the interface with (111) planes, hence lowering interface energy[6].

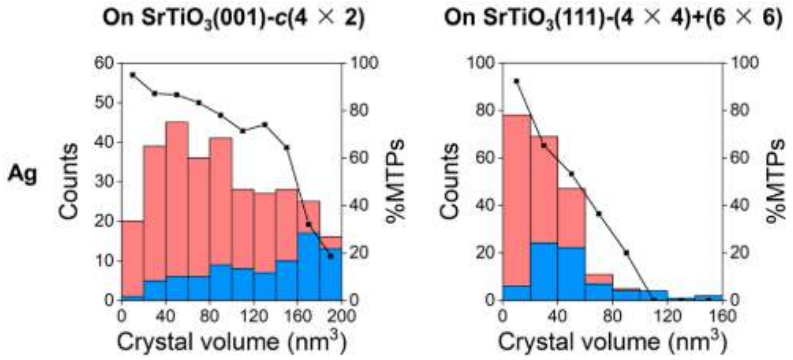

Figure 16: Populations of Ag nanocrystals on $SrTiO_3(001)-c(4\times2)$ and $SrTiO_3(111)-(4\times4)+(6\times6)$ versus crystal volume, where MTPs are represented by red, single crystals are represented by blue, and the black line is the percentage of MTPs. The critical volume is defined as the volume at which 50% of nanocrystals are MTPs and 50% are single crystals, which was $141\pm51nm^3$ on $c(4\times2)$ and $53\pm26nm^3$ on $(4\times4)+(6\times6)$[6]. Reproduced from [6]

2.5 Alkali Metal Deposition

Alkali metal deposition onto oxides has not been thoroughly studied[95], with TiO_2 being the only oxide with a relatively substantial amount of research dedicated to this interaction[125,126]. For this reason, this section will mainly treat alkali deposition on TiO_2, which will be complimented by $SrTiO_3$ studies when appropriate. This is suitable because $SrTiO_3$ and TiO_2 surfaces are structurally and electronically similar, as will be explained

in Section 2.5.2. One may thus reasonably expect that these two materials respond similarly to alkali metals deposition. It does indeed seem that the bonding behaviour of alkali metals on $SrTiO_3$ and TiO_2 surfaces are highly comparable, as will be seen in Section 2.5.3. This approach does, however, require a familiarity with TiO_2 surfaces, specifically $TiO_2(110) - (1\times1)$, which is why a brief overview of this surface is given in Section 2.5.2. Before considering oxides in particular, however, a general treatment of alkali metal interactions with surfaces will be given in Section 2.5.1, taken mainly from the rich literature on this topic in the context of semiconductors.

2.5.1 Alkali Metal Interactions with Surfaces

The strong electropositivity of alkalis make them highly reactive[127] and prone to transferring electronic charge to the surface onto which they adsorb[127–130]. The similar electronic configurations of the alkali metals Li, Na, K and Cs make their chemical and physical properties alike[46], and one may consequently expect them to have similar behaviour on a given surface. There are, however, differences in alkali metal valence orbital structure that may influence bonding geometry. Li, for example, has 2s and 2p orbitals that are close in energy, enabling a larger variety of bonding hybridisations and geometries[131]. Li thus has a greater p-type character in its valence band than Na, giving it a more directional bonding e.g. on Si(111)[132]. One must also take into consideration the extreme size and electropositivity of Li, making its adsorption behaviour especially dependent on the local electronic and geometric structure of the surface[127,132]. This has been used to explain the remarkably highly anisotropic surface diffusivity of Li on e.g. W(112)[127]. On oxides, alkali metal bonding tends to be driven by coordination, making them prone to choosing adsorption sites that maximise their O availability[11,125] while reducing the repulsion from substrate cations[133]. On semiconductors, they instead tend to be driven by saturation of dangling bonds[48,134,135], aiming to produce a surface bonding arrangement where dangling bonds are either empty, filled, or saturated by the alkali metal[48]. In general, adsorption site preference is expected to be determined more by local bonding configurations on oxides than on metals and elemental semiconductors, while alkali-alkali interactions play a greater role in the case of the latter two[126].

Four phenomena were identified from the literature on alkali metal deposition that

are particularity relevant to this project. Firstly, on a general surface, the ionicity of the alkali-surface bond is heavily influenced by their coverage on the surface. At low coverages, alkalis form heavily ionic bonds to the surface, producing strong surface dipoles[95,127,130,136]. As coverage increases, alkalis are expected to become increasingly depolarised due to dipole-dipole repulsion between neighbouring adsorbates, thus increasing covalency and decreasing adsorption strength with increasing coverage[127,130,136]. Secondly, alkali metals produce surface states on a variety of surfaces. When deposited onto Si, for example, alkali orbitals mix into the Si conduction band, producing strongly hybridised and highly reactive unoccupied states close to the Fermi level[134]. Alkali-induced reduction may push the Fermi level into the conduction band, thus filling unoccupied states and producing surface states that cause local metallisation[8,134]. Thirdly, alkali metals have demonstrated a significant degree of mobility on Si surfaces. One may find this somewhat counter-intuitive due to the expected strength of the charge transfer and resultant adsorption bond[137], however, for sub-monolayer coverages of Li and K on $Si(111)-(7\times7)$, both alkalis form clusters smaller than 10 atoms that readily diffuse across the surface[137]. Fourthly, there is a maximum threshold to the charge a surface can receive before it must change reconstruction[138]. The reductive power of alkali metals thus make them able to induce new reconstructions, which has been frequently reported on Si[9,48,132,134,139–141]. This has been attributed to changes in Si bonding preferences due to filling of unoccupied Si states[134]. Reconstruction induction is dependent on the original reconstruction, coverage and temperature[9,48,134]. For example, on $Si(001)-c(4\times2)$, 0.5 ML Li induces a $c(2\times2)$ reconstruction and 1.0 ML Li induces a $c(2\times1)$ reconstructions[9,134]. Various alkali metals induce (3×1) reconstruction on $Si(111)-(2\times1)$[48,135,141], with the amount of the surface that is converted depending on the amount of alkali deposited[135]. When Cs adsorbs to the $Si(111)-(2\times1)$ reconstruction, 1/3 ML and 100^oC annealing suffices to produce the (3×1) surface structure, but for $Si(111)-(7\times7)$, it is only seen after 300^oC to 500^oC annealing[48].

2.5.2 Structure of $TiO_2(110)-(1\times1)$

Rutile $TiO_2(110)$ is probably the most extensively studied oxide surface of all[11,58,81]. This is the lowest energy termination of rutile TiO_2 and has a stable, non-reconstructed (1×1) surface[11,125]. $TiO_2(110)-(1\times1)$ is composed of two Ti polyhedra, bulk-like TiO_6 and $TiO_5[]$[11,142]. O similarly has two coordination environments, either bulk-like

3-fold or 2-fold[56]. These coordination environments make $TiO_2(110)-(1\times1)$ structurally similar to $SrTiO_3(001)$[92], and are due to the periodic rows of O protruding from the $TiO_2(110)-(1\times1)$ surface. 2-fold coordinated O is found in the rows, 5-fold coordinated Ti and 3-fold coordinated O between rows, and 6-fold coordinated Ti under rows[142] (see Figure 17). 3-fold coordinated O is commonly referred to as in-plane O and 2-fold coordinated O is referred as bridging O[56]. $TiO_2(110)-(1\times1)$ has two main alkali metal adsorption sites which are referred to as the "in-between" and "adjacent" sites[11,56,125,126,143,144], displayed in Figure 17. When alkali metals adsorb to either of these sites they are coordinated by three O[125]. Step edges on $TiO_2(110)-(1\times1)$ produce additional coordination environments, e.g. hosting TiO_4 units[11]. $TiO_2(110)$ also hosts a (1×2) reconstruction with similar coordination and adsorption sites that emerges at high temperatures due to removal of every other row from the (1×1) structure[125].

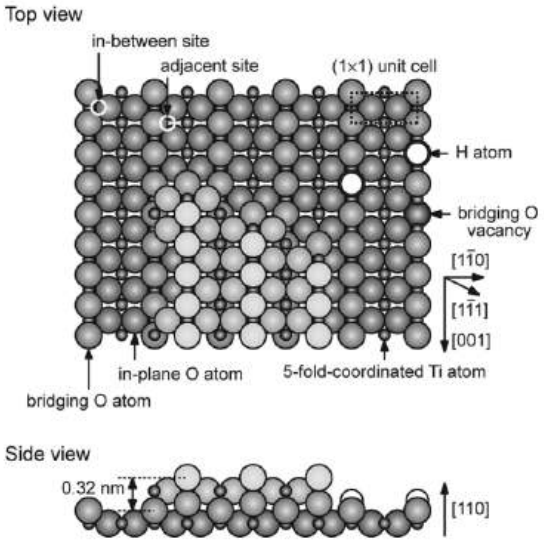

Figure 17: Structure of rutile $TiO_2(110)-(1\times1)$, where Ti and O are represented as small and large balls, respectively. Adsorption sites and the two different surface coordination environments for O can be seen in the "Top view" image, and the rows of O in the "side view" image. In the in-between site, an alkali metal adsorbate bonds two bridging O and one in-plane O, and in the adjacent site, it bonds one bridging O and two in-plane O[11,56,126,145]. Reproduced from [145].

The discussion of $TiO_2(110)$ surface electronic structure can fortunately be held brief, as TiO_2 surfaces have electronic structures similar to those of $SrTiO_3$. This is firstly because the bulk electronic structures of $SrTiO_3$ and TiO_2 are highly similar around the band gap[82,92], which is largely due to the low-lying energy levels of Sr[82], making it possible to approximate Sr as a +2 point charge[17]. Secondly, as is typical for d^0 transition

metal oxides[92], both $SrTiO_3$[92] and TiO_2[11,17] have surface electronic structures similar to their bulk. The syllogistic conclusion is thus that $SrTiO_3$ and TiO_2 surfaces have similar electronic structures around the band gap. This is exemplified by the electronic structure of TiO_2(110) sharing the following features with $SrTiO_3$(001), which were discussed in Section 2.4.4: an O 2p-dominated valence band split into a lower bonding and upper non-bonding region[82], a Ti 3d-dominated the conduction band split into e_g and t_{2g}[82], significant covalency between O 2p and Ti 3d[11,17,82], enhanced surface covalency[17,82], decreased surface band gap[17,82], lack of intrinsic surface states[11,17,82,92], and a Ti 3d band gap surface state that forms due to O vacancies[11,81,82]. Interestingly, TiO_2(110) has also been observed to form surface states due to alkali adsorbates[11,96,129,146,147]. This surface state is physically similar in both the case of O vacancies and alkali adsorbates[11,56,65,148] and will be treated detail in 2.5.3.

2.5.3 Alkali Metal Deposition on TiO_2(110) and $SrTiO_3$(001)

2.5.3.1 General Bonding Characteristics

Building on Section 2.5.1 and 2.5.2, one may expect that alkali metal bonding characteristic on TiO_2 and $SrTiO_3$ surfaces are fundamentally similar. This is indeed what has been observed. On both surfaces, the first alkali metals to adsorb transfer charge to Ti ions[95,96,126,129,143,146,149–153] and form heavily ionic bonds with O[56,125,133,154,155]. This produces strong dipoles on the surface[11,56,128,144–146,148,152,156,157]. However, as coverage increases, so does dipole repulsion[11,56,133,142,143,146,151,152,154,158,159], leading alkali ions to depolarise and form increasingly covalent O bonds[11,56,126,144,145,155,156,158]. Since Na is the most well-studied alkali on TiO_2(110)[11,145], which with little doubt is the most well-studied alkali-on-oxide surface system, the evolution of the alkali metal bond as a function of coverage will be illustrated with Na on TiO_2(110) as the example.

Na adsorbates on TiO_2(110) transfer electrons to Ti^{4+} ions, reducing them to Ti^{3+}[143,151], and subsequently forming effectively fully ionic Na-O bonds[56,145,148,158] and strong Na dipoles[125,142]. As coverage increases, so does Na-Na repulsion[56,142,143,151,158], and at some critical coverage, Na and Ti levels start crossing[56]. At this coverage, Na levels subsequently start increasing in occupation, leading to a markedly lower ionicity in the Na-O bond[56]. This is when the character of the Na bond changes most dramatically[56], and as coverage

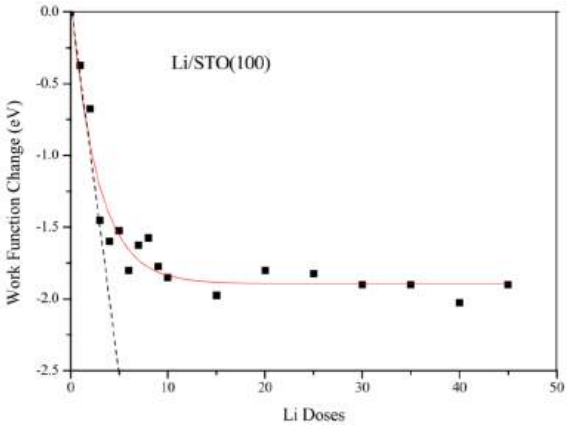

Figure 18: Work function versus Li coverage after Li deposition onto $SrTiO_3(001)$, where 10 doses correspond to one monolayer coverage. The magnitude of the derivative is greater the smaller the coverage, indicating that the lower the coverage, the more ionic the Li bond. Reproduced from [155].

increases beyond this point, the bond becomes increasingly covalent[56,126,145,156,158]. This is expressed by the $TiO_2(110) - (1\times1)$ work function ceasing to change when 0.3 ML Na has been deposited, indicating that charge transfer has plateaued[151]. Notable covalency is detected in XPS at 0.2 ML coverage and above[158] and Bader charge calculations indicate that bonding is predominantly covalent at circa 0.5 ML[56]. At 0.5 ML, furthermore, Na-Na interactions are predicted to dominate adsorption energetics over precise adsorption site geometry[56], with adsorption site geometry being optimised to screen Na-Na repulsion to accommodate the maximum number of Na atoms[56,126]. A similar pattern of deceasing ionicity with coverage has been documented also for Li[146,149], K[133] and Cs[159] on $TiO_2(110)$, as well as Cs[128,157,160] and Li[155] on $SrTiO_3(001)$ (see Figure 18). These trends, however, only reveal general features of the bonding between alkali adsorbates and $TiO_2(110)$ or $SrTiO_3(001)$, and do not provide atomic-scale information about e.g. bonding geometries and the resulting surface structures, which may differ between alkali adsorbates and surfaces. One study indicates that the differences between surfaces may in fact be significant, as clear differences were observed in the bonding character of the initially adsorbing Na between $TiO_2(110) - (1\times1)$ and (1×2)[125]. Photoemission spectroscopy indicated that the initial Na to adsorb on $TiO_2(110) - (1\times2)$ forms a 1.15 eV stronger bond than on (1×1)[125]. Na on (1×2), in addition, has a valence spectrum more similar to typical alkali-oxide compounds than (1×1), indicating different O coordination around Na on these two surfaces[125]. This shows the importance of detailed atomic-level structure for bonding, which will be treated below.

2.5.3.2 Low Coverage Adsorption

As mentioned in Section 2.5.2, two primary adsorption sites have been identified on $TiO_2(110)-(1\times1)$; the in-between site, coordinated by two bridging O and one in-plane O, and the adjacent site, coordinated by one bridging O and two in-plane O (see Figure 19a). Some other low-energy sites are also available [145], as can be seen in Figure 19b. Studies involving adsorption site preference have been conducted for Na[56,125,126,148,161] Li[11,145,146], K[133,144]. Which site is ultimately preferred is expected to be driven by minimisation of repulsive interactions with Ti and maximisation of the attractive interactions with O[133]. In addition, the native $TiO_2(110)-(1\times1)$ atoms around the adsorption site experience significant relaxation as the alkali metal-O bond forms[56,96,125,142,143,146,162], which influences the favourability of the adposition site[96]. It is primarily the Ti-O bonds of the O atoms bonding the alkali adsorbate that change[56,146,162] and the bridging O atoms are expected to be most displaced[143], with calculations predicting displacements of up to 0.2 Å[125].

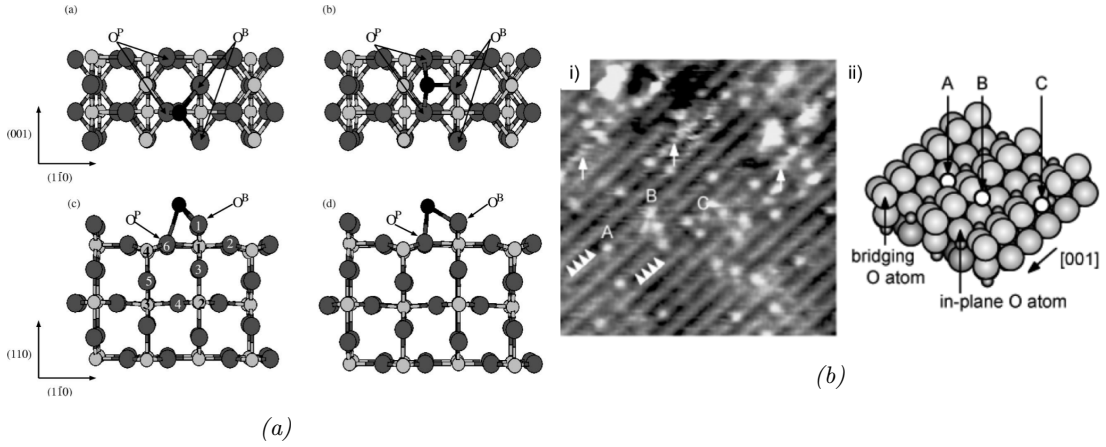

Figure 19: Alkali adsorption sites on $TiO_2(110)-(1\times1)$. Image a) shows a schematic of Na adsorbed on the in-between site (left), bonding two bridging O and one in-plane O, and adjacent site (right), bonding one bridging O and two in-plane O. O^P and O^B are in-plane O and bridging O, respectively. Image b) shows i) an STM image ($10\times10\,nm^2$) indicating three Li adsorption sites; a 4-fold coordinated hollow site (A), the adjacent site (B), and an O vacancy site (C). Arrowheads indicate an unidentified species. Image ii) shows a schematic of these adsorption sites. Reproduced from [56] and [145]).

Na will again serve as the example, this time for alkali adsorption site preference on $TiO_2(110)-(1\times1)$. The most common conclusion in the literature is that the in-between site is the most preferred one for lone Na atoms at low coverages before Na-Na interactions become a significant factor[56,125,126,143,161,163]. The key reasons for why the in-between site would be preferred are likely lower Na-Ti electrostatic repulsion[125] and lower

coordination of bridge than in-plane O[56,151]. This allows for more charge transfer at the in-between rather than the adjacent site, calculated by one study to be $+0.91|e|$ vs. $+0.90|e|$, respectively. The same study found the in-between site to have a greater adsorption energy by 0.24 eV[56]. The adjacent site has, however, been found to start dominating at high coverages[126,143]. This could be due to alkali-alkali repulsion, as explained in the sub-section above. The prevailing model is hence that Na adsorbs to in-between sites at low coverage, but as coverage increase, the adjacent site becomes less energetically disadvantaged until it becomes preferable. It should, however, be said that there is not universal agreement about which site is the most preferred at low coverage[11,56,143], with both some experimental[142] and theoretical studies[148] finding a preference for the adjacent site.

In the case of both Li[11,145] and K[11,133,144], the in-between site is often proposed as the preferred adsorption site. Li has, in addition, like Na been proposed to switch to the adjacent site at high coverage[145]. Studies pertaining to K adsorption site preference have been less conclusive in terms of site preference as coverage increases[143], and it has been suggested that K does not switch to the adjacent site but instead binds two bridging O[133]. At coverages that yield significant alkali-alkali interactions on the surface, superstructures of periodically arranged alkali adsorbates have been reported on both $TiO_2(110)-(1\times1)$ and (1×2)[11]. On $TiO_2(110)-(1\times1)$, Na has displayed two such superstructures, $p(4\times2)$ at 0.3 ML coverage and a $c(4\times2)$ at 0.5 ML coverage[151,158] (see Figure 20). K has, similarly, been observed to form superstructure with a $c(2\times2)$ ordering on the same surface at circa at 0.5 ML coverage[11]. The structural models proposed for these long-range ordered structures have, however, been put into question by some authors[126], and some publications report that superstructures were not reproduced, e.g. for Na on $TiO_2(1\times1)-(1\times1)$[125].

2.5.3.3 High Coverage Adsorption

At high coverage in the order of one to a few monolayers, the small distance between alkalis together with their now weak dipoles allow for orbital overlap, producing metallic bonding states that start filling at a critical coverage[56,142]. Such structures have, to the best knowledge of the author, not been studied in STM, but are evidenced by spectroscopic data for both $TiO_2(110)$ and $SrTiO_3(100)$. On $TiO_2(110)-(1\times1)$, metallic alkali bonding has

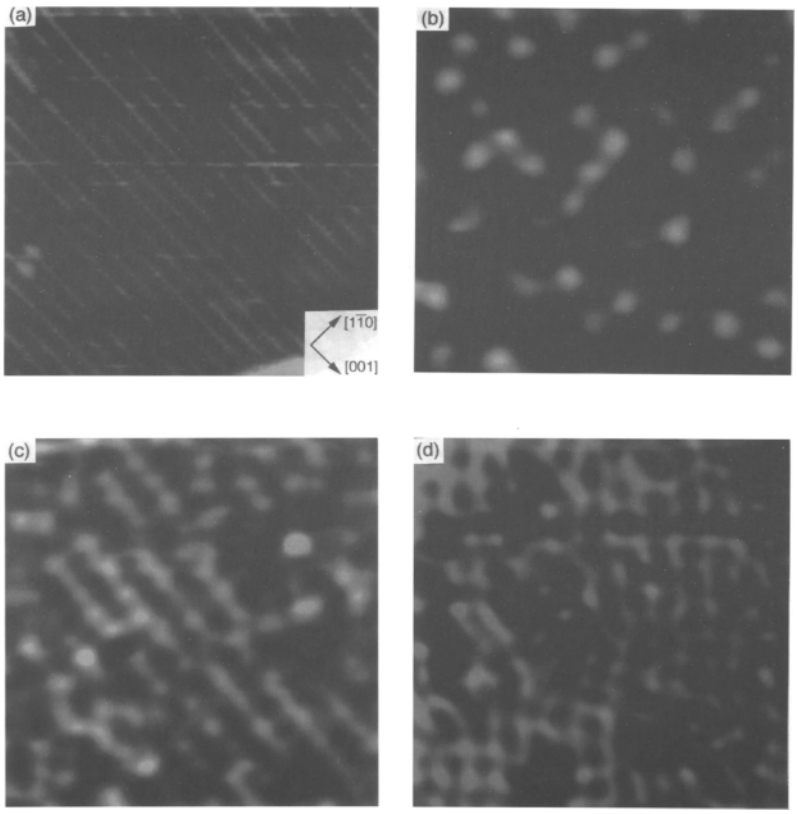

Figure 20: STM images ($14\times14nm^2$) of Na superstructures on $TiO_2(110)-(1\times1)$, where a) shows the clean surface, b) dispersed Na particles, c) the $p(4\times2)$ superstructure, and d) the the $c(4\times2)$ superstructure. Reproduced from [158].

been observed for 1 ML Cs[159] and 2-3 ML Na[126], and has been predicted by calculations of K[133]. The study on Cs provides an interesting example, as 1 ML Cs coverage produces a change in the Cs 3d:Ti 2p XPS peak ratio, which grows constantly with coverage below 1 ML, but thereafter tends towards being constant[159]. This was interpreted as Cs initially having a 2D growth mode which switches to 3D at circa 1 ML coverage[159]. In the case of alkalis on $SrTiO_3(001)$ surfaces, some metallic Cs have been observed to exist already at a coverage of 0.5 ML[128,157], whereas neither Li[128,155] nor K[128,152] form metallic states at this coverage. This may be explained by weaker Cs-$SrTiO_3(001)$ interaction together with stronger Cs-Cs interaction, and is corroborated by Cs adsorption not significantly altering the Ti/O Auger peak ratio, indicating no significant driving force to form Cs_xO_y compounds[128]. The opposite is true for Li, as Auger electron spectroscopy indicates that Li reacts with the surface to form Li-O compounds[128]. Such alkali-O compounds are increasingly likely to form at higher temperatures, as alkali metals are substantially more prone to reduce the $TiO_2(110)$ surfaces as temperature increases[11]. This redox activity would likely produce alkali oxides[11,149] like K_2O[11], but could also result in alkali titanates[149,159],

such as $Na_2Ti_2O_5$ and $K_2Ti_2O_5$[159].

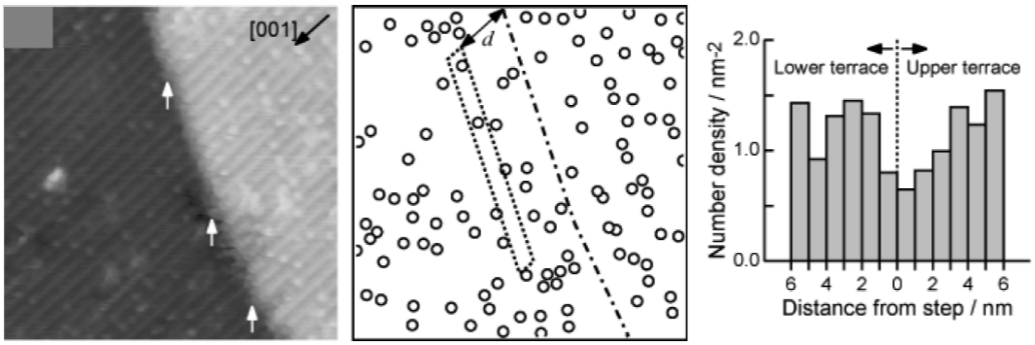

Figure 21: a) STM image of Li adsorbed around a step edge on $TiO_2(110)-(1\times1)$ ($16\times16\,nm^2$). Arrows indicate features attributed to Li atoms attached to the step edge. b): Model of the STM image, where circles signify Li atoms, the dashed line the step edge, and the dotted rectangle an area 1 nm in width that was used for measuring Li number density. c) Li number density as a function of distance from the step edge, where each gray bar corresponds to a rectangle like the one indicated in b). Number density tends to increase away from the step edge. Reproduced from [145].

2.5.3.4 Noteworthy STM Observations

Three reported behaviours of alkali metals on $TiO_2(110)$ surfaces are especially noteworthy for the purpose of this project. Firstly, STM shows that alkalis adsorbates have high mobility on $TiO_2(110)-(1\times1)$. At room temperature, Li has been observed to actively switch adsorption sites with a 30% to 90% probability of remaining between scans depending on the site[145]. The probabilities of leaving adjacent and in-between sites between scans, for example, were calculated to be 80% and 60%[145]. One calculation supports this observation, indicating that K on $TiO_2(110)$ has a comparatively flat potential energy surface[144].

Secondly, alkali metals have a significant interaction with step edges. STM reveals that the concentration of Li particles is reduced within a few nm of step edges on $TiO_2(110)-(1\times1)$[145], as displayed in Figure 21. The authors suggest that this is due to Li atoms attaching to step edges, the electronic structure of which is more perturbed by the associated charge transfer than terraces, which disincentivises further charge transfer in the step edge vicinity[145]. Step edge interactions have been observed also spectroscopically. Comparing the stepped $TiO_2(441)$ surface to flat $TiO_2(110)$, the work function of the former changes significantly less than the latter at the same coverage of 1.0 ML Na[151]. At this coverage, the stepped $TiO_2(441)$ surface experiences a work function decreased by 2.3 eV, compared to the 3.4 eV of the flat $TiO_2(110)$ surface[151]. This indicates a smaller

charge transfer to the stepped surface[151].

Thirdly, it has been suggested that alkali metals may have been seen to induce reconstructions on $TiO_2(110)$. There is namely one publication which proposes that Na could have induced a (2×2) reconstruction on $TiO_2(110)-(1\times2)$ at a coverage as low as circa 0.01 ML Na[164] (see Figure 22). The structural model presented for this reconstruction suggests that it is generated by displacing three O from the O rows along [001] in the $[1\bar{1}0]$ direction. The (2×2) formation was proposed to be a response to reduction from Ti^{4+} to Ti^{3+}[164]. The (2×2) reconstruction could allow Na to increase O coordination by enabling a 4-fold coordination, hence minimising further charge transfer in the vicinity of already reduced Ti^{3+}[164]. The authors noted that this would be the first observation of an alkali-induced reconstruction of an oxide surface if their proposal is indeed correct[164].

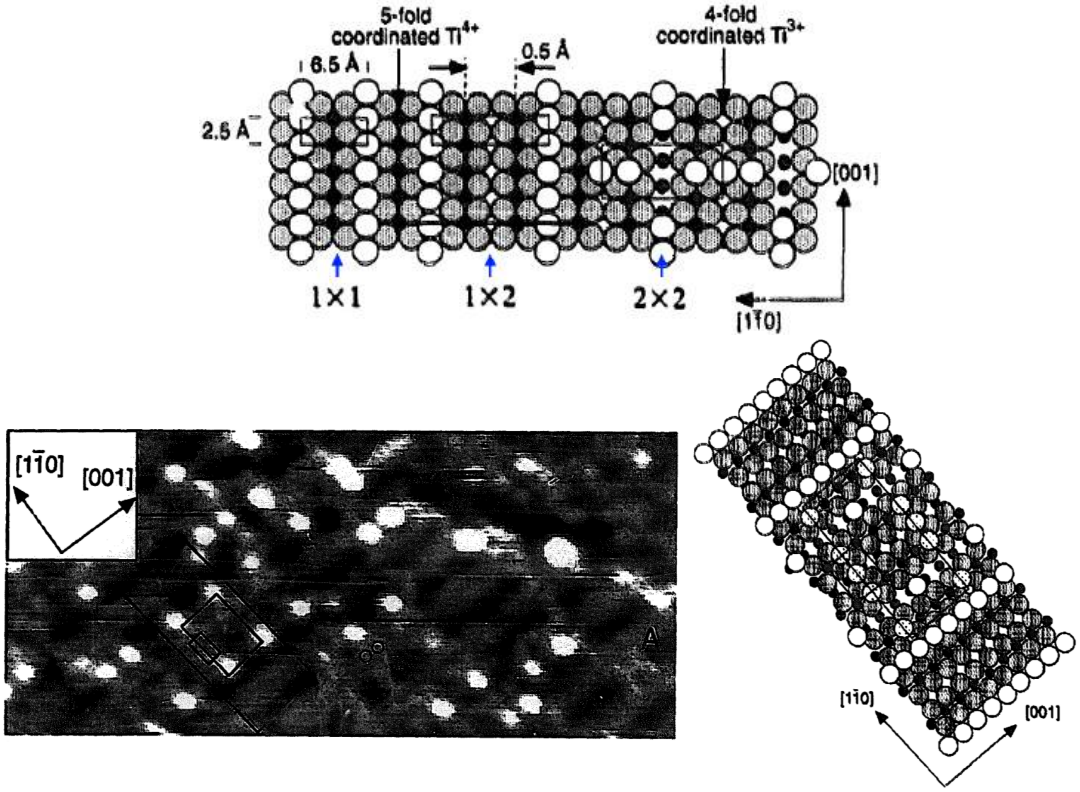

Figure 22: Models and STM image of the proposed (2×2) reconstruction. Large white and gray circles are bridging and in-plane O, respectively, small black circles are Ti, and small white circles are Na. Top: model of the $TiO_2(110)-(1\times1)$, (1×2), and (2×2) reconstructions, where the displacement of bridging O in the $[1\bar{1}0]$ direction for the generation of (2×2) is made clear. Bottom left: STM image ($10\times20nm^2$) with (2×2) indicated by the black rectangle. Bottom right: model of the STM image, where the suggested 4-fold coordination of Na in (2×2) is visible at the corners of the black rectangle showing the (2×2) surface unit cell. Reproduced from [164].

2.5.3.5 Electronic Effects

As an alkali adsorbs to $TiO_2(110)-(1\times1)$, charge around the adsorption site is redistributed to accommodate the alkali ion and transferred electron[56]. The electron transferred to surface is frequently calculated to concentrate at 5-fold coordinated surface Ti atoms near the adsorption site[11,133,144,145,148,151,161,163]. This charge, however, is also frequently calculated to have a significant degree of delocalisation, thus being spread over this 5-fold Ti and some of the O atoms it bonds[56,145,147,148,161]. The bridging O has been identified to be particularly willing to host some of the received charge[145]. Some studies find the excess charge to be particularly delocalised and shared between a few Ti atoms close to the adsorption site[148]. The delocalisation of the excess charge is expected to increase with coverage and attain more alkali orbital character[56]. The transferred charge stays near the alkali adsorbate, with one study finding that 0.4 electrons remain within 5.5 Å from Na adsorbed to both the in-between and adjacent sites of $TiO_2(110)-(1\times1)$[56]. Some authors have, however, found that the charge is instead concentrated at a 6-fold Ti that bonds bridging O from below[56]. The Ti orbital that accepts the lion's share of the alkali-donated charge is a Ti 3d orbital[11,96,129,143,144,148,151,161]. It has been suggested that this orbital specifically is the $3d_{x^2-y^2}$[148,150,161,163], which is an e_g orbital and directed towards the octahedrally coordinating O ligands. Filling this orbital would thus be in line with O accepting some of the charge and consequently increasing covalency with the Ti in question.

The electron received into the Ti 3d state can produce a surface state in the band gap, which is widely reported for alkalis on $TiO_2(110)$ surfaces[11,56,95,96,129,143,144,146–148,161]. A UPS spectrum of this state is displayed in Figure 23a. Due to its greater electropositivity, Li produces the surface state at lower coverage than Na[148]. It has been suggested that at higher coverage, the Ti states that accept the excess charge increase in energy due to increased electron-electron repulsion until their levels start crossing[56], resulting in a Ti 3d state just beneath the conduction band which is not localised at any individual Ti atom[56]. Some studies have, furthermore, found the band gap state to have a notable degree of spin-polarisation[11] and hybridisation of Ti 3d with e.g. Ti 4s[150] or Li 2s[147].

The alkali-induced surface state in $TiO_2(110)$ is similar to the O vacancy surface state, as explained in Section 2.5.2. $SrTiO_3(001)$ and $SrTiO_3(111)$ also produce this O vacancy

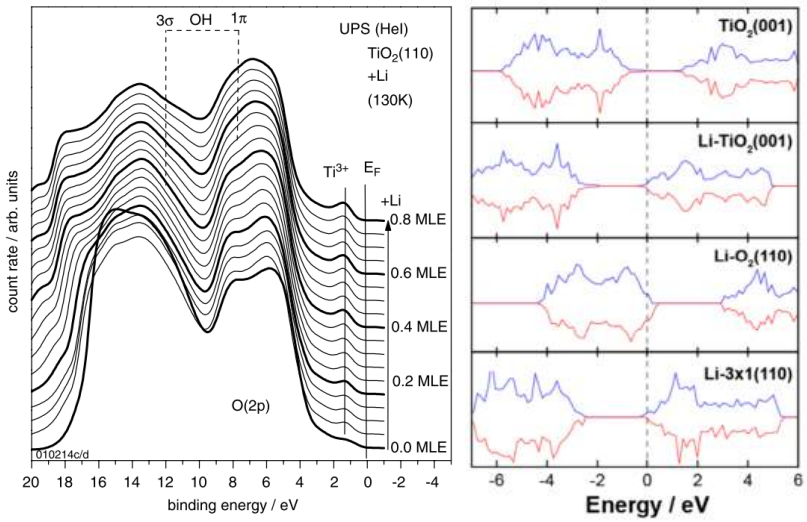

(a) *(b)*

Figure 23: Alkali-induced band gap surface state in rutile TiO_2 and possibly $SrTiO_3$: Left: UPS of Li deposition onto $TiO_2(110)-(1\times1)$, showing the growth of the surface state with increasing monolayer equivalents (MLE). Right: DFT calculated DOS for a single Li adatom on various $SrTiO_3$ terminations which, top to bottom, are clean $SrTiO_3(001)-TiO_2$, Li on TiO_2-terminated $SrTiO_3(001)-(1\times1)$, Li on O_2-terminated $SrTiO_3(110)-(1\times1)$, and Li on $SrTiO_3(110)-(3\times1)$. Reproduced from [146] and [153]

surface state, as mentioned in Section 2.4.4, which like that of $TiO_2(110)$ is of Ti 3d character and located in the band gap. One may as such anticipate that the $SrTiO_3$ surface also could produce the alkali-induced surface state. There is some evidence that this is indeed the case. One study namely finds that Li adsorption onto both O_2-terminated $SrTiO_3(001)$ and $SrTiO_3(110)-(1\times3)$ make some conduction band Ti 3d states occupied, correlating with the Ti^{3+} found by XPS in the same study[153] (see Figure 23b). It was also found that Li adsorption energy was strongest in a 4-fold coordinated site on the O_2 surface, 0.61 eV stronger then TiO_2, and that binding energy decreased with decreasing excess O per (1×1)[153]. Na has similarly been calculated to attain a 4-fold coordinated site on TiO_2-terminated $SrTiO_3(001)$,[154], where it produces a significantly greater adsorption energy than the SrO-terminated surface[154]. Charge was more localised around Na on the SrO surface, whereas on the TiO_2 surface, charge donated by Na was comparatively evenly distributed between Ti and O, leading to a greater total charge transfer[154]. Alkali adsorption on $SrTiO_3$ hence seems to have similarities to TiO_2 in addition to the band gap state, including significant Ti participation in carrying the accepted charge and adsorption site preferences being heavily dictated by the coordination of O.

2.6 Conclusion

Alkali metals have not been extensively researched on oxide surfaces in general, with only TiO_2(110) having significant microscopic, spectroscopic and theoretical data sets available, which was presented in Sections 2.5.3. There are a number of insights from this data that can be carried over to the case of alkali metals on $SrTiO_3$, with some insights already having reasonable support from existing studies. Alkali metals on TiO_2(110) and $SrTiO_3$(001) bond to the surface more covalently the higher their coverage, which is true for alkali metal deposition on surfaces in general. The electrons transferred to the TiO_2(110) surface fill an unoccupied Ti 3d orbital which produces a band gap surface state, similar to the O vacancy state observed in $SrTiO_3$(001) and $SrTiO_3$(111). The electrons accepted by TiO_2(110) are thus concentrated at Ti atoms but have a significantly delocalised wavefunction, with at least some neighbouring O atoms accepting a notable amount of the charge. O coordination is crucial for adsorption site selection on TiO_2(110) with O under-coordination probably playing a large role, and step edges have an interaction with the alkali adsorbates that reduces charge transfer to the substrate. It seems, however, that no alkali-on-TiO_2 study has thus far involved annealing. Considering the necessity of annealing for obtaining the equilibrium morphology of less reactive metals on $SrTiO_3$ (Section 2.4.5) and the dramatic change annealing induces for alkali metals on semiconductors (Section 2.5.1), annealing could likely reveal alkali-on-$SrTiO_3$ surface structures that are much different from the structures reported on TiO_2 to date. The following chapters will show that this is indeed the case.

3 Experimental Methods

3.1 Introduction

Three techniques were used in this project, namely scanning tunnelling microscopy (STM), X-ray photoelectron spectroscopy (XPS), and density functional theory (DFT). This chapter provides a brief introduction to these techniques and details how they were implemented. STM and XPS are were carried out in separate ultra-high vacuum (UHV) systems within the Department of Materials. DFT calculations were conducted on the Advanced Research Computing (ARC) system.

3.2 Scanning Tunnelling Microscopy

STM is a type of scanning probe microscopy where electron density is measured to generate images of surfaces[165]. As the name implies, STM relies on quantum mechanical tunnelling[166]. This phenomenon results from the fact that even though a particle's wavefunction decays beyond a potential barrier, its amplitude is still non-zero, enabling the particle to emerge on the other side if the barrier is narrow enough[165]. This is exploited in STM by scanning an atomically sharp metallic tip a few Å above a conducting surface with a bias between the two, generating a current as electrons tunnel across[167] (see Figure 24).

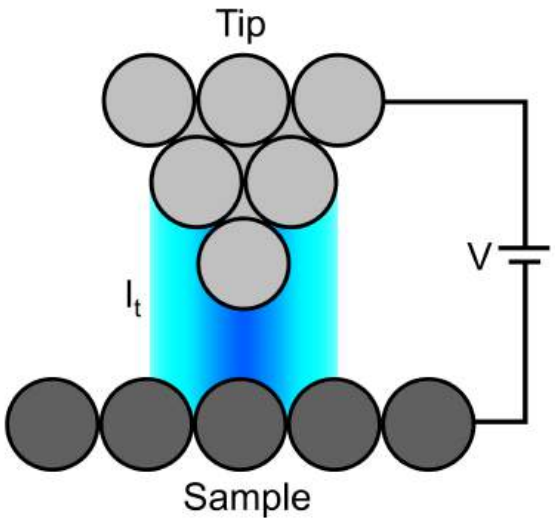

Figure 24: Generic STM operation where a tip is scanned over a sample under a bias V to generate a tunnelling current I_t by electrons tunnelling across the gap.

3.2.1 Quantum Mechanical Tunnelling

Bardeen's theory is the most common mathematical formulation of quantum tunnelling[166]. It starts with the time-dependent Schrödinger equation to derive an expression for the tunnelling current between two electrodes, such as a sample and a tip in STM. Considering a sample and a tip separated by a vacuum d in the z direction, one can treat sample and tip states in isolation when d is large. In this case, sample states are governed by the sample Hamiltonian $\hat{H}_s$ and tip states are governed by a separate tip Hamiltonian $\hat{H}_t$. The time evolution of a specific sample state $|\psi_\mu\rangle$ is then given by $i\hbar\frac{\delta}{\delta t}|\psi_\mu\rangle = \hat{H}_s|\psi_\mu\rangle$, for which the energy eigenvalue E_μ is given by $\hat{H}_s|\psi_\mu\rangle = E_\mu|\psi_\mu\rangle$ and the solution takes the form $\psi_\mu(t) = \psi_\mu(0)e^{-iE_\mu t/\hbar}$.

When, however, the separation between sample and tip is so small that $|\psi_\mu\rangle$ significantly overlaps with a tip state $|\chi_\nu\rangle$ as they decay into the vacuum (see Figure 25), electrons in $|\psi_\mu\rangle$ have some finite probability of tunnelling into $|\chi_\nu\rangle$. In this situation, energy eigenvalues must be found using the combined sample and tip Hamiltonian $\hat{H}$[166]. Under the assumption that the overlap between wavefunctions is small compared to their totality, one can for short times t make a perturbation theory-type argument[168] that $\psi_\mu(t)$ stays close to $\psi_\mu(0)e^{-iE_\mu t/\hbar}$. One can then modify $\psi_\mu(t)$ by adding a sum over all tip states $\chi_\nu(0)$ weighted by the transmission coefficients $c_\nu(t)$:

$$\psi_\mu(t) = \psi_\mu(0)e^{-iE_\mu t/\hbar} + \sum_\nu c_\nu(t)\chi_\nu(0)e^{-iE_\nu t/\hbar}. \tag{1}$$

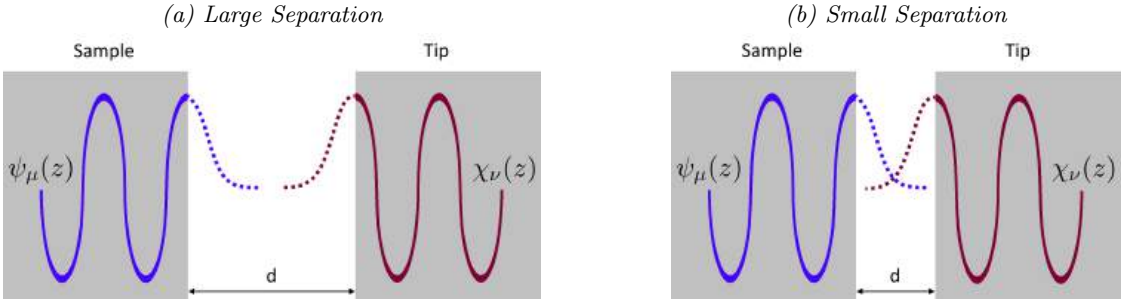

Figure 25: Schematic of wavefunction decay into the vacuum a) without significant overlap when the separation d is large and b) with significant overlap when d is small, enabling quantum tunnelling .

3.2.2 The Tunnelling Current

The transitions coefficients $c_\nu(t)$ in Equation 1 serve to describe the likelihood of transmission to a specific tip state. These coefficients are the central quantity in Bardeen's theory that must be found to establish an expression for the tunnelling current. Strategies for evaluating this expression are readily available in the literature, for example in references [166] and [168], but require excessive mathematical detail, for which reason this treatment will proceed descriptively. Reflecting on the physics of STM, one may start by noticing that tunnelling must obey the conservation of energy[169], which motivates the assumption that the transition from $|\psi_\mu\rangle$ to $|\chi_\nu\rangle$ only occurs when $E_\mu \approx E_\nu$. This can be described by the Dirac delta $\delta(E_\mu - E_\nu)$. Tunnelling must also obey the Pauli exclusion principle, as an electron can only transition from $|\psi_\mu\rangle$ to $|\chi_\nu\rangle$ if $|\psi_\mu\rangle$ is occupied and $|\chi_\nu\rangle$ is not, captured by the Fermi functions $f(E_\mu)$ and $\big[1 - f(E_\nu + eV)\big]$, respectively, were V is the potential between sample and tip. One must additionally consider that the amplitude of electron transfer is greater between some states than others[166], which is described by the tunnelling matrix element $M_{\mu\nu}$. Lastly, in order to capture all possible transitions from sample to tip, one sums over all sample state indices μ and tip state indices ν. After these considerations, one can appreciate the following expression for the tunnelling current, I_t, which follows from Bardeen's theory[170]. The prefactor $2\pi/\hbar$ in this equation comes from the precise evaluation of $c_\nu(t)$.

$$I_t = \frac{2\pi e}{\hbar} \sum_{\mu,\nu} f(E_\mu)\big[1 - f(E_\nu + eV)\big]\, |M_{\mu\nu}|^2\, \delta(E_\mu - E_\nu). \tag{2}$$

3.2.3 Tip-Sample Separation

$M_{\mu\nu}$ contains essential information for the STM operator, as it reveals the significance of tip-sample separation for the magnitude of the tunnelling current. $M_{\mu\nu}$ captures the fact that only tunnelling events associated with a constructive interference contribute to the current[169], and is given by the following surface integral, valid over any area that lies entirely within the vacuum region[170]:

$$M_{\mu\nu} = \frac{\hbar^2}{2m} \int \big[\psi_\mu(z)\nabla\chi^*_\nu(z) - \chi^*_\nu(z)\nabla\psi_\mu(z)\big]\, dxdy. \tag{3}$$

One can approximate $M_{\mu\nu}$ by substituting into Equation 3 the expressions for wave-

function decay in the vacuum, namely $\psi_\mu(z) = \psi_\mu(0)e^{-k_\mu z}$ and $\chi_\nu(z) = \chi_\nu(d)e^{-k_\mu(z-d)}$. Assuming decay constants for both wavefunctions are the same[166], i.e. $k_\nu = k_\mu$, one finds that:

$$M_{\mu\nu} = \frac{\hbar^2}{2m}\int 2k_\mu\psi_\mu(0)\chi_\nu(d)e^{-k_\mu z}e^{k_\mu(z-d)}\,dxdy = \Big[\int m_{\mu\nu}\,dxdy\Big]e^{-k_\mu d}. \tag{4}$$

Assuming for the sake of argument that $\int m_{\mu\nu}\,dxdy$ is a constant, it follows from Equation 4 that $I_t \propto e^{-k_\mu d}$. This inverse exponential dependence of tunnelling current on the separation between tip and sample is the source of the extreme vertical and lateral resolution that enables atomic scale imaging in STM. Increasing this separation by only 1 Å decreases the tunnelling current by approximately one order of magnitude[165], making a vertical resolution of 0.1 Å and lateral of 0.01 Å possible under good conditions.

3.2.4 Topography versus Electronic Structure

Because the tunnelling current depends on both tip-sample separation and local density of states, the image contrast is a function of both topography and electronic structure. These two influences can be deconvoluted by varying the applied bias. In the absence of an applied bias, electrons tunnel between tip and sample until Fermi levels have equilibrated and a steady state is reached[167]. A positive sample bias V causes tip energy levels to move up by eV relative to the sample, making electrons from filled tip states tunnel into empty sample states (see Figure 26). Vice versa, a negative sample bias causes electrons to tunnel from filled sample states to empty tip states. If one hence takes a series of images of the same area, one can change the electronic states responsible for tunnelling and isolate the contrast due to topography.

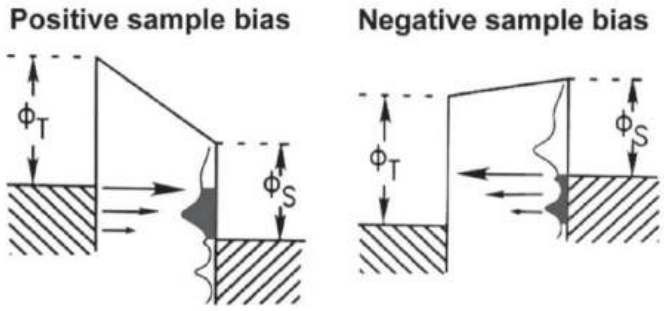

Figure 26: Tunnelling under positive and and negative sample bias, where Φ_T is the tip work function and Φ_S is the sample work function. Reproduced from [167].

3.2.5 The STM Instrument

The STM system used throughout this project was a JEOL JSTM 4500s (see Figure 27). This UHV system is composed of a three chambers, namely a load lock, a treatment chamber, and an imaging chamber, where the STM instrument itself is installed in the latter. The treatment chamber is equipped with an Ar-ion sputtering gun and the alkali evaporator used to deposit Li and Na onto $SrTiO_3$ surfaces. The baseline pressure in the treatment chamber was typically between 1.0 to 3.0 $\times$ 10^{-8} Pa and that of the imaging chamber 0.5 to 0.8$\times 10^{-8}$ Pa, both pumped by ion pumps. The load lock was pumped by a turbo-molecular pump, capable of pressures around 10^{-6} Pa. Samples and tips were always pumped at least 4 hours before opening the load lock to ensure minimal contamination in the treatment chamber. All STM data presented in this work were captured scanning the tip in constant current mode.

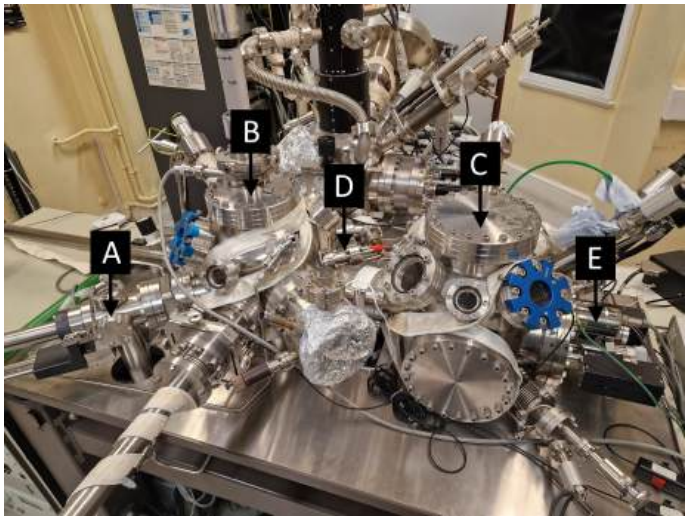

Figure 27: Picture of the JEOL JSTM 4500s system, showing the load lock (A), treatment chamber (B), imaging chamber (C), the alkali metal evaporator (D) and the STM stage unit (E).

3.2.6 Sputtering

Ar-ion sputtering was part of the preparation of all reconstructions presented in this work. The purpose of sputtering is primarily to break up the surface so that the desired reconstruction may be crystallised, but also to clean off deposited materials so that samples may be reused. The sputtering gun used as a VG Microtech EX03 sputtering gun. It operates by bombarding a stream of Ar gas with electrons, causing ionisation, after which the resulting Ar-ions are accelerated towards the sample. The pressure during sputtering

was maintained at circa 4.5×10^{-4} Pa by the turbo-molecular pump of the load lock. The efficacy of the sputtering process was monitored by measuring the incident Ar-ion current, which had a magnitude of 2.5 to 3.0 μA for all samples. A sputtering duration of 10 minutes was used to prepare samples for reconstruction annealing if there was no prior alkali deposition onto the sample, in which case they were sputtered for 30 minutes.

3.2.7 Annealing

Samples were heated using a direct current with the temperature being a function of power. The relationship between temperature and power was established by Peiyu Chen[171], a former group member who also worked on $SrTiO_3$ surfaces. She used an optical pyrometer that could measure temperatures above 850 ^{o}C with an error margin of 20 ^{o}C. She fitted pyrometer data points with a cubic polynomial to estimate the temperate as a function of power below the measurable temperature. Variations in the clamping forces attaching samples to their holders lead to differences in sample conductivity and a temperature gradient across samples, meaning the error in temperature was in reality greater then the 20 ^oC error of the pyrometer. The temperature gradient varied between samples, which may be used to estimate the total error in sample temperature. During the course of this thesis, it was commonly observed for hotter and colder areas on opposite sides of samples to display different surface structures. For samples with steep temperature gradients, those structures present in the hotter area were occasionally observed in the colder area after the annealing temperature had been increased by 100 ^oC. One may hence approximate the opposite ends of such samples to diverge from each other by 100 ^oC and by 50 ^oC from the centre. As the centre of the sample was always assumed to be at the nominal annealing temperature, 50 ^oC serves as a reasonable indication for the total uncertainty in sample temperature.

3.2.8 Alkali Metal Deposition

Li and Na were deposited by an evaporator built as part of this project. Details of the construction, operation and calibration of this evaporator will be given at length in Chapter 4 and will hence not be described here. The alkali metal sources used were Li and Na dispensers supplied by SAES Getters, which were heated by a direct current. $SrTiO_3$ samples were placed in front of the evaporator at a distance of 3 cm with the number of

monolayers (ML) deposited controlled by the deposition duration. Two distinct scenarios were investigated; one where a $SrTiO_3$ surface responds to a low alkali metal coverage ($0 < 0.3$ ML), and one where an alkali metal overlayer covers the underlying $SrTiO_3$ surface ($1.0 < 2.0$ ML). The first scenario was studied using two deposition quantities, one very low and one low, corresponding to coverages of $0 < 0.1$ ML and $0.1 < 0.3$ ML, respectively. The very low deposition corresponded to a deposition time of 5 min for Li and 1 min for Na, the low deposition to 25 min for Li and 5 min for Na, and the high deposition to 125 min for Li and 25 min for Na. It should be noted that there was one exception to these deposition durations, namely a $1.0 < 2.0$ ML Na-on-$SrTiO_3$(111) experiment where the dispenser was running out and a total deposition time of 60 min was needed for full coverage of the surface.

3.2.9 STM Sample Preparation

The surfaces studied in this project were the $c(4\times2)$ reconstruction of the $SrTiO_3$(001) termination and the (4×4), (5×5), and (6×6) reconstructions of the $SrTiO_3$(111) termination. All $SrTiO_3$ samples were single-crystal $7\times2\times0.5$ mm^3 wafers doped with 0.5% Nb by weight, supplied by PI-KEM. Prior to installation into the UVH system, they were cleaned by ultrasonic bath for 3×3 minutes in acetone and 3×3 minutes in ethanol. After cleaning, samples were mounted in a sample holder (see Figure 28) and inserted into the load lock to be pumped for at least 4 hours before insertion into the treatment chamber. The treatment chamber was used for degassing, Ar-ion sputtering, and annealing. The annealing conditions to make the $SrTiO_3(001) - c(4\times2)$ reconstruction was 1200^{o}C for 0.5 hours, and the conditions for all (111)-terminated reconstructions were 1100^{o}C for 1.5 hours. The (111) reconstructions were strongly dependent on the temperature gradient across the sample, with (4×4), (5×5), and two variations of (6×6) appearing in different areas of the same sample. After alkali metal deposition as outlined in 3.2.8, samples were annealed at increments of 100^oC from 400^oC to 800^oC.

3.2.10 Tip Making

All STM tips were made via electrochemical etching of tungsten (W) wires. Wires 0.3 mm in diameter were cut into segments and sandpapered, after which they were attached to a tip holder (see Figure 28) and immersed into a solution of 2.5 M NaOH. W segments

constituted the anode of the electrochemical reaction and another beaker hosting the cathode, also immersed in 2.5 M NaOH, was connected by a salt bridge. The solution contains Na^+ and OH^- ions where the application of a bias between the electrodes causes the latter to react with W, as per[172]:

$$\text{Cathode: } 6H_2O + 6e^- \rightarrow 3H_2(g) + 6OH^-, \tag{5}$$

$$\text{Anode: } W(s) + 8OH^- \rightarrow WO_4^{2-} + 4H_2O + 6e^-, \tag{6}$$

$$\text{Total: } W(s) + 2OH^- + 2H_2O \rightarrow WO_4^{2-} + 3H_2(g). \tag{7}$$

The water tension above the W segment causes a meniscus, with the lower amount of surrounding solution reducing the number of OH^- diffusing towards the anode at the top of the meniscus[172]. This decreases the efficacy of etching at the very top of the segment. At the same time, the WO_4^{2-} formed in the reaction has a degree of adhesion to the segment, causing it to flow down along its side[172]. This WO_4^{2-} flow shields the lower part of the segment from etching. In unison, these two effects produce a reaction schwerpunkt where etching has the greatest potency. When the W wire is so thin at the schwerpunkt that the weight of the material beneath cannot be sustained, the segment breaks. This causes a dramatic rise in resistance that is registered by a comparator in the power supply, which terminates the voltage. The remaining W segment is now an atomically sharp tip with the reaction schwerpunkt as its apex, suitable for STM after cleaning in deionised water, acetone and methanol.

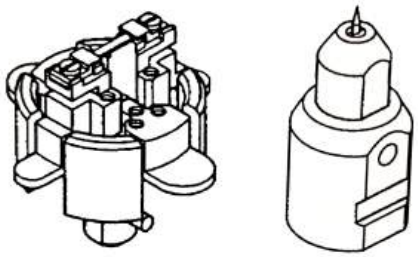

Figure 28: Pictures of the sample holder (left) and tip holder (right). Reproduced from the STM system manual.

3.2.11 STM Data Processing

The scanning probe microscopy analysis software *Gwyddion*[173] was used to process all STM images. This software was employed to, for example, correct scanning artifacts such as scars, measure heights and lengths, and to study periodicities via fast Fourier transforms (FFTs). Some images were additionally processed in *SmartAlign*, a software designed to correct aberrations and increase signal-to-noise ratio in scanning probe microscopy data[174]. This is achieved by aligning multiple successive images from the same area and extracting their multi-frame average. SmartAlign can as a result be used to discern between physical features and image-specific aberrations, which is particularly useful for small and electronic features.

3.3 X-ray Photoelectron Spectroscopy

XPS measures electrons emitted from a material upon X-ray irradiation to obtain information about its surface chemistry[175]. This is achieved by exploiting the photoelectric effect, by which electrons are emitted from a material as photoelectrons if they are excited by sufficiently energetic photons. The data generated in XPS includes qualitative information about the elements present, quantitative information about surface composition, as well as bonding environments[175].

3.3.1 Binding Energy

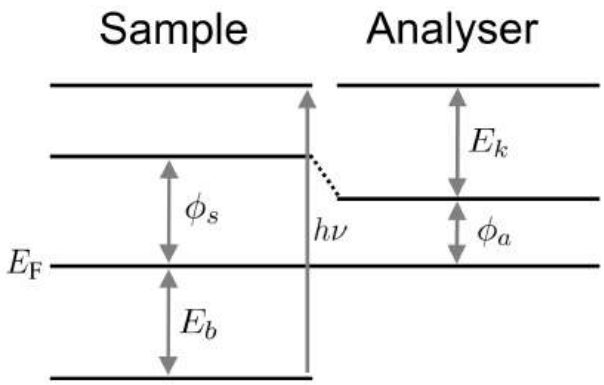

Figure 29: Schematic of the energies at play in the calculation of binding energy from XPS as per Equation 8.

A basic XPS instrument is composed of an X-ray source, an electron analyser that measures the kinetic energy of photoelectrons, a detector that counts the number of photoelectrons, as well as data acquisition and processing capabilities[176]. In order to escape the material and travel to the analyser, an electron in a given orbital must receive enough photon energy to overcome the orbital's binding energy E_b, the sample work function ϕ_s and have some kinetic energy E_k for the journey[175]. E_b is defined with respect to the Fermi level E_F, which is the same for both sample and analyser as they are in electrical contact[177] (see Figure 29). As E_k is measured by the analyser, its work function ϕ_a must be taken into account when calculating E_b:

$$E_b = h\nu - E_k - \phi_a. \tag{8}$$

The spectrum acquired from measuring E_b consists of binding energy peaks against a continuous background[176]. Peaks are associated with electrons that were emitted directly from specific orbitals, e.g. the 1s orbital of carbon, without being scattered in the material. The background is produced by electrons that have lost some energy due to inelastic scattering in the material[177]. Auger peaks also feature in XPS spectra for some elements.

3.3.2 Surface Chemistry

XPS is surface-sensitive to a point where the data obtained is representative only of the top few atomic layers of the material analysed[176]. This is because an X-ray-generated photoelectron in a material has a short inelastic mean free path (IMFP), defined as the average distance travelled at a given kinetic energy before inelastic scattering[177]. Such electrons must have an energy less than the X-ray source, which would be e.g. 1486.6 eV in the case of the commonly used Al Kα X-ray source[177], giving the typical XPS photoelectron an energy of a few hundred eV. For this reason, the IMFP is typically less than 3 nm, with the exact value depending on the material and electron energy, as can be seen in the universal curve displayed in Figure 30. A closely related concept is the effective attenuation length (λ), which differs from IMFP in that λ also accounts for elastic scattering[177]. This makes λ typically circa 10% smaller than IMFP[178]. λ plays a prominent role in Chapter 4, where it will be used to mathematically model the substrate signal attenuation due to an overlayer through Beer-Lambert's law. This law describes

the intensity I of electrons emitted from a depth greater than d given the total number of electrons generated in the sample I_0[177,178], according to $I = I_0 e^{(-d/\lambda)}$. This relationship can, furthermore, be used to show that circa 95% of X-ray-generated photoelectrons escape from a depth of less than 10 nm, which is often cited as the sampling depth of XPS[177].

Elements are identified by the general position of peaks, as these are characteristic of the orbital of the element from which the measured electron originated[175]. Bonding environment is determined by peak position shifts, whereby the position of an elemental orbital moves due to changes in its valence state[176]. This may be caused by changes in formal oxidation states or polar bonds with neighbouring atoms, allowing for redox reactions and the character of chemical bonds to be determined. If an atom loses electron density due to oxidation of a more electronegative neighbour, this will appear as an increase in the binding energy of its peak, and vice versa in the case of gained electron density[177]. See Figure 31 for an example of the Ti 2p peak of $SrTiO_3$ forming a lower binding energy peak due to reduction of Ti^{4+} to Ti^{3+}. The relative quantity of elements is established by comparing the intensity of peaks. Before such a quantitative analysis can be made, peak area corrections must be made to account for their relative sensitivity[177]. This includes both the intrinsic sensitivity of the orbital measured as well as calibrations specific to the XPS instrument used, such as its transmission function.

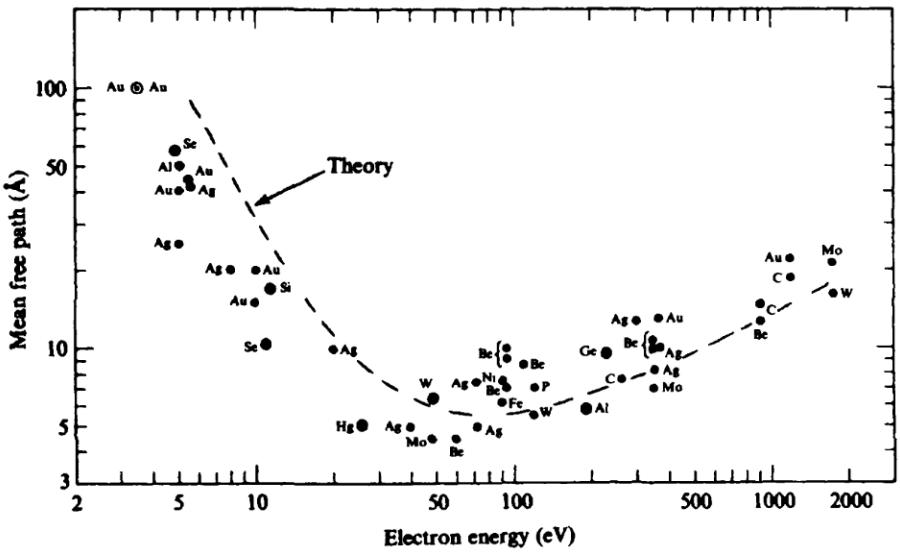

Figure 30: The universal curve of the inelastic mean free path of electrons in solids. Reproduced from [179].

3.3.3 Peak Splitting

Spin-orbit coupling causes p, d and f orbital peaks to split into two, one for each spin state $s = 1/2$ or $s = -1/2$. The spin-orbit split peaks have a fixed area ratio determined by the angular momentum quantum number l[175]. The total angular momentum of an orbital, j, has allowed values given by $|l - s| \leq j \leq l + s$. A d orbital, for example, has $l = 2$ and $s = 1/2$, producing allowed j values of $3/2$ and $5/2$. The ratio of areas between two spin-orbit split peaks is given by the degeneracy g, as per $g = 2j + 1$[177]. As such, the intensity ratios of the two spin-orbit split peaks for p, d, and f orbitals are $1 : 2$, $2 : 3$, and $3 : 4$, respectively. See Figure 31 for an example of p orbital splitting for Ti 2p. The s orbital, lacking orbital angular momentum, always appears as a single peak.

The electronic structure of the analysed material may contain features such as shake-up peaks, shake-down peaks, plasmon peaks, and multiplet splitting, all of which appear as additional peaks at a lower binding energy than the main peak[177]. Shake-up and shake-down peaks are produced when an electron emitted from a core orbital interacts with a valence electron, exciting it to a higher energy level and hence losing energy itself[177]. Shake-up peaks are due to valence electron excitations to higher energy bound states, whereas shake-down peaks are due to valence electron excitations to unbound states[176]. Emitted core electron interactions with plasmons in metals can produce a similar effect, where valence electrons are excited into one of the many unfilled states available just above the Fermi level. This allows for a great variety of transitions that differ little in energy, often appearing as a continuous "tail" coming off the higher binding energy side of the main peak[177]. Multiplet splitting occurs when an unpaired electron in an ionised atom couples with unpaired valence electrons, producing a variety of final states for the ionised atom that yields a plurality of peaks[176].

3.3.4 Spectrum Acquisition

Electrons travelling to the analyser are retarded by the extractor lens to a specific pass energy, which is set by the XPS user[177]. In general, the smaller the pass energy, the better the energy resolution, but the fewer the counts, resulting in a trade-off between resolution and intensity[180]. The XPS user must also select the energy step size, i.e. the distance

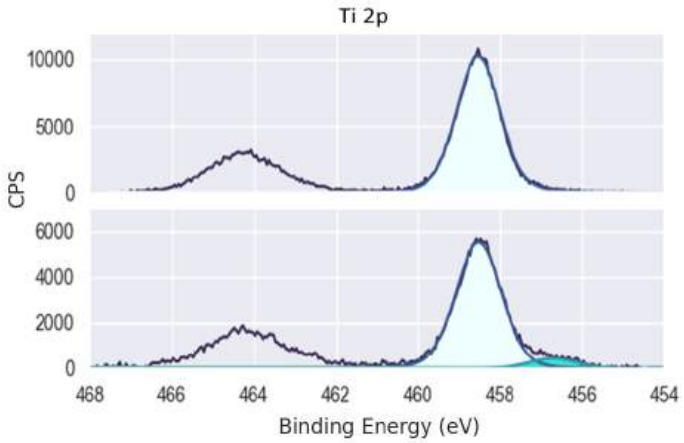

Figure 31: Counts per second (CPS) vs binding energy for the Ti 2p peak of $SrTiO_3$. The top and bottom spectra are before and after Li deposition, respectively. Spin-orbit splitting occurs with the main Ti $2p_{2/3}$ Ti^{4+} peak filled in light blue. Li reduction causes a Ti^{3+} peak to emerge, which is indicated by turquoise.

between two binding energy data points in a spectrum, where smaller steps result in higher resolution but longer scan times. If the signal of a peak is so weak that its spectrum is significantly obscured by noise, one can increase the number of scans, resulting in noise reduction for each scan. The XPS operator must calibrate these parameters to ensure that important spectrum information is not lost and that spectra are sufficiently free of noise to be reliable[180].

3.3.5 XPS Operation and Sample Preparation

The XPS instrument used was a PHI VersaProbe III equipped with a 1486.6 eV monochromatic Al Kα X-ray source at a 45^o angle to the analyser. This instrument is composed of an introduction chamber and a UHV XPS analysis chamber, where the former is capable of pressures below 10^{-5} Pa and the latter had a baseline pressure of 1.0×10^{-7} Pa to 3.0×10^{-7} Pa. The analysis chamber is also equipped with an Ar-ion sputtering gun which was used for some experiments presented in this project. To obtain wide-range survey spectra, a pass energy of 224 eV and a step size of 0.28 eV were employed. A pass energy of 26 or 55 eV and a step size of 0.05 eV were used to obtain the elemental orbital spectra. The same PI-KEM $SrTiO_3$ wafers and cleaning conditions were employed as presented in section 3.2.9. All $SrTiO_3$ surfaces were prepared either through cleaving, in which case they were cleaved in situ in the XPS introduction chamber, or annealing in the STM treatment chamber, in which case deposition and annealing methods are the same as those used in Section 3.2.9.

XPS data was processed in CasaXPS. A Shirley background was used for all spectra. As is common in the literature[177], adventitious carbon was used for binding energy calibrations, assuming a C 1s binding energy of 284.8 eV[181,182]. The most significant peak for this thesis is the Ti $2p_{3/2}$ peak, for which all samples were analysed constraining the full-width half maximum from 1.2 to 1.4 and the binding energies of Ti^{4+}, Ti^{3+} and Ti^{2+} from 458.7 eV to 458.2 eV, from 457.2 eV to 456.7 eV, and from 456.2 eV to 455.7 eV, respectively. XPS spectra throughout the thesis will be displayed as counts per second (CPS) versus binding energy in eV.

3.4 Density Functional Theory

DFT is a theory of many-particle systems that has achieved considerable success in predicting the properties of real materials. Foundational to DFT is the idea that all properties of a system composed of interacting particles can be regarded as a functional of the ground state charge density[183], which was established by the theorems of Hohenberg and Kohn in 1964[184]. Building on this foundation, Kohn and Sham published their eponymous equations in 1965, showing how one through a series of approximation can find the ground state charge density[185]. All subsequent DFT is based on these crucial developments.

3.4.1 The Hohenberg-Kohn Theorems

The Hohenberg and Kohn theorems pertain to systems of interacting particles under the influence of an external potential, which includes those systems for which one can formulate the Hamiltonian as a function of electron coordinates only[183]. One may arrive at such a Hamiltonian through the Born-Oppenheimer approximation, by which one assumes that nuclei move so much slower than electrons that their positions can be assumed to remain fixed[186]. Consequently, nuclei have no kinetic energy, their Coulomb repulsion is a constant that can be subtracted from the total energy, and the electron-nuclei Coulomb potential can now be treated as an external potential acting on the electrons, $V_n(\mathbf{r}) = -\sum_I Z_I/|\mathbf{r} - \mathbf{R}_I|$ in atomic units. The Hamiltonian is then composed of $V_n(\mathbf{r})$, the electron kinetic energy and electron-electron Coulomb interaction, all of which are functions of the electron positions $\mathbf{r}$ alone:

$$\hat{H}\,|\Psi\rangle = \Big[-\sum_i \frac{\nabla_i^2}{2} + \sum_i V_n(\mathbf{r}_i) + \sum_{i \neq j} \frac{1}{|\mathbf{r}_i - \mathbf{r}_j|} \Big]\,|\Psi\rangle = E\,|\Psi\rangle\,. \tag{9}$$

The first Hohenberg-Kohn theorem states that the ground state charge density of the system determines uniquely, except for a constant, the external potential [183]. The second theorem states that there is an energy functional of the charge density, for which the ground state energy of the system is the global minimum, and that the charge density that minimises the functional is the exact ground state charge density [183]. From the first theorem, it follows that a given ground state charge density, $n_0(\mathbf{r})$, yields one unique external potential, $V_n(\mathbf{r})$ hence one unique Hamiltonian, $\hat{H}$. By solving the Schrödinger equation for this Hamiltonian, one finds the wavefunctions, $|\Psi_i\rangle$, where the solution that gives the ground state energy is the unique ground state wavefunction $|\Psi_0\rangle$[183] (see Figure 32). From the second theorem, it follows that given a correct ground state charge density $n_0(\mathbf{r})$, minimising the energy functional $E[n]$ with this charge density as input renders the ground state energy. Minimising $E[n]$ hence provides $n_0(\mathbf{r})$ and unlocks all available information about the properties of the system.

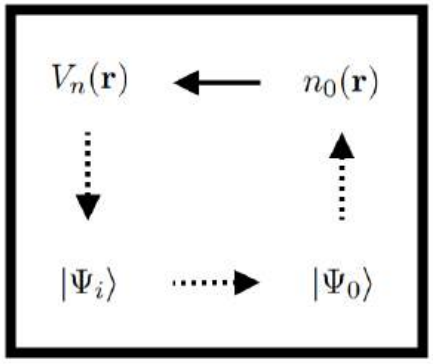

Figure 32: Schematic of the first Hohenberg-Kohn theorem. The dashed arrows represent solutions to the Schrödinger equation and the solid arrow represents the theorem. Inspired by [183].

3.4.2 The Kohn-Sham Equations

For the Hamiltonian in Equation 9, the total energy functional can be described as $E[n] = \langle\Psi|\,\hat{H}\,|\Psi\rangle = F[n] + \int V_n(\mathbf{r})n(\mathbf{r})dr$, where $F[n]$ is a functional pertaining to electron kinetic energy and electron-electron Coulomb interaction[187]. This $F[n]$ is currently too complex for $E[n]$ to be feasibly evaluated due to the correlated nature of electron interactions, meaning that a simpler Hamiltonian must be formulated. Following Kohn and Sham, one

first makes the rather drastic *independent electron approximation*, where one assumes that electrons are non-interacting[186]. Electrons can within this approximation be described by individual single-particle wavefunctions, $|\Phi_i\rangle$, to which a single-particle Hamiltonian, $\hat{H}_e(\mathbf{r}_i)$, can be applied to find their ground state energies ϵ_i, $\hat{H}_e(\mathbf{r}_i)\,|\Phi_i\rangle = \epsilon_i\,|\Phi_i\rangle$. $\hat{H}$ can then be rewritten as a sum of such single-electron Hamiltonians:

$$\hat{H}\,|\Psi\rangle = \Big[\sum_i \hat{H}_e(\mathbf{r}_i)\Big]\,|\Psi\rangle = E\,|\Psi\rangle\,. \tag{10}$$

To retain this much more soluble single-particle description, some of the physics ignored by the independent electron approximation must be reintroduced. First, one notes that the independent electrons must feel an average potential due to the presence of the other electrons[186]. This is captured by the *mean-field approximation* that introduces the *Hartree potential*, $V_H(\mathbf{r})$, derived from Poisson's equation used on the charge density. Next, one must model non-local effects individual electrons have on each other, which is done by introducing two potentials[186]. Firstly, one must consider the Pauli exclusion principle, which is accounted for by the *exchange potential*, $V_X(\mathbf{r})$. Secondly, one must consider the fact that the probability of finding one electron at a given position is reduced if another is nearby, making electron positions correlated, which is captured by the *correlation potential*, $V_C(\mathbf{r})$. $V_X(\mathbf{r})$ and $V_C(\mathbf{r})$ are typically grouped together into the exchange-correlation potential, $V_{XC}(\mathbf{r})$. One may after these approximations state the famous Kohn-Sham equation, central to all modern materials modelling[186]:

$$\Big[-\frac{\nabla^2}{2} + V_n(\mathbf{r}_i) + V_H(\mathbf{r}_i) + V_{XC}(\mathbf{r}_i)\Big]\,|\Phi_i\rangle = \epsilon_i\,|\Phi_i\rangle \tag{11}$$

V_{XC} in Equation 11 relates to the exchange-correlation functional $E_{XC}[n]$ according to $V_{XC}(\mathbf{r}) = \delta E_{XC}[n(\mathbf{r})]/\delta n(\mathbf{r})$. One may think of the total energy functional $E[n]$ as being composed of two terms, $E_{XC}[n]$ and a term pertaining to the independent electron assumption, $E_{IE}[n]$, hence $E[n] = E_{IE}[n] + E_{XC}[n]$. Deriving an $E_{XC}[n]$ with sufficient generality to model any material has always been and remains one of the main challenges of DFT. Two common types of exchange-correlation functionals are the Local Density Approximation (LDA) and the Generalised Gradient Approximation (GGA). Both these functionals make use of the per-particle exchange-correlation energy of a homogeneous electron gas, where GGA also accounts for the gradient of this quantity[188].

3.4.3 Wavefunctions in Periodic Systems

DFT calculations typically involve only a few hundred atoms at most, yet DFT is able to predict the properties of macroscopic materials. This is due to the periodicity of crystals, which allows for the application of Bloch's theorem to their wavefunctions[189]. Bloch's theorem states that in a periodic system, a wavefunction $\Psi_{n\mathbf{k}}(\mathbf{r})$ that is translated by a lattice vector $\mathbf{R}$ (by the translation operator $\hat{T}_{\mathbf{R}}$) only changes by a corresponding phase factor $e^{i\mathbf{kR}}$, i.e. $\hat{T}_{\mathbf{R}}\Psi_{n\mathbf{k}}(\mathbf{r}) = \Psi_{n\mathbf{k}}(\mathbf{r}+\mathbf{R}) = e^{i\mathbf{kR}}\Psi_{n\mathbf{k}}(\mathbf{r})$[190]. Such crystal wavefunctions can be formulated as Bloch states $\Psi_{n\mathbf{k}}(\mathbf{r})$ composed of the general phase factor $e^{i\mathbf{kr}}$ and the wavefunction of the unit cell $u_{n\mathbf{k}}(\mathbf{r})$, i.e. $\Psi_{n\mathbf{k}}(\mathbf{r}) = e^{i\mathbf{kr}}u_{n\mathbf{k}}(\mathbf{r})$[191]. $e^{i\mathbf{kr}}$ is a plane wave, and since it determines the phases of Bloch states, it also governs the interference between Bloch states as a function of the wavevector $\mathbf{k}$[191] (see Figure 33). Relative phases given by $e^{i\mathbf{kr}}$ determine whether interference is constructive, destructive, or absent, meaning $e^{i\mathbf{kr}}$ expresses band dispersion. This is why Brillouin zone boundaries, equivalent to Bragg planes, often have special properties, such as being the location of the band gap, because the condition for constructive interference between two waves with wavevectors $\mathbf{k}$ and $\mathbf{k}'$ is that they differ by a reciprocal lattice vector $\mathbf{G}$, i.e. $\mathbf{k} - \mathbf{k}' = \mathbf{G}$[191].

The unit cell function $u_{n\mathbf{k}}(\mathbf{r})$ describes the structure of the wavefunction within the unit cell, meaning it encodes information about the orbitals from which electronic states in the material arise. It necessarily has the periodicity of the lattice, i.e. $u_{n\mathbf{k}}(\mathbf{r}) = u_{n\mathbf{k}}(\mathbf{r}+\mathbf{R})$[190] (see Figure 33). The role of $u_{n\mathbf{k}}(\mathbf{r})$ in determining a Bloch state $\Psi_{n\mathbf{k}}(\mathbf{r})$ is well illustrated by considering $\Psi_{n\mathbf{k}}(\mathbf{r})$ at the limit of no dispersion, i.e. at the Γ point where $\mathbf{k} = [0, 0, 0]$, which gives $\Psi_{n\mathbf{k}}(\mathbf{r}) = e^0 u_{n\mathbf{k}}(\mathbf{r}) = u_{n\mathbf{k}}(\mathbf{r})$. The fact that $u_{n\mathbf{k}}(\mathbf{r})$ is defined by the unit cell allows for the formulation of $\Psi_{n\mathbf{k}}$ as an expansion of orbital wavefunctions localised at unit cell atoms, e.g. as a linear combination of atomic orbitals (LCAO)[192]. Such a formulation may be built starting from orbital wavefunctions of the form $\phi_l(\mathbf{r} - \mathbf{t}_i)$, which is centred at the unit cell position $\mathbf{t}_i$ of atom number i and has angular momentum character l (which could be s, p, d, or f). One may then use $\phi_l(\mathbf{r} - \mathbf{t}_i)$ to construct a basis of orbital-like wavefunctions $\Xi_{\mathbf{k}li}(\mathbf{r})$ that obey Bloch's theorem, which may take the form $\Xi_{\mathbf{k}li}(\mathbf{r}) = N^{-1/2}\sum_{\mathbf{R}} e^{i\mathbf{kR}}\phi_l(\mathbf{r} - \mathbf{t}_i - \mathbf{R})$. The crystal wavefunctions can then be built from $\Xi_{\mathbf{k}li}(\mathbf{r})$ basis vectors as $\Psi_{n\mathbf{k}} = \sum_{l,i} C_{\mathbf{k}nli}\Xi_{\mathbf{k}li}(\mathbf{r})$[192].

The wavefunctions of a periodic system are, however, typically most naturally described using a plane wave basis[193]. In a plane wave basis, $\Psi_{n\mathbf{k}}$ is represented as a Fourier series of plane waves $e^{i(\mathbf{k}+\mathbf{G})\mathbf{r}}$ according to $\Psi_{n\mathbf{k}}(\mathbf{r}) = \sum_{\mathbf{G}} C_{n\mathbf{G}} e^{i(\mathbf{k}+\mathbf{G})\mathbf{r}}$[194]. The subscript n represents the band index, which for some set of Bloch states at a specific $\mathbf{k}$ acts as a proxy for their relative energy levels[190]. The set of all Bloch states with a given n collectively form a band, which can be viewed as a single quantum mechanical state with an energy level $\epsilon_n(\mathbf{k})$ that changes gradually with $\mathbf{k}$ across the periodicities found within the Brillouin zone[190]. The $\mathbf{k}$-dependence of a band is determined both explicitly by $e^{i\mathbf{kr}}$ and implicitly by the $u_{n\mathbf{k}}(\mathbf{r})$ of its constituent Bloch states. A consequence of Bloch's theorem is that it suffices to solve the Kohn-Sham equations for the wavefunctions within a single real-space unit cell to obtain the total ground state energy[189]. An exact treatment would evaluate the wavefunctions at all k-points in the first Brillouin zone, but there are as many such k-points as there are unit cells in the crystal[190]. For this reason, practical DFT employs an approximate solution where only a few strategically sampled k-points are considered[189].

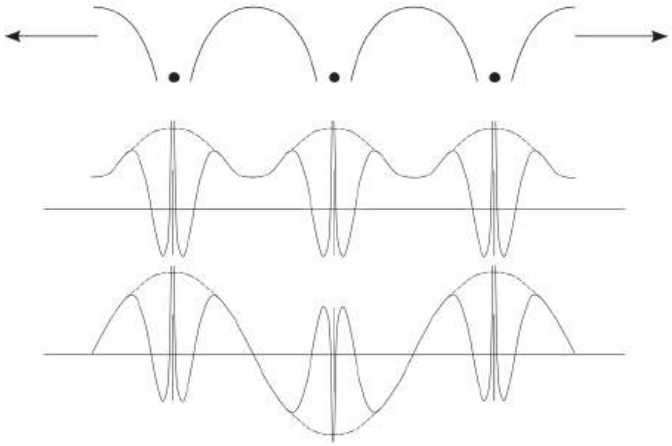

Figure 33: A periodic potential (top) giving rise to two Bloch states, one without phase change (middle) and one with phase change (bottom). The wavefunctions' envelopes are the plane waves $e^{i\boldsymbol{kr}}$ and their interiors are $u_{n\boldsymbol{k}}(\boldsymbol{r})$. Reproduced from [195].

3.4.4 Calculation Methodology

All calculations in this project were performed using GPAW[194], a Python package built atop the atomic simulation environment (ASE)[196]. GPAW uses the projector augmented-waves (PAW) method introduced by Blöchl[197]. This method divides space into regions

where electron wavefunctions are core-like and where they are valence-like. Valence wavefunctions near the core oscillate rapidly due to the requirement of many Fourier components, making them computationally expensive to describe. PAW solves this issue by applying a linear transformation from valence wavefunctions to pseudo-wavefunctions, which have the convenient property that they are similar to the valence wavefunctions in the valence-like region but smooth near the core. Valence wavefunctions can then be restored from the pseudo-wavefunctions by the inverse transformation.

GPAW uses the self-consistent field (SCF) method[194] to solve the Kohn-Sham equations. The initial external potential is calculated from the atomic positions provided by a *crystallographic information file* together with the potentials of the atomic species' PAW setups. An initial guess for charge density is needed as the Hartree and exchange-correlation potentials depend on it, which in turn means an initial guess for the wavefunctions is needed as $n(\mathbf{r}) = \sum_i \phi_i^*(\mathbf{r})\phi_i(\mathbf{r})$. GPAW constructs these initial wavefunctions by a linear combination of atomic orbitals of the system's valence states. This provides an initial charge density, after which the first SCF loop can start. A schema for this procedure is provided in Figure 34. In each step in the SCF loop, the Kohn-Sham equations are solved by diagonalising the Hamiltonian to calculate eigenvalues. When the energy and density differences between one step and the next are less than the criteria set for convergence, the iteration is completed.

3.4.5 Calculation Parameters

The PAW method's analogue to pseudo-potentials are the PAW setups, and the ones used for this project were GPAW's standard PBE setups. The default GPAW values for SCF convergence were used, namely $5 \cdot 10^{-4}$ eV/electron for energy and $1.0 \cdot 10^{-4}$ electrons/electron for density. A plane wave basis set was used to represent wavefunctions. A Monkhorst-Pack grid was used for k-point sampling. All k-space paths used for Brillouin zone sampling had the property that they included all special, high-symmetry k-points in the 2D Brillouin zone defined by the reciprocal vectors to the surface unit cell. Several convergence tests were performed to select the values for key parameters, with details presented in section 3.4.6. Definitions of the central quantities used to analyse calculation results, such as adsorption energy, are given in Appendix I.

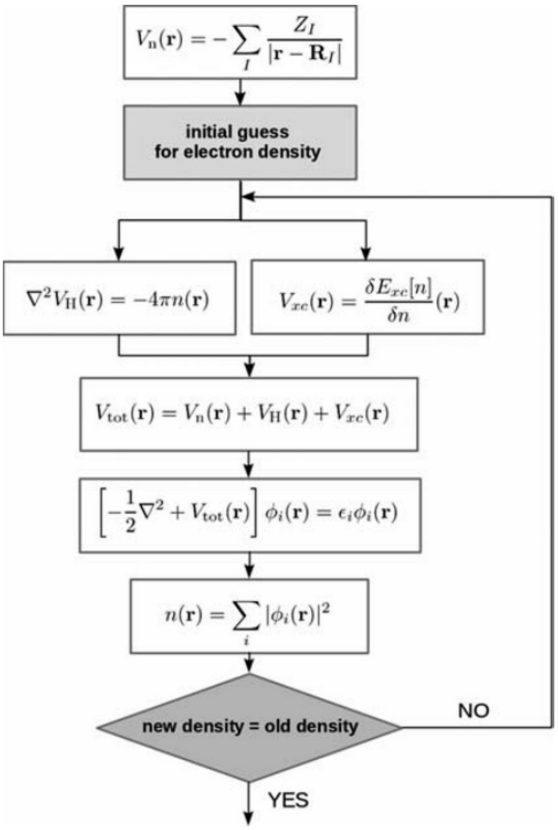

Figure 34: Representation of the self-consistent field method for solving the Kohn-Sham equations. The "new density = old density" condition will be met if the density of the current iteration differs from the old one by less than the convergence criteria threshold. Reproduced from [198].

Some consideration was given to the choice of exchange-correlation functional, as a significant variety has been used in the literature on $SrTiO_3$ surfaces, including LDA[109], PBE[61,85,116,123,154,199–201], PBEsol[105], combined PBE0 and TPSSh[12], and combined revTPSS and MS2[103]. The GGA derived PBE was ultimately chosen for this project as it is non-empirical, provides good balance between speed and accuracy, and is one of the most universally applicable functionals[202]. Two variations of PBE, namely RPBE and revPBE, have performed better than standard PBE in some adsorption calculations, and were therefore considered. Specifically, RPBE and revPBE generally overestimate the adsorption energies of molecules on transition metal surfaces less than PBE[203,204]. No studies could, however, be found suggesting that RPBE or revPBE perform better in the case of oxide surfaces in general nor metal adsorption onto oxides in particular. RPBE and revPBE were, moreover, not employed in the literature on $SrTiO_3$ surfaces that was studied for this project. There is as such no strong motivation for the changes added to PBE by RPBE or revPBE, which is why standard PBE was chosen. A test was car-

ried out to compare LDA, PBE, RPBE, and revPBE using Li and Na adsorption on the $SrTiO_3(001) - (3\times1)$ (see Figure 35). This test showed that all PBE-type functionals adsorbed both alkalis to the same position, but LDA did not. RPBE and revPBE do, as suggested by the literature, produce smaller adsorption energies, in this test by circa 0.5 eV for Li. Consideration was additionally given to whether GGA+U should be used. This option was, however, discounted, as GGA+U produces additional local minima in the potential energy surface[205]. This introduces risk into calculations focused on adsorption, as adsorbents may relax into positions corresponding to these local minima caused by U.

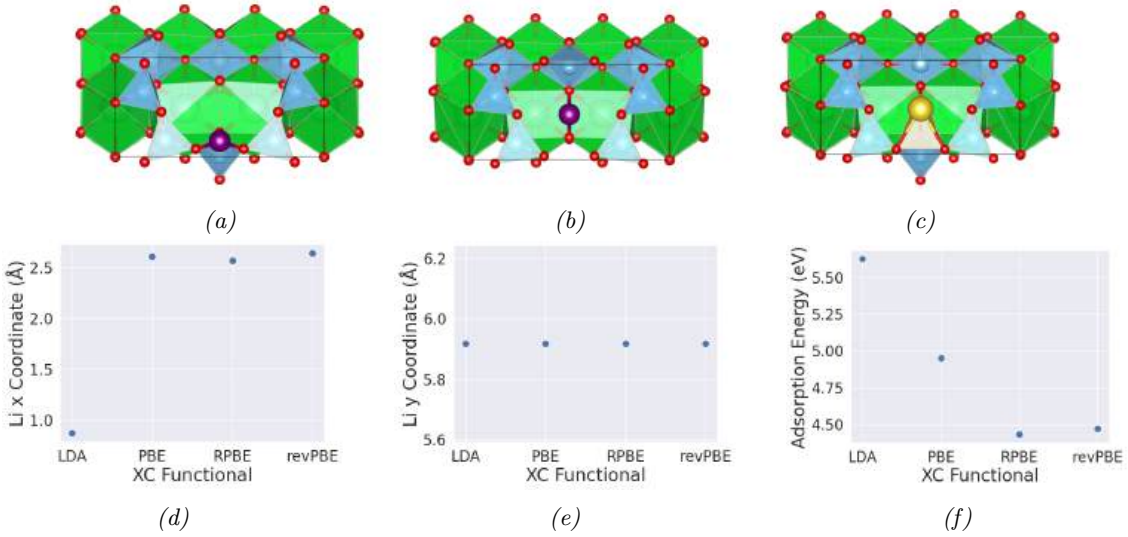

Figure 35: LDA, PBE, RBE and revPBE comparison for Li and Na adsorption onto $SrTiO_3(001)-(3\times1)$. Red, blue, purple and yellow balls are O, Ti, Li, and Na, respectively, and blue and green polyhedra indicate O coordination around Ti and Sr, respectively. a) and b) show the relaxed Li adsorption positions for LDA and PBE-type functionals, respectively. c) shows the relaxed adsorption site for Na of all functionals. d) and e) show the x and y positions for Li adsorption for all functionals, where x is along the vertical and y along the horizontal directions of the cells displayed in a) and b). f) shows the Li adsorption energies for all functionals.

3.4.6 Convergence Tests

Convergence tests were conducted to ensure that the values of key calculation parameters were strict enough that further increasing their precision would not substantially increase the accuracy of calculations. Surface slab convergence tests were conducted using $SrTiO_3(110) - (3\times1)$ as a benchmark. The number of layers in the slabs was taken from the literature on $SrTiO_3$ surface calculations, where 13 layers is standard[12,36,40,105,109,116]. Slabs calculated before the vacuum convergence test were separated by 24 Å, which perhaps was overly cautious, considering that the literature typically reports vacuum values

of the magnitude 12 Å[109], 14 Å[200], or 15 Å[40,206].

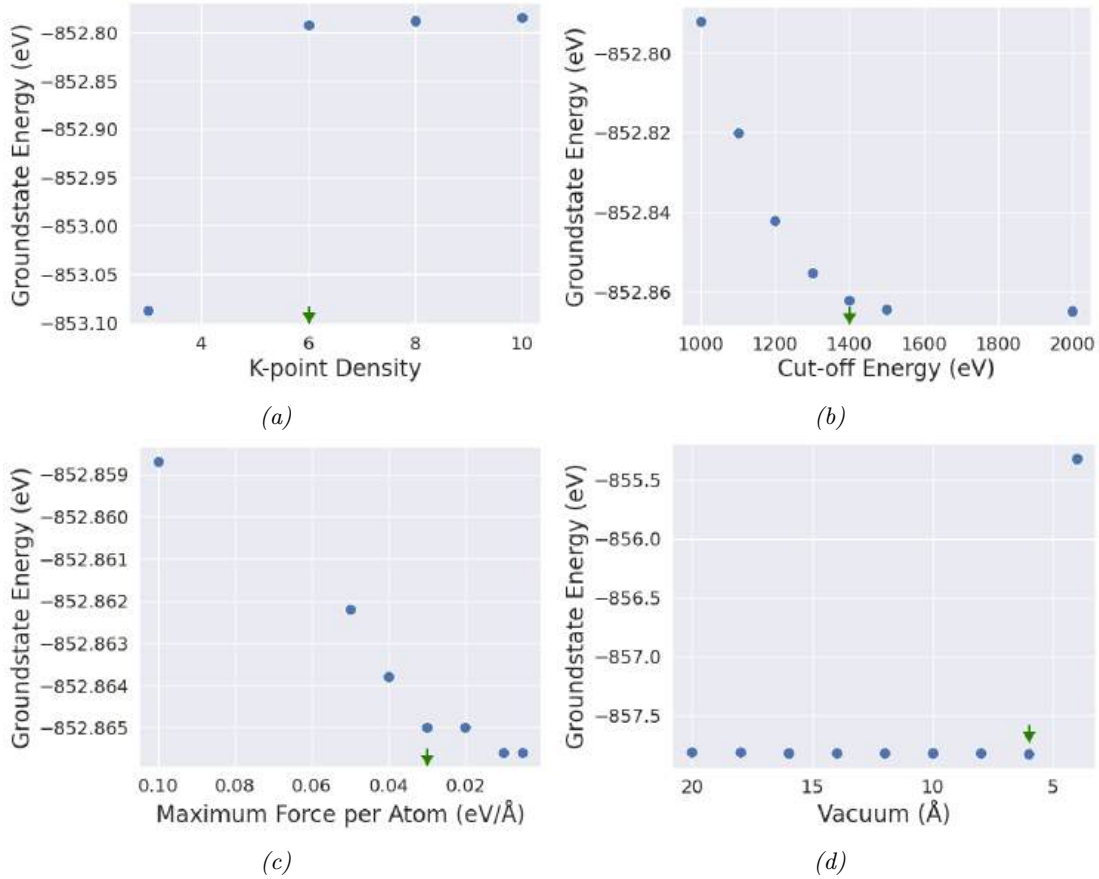

Figure 36: Convergence tests of key calculation parameters on $SrTiO_3(110) - (3\times1)$, showing the tests pertaining to a) k-point density, b) energy cut-off, c) maximum force per atom, and d) the height of vacuum above the cell. The points at which sufficient convergence is achieved is indicated by the green arrows.

The first surface slab convergence test performed concerned the k-points density, the second plane energy cut-off, the third the maximum force on atoms before relaxation, and the fourth the vacuum above the slab. The value obtained for a previously converged parameter was used for subsequent convergence tests. The results for these four convergence tests can be seen in Figure 36. The values displayed in the k-point density convergence test refer to the number of k-points per bulk unit cell length in the real-space direction in question. Convergence was achieved at a density of 6 k-points per bulk unit cell. For the 11.83 Å × 5.58 Å surface of the (3×1) slab, this is equivalent to a k-point density of 2×4. Plane-wave energy cut-off and atomic force were deemed to have been converged at values of 1400 eV and 0.03 eV/Å, respectively. The vacuum convergence test was conducted starting with one Li placed one unit cell above the surface. Vacuum convergence is clearly

achieved at 6 Å on each side of the slab, but to have margin for larger deposition quantities, a vacuum of 8 Å on each side of the slab was chosen. All subsequent calculations in this project were conducted using these values.

3.4.7 Spin Polarisation

Spin-polarisation is only necessary if alkali adsorption leads to the acquisition of a net magnetic moment due to differences in the spin-up and spin-down density of states. The need for spin polarisation was investigated at a stage in the project when Li and Na adsorption calculations on (2×1), $c(4\times2)$, (3×1) and (2×2) were completed. All these calculations had an initial magnetic moment of 0.1 μ_B per atom and all attained a final total magnetic moment of less than 0.0002 μ_B. The spin-polarised density of states for (3×1) with and without three Li adsorbates is shown as an example in Figure 37. In addition, a dedicated spin-polarisation test was conducted on the (3×1) reconstruction to ensure that a large enough initial magnetic moment was applied. In this test, four initial magnetic moments per atom were tested, namely 0.1, 0.5, 1.0 and 5.0 μ_B, as well as four adsorption conditions, namely one Li, two Li, one Na and two Na. The result was that no final total magnetic moment was ever greater than 0.004 μ_B, meaning that spin polarisation could be turned off. All calculated structures were re-relaxed without spin-polarisation and all subsequent calculations were performed without spin-polarisation. The same conclusion has been reached in previous studies of adsorption on $SrTiO_3$, e.g. in the case of Pt[40] and Ag[123].

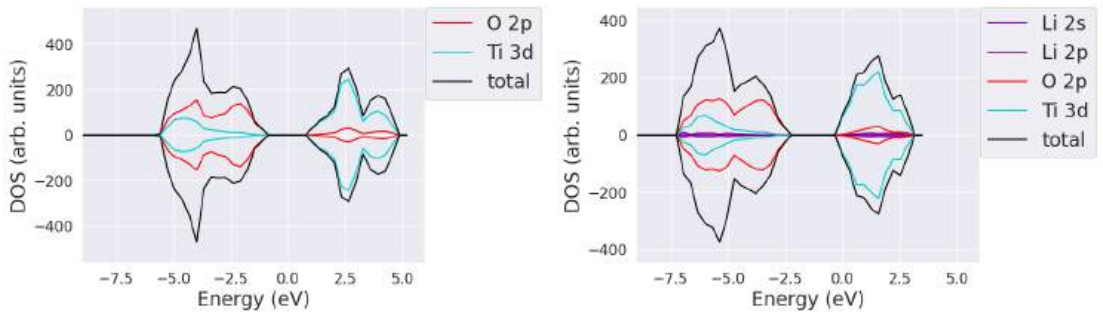

Figure 37: Spin-polarised density of states for $SrTiO_3-(3\times1)$, showing a) the clean surface and b) three Li adsorbed. No significant magnetic moment is present.

3.5 Conclusion

This chapter has presented the basic theoretical underpinning and practical implementation of STM, XPS, and DFT, as well as the sample preparation conditions and experimental setups for studying Li and Na deposition on $SrTiO_3$ surfaces. With the structural data obtained in STM, the chemical data obtained in XPS, and the quantum mechanics modelled in DFT, these three methods in unison should produce a multi-faceted picture of the physics underlying the interaction between alkalis and $SrTiO_3$ surfaces.

4 The Alkali Metal Evaporator

4.1 Introduction

This chapter outlines the construction and calibration of the evaporator that was built to deposit Li and Na on $SrTiO_3$ to produce the surfaces studied in the STM. Custom-made parts were manufactured by the workshop of the Department of Engineering. The evaporator deposition rate was calibrated using the XPS system described in Chapter 3. This calibration method was used after many quartz crystal microbalance (QCM) experiments had failed, presumably due to the evaporation rate being beneath the limit of QCM detection.

4.2 Evaporator Construction

The active component of the evaporator is an alkali metal dispenser supplied by SAES Getters, an example of which can be seen in Figure 38b. The active dispenser material is composed of an alkali metal chromate, Li_2CrO_4 for Li dispensers and Na_2CrO_4 for Na dispensers, and the alloy St 101 (Zr84wt%-Al16wt%). The dispenser contains this material within a metal casing connected to the internal circuit of the evaporator, allowing the dispenser to be heated by direct current as per the graph in Figure 38c. Above a certain temperature, circa 800^oC for Li and 720^o for Na, a reaction starts where the alloy reduces the alkali metal chromate, causing a decomposition whereby alkali metal atoms are ejected from the material and released into the atmosphere. The evaporator in which dispensers were installed was constructed by refurbishing a pre-existing Ba evaporator. Most central parts were inherited from this older evaporator, some of which are shown in Figure 38a, including Cu wires with ceramic insulation, steel rod for structural support, and a ceramic stage on which dispensers were held. Several parts did, however, have to be manufactured to adapt the evaporator for alkali metal usage, including the clamps holding the dispenser in Figure 38b. CAD drawings of three of these manufactured parts are shown in Figures 38d-38f.

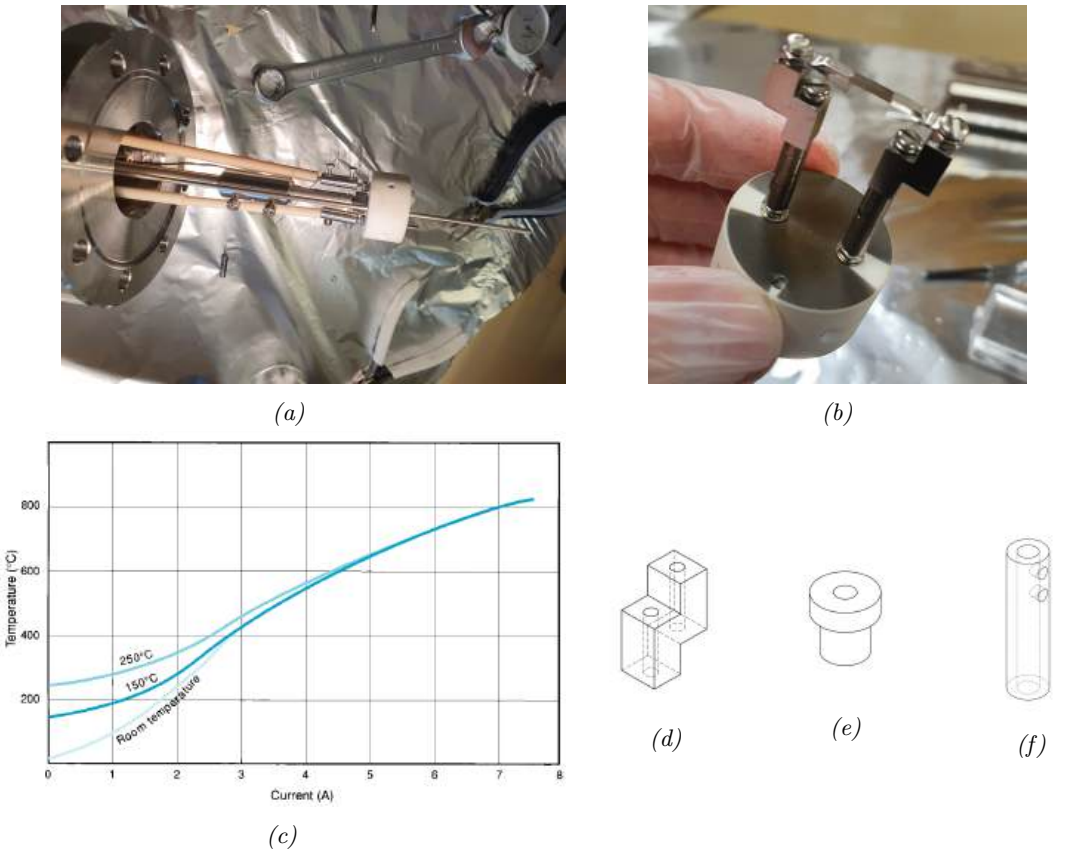

Figure 38: Evaporator parts, where the top row shows a) the evaporator skeleton consisting of a central steel rod supporting a ceramic stage on which dispensers were held, as well as the internal circuit composed of Cu wires clad in ceramic insulation. b) shows a close up of the ceramic stage with a dispenser held by two custom-made clamps. The bottom row shows c) temperature versus current for SAES getter dispensers (reproduced from the dispenser manual), as well as CAD drawings of some custom-made components: d) the clamps holding the dispenser in b), e) a ceramic insulator for the shutter, and f) steel contacts that connect the evaporator circuit to an external power supply.

4.3 Calibration

The evaporation rate was calibrated by calculating the attenuation of the substrate XPS signal as a function of deposition time. This allows for an evaluation of the thickness of the overlayer covering the substrate, which together with the stoichiometry of the overlayer enables an approximation of the amount of alkali metal deposited. There are several examples in the literature of this method being used to calibrate the rate of SAES Getters alkali metal dispensers[128,149,159]. Deposition was conducted in the introduction chamber of the XPS instrument. For this purpose, a custom-made interface was manufactured to install the evaporator in the XPS introduction chamber opening without compromising its baseline pressure of circa 5.0×10^{-5} Pa.

4.3.1 In-situ XPS Deposition

XPS spectra were acquired between depositions to obtain an incrementally increasing coverage of alkali metal on the substrate. A Cu substrate was used for both Li and Na experiments, which produced a clear Na signal, as can be seen in Figure 39. The results for Li, however, were unsatisfactory due to weak Li signals, and after three attempts on Cu a Si substrate was used instead. This produces a significant Li signal, as can be seen in Figure 40. Na was as such calibrated on a Cu substrate, and Li on a Si substrate. The reason for the inadequate Li results on Cu will be discussed in Section 4.4.1. $SrTiO_3$ was not used as substrate because its more complex stoichiometry introduces additional surface chemistry uncertainty, as the surface could potentially become enriched in Ti or Sr.

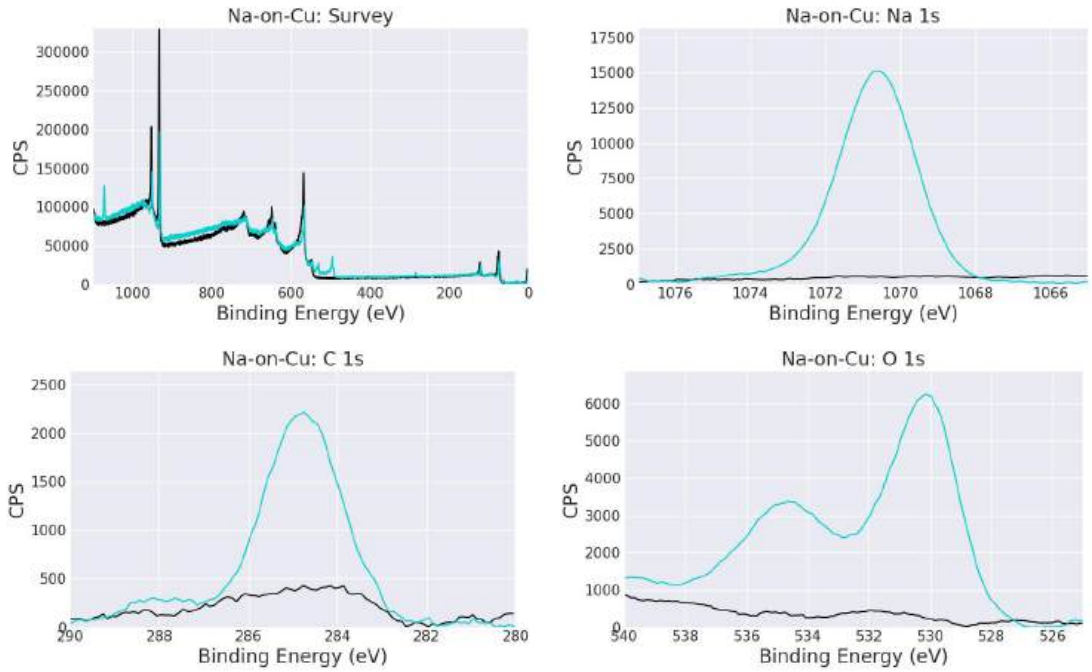

Figure 39: XPS spectra of Na deposited on a Cu substrate separated 3.0 cm from the dispenser at a heating current of 7.0 A. The black lines correspond to the clean substrate and the turquoise lines to 50 min deposition. A single moving average of 15 points smoothing was applied to all spectra except the survey.

The substrate materials were clamped onto the sample holder at two different heights; one at the base of the sample holder with a 3.0 cm distance to the dispenser, and one at a ridge raised to have a 2.5 cm distance to the dispenser. The former will be referred to as the "base" position, and is equal to the distance between dispenser and sample in

the STM instrument, while the latter will be referred to as the "ridge" position and was included to test the influence of dispenser-sample distance on evaporation rate. Figures 39 and 40 show the XPS spectra obtained for deposition of Na on Cu, and Li on Si, at the base position.

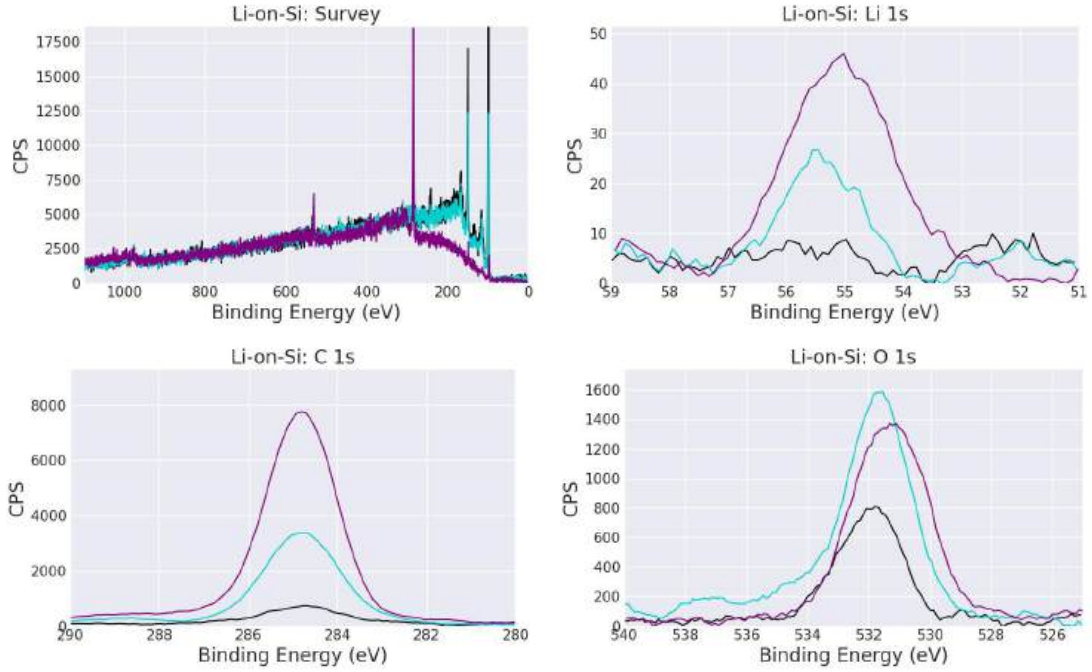

Figure 40: XPS spectra of Li deposited on a Si substrate separated 3.0 cm from the dispenser at a heating current of 8.0 A. The black lines correspond to the clean substrate, the turquoise lines to 138 min deposition, and the purple lines to 918 min deposition. A single moving average of 15 points smoothing was applied to all spectra except the survey.

Figures 39 and 40 display a significant presence of C and O contaminants, making the stoichiometry of the overlayer vital for calculating the amount of alkali metal deposited. Stoichiometry was calculated by assuming the overlayer is composed of only C, O and the alkali metal in question, then comparing their calibrated peak areas. For a raw peak area A_R, the calibrated peak area A_C can be found by division with the total sensitivity factor S_{tot} as[178,207]:

$$A_C = \frac{A_R}{S_{tot}} = \frac{A_R}{\lambda \cdot T_C \cdot D_C \cdot S_R}, \tag{12}$$

where λ, T_C, D_C, and S_R are the effective attenuation length, transition function correction, angular distribution correction, and relative sensitivity factor, respectively. S_{tot} is thus not unit-less, however, units are cancelled by division when A_C is used to

calculate stoichiometry. λ for a photoelectron in the overlayer can be approximated by the following empirical formula[208]:

$$\lambda = \frac{0.65 + 0.007\, E_k^{0.93}}{Z^{0.38}}\, nm, \tag{13}$$

where E_k is the kinetic energy of the photoelectron and Z is the average atomic number of the overlayer. T_C accounts for the fact that the electron transfer from sample to detector has an efficacy that depends on E_k and the analyser pass energy E_p. The formula used for T_C was:

$$T_C = E_p * \left(\frac{a^2}{a^2 * (E_k/E_p)^2} \right)^b, \tag{14}$$

where E_p, E_k, a, b are the instrument pass energy, photoelectron kinetic energy, an empirical parameter equal to 40 and an empirical parameter equal to 0.2 respectively. D_C accounts for the analyser angle θ and was calculated as:

$$D_C = \frac{1 - \frac{\beta}{4}(3cos(\theta) - 1)}{4\pi}, \tag{15}$$

where β is the asymmetry parameter which depends on the element and orbital in question. Values for β, as well as formulas for T_C and D_C were taken from the Multipack PHI MultiPak Software Manual Version 9. The values for the empirical parameters a and b were taken from the Multipak software connected to the XPS instrument. The values for S_R used were the theoretically derived Scofield relative sensitivity factors. The value for average Z in the overlayer was approximated to be 6.5, as this was the average value of all experiments when ignoring λ in Equation 12. Once A_C for each element i in the overlayer has been calculated, its fraction in the overlayer stoichiometry x_i can be found simply as:

$$x_i = \frac{A_{C,i}}{\sum_j A_{C,j}}. \tag{16}$$

The stoichiometries obtained for the overlayers of all four calibration experiments are given in Table 1. This table makes it clear that the overlayer is composed mainly of C for all experiments, with O having the second greatest presence and the alkali metal being the most scarce. Noteworthy is the circa two to three times greater presence of Na than

Li, as well as the standard deviation in composition between depositions.

Experiment	Alk			C			O		
	Mean	Max	SD	Mean	Max	SD	Mean	Max	SD
Na-on-Cu (base)	7.6	20.7	8.3	66.9	85.0	20.3	25.5	52.2	12.5
Na-on-Cu (ridge)	11.2	18.7	6.60	59.2	80.6	18.4	29.6	50.4	12.8
Li-on-Si (base)	4.3	8.0	2.3	68.8	79.7	9.1	26.9	42.0	11.0
Li-on-Si (ridge)	4.3	10.2	2.5	79.8	90.4	8.6	15.9	27.1	8.1

Table 1: Stoichiometry represented in percent for all evaporator calibration experiments, showing the mean, maximum, and standard deviation (SD) of all depositions for the experiment in question.

4.3.2 Rate Calculation

The Cu and Si spectra of Figure 41 show the attenuation of these two signals at the base position of the sample holder due to the overlayer, which causes substrate peak areas to reduce in size each deposition. This attenuation was used to calculate the thickness of the overlayer, as per[180]:

$$A_n = A_0 \exp\left(\frac{-d}{\lambda\, cos(\alpha)}\right) \;\therefore\; d = -\lambda\, cos(\alpha)\, ln\left(\frac{A_n}{A_0}\right), \tag{17}$$

where A_0 is the raw peak area without overlayer, A_n is the raw peak area with the overlayer after n depositions, d is the overlayer thickness, and α is the analyser angle.

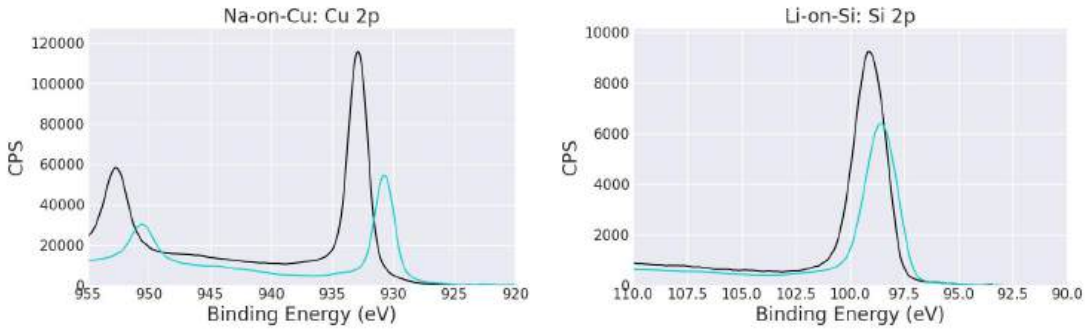

Figure 41: XPS spectra of the Cu substrate signal corresponding to the Na deposition experiment presented in Figure 39 (left) and the Si substrate signal corresponding to the Li deposited experiment presented in Figure 40 (right). The black lines correspond to the clean substrate, and the turquoise lines to 50 min Na deposition in a) and 138 min Li deposition in b). A single moving average of 15 points smoothing was applied.

Having now obtained the thickness d and elemental fractions x_i of the overlayer, a simple model was created to estimate the amount of alkali metal deposited. This model relies on the central assumption that the overlayer is homogenous, meaning that its struc-

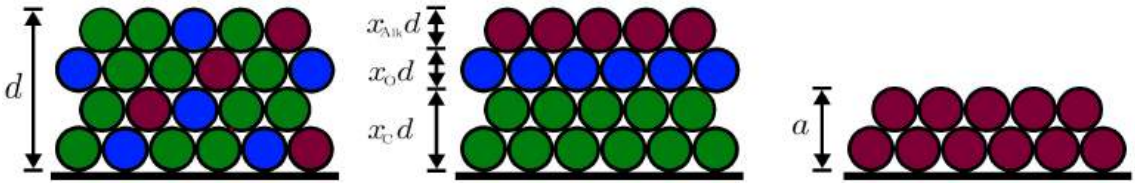

Figure 42: Schematics of the model used to estimate the alkali metal contribution to overlayer thickness, where green, blue and, red represent C, O, and alkali metal. The left-most schematic illustrates the assumption that the overlayer is homogenous, with negligible differences in layer composition and interatomic distances. The central schematic illustrates the consequence of this assumption, namely that each element contributes the same fraction to the overlayer thickness d as it does to its stoichiometry, there $x_C d$, $x_O d$ and $x_{Alk} d$ are the thickness contributions of C, O and the alkali metal, respectively. The rightmost schematic shows a pure alkali metal overlayer with BCC lattice constant a.

ture both globally and locally is treated on an average basis given by its stoichiometry. A schematic of such a homogenous overlayer is displayed on the left of Figure 42. Global homogeneity assumes that overlayer composition does not vary with distance from the substrate. This entails that wherever one cuts the overlayer, one is faced by a surface that has stoichiometric composition. Local homogeneity means that differences in local atomic environments are neglected such that all interatomic distances are treated as the average interatomic distance. This in turn leads to each element contributing an amount to the overlayer thickness d that is directly proportional to its contribution to the overlayer stoichiometry x_i. Element i is thus assumed to contribute $x_i d$ to the overlayer thickness, as displayed in the central schematic of Figure 42. If one then considers a pure alkali metal overlayer with BCC crystallography, one may define one monolayer as having a thickness of half the BCC unit cell, $a/2$, as displayed in the rightmost schematic of Figure 42. Dividing the overlayer thickness due to alkali metals, $x_i d$, by this monolayer thickness, one may finally estimate the number of deposited alkali metal monolayers t_{ML}, in the overlayer as:

$$t_{ML} = \frac{2x_i d}{a}. \tag{18}$$

The gradient of t_{ML} as a function of deposition time is the deposition rate in ML/min, which are given by the red trend lines in the graphs of Figure 43. Deposition rate values are given in Table 2 together with their associated uncertainty. Two sources of potential errors were considered when calculating uncertainty; firstly, the uncertainty in the overlayer thickness, Δd, which depends on the uncertainty in the raw peak area of the substrate signal ΔA_n. Secondly, the uncertainty in the fraction alkali metal in the overlayer, Δx_i, which depends on the uncertainty in the raw peak area of the alkali metals, $\Delta A_{R,a}$. The

magnitude of ΔA_n and $\Delta A_{R,a}$ were calculated using the signal-to-noise ratio (SNR) of the XPS signals by dividing the peak area in question by its SNR value, as per $\Delta A = A/(SNR)$. SNR values were generated in CasaXPS using Poisson statistics. Δd follows from differentiation of Equation 17 and the SNR of the substrate signal, yielding:

$$\Delta d = \frac{dd}{dA_n}\Delta A_n = -\lambda\, cos(\alpha)\, \frac{1}{A_n}\frac{A_n}{(SNR)} = \frac{-\lambda\, cos(\alpha)}{(SNR)}. \tag{19}$$

Δx_i was assumed to proportional to $\Delta A_{R,a}$, meaning that the fraction of alkali metal in the overlayer can not be known to a greater certainty than the certainty of the raw peak area of the alkali metal signal, thus:

$$\Delta x_i \approx \frac{\Delta A_{R,a}}{A_{R,a}} \approx \frac{1}{SNR}. \tag{20}$$

The total uncertainty in the overlayer thickness due to the alkali metal, Δt_{ML}, is then given by error propagation using the partial derivatives of Equation 16 with respect to d and x_i and the uncertainties Δd and Δx_i:

$$\Delta t_{ML} = \sqrt{\Big(\frac{\delta t_{ML}}{\delta x_i}\Delta x_i\Big)^2 + \Big(\frac{\delta t_{ML}}{\delta d}\Delta d\Big)^2}. \tag{21}$$

Some notable trends are present in Table 2, such as the Na rate being 4.5 times higher than the Li rate both on the base and ridge positions, as well as the rate being 26% higher on the ridge than base for both Na and Li. The Li rate is significantly more uncertain than that of Na, which is due to the higher SNR in the Li signal. For example, the highest SNR attained in the case of the Li signal was 3.48, whereas the Na signal produces SNR values as high as 49.75. A notable aspect of the deposition rate experiments can be seen in the Na-on-Cu (ridge) graph of Figure 43, where the amount of Na is reduced after circa 100 min deposition. There is thus some loss mechanism that removes alkali metal from the substrate, most likely associated with the heat from the evaporator. This and other unquantified sources of uncertainty will be discussed in Section 4.4 below.

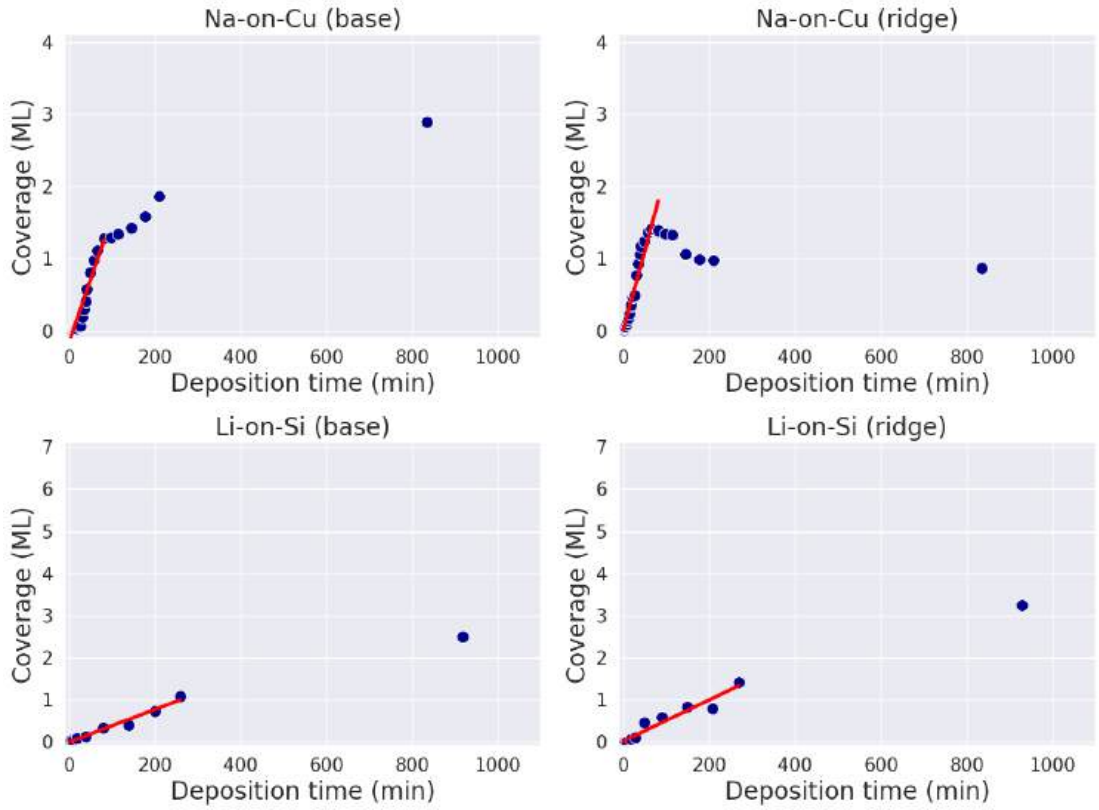

Figure 43: Overlayer thickness in monolayers as a function of deposition time for Na on Cu substrates and Li on Si substrates, with substrates attached either to the base or ridge of a sample holder. Each blue point is the overlayer thickness after a certain deposition and the red line is the evaporation rate.

Experiment	Rate (ML/min)	Δd^{max} (%)	Δx_i^{max} (%)	Δt_{ML}^{max} (%)
Na-on-Cu (base)	0.0174	4.5	2.5	5.1
Na-on-Cu (ridge)	0.022	3.9	2.2	4.5
Li-on-Si (base)	0.0039	3.2	28.7	28.9
Li-on-Si (ridge)	0.0049	6.8	27.7	28.5

Table 2: Rates and uncertainties of the calibration experiments. The rates are equivalent to the gradients of the linear trend lines in Figure 43. Δd^{max}, Δx_i^{max}, and Δt_{ML}^{max} are the uncertainties associated with deposition that produces the greatest coverage for the experiment in question, calculated in Equations 19, 20, and 21, respectively. The uncertainty of the greatest coverage was chosen to be displayed here as it gives an indication of the ultimate certainty that could be attained in each experiment.

4.4 Discussion

4.4.1 Unquantified Errors

The assessment of uncertainty in the evaporation rates has so far been quantitative in nature and only considered the raw XPS data, but there are less unquantifiable sources of potential errors that require attention. Particularly important are effects pertaining to the three orders of magnitude higher pressure of the XPS introduction chamber than

the STM preparation chamber, which is expected to introduce at least the following three uncertainties in evaporation rate. Firstly, the contamination of the XPS introduction chamber is so substantial that the composition of the overlayer is mainly C and O and varies considerably between depositions, as discussed in Section 4.3.1 and displayed in Table 1. This contamination and stoichiometric inconsistency, together with the crude assumption that differences in interatomic distance in the overlayer can be neglected, mean that the model created to estimate the number of alkali monolayers certainly is simplistic. Secondly, the substantially higher pressure in the XPS introduction chamber will cause greater scattering of alkali metals with gas molecules before reaching the substrate than in the STM preparation chamber, which reduces the rate of the former with respect to the latter. This effect should be considered especially in the case of Li deposition due to its small mass. Thirdly, as mentioned in the concluding remark of Section 4.3.2, there is a loss mechanism which in the case of the Na-on-Cu (ridge) experiment is sufficiently potent to reduce the amount of alkali metal present on the substrate once the dispenser starts depleting, as can be seen in Figure 43. This loss mechanism is very likely due to heat transfer from the dispenser. This is supported by the reduction in Na on the ridge but not on the base of the sample holder, as the former is 0.5 cm closer to the dispenser and would thus be exposed to greater heat power per unit area. One may additionally speculate that the heat transfer from dispenser to sample could be the reason why Li-on-Cu experiments were less successful than Li-on-Si ones, as it could be that the heat energy causes Li diffusion into the Cu substrate, or that Li is more easily desorbed from Cu than Si.

As mentioned in Section 4.2, the dispensers are operated at temperatures between 750 ^oC and 820 ^oC. The dispenser heat transferred to the environment can be assessed by considering two heat transfer contributions from a surface of area A at temperature T; convection (Q_c) and radiation (Q_r), where the former describes heat energy transferred by massive particles in a fluid and the latter describes electromagnetic heat transfer. Convection can be modelled by Newton's law of cooling, $Q_c = hA\Delta T$, where h is the convective heat transfer coefficient and ΔT is the temperature difference between the surface and the environment. Radiation can be modelled by the Stefan-Boltzmann law, $Q_r = \epsilon\sigma AT^4$, where σ is the Stefan-Boltzmann constant and ϵ is the emissivity of the material in ques-

tion, which for an ideal black-body would be unity[209]. Radiation can thus be assumed to be equal in the XPS introduction and STM preparation chambers, but convection will differ since the convective heat transfer coefficient increases with increased environmental pressure[210]. For example, one study reports that at 100 ^oC, σ is unaffected by changes in pressure, but h increases by a factor of 5 between 18 Pa and 220 kPa[210]. The strong pressure dependence of h and the three orders of magnitude higher pressure in the XPS introduction chamber compared to the STM preparation chamber mean that one must consider whether convection makes a significant contribution. It may, however, be the case that the 5.0×10^{-5} Pa baseline pressure of the XPS introduction chamber is already so low as to make convection insignificant compared to radiation. In any case, radiation being equal in both chambers and convection being higher in the XPS introduction chamber necessitates that the heat transfer from dispenser to sample in the XPS chamber is greater, regardless of the exact magnitude of the convective contribution. Perhaps most importantly, it seems that heat transfer is strongly dependent on the dispenser-sample separation, since the amount of Na is not reduced on the sample holder base, which has the same dispenser-sample separation as the STM preparation chamber. Because the heat transfer is greater in the XPS introduction chamber, this fact reasonably allows for the conclusion that heat transfer should not be sufficiently potent to remove alkali metal from $SrTiO_3$ samples in the STM introduction chamber, assuming that Li and Na have at least similar adhesion strength to $SrTiO_3$ as Li has to Si and Na has to Cu.

The total effect of scattering and heat transfer due to the higher XPS introduction chamber pressure are difficult to quantify, but their influence is certain to reduce the evaporation rate in the XPS introduction chamber to some extent compared to the STM preparation chamber. There is, however, reason to believe that rates obtained are at the very least within the correct order of magnitude. First of all, the calibration experiments display a high degree of consistency between experiments, which is illustrated by two important results. Firstly, the ratio between Na and Li rates on both base and ridge positions was 4.5. Secondly, both the Na and Li rates were 26% greater on the ridge than base. This consistency in ratios between Na and Li values is a positive indication that the experiments have yielded meaningful results. In addition, the higher rate on the ridge position meets the expectation that a dispenser closer to the sample should provide

a greater amount of alkali metal per unit time and area, which further strengthens the credibility of the rates. The rate obtained for Na should be particularly reliable due to its significantly smaller errors, for which there is some support in the literature. When publications do report the rates obtained for SAES Getters alkali metal dispensers, there is a significant spread in reported values due to differences in dispenser operation. For example, some authors operate dispensers at constant current[128,149,157], others at constant pressure[145,151], and various heating currents and sample-dispenser separations have been employed[9,139,162,211]. For this reason, reported Na rates range from 0.026 ML/min[151] to 0.067 ML/min[158], where the former is within the error margin of the rate obtained in the calibration experiments presented in this chapter.

4.4.2 Insights from STM Experiments

The expectation that the STM preparation chamber would see higher evaporation rates due to its lower pressure caused a concern for over-deposition. This concern was rational, however, it led to a somewhat less rational decision, namely to reduce the dispenser heating current from 7.0 A to 6.5 A for Na and from 8.0 A to 7.5 A for Li once the evaporator was installed in the STM instrument. This reduces the dispenser yield by circa 35% according to the dispenser manual, and should thus produce a similar reduction in evaporation rate. The reasoning behind this was to gain some safety margin against over-deposition, however, a more rigorous course of action would have been to keep the current for which the evaporator had been calibrated and instead reduce deposition time. Despite this margin, however, the Na evaporation rate was still underestimated compared to the rate obtained in the calibration experiments, which was first revealed in an high coverage Na-on-$SrTiO_3$(001) experiment. This experiment deposited Na for 25 min, which according to the values obtain in the calibration experiments should not have produced more than 0.65 ML coverage. It was, however, found that this deposition time produced a coverage of circa 1.0 to 1.5 ML. The evaporation rate was subsequently adjusted in the following manner; first, the new rate was assigned a value that matched the STM data, namely twice that of the old rate. Secondly, as the error in the old rate was most likely due to the pressure effects discussed in 4.4.1, the error as a percentage of the rate magnitude was assumed to be unchanged, i.e. circa 50%. The final Na rate assumed for STM deposition experiments was thus 0.05 ± 0.025 ML/min at a heating current of 6.5 A. This adjustment

is significant for high coverage experiments, but for the lowest coverages investigated, it amounts to no more and a change of 0.02 ML. This can be compared to one previous study that estimates the accuracy of the Na coverage to be circa 0.05 ML for sub-monolayer[125], which is an accuracy still maintained by the XPS calibration experiments presented in this chapter despite the rate underestimation.

The greater uncertainty in the Li rate compared to that of Na obtained in these XPS experiments warranted a separate method to verify its validity. Such a method became available once Na dispensers were exchanged for Li in the evaporator, as the magnitude of the Li rate compared to that of Na could be estimated by the pressure of the UHV chamber during evaporator operation. This is possible as one can reasonably assume that for a fully degassed dispenser, the increase in the pressure in the chamber above its baseline should be due to alkali evaporation from the dispenser. As such, if the Na dispenser causes a pressure increase of p_{Na} and the Li dispenser causes a pressure increase of $p_{Li} = p_{Na}/n$, then the Li rate should be $1/n$ of the Na rate. In the three Na experiments preceding the first Li experiment, the average pressure one minute after reaching the deposition current was $6.73 \pm 1.40 \times 10^{-7}\ Pa$. In the first Li experiment, the pressure one minute after reaching the deposition current was $1.16 \times 10^{-7}\ Pa$. This gives a Na/Li pressure ratio of 5.8. Succeeding Li deposition found a similar ratio, as this experiment and the four subsequent ones found an average pressure one minute after reaching deposition current of $1.70 \pm 0.34 \times 10^{-7}\ Pa$, giving a Na/Li pressure ratio of circa 4.0. This is similar to the Na/Li rate ratio of 4.5 consistently obtained in the XPS experiments for both base and ridge positions, lending a good amount of credence to this ratio. The Li rate was consequently rounded to 1/5 of the Na rate. If one then assumes that Li experiences an rate increase similar to that of Na in the STM preparation chamber compared to the XPS introduction chamber, it follows that the Li rate should be adjusted by the same factor of two that was applied to the Na rate. The final Li rate assumed for STM deposition experiments was thus 0.01 ± 0.005 ML/min at a heating current of 7.5 A.

4.5 Conclusion

An alkali metal evaporator was constructed by refurbishing a pre-existing Ba evaporator to make it compatible with a SAES Getters alkali metal dispenser. The evaporator was

calibrated using attenuation of the substrate XPS signal. The rate obtained for Na is in reasonable agreement with literature and has acceptable errors in its raw XPS data. It was, however, found in subsequent STM experiments that the Na rate had been underestimated, most likely due to effects such as increased scattering and convection heating caused by the three orders of magnitude higher pressure in the XPS introduction chamber. This underestimation called for a doubling of the XPS calibrated Na rate to a final value of 0.05 ± 0.025 ML/min. The Li rate obtained in XPS experiments has a significantly greater associated error, however, both XPS experiments and the pressure during operation in subsequent STM experiments indicate that the Li rate is circa 1/5 that of Na. This gives credibility to the rough Li rate obtained through XPS, thus, assuming that the efficacy of Li deposition in the STM preparation chamber compared to the XPS introduction chamber changes by the same factor as Na, the Li rate obtained in the XPS experiments was also doubled to a final value of 0.01 ± 0.005 ML/min. Most important, however, is that the rates obtained are sufficiently accurate to achieve the goal of this thesis, namely to study alkali metal interactions with $SrTiO_3$ at the limit of low coverage, where the reconstruction dominates the surface, and high coverage, where the surface is covered by one to two alkali metal monolayers. For this purpose, the evaporation rates attained in this chapter are sufficiently precise, as will be seen in subsequent chapters.

5 Na on $SrTiO_3(001)$

5.1 Introduction

This chapter describes the interaction of Na with $SrTiO_3(001) - c(4\times2)$, which was investigated using STM and DFT data. Three Na coverages were studied in the STM: $0 < 0.1$ ML, $0.1 < 0.3$ ML, and $1.0 < 2.0$ ML, where the two lower coverages will be treated together as they generated the same types of surface structure. For each coverage, STM data will first be presented in order of annealing temperature, after which key surface structures are characterised. The $(\sqrt{5}\times\sqrt{5}) - R26.6^o$ reconstruction, known from previous studies[51,113], was induced on $SrTiO_3(001)$ by Na exposure. The periodicity of this reconstruction will be established in Section 5.2.1, but to avoid introducing new nomenclature, it will be referred to as $(\sqrt{5}\times\sqrt{5}) - R26.6^o$ throughout the chapter. Some XPS data will, additionally, be used to aid the characterisation of the $0 < 0.1$ ML coverage. The DFT results displayed in Section 5.4 will be used to analyse how Na adsorption is influenced by the surface structure of $c(4\times2)$. Since this is the first chapter treating the interaction between $SrTiO_3$ surfaces and alkali metals, the DFT study will include two general aspects of alkali metal adsorption on $SrTiO_3$ surfaces which are similar for both alkali metals on all $SrTiO_3$ reconstructions and expected from the literature covered in Chapter 2, and will thus not be treated in Chapters 6-8. The first of these general aspects is the electronic structure of clean $SrTiO_3$ surfaces, covered in Section 5.4.1, and the second is the response of $SrTiO_3$ to increasing alkali metal coverage, covered in 5.4.2.

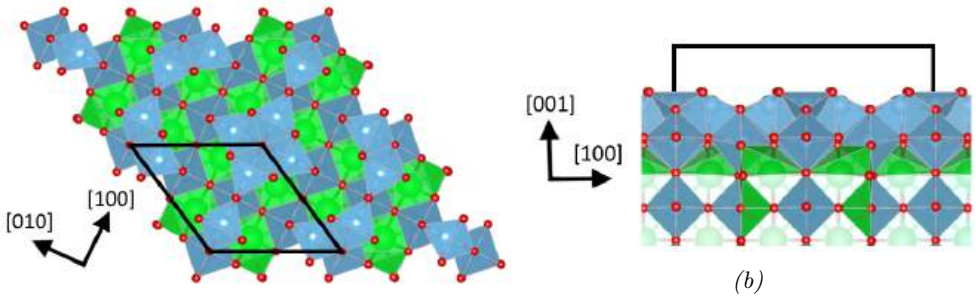

(a) *(b)*

Figure 44: The relaxed $SrTiO_3(001)-c(4\times2)$ reconstruction used for DFT adsorption calculations. Figure a) displays the top view parallel to the surface normal, showing how this structure is generated by rows of TiO_5[] quartets, and b) displays the side view, where the TiO_2 double layer can be seen. Green, blue, and red blue balls are Sr, Ti, and O, respectively, and green and blue polyhedra represent O coordination around Sr and Ti, respectively. The black lines indicate the surface unit cell.

A brief reminder of the atomic structure of $SrTiO_3(001)-c(4\times2)$ is in order before the Na deposition data is presented. This reconstruction is generated by the arrangement of $TiO_5[]$ units into square-like quartets on a bulk-like TiO_2 layer, as displayed in Figure 44. Quartets have corner-sharing units in the [100] direction and are disconnected in the [010] direction, forming lines of quartets along [100]. The lines of quartets are displaced by half a quartet, equivalent to two unit cells, in the [100] direction, hence generating the $c(4\times2)$ symmetry. A STM image of the $c(4\times2)$ reconstruction can be seen in Figure 45a, where the same surface unit cell as displayed in Figure 44 is marked by the black diamonds in the inset image.

5.2 Low and Medium Depositions

Because the $0 < 0.1$ ML and $0.1 < 0.3$ ML Na depositions are treated together, the evolution of the $0 < 0.1$ ML with respect to annealing temperature will be explained in detail as a starting point to present the observed surface structures. The $0.1 < 0.3$ ML deposition will thereafter be given a briefer presentation where key similarities and differences are highlighted.

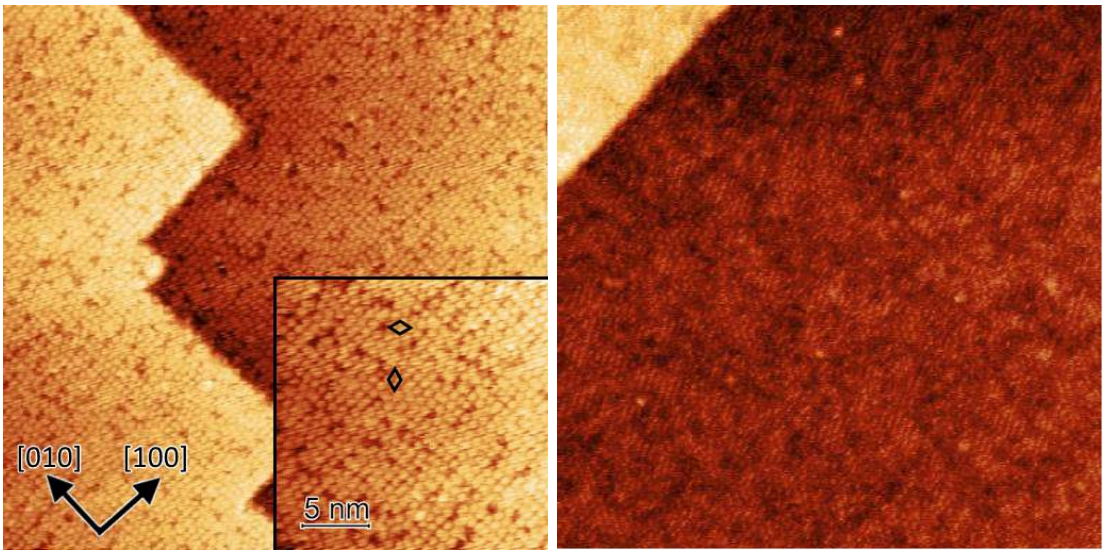

(a) *(b)*

Figure 45: STM images of a) the $SrTiO_3(001)-c(4\times2)$ reconstruction (U=1.6 V, I=0.2 nA, $50\times50\,nm^2$) and b) the same sample after $0 < 0.1$ ML deposition and 400 °C annealing (U=0.8 V, I=0.1 nA, $50\times50\,nm^2$). The black diamonds in the inset of a) represent the surface unit cell of $c(4\times2)$. Step edge heights are a) 0.39 ± 0.02 nm and b) 0.39 ± 0.01 nm. The scattered spots in b) protrude the surface by 0.13 ± 0.02 nm.

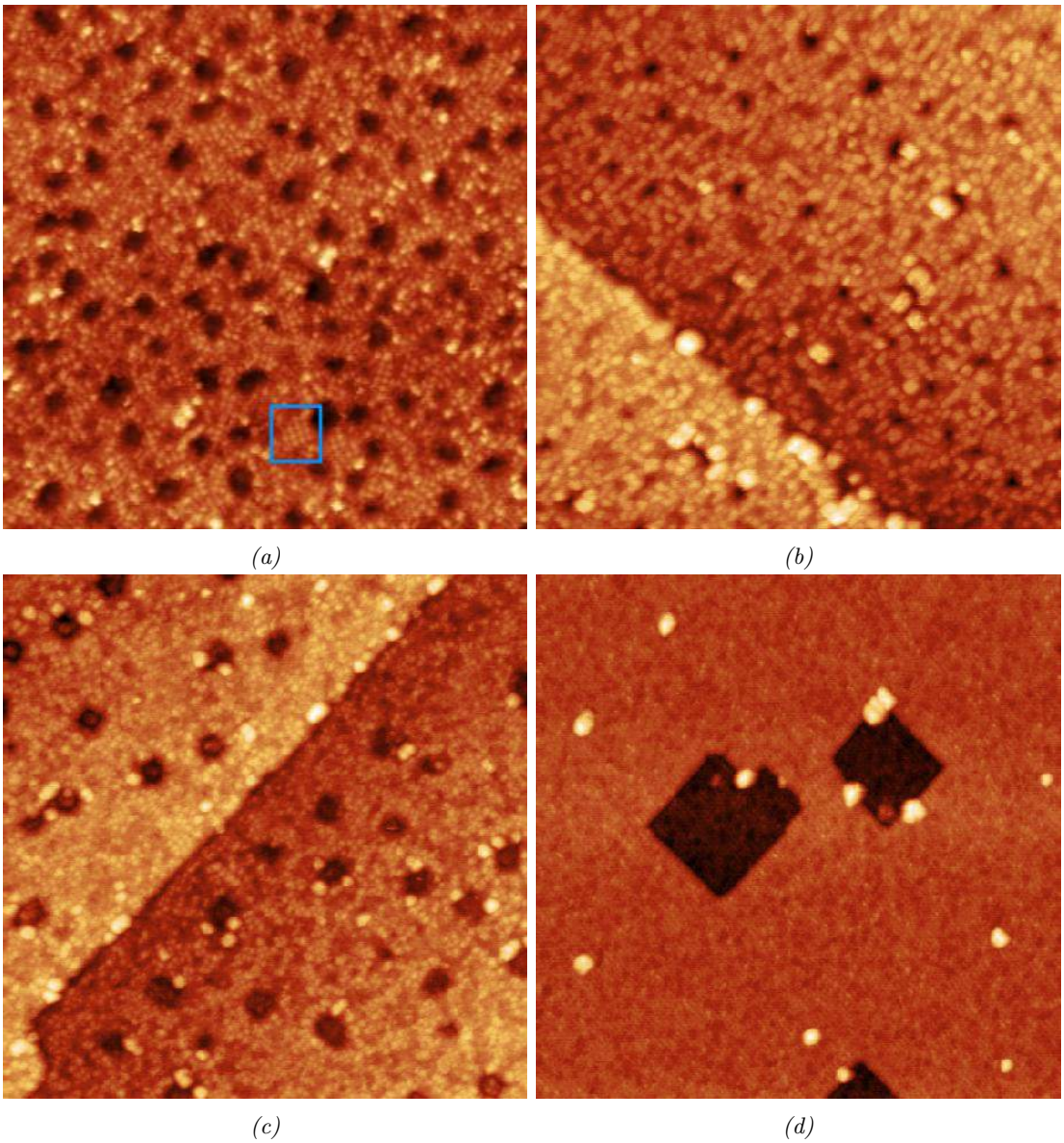

Figure 46: STM images of $0 < 0.1$ *ML Na deposited onto* $SrTiO_3(001) - c(4\times2)$ *after annealing to a) 500 °C (U=0.8 V, I=0.1 nA,* $60\times60\,nm^2$*), b) 550 °C (U=1.0 V, I=0.1 nA,* $60\times60\,nm^2$*), c) 600 °C (U=1.0 V, I=0.1 nA,* $80\times80\,nm^2$*), and d) 750 °C (U=0.8 V, I=0.4 nA,* $80\times80\,nm^2$*). Figures a) to c) show the evolution of the surface after the first transformation and d) shows the high-T surface produced by the second transformation. The blue rectangle in a) marks a region of* $\sqrt{5}\times\sqrt{5}-R26.6^o$ *reconstruction. Holes are* 0.2 ± 0.04 *nm deep in a),* 0.41 ± 0.03 *nm deep in b), and* 0.40 ± 0.04 *nm deep in c). The diameter of holes grows form* 3.4 ± 0.98 *nm in b) to* 4.8 ± 2.89 *nm in c). Nanoparticles in b) and c) have diverse sizes, with 7 largest particles in b) being* 0.52 ± 0.09 *in height and* 2.51 ± 1.28 *in width. The holes d) differ in size, having a depth of* 0.46 ± 0.01 *nm and diameter of* 17.35 ± 10.62 *nm, and the 7 largest particles are* 0.62 ± 0.04 *in height and* 2.57 ± 0.51 *in width.*

At $0 < 0.3$ ML coverage, the $SrTiO_3(001)$ surface undergoes two transformations, one at lower and one at higher annealing temperature, which will be referred to as the first and second transformation. An example of the $c(4\times2)$ reconstructed surface onto

which Na was deposited is shown in Figure 45a. An image after deposition but before the first transformation is displayed in Figure 45b, showing scattered spots that likely correspond to Na-based particles. Step edges in both Figure 45a and 45b are in good agreement with the $SrTiO_3(001)$ unit cell length of 0.39 nm. After 500 ^oC annealing, the first transformation has been activated, which generates a surface distinguished by holes and domains of $\sqrt{5}\times\sqrt{5}-R26.6^o$, as displayed in Figures 46a-46c. The holes produced by the first transformation initially have a depth of circa 0.2 nm, as per Figure 46a, which is close to half a $SrTiO_3(001)$ unit cell and indicative of the outermost surface layer being removed. Holes then grow with increasing annealing temperature and eventually settle at depth similar the 0.39 nm unit cell length obtained for step edges in Figure 45, while increasing their diameter by circa 40% between 550 ^oC and 600 ^oC annealing. Following 750 ^oC annealing, the second transformation of the surface ensues, producing the surface displayed in Figure 46d. This surface will henceforth be referred to as the high-T surface. This transformation substantially increases the size of holes, from a diameter of 4.8 ± 2.89 nm to 17.35 ± 10.62 nm, and the size distribution of nanoparticles becomes narrower, with the standard deviation in both height and width reducing by circa 60 % of. Notably, nanoparticles in Figures 46b-46d seem to preferentially locate to step edges.

The equivalent evolution for the $0.1 < 0.3$ ML deposition can be seen in Figure 47. Figure 47a shows the $c(4\times2)$ surface after deposition and 300 ^oC annealing, Figure 47b shows the result of the first transformation, and Figures 47c-47e show the result of the second transformation. It is noteworthy that the second transformation appears to occur at 200 ^oC lower temperature for $0.1 < 0.3$ ML, which is temperature separation greater than the uncertainty in temperature of circa $\pm 50^oC$ with respect to the nominal annealing temperature (as discussed in Chapter 3). It may thus be that a greater Na concentration reduces the temperature required for the second transformation. Figures 47d and 47e displays a notable difference in the high-T surface between the $0 < 0.1$ ML and $0.1 < 0.3$ ML deposition, namely that holes and step edges grow rounder at annealing temperatures above 600 ^oC for the $0.1 < 0.3$ ML coverage. Following 750 ^oC annealing, all traces of Na influence on the surface disappear and the $c(4\times2)$ reconstruction returns, as can be seen in Figure 47f.

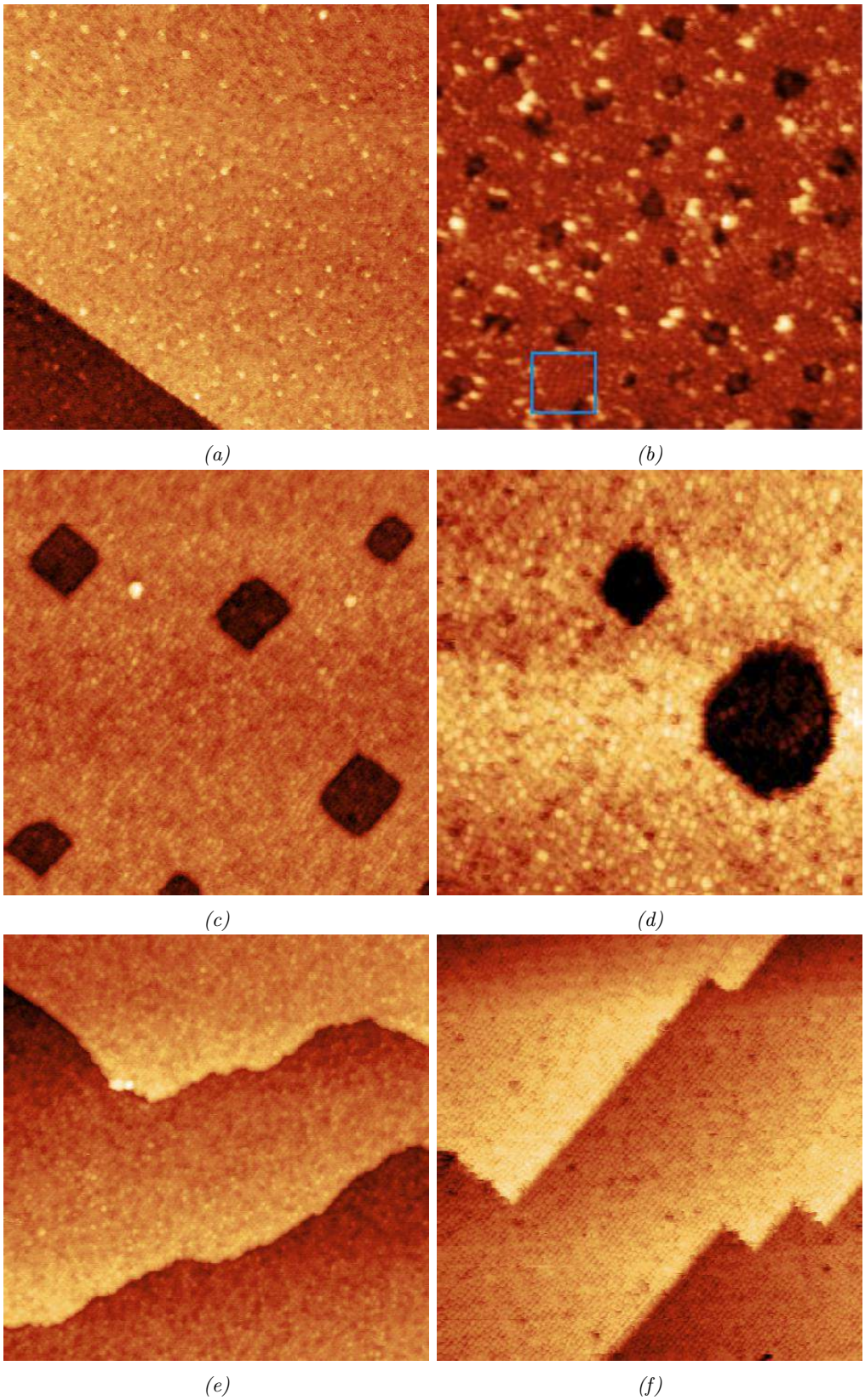

Figure 47: STM images of $0.1 < 0.3$ *ML Na deposited onto* $SrTiO_3(001) - c(4\times2)$ *after annealing to a) 300 °C (U=1.6 V, I=0.8 nA,* $80\times80\,nm^2$*), b) 500 °C (U=1.6 V, I=0.8 nA,* $50\times50\,nm^2$*), c) 550 °C (U=1.0 V, I=1.0 nA,* $60\times60\,nm^2$*), d) 600 °C (U=0.8 V, I=1.4 nA,* $40\times40\,nm^2$*), e) 600 °C (U=0.8 V, I=1.4 nA,* $80\times80\,nm^2$*), and f) 750 °C (U=0.8 V, I=1.4 nA,* $60\times60\,nm^2$*). a) shows the* $SrTiO_3(001) - c(4\times2)$ *surface covered with Na, b) shows the surface after the first transformation, c)-e) show the high-T surface produced by the second transformation, and f) shows the return of the* $c(4\times2)$ *reconstruction. The blue rectangle in b) marks a domain of the* $(\sqrt{5}\times\sqrt{5}) - R26.6^o$ *reconstruction. It may be worth noting that the surface in f) appears to also contain some areas of* (2×2) *ordering.*

5.2.1 Characterisation

A characterisation of the periodic features generated by the two transformations is presented in Figure 48. Figure 48a shows one of the areas used to confirm the identity of the $(\sqrt{5}\times\sqrt{5}) - R26.6^o$ reconstruction, which is known from the literature[51,113] and was treated in Chapter 2. The high-T surface has, to the best knowledge of the author, not been previously reported. Two periodic structures were identified on this surface; dots with $\sqrt{5}\times$ ordering and rows with (2×1) ordering. The former is indicated by the lines in Figure 48b, where the dots marked by the two black lines align to form a small patch of $(\sqrt{5}\times\sqrt{5})-R26.6^o$, which indicates that areas of this reconstruction may have survived the second transformation. The (2×1) rows were more challenging to characterise and could not be properly discerned until SmartAlign was applied. The blue rectangle in Figure 48c shows a particularly clear row, and the line in the bottom left corner measures a $2\times$ periodicity across rows.

XPS may give some further assistance in the characterisation of the high-T surface. Once the sample that received the $0 < 0.1$ ML Na deposition had received its final annealing treatment at 800 ^oC, XPS spectra were acquired along its length to investigate chemical differences resulting from the temperature gradient. As explained in Chapter 3, the two ends of the sample are estimated to differ in effective annealing temperature by up to 100 ^oC. Figures 49c and 49d show the colder and hotter ends of the sample, demonstrating that Ti reduction has been nullified to remove the 3+ and 2+ oxidation states. The surface at the colder end of the sample is dominated by the high-T surface, as can be seen in Figure 49a. At the hotter end of the sample, the $c(4\times2)$ reconstruction has returned, as can be seen in Figure 49b. It thus seems that the high-T surface is associated with Ti reduction, and that the return of the reconstruction results from a nullification of this reduction.

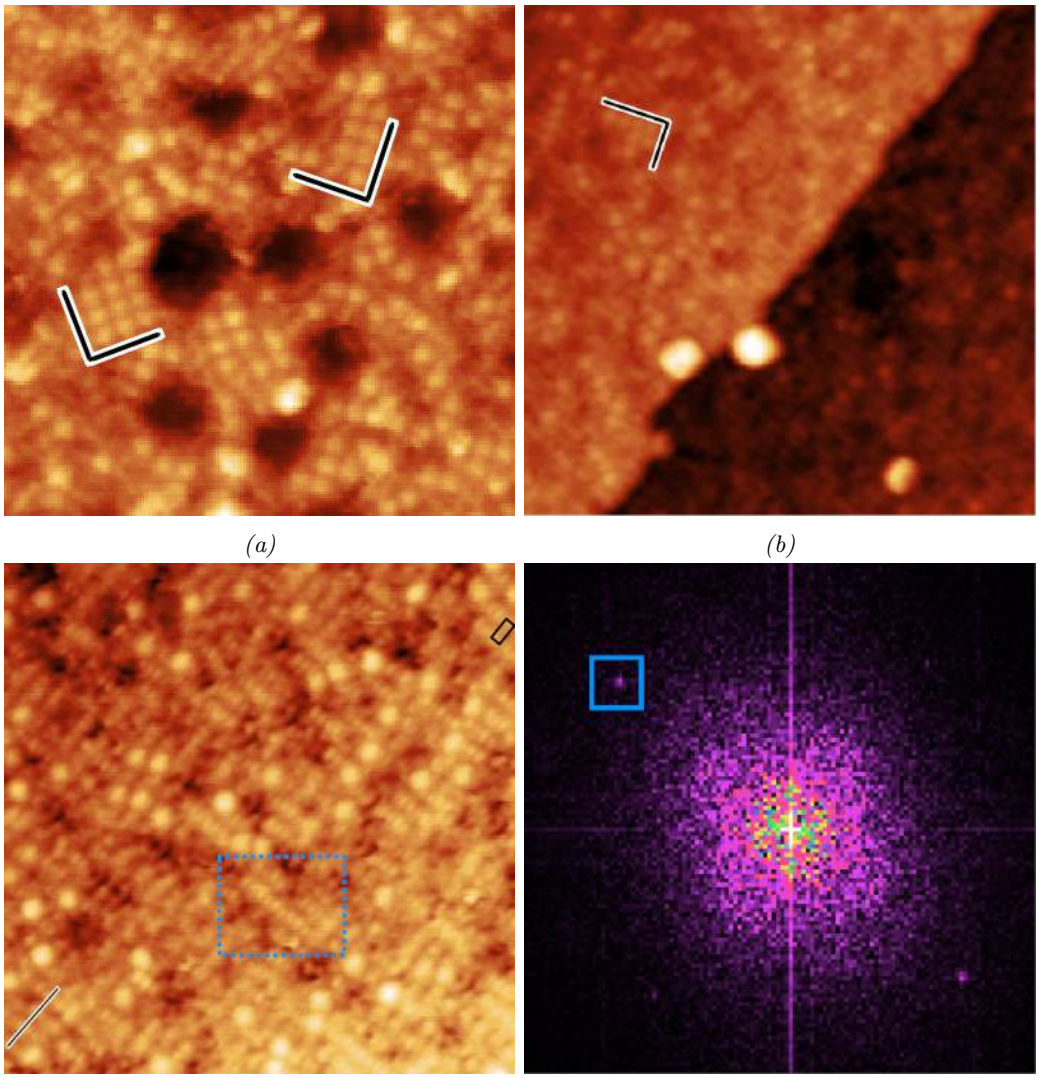

(a) *(b)*

(c) *(d)*

Figure 48: Characterisation of periodic structures of the two transformations observed following $0 < 0.3$ *ML Na deposition on* $SrTiO_3 - c(4\times2)$ *and annealing up to 800 °C. a) shows a surface produced by* $0 < 0.1$ *ML Na deposition and 500 °C annealing (U=0.8 V, I=0.1 nA,* $20\times20\,nm^2$*) (averaged over 9 images in SmartAlign), where lines are drawn along vectors inclined* -26.6^o *or* 26.6^o *to* $SrTiO_3\langle100\rangle$*. These are the possible directions of the* $\langle210\rangle$ *basis vectors for* $(\sqrt{5}\times\sqrt{5}) - R26.6^o$*, along which dots also have* $\sqrt{5}\times$ *periodicity with respect to* $SrTiO_3\langle100\rangle$*, confirming that this reconstruction is indeed* $(\sqrt{5}\times\sqrt{5}) - R26.6^o$*. Figure b) shows the high-T surface after the* $0 < 0.1$ *ML coverage was annealed to 700 °C, (U=1.0 V, I=0.2 nA,* $56.6\times57.0\,nm^2$*), averaged over 8 images in SmartAlign. This surface contains dots arranged parallel to one of the* $\langle210\rangle$ *basis vectors of* $(\sqrt{5}\times\sqrt{5}) - R26.6^o$*, indicated by black lines, along which they also have the periodicity of this reconstruction. Figure c) shows the* $0.1 < 0.3$ *ML coverage after 600 °C annealing (U=0.8 V, I=1.4 nA,* $20\times20\,nm^2$*), averaged over 4 images in SmartAlign. The line at the bottom left is drawn across rows aligned with* $[010]$*, the spacing of which has* 0.76 ± 0.02 *nm periodicity in* $[100]$*, i.e. within 2% of* $2\times$*. The blue dashed rectangle shows a particularly clear row. Measuring the length of this row together with four others and counting the number of dots along their lengths yield a periodicity of* 0.40 ± 0.01 *nm, close to one* $SrTiO_3(001)$ *unit cell, which together with the* $[010]$ *directionality of rows indicate* $1\times$ *periodicity. This is supported by the FFT of c) shown in f), where the point in the blue rectangle and its reflection were measured to be equivalent to* 0.38 ± 0.01 *nm periodicity.*

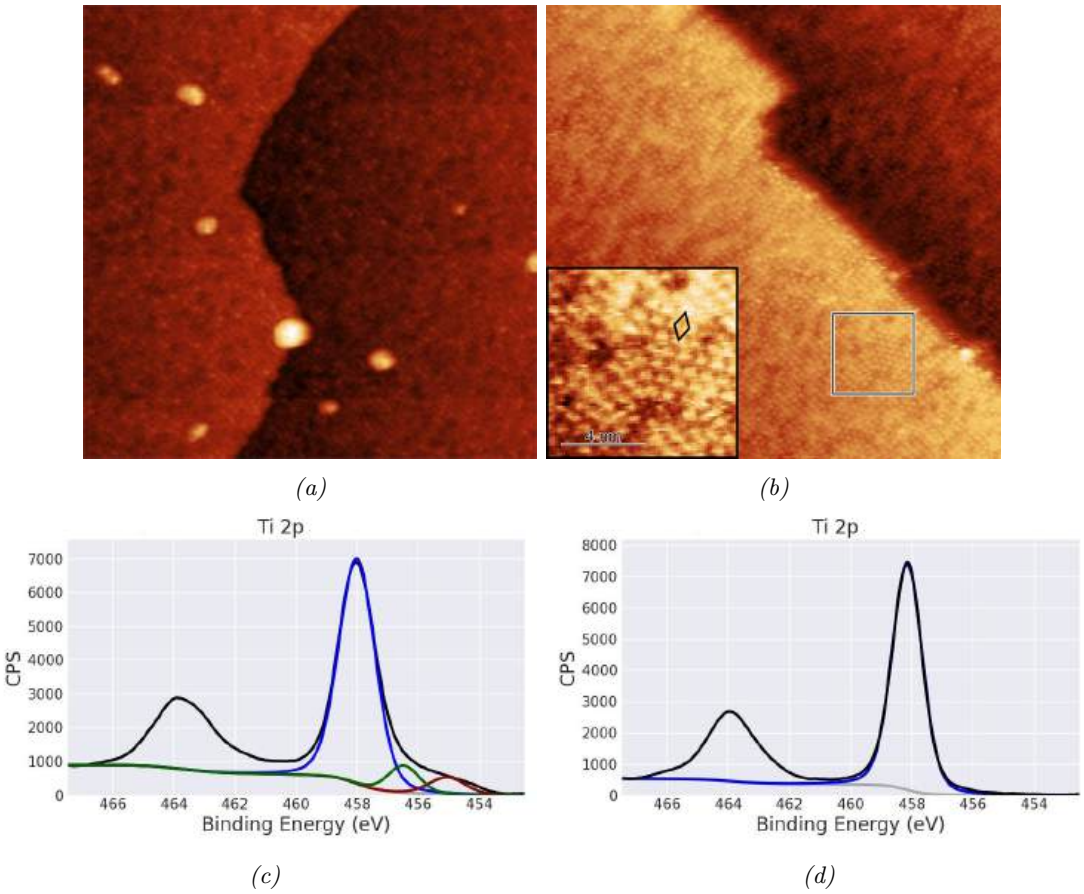

Figure 49: STM images and corresponding XPS spectra of the $0 < 0.1$ *ML Na sample after annealing to 800* ^oC*. Figure a) shows the colder side of the sample (U=1.0 V, I=0.1 nA,* $60{\times}60nm^2$*) and b) the hotter side of the sample (U=1.2 V, I=0.1 nA,* $50{\times}50\,nm^2$*). The surface in a) is the high-T surface and b) is* $SrTiO_3(001) - c(4{\times}2)$ *reconstruction. The inset of b) marks the surface unit cell of* $c(4{\times}2)$ *by the black diamond. c) shows the Ti 2p XPS spectrum of the colder end of the sample corresponding to the surface in a), and d) shows the Ti 2p XPS spectrum of the hotter end of the sample corresponding to the surface in b). The black line is the total signal, the blue, red and green lines are* Ti^{4+}*,* Ti^{3+}*, and* Ti^{2+} *signals, respectively, and the gray line is the Shirley background. The sample was exposed to air before insertion into the XPS instrument.*

5.3 High Deposition

The high deposition STM experiment pertains to $1.0 < 2.0$ ML Na deposited onto $SrTiO_3(001) - c(4 \times 2)$. An overview of the evolution of this coverage as a function of annealing temperature is given in Figures 50 and 51. Figure 50a shows the surface after 400 ^oC annealing, which is covered by irregular, amorphous nanoparticles, while step edges can still be identified. Following 500 ^oC, the colder side of the sample produces the surface displayed in Figure 50b, which is dominated by amorphous holes and islands. Both the depth of holes and the height of islands differ from the $SrTiO_3(001)$ unit cell length by 10-20 %, whereas step edge heights are within error of the unit cell. At the hotter end of the sample, shown in Figure 50c, holes have been removed and islands have become

more rounded. Islands, furthermore, retain a similar height to the surface in Figure 50b, and step edges are still within error of the $SrTiO_3(001)$ unit cell length. The two ends of the sample should be less than 100 ^oC annealing apart in annealing temperature, as discussed in Chapter 3. After 600 ^oC, the hotter end of the sample produces the surface seen in Figure 50d, lacking amorphous islands but retaining nanoparticles. The surfaces in Figures 50c and 50d appear to have acquired some degree of order, which will be subject to an attempted characterisation in Section 5.3.1.

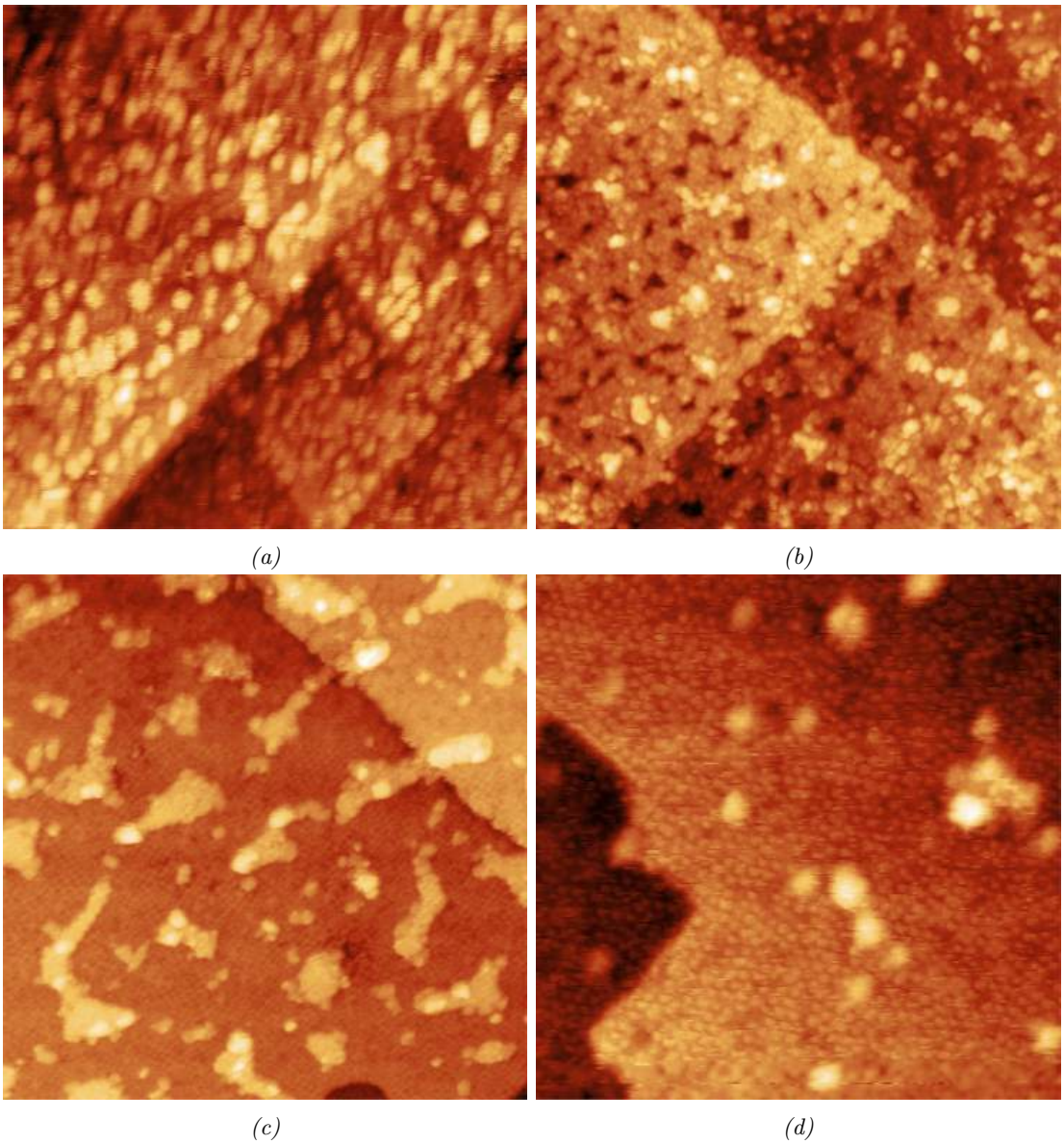

Figure 50: STM images of $1.0 < 2.0$ *ML Na deposited onto* $SrTiO_3(001) - c(4\times2)$ *after annealing to a) 400 °C (U=2.0 V, I=0.1 nA,* $100\times100\,nm^2$*), b) 500 °C (colder side of the sample) (U=0.8 V, I=0.1 nA,* $80\times80\,nm^2$*), c) 500 °C (hotter side of the sample) (U=1.2 V, I=0.2 nA,* $60\times60\,nm^2$*), and d) 600 °C (hotter side of the sample) (U=1.0 V, I=0.1 nA,* $30\times30nm^2$*). b) displays* 0.45 ± 0.02 *nm deep holes and* 0.46 ± 0.06 *nm tall islands, as well as step edges with a height of* 0.41 ± 0.02 *nm. Island in c) are* 0.45 ± 0.03 *nm tall and step edges have a height of* 0.402 ± 0.021*. Step edges in d) have a height of* 0.40 ± 0.03 *nm and particles are* 0.46 ± 0.05 *nm tall.*

Figure 51a shows the formation of holes at the colder side of the sample after annealing to 700 ^oC. Both holes and step edges in this image have mean heights of 0.40 ± 0.02 nm, thus similar to the $SrTiO_3(001)$ unit cell length. This suggests that the $SrTiO_3$ substrate is being imaged, whereas the divergence from this value of holes and islands after annealing at 500 ^oC and 600 ^oC suggests that the surface may have been covered by a Na-based overlayer. At the hotter side of the sample, the second transformation has ensued to produce the high-T surface, displayed in Figure 51b. The holes in this image were measured to have similar depths to previous measurements of the high-T surface, being circa 20 % deeper the $SrTiO_3(001)$ unit cell.

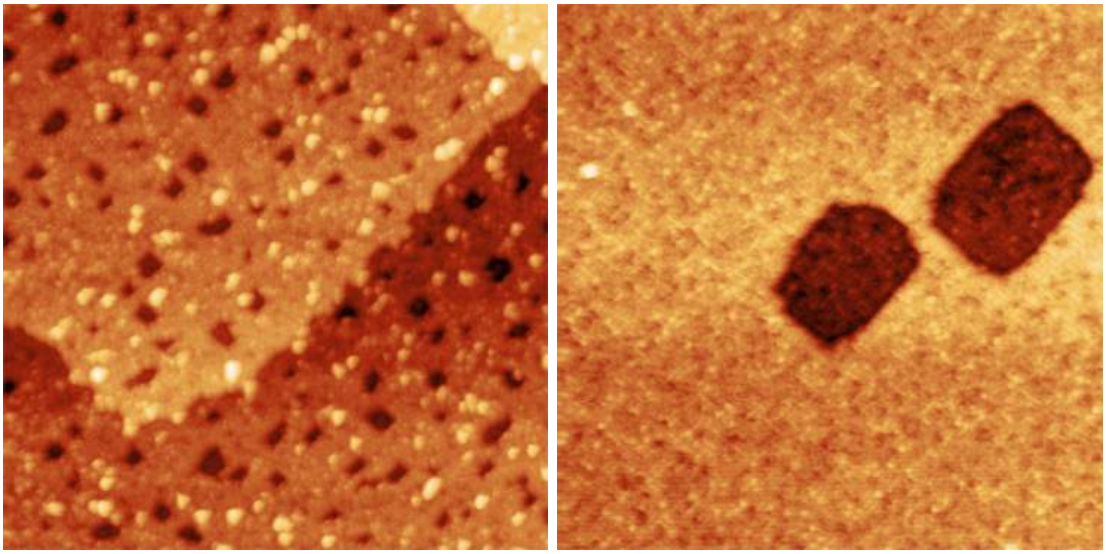

(a) *(b)*

Figure 51: STM images of $1.0 < 2.0$ *ML Na deposited onto* $SrTiO_3(001) - c(4\times2)$ *after annealing to 700* ^oC *where a) shows the colder side of the sample (U=1.0 V, I=0.1 nA,* $100\times100\,nm^2$*) and b) the hotter side of the sample (U=1.0 V, I=0.1 nA,* $60\times60\,nm^2$*). Holes have depths of* 0.40 ± 0.02 *nm in a) and* 0.48 ± 0.03 *nm in b). The step edge height in a) is* 0.40 ± 0.04 *nm.*

5.3.1 Characterisation

A qualitative assessment of Figures 50c-50d lead to the suspicion that surfaces in these images firstly contain ordered structures, and secondly that the degree of ordering increases as annealing temperature is raised from 500 ^oC to 600 ^oC. A quantitive analysis indicates that this is indeed the case, as shown in Figure 52. A cropped image and a FFT of Figure 50c are displayed in Figures 52a and 52d, respectively. Figure 52a shows three lines along rows of periodic features, which seems be driven towards alignment with $SrTiO_3[100]$. The points in the FFT of Figure 52d are diffuse and therefore limited in their utility for

establishing periodicity, but the points in the blue rectangle are close to 2× periodicity with respect to $SrTiO_3$[010]. The diffuse character of these points compared to the ones in the FFT of the $c(4\times2)$ reconstruction displayed in Figure 52c is, furthermore, compatible with a short-range ordered overlayer where different areas attain different degrees of compliance with a preferred epitaxy due to lattice mismatch. Such an overlayer is, furthermore, supported by the differences in inclination of the lines in Figure 52a.

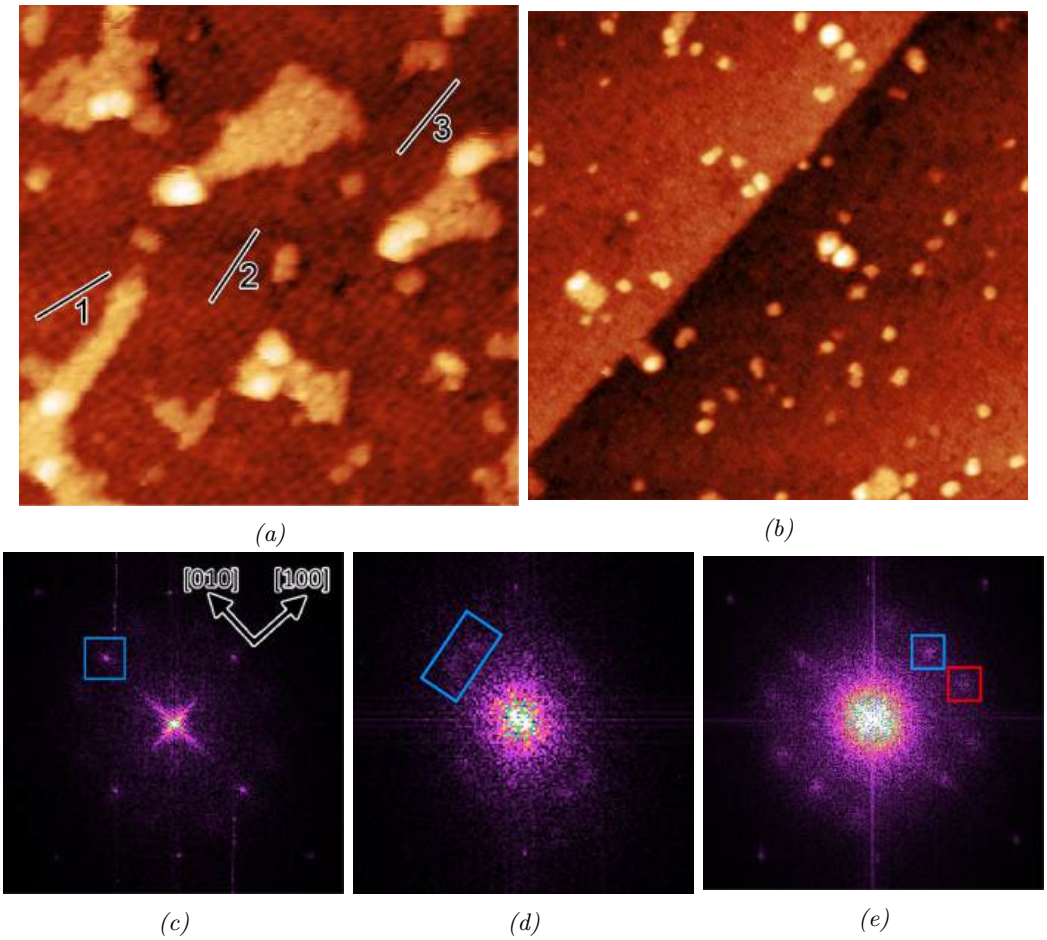

Figure 52: STM and FFT images of the surfaces produced by $1.0 < 2.0$ *ML Na coverage on* $SrTiO_3(001)-c(4\times2)$ *after 500-600 °C annealing. STM images in the top row show a) the hotter side of the 500 °C annealed sample (U=1.2 V, I=0.2 nA,* $30\times30\,nm^2$*) and b) the hotter side of the 600 °C annealed sample (U=1.0 V, I=0.1 nA,* $30\times30 nm^2$*) (averaged over 7 images in SmartAlign), where the former is a crop of Figure 50c. The lines in a) indicate the directions for three rows with periodic features, where line 1, 2 and 3 have angles* -13.8^o*,* 5.8^o*, and* 11.7^o *with respect to* $SrTiO_3$[100]*, respectively, corresponding to a mean angle of* $1.2^o \pm 13.3^o$*. The FFTs in the bottom row were produced from c) the* $SrTiO_3(001)-c(4\times2)$ *reconstruction in Figure 45a, d) the surface in a), and e) the surface in b). The point in the blue rectangle in c) indicates* $2\times$ *periodicity with respect to* $SrTiO_3$[010]*. In d), the two points in the blue rectangle have a periodicity of* 0.75 ± 0.03 *nm and are found at angles* $75.7^o \pm 5.8^o$ *and* $94.9^o \pm 6.8^o$ *with respect to* $SrTiO_3$[100]*. In e), the point in the blue rectangle has a periodicity of* 0.73 ± 0.03 *nm and is found at an angle of* $5.2^o \pm 0.25^o$ *to* $SrTiO_3$[100]*. A point sharing this periodicity is also found at* $94^o \pm 0.10^o$ *to* $SrTiO_3$[100]*. The point in the red rectangle in e) has a periodicity of* 0.67 ± 0.01 *nm and an angle of* $35.9^o \pm 0.5^o$ *to* $SrTiO_3$[100]*, with points that share this periodicity also being found at angles* $122.3^o \pm 0.4^o$ *and* $155.8^o \pm 0.4^o$*.*

An increase in ordering results after 600 ^oC annealing, as can be seen by the FFT in Figure 52e. Points in this image have become more focused than those in Figure 52d and now seemingly come in two different periodicities. The first periodicity is 0.73 ± 0.03 nm and is found at angles $5^o \pm 0.3^o$ and $94^o \pm 0.2^o$ to $SrTiO_3[100]$, where the point corresponding to $5^o \pm 0.3^o$ is marked by the blue rectangle. These points are thus within 7% of 2× periodicity and within 5^o of alignment with $SrTiO_3\langle 100\rangle$. The second periodicity is 0.67 ± 0.01 nm and is found at angles $35.9^o \pm 0.5^o$, $122.3^o \pm 0.4^o$, and $155.8^o \pm 0.4^o$, where the point corresponding to $35.9^o \pm 0.52^o$ is marked by the red rectangle. These values could hypothetically correspond to $\sqrt{3}\times$ periodicity, but this is not an allowed symmetry on the (001) termination, which lends further support to the idea that an Na-based overlayer covers the surface where hexagonal symmetries are allowed. The potential overlayer being specifically hexagonal finds further support in the rotational symmetry of the FFT, because if one treats the two types of periodicities in Figure 52e as degenerate, a clear hexagonal-type symmetry results where neighbouring points are related by $30^o \pm 1.5^o$ rotations (barring the missing point at circa 60^o and its reflection). This will be further explored in Section 5.6.

5.4 Bonding Interactions

This section describes the use of DFT to analyse the impact of Na adsorption on bonding in the $SrTiO_3 - c(4\times 2)$ surface. Coverage was defined by assuming that an Na metal overlayer would adopt BBC crystallography with a lattice parameter of 0.42 nm, which is within 8 % of the lattice parameter of $SrTiO_3(001)$. One may consequently assume that this overlayer would have a density of one Na per $SrTiO_3(001)$ bulk unit cell, meaning a single Na adsorbate per $SrTiO_3(001) - c(4\times 2)$ surface unit cell produces a coverage of 1/4 ML = 0.25 ML. The electronic structure of the $SrTiO_3(001) - c(4\times 2)$ surface is displayed in Figure 53. The DOS spectra in Figures 53a show features expected from the literature in Chapter 2, including a valence band dominated by O 2p, conduction band dominated by Ti 3d, a valence band split into a lower energy bonding a higher energy non-bonding region, and a significant presence of Ti 3d in the bonding region. This Ti 3d presence indicates hybridisation between O 2p and Ti 3d, which is further emphasised in the band structures shown in Figures 53b.

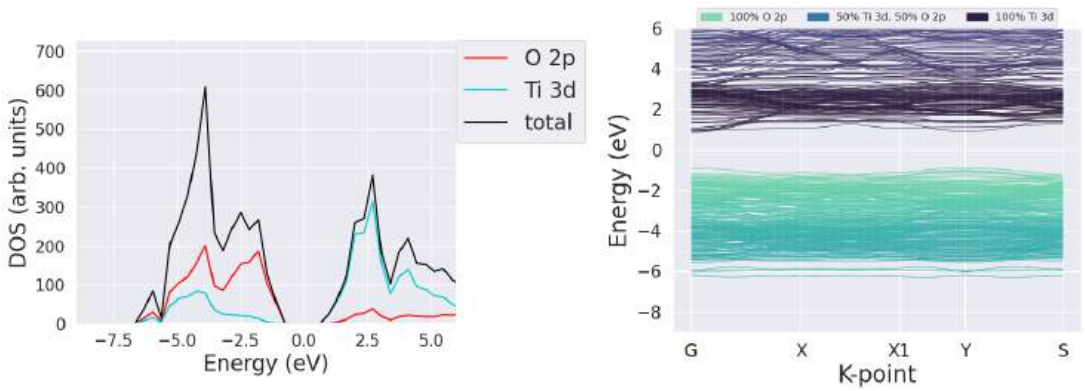

(a) *(b)*

Figure 53: Calculated electronic structure of the clean $SrTiO_3(001) - c(4\times2)$ surface, showing a) DOS and b) band structure. Bands in b) are given colours based on their degree of O 2p-Ti 3d mixing, where a darker colour indicates more Ti 3d mixing. The valence band begins at -6.31 eV and ends at -1.11 eV, putting the valence band centre at -3.71 eV. The bonding region will be defined as the energies between the valence band beginning and centre, and the non-bonding region will be defined as the energies between the valence band centre and end. By this definition, the bonding region centre is at -5.00 eV, and the non-bonding centre is at -2.41 eV. The Ti 3d/O 2p ratio in the bonding region is circa 1/2. The bonding/non-bonding ratio for O 2p is 0.74, while that of Ti 3d is 2.69.

5.4.1 Low Coverage

Adsorbing single Na atoms from six different initial positions results in three distinct adsorption sites, which are displayed in Figures 54a-54c. All sites are of the hollow type, meaning Na bonds more than two surface atoms. One may divide these adsorption sites into two categories; one site located atop a $TiO_5[]$ quartet, which will be called "above", and two sites located between $TiO_5[]$ quartets, which will be called "between-A" and "between-B". The adsorption energies of the above, between-A, and between-B sites are -2.78 eV, -5.07 eV, and -5.17 eV, respectively, making between-B the most favoured. Figures 54g-54i display the change in electron density between adsorption calculations of the three sites and the calculation of the clean surface, indicating that Ti plays a more active role in accommodating the charge received when Na adsorbs to one of the between sites.

The most over-coordinated atom on the $c(4\times2)$ surface is the O atom at the centre of the $TiO_5[]$ quartets, which has been remarked previously in the literature[35]. This O was calculated to have a BVS of -2.36 eV in the clean surface. All adsorption sites increase this over-coordination, but the above site most severely so, as above, between-A and between-B assign its BVS to -2.48 eV, -2.42 eV, and -2.38 eV, respectively. Similarly,

the most under-coordinated O atoms on the surface are the bulk-like O facing the vacuum in the penultimate TiO_2 layer, which have BVS values of circa -1.80 in the clean surface. The above site increases their under-coordination, rendering a minimum BVS value of -1.78, whereas the between sites decrease their under-coordination to a minimum of -1.88 for between-A and -1.82 for between-B. The above site, additionally, produces more severe under-coordination in the Ti atoms of the TiO_5[] quartet. These Ti atoms have a minimum BVS value of +3.80 the clean surface, which is reduced to +3.67 for the above site. Between-A reduces this value to +3.70 and between-B to +3.79. The between sites, as such, cause less O over-coordination than the above site and reduce O and Ti under-coordination to a greater extent.

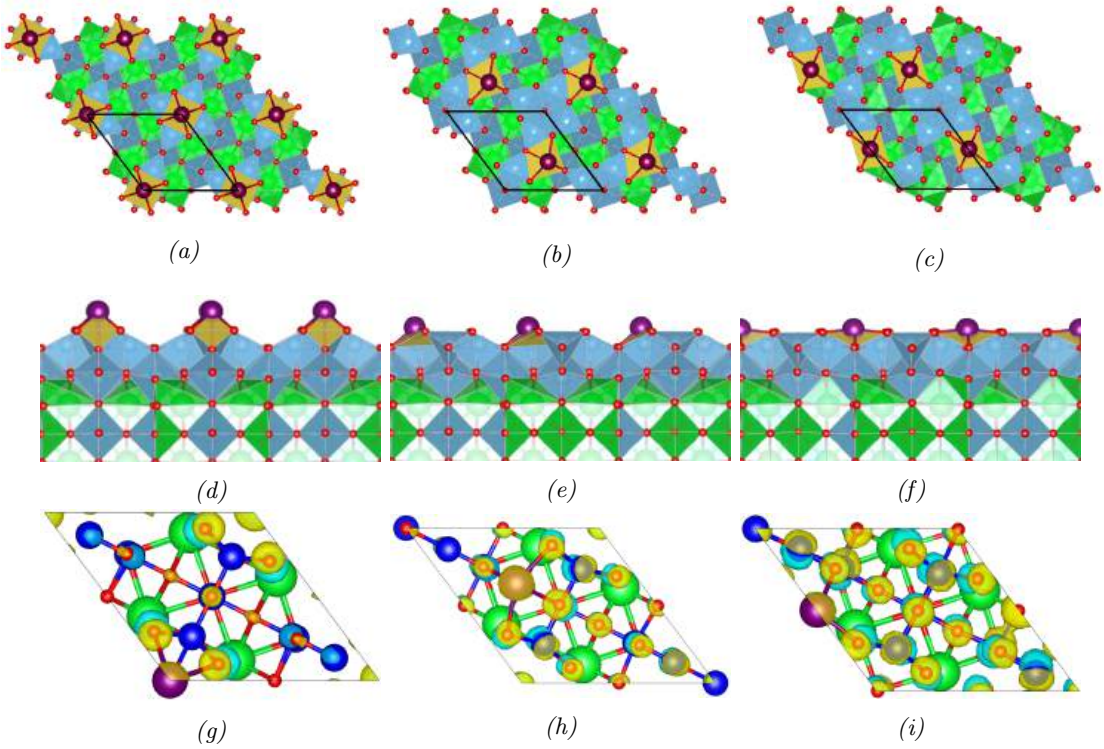

Figure 54: The three attained Na adsorption sites on $SrTiO_3(001)-c(4\times2)$, where green, blue, red, and purple balls are Sr, Ti, O and Na, respectively. Green, blue, and yellow polyhedra represent O coordination around Sr, Ti and Na, respectively. Na adsorption to the above, between-A, and between-B sites are shown from the top view in a), b), and c), respectively, and from the side view in d), e), and f), respectively. The $c(4\times2)$ surface unit cell is marked by the black diamond. Na at the above site is coordinated by five O, while Na at the between sites is coordinated by four. The above site is coordinated by five TiO_x units, while the between sites are coordinated by six. g), h) and i) show electronic charge density changes with respect to the clean surface for the above, between-A and between-B adsorption sites, respectively. These charge density changes were obtained by subtracting the charge densities of adsorption calculations from that of the clean surface calculation. Yellow clouds correspond to gained electron density with respect to the clean surface, and blue clouds correspond to lost electron density, with the cut-off value for the clouds being $\pm0.05|e|$.

Differences in bonding character between adsorption sites are displayed in Figure 55. Figures 55a-55c show that adsorption strength increases with the proximity of average BVS values to the formal oxidation values of +4, -2 and +1 for Ti, O and Na, respectively. Figure 55d shows that adsorption strength also increases with small Ti and O BVS standard deviations. The BVS analysis thus indicates that a narrow spreads of BVS values close to formal oxidation states lead leads to strong adsorption, suggesting that more bulk-like bonding is energetically preferable. Figure 55e shows that the band centra for Ti 3d and O 2p attain lower energy levels as adsorption strength increases. Stronger Na adsorption sites hence seem stabilise Ti 3d and O 2p by allowing them to become more strongly bonded to their respective atoms. Na 2s+2p band centra are found between -4.6 eV and -4.9 eV, which barely puts them in the non-bonding region while being close to the valence band centre of -4.93 eV, as per the DOS in Figure 55f.

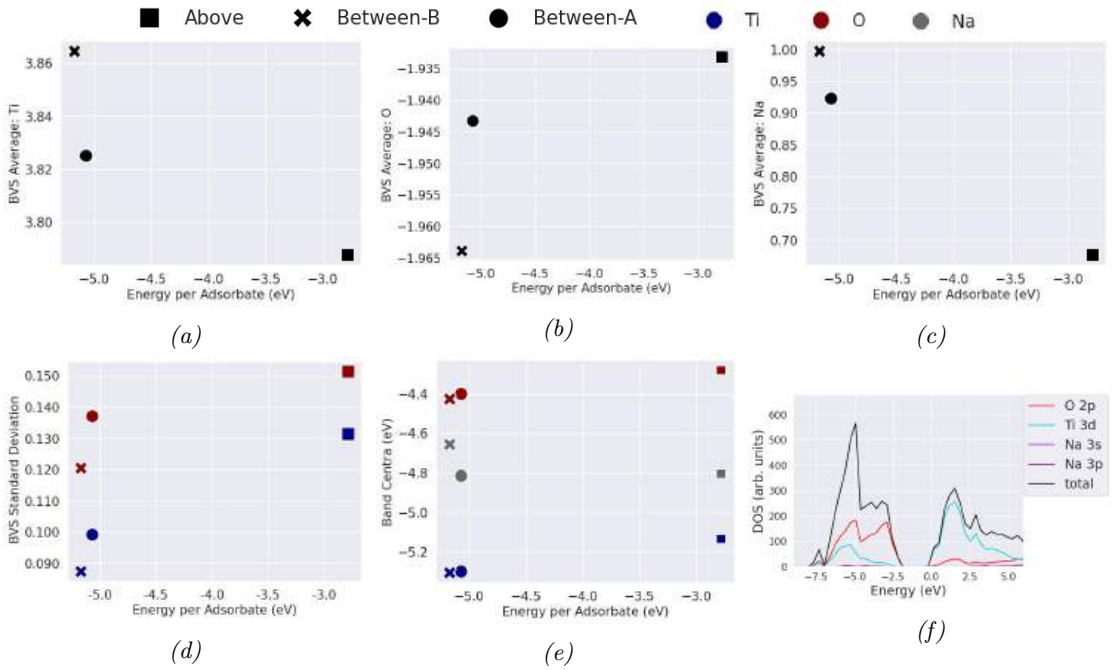

Figure 55: Key bonding data with respect to adsorption energy for the three Na adsorption sites on $SrTiO_3(001) - c(4\times2)$. The top row shows the average BVS for Ti, O, and Na in a), b) and c), respectively. The bottom row shows d) the BVS standard deviation for Ti (blue) and O (red), e) the band centra of Ti 3d (blue), O 2p (red), and Na 3s+3p (grey), and f) DOS of the most strongly bonded adsorption sites, i.e. between-B. Ti and O BVS were calculated from atoms in the surface, defined as those that are located above the outmost SrO layer. The centre of the valence band in f) is -4.93 eV, the centre of the bonding region is -6.29 eV, and the centre of the non-bonding region is -3.57 eV.

5.4.2 High Coverage

The atomic arrangement obtained from calculations of Na coverages up to 1.5 ML are shown in Figures 56a-56f. The adsorption strength per adsorbate decreases approximately linearly with increasing coverage, as can be seen in Figure 57a. At 1.0 ML Na coverage, there seems to be a change in the character of the Ti-O bond. Figure 57b shows that the separation of O 2p and Ti 3d band centra reaches a minimum at 1.0 ML and thereafter increases at 1.5 ML. This indicates that the Ti-O bond attains its most covalent character at 1.0 ML Na coverage, after which it becomes more ionic. In addition, as coverage increases from 0.25 ML to 1.0 ML, the BVS of Ti and O tend towards 3 and -2, respectively, as can be seen in Figures 57c and 57d. At 1.5 ML, however, this trend is broken as O BVS plateaus and Ti BVS starts approaching 4+. Since BVS may be interpreted as a proxy for effective oxidation state, this indicates that charge transfer to the surface peaks at 1.0 ML. This is further evidenced by considering the charge distribution changes resulting from Na adsorption, calculated form the charge density changes displayed Figures 56g-56i. The charge distribution change with respect to the clean surface per atom (excluding Na) for the 0.5 ML, 1.0 ML and 1.5 ML coverages is 0.073 $|e|$, 0.174 $|e|$, and 0.155 $|e|$, respectively, meaning that magnitude of charge redistribution in the surface peaks at 1.0 ML.

DOS spectra suggests that Na bonding to the surface becomes more covalent as coverage increases and charge transfer decreases, which is shown by comparing of the DOS spectra for 1.0 ML and 1.5 ML in Figures 57e and 57f, respectively. These spectra see a band gap state emerging due to conduction band states moving below the Fermi level. This state is dominated by Ti 3d for the 1.0 ML coverage, but has an approximately equal ratio of Ti 3d and Na 3s+3p orbitals for 1.5 ML coverage, indicating a significant increase in filled Na orbitals as coverage increases from 1.0 ML to 1.5 ML Na. This DOS data, furthermore, suggests that the Ti reduction observed in XPS in Figure 49 is due to filling of Ti 3d states, as expected from the literature in Chapter 2.

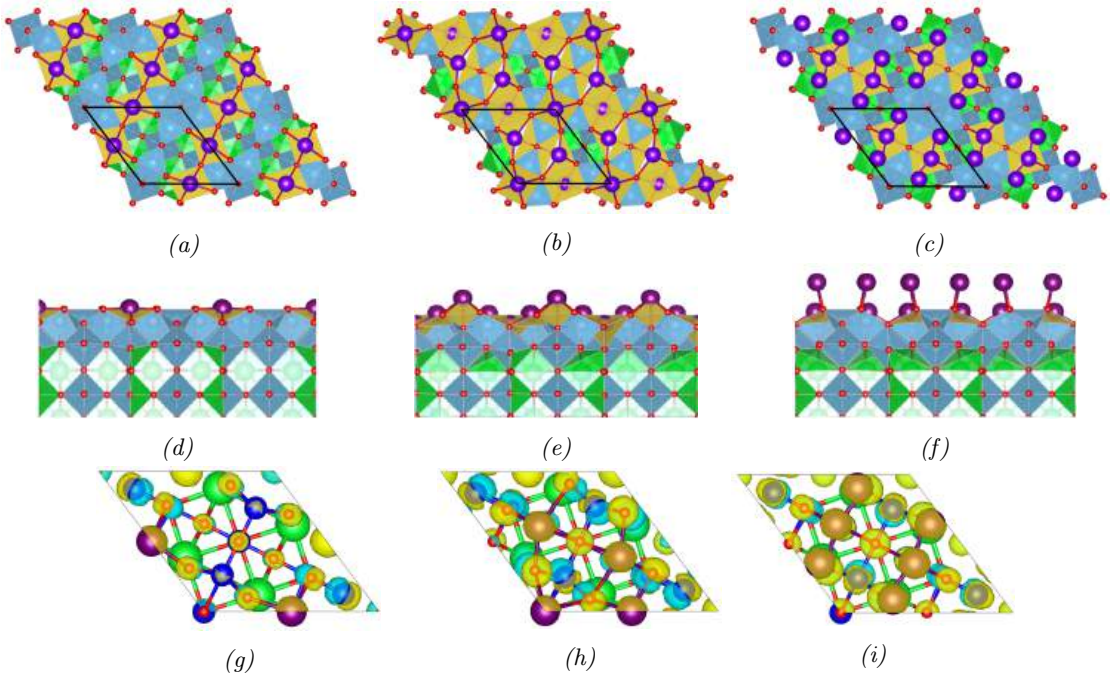

Figure 56: Multiple Na adsorbates on $SrTiO_3(001) - c(4\times2)$, where the atomic structure of the surface with coverages of 0.5 ML, 1.0 ML and 1.5 ML Na are displayed from the top view parallel to the surface normal in a), b), and c), respectively, from the side view in d), e), and f), respectively, and with electron density changes compared to the clean surface in g), h), and i), respectively. The same colour scheme was used as in Figure 53.

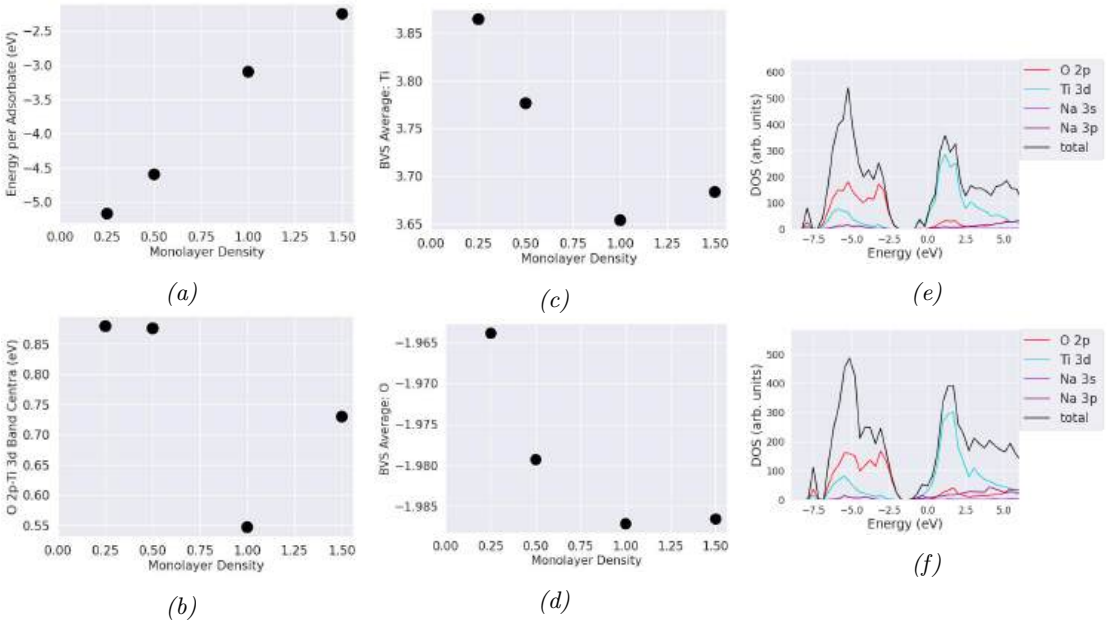

Figure 57: Calculated changes in surface bonding as a function of coverage, showing monolayer density against a) average adsorption energy, b) O 2p-Ti 3d band centra separation c) average surface Ti BVS, and c) average surface O BVS, as well as the DOS associated with e) 1.0 ML and f) 1.5 ML Na coverage. The band gap state produced by the conduction band creeping below the Fermi level has a composition of 94% Ti 3d, 5 % O 2p, and 1% Na 3s+3p for 1.0 ML and 52% Ti 4d, 3% O2p, and 45% Na 3s+3p for 1.5 ML.

5.5 Discussion

$0 < 0.3$ ML Na deposition induces two transformations in the $SrTiO_3(001) - c(4 \times 2)$ surface, one at lower annealing temperature and one at higher, which were called the first and second transformations, respectively. The first transformation ensues after 400 ^oC annealing and induces two structures; step edge holes and the $\sqrt{5} \times \sqrt{5} - R26.6^o$ reconstruction. These two structures coincide and were never observed separately. They may be understood by considering the mechanisms by which $SrTiO_3(001)$ may accommodate the strongly electropositive Na adsorbates. The formation of the holes is likely connected to Na etching, whereby Na bonds O in the outmost surface layer, which is likely to over-coordinate O in the the affected TiO_x unit. This in turn would lead to the dissolution of TiO_x unit, creating the initial holes reported in Figure 46a which have depths of circa 0.2 nm, equivalent to the height of the outermost atomic layer. Such a reaction is supported by the presence of $\sqrt{5} \times \sqrt{5} - R26.6^o$, as this reconstruction forms due to surface region reduction, which will be discussed later in this section. At higher annealing temperatures, holes grow and settle at a depth of circa 0.4 nm, which corresponds to one $SrTiO_3(001)$ unit cell, making these holes small enclosures of step edges. It thus seems that the surface energy contribution of the 0.2 nm initial holes is reduced if their sides become step edges. This may be understood by considering firstly that step edges are commonly observed on $SrTiO_3(001) - c(4 \times 2)$, while patches of missing outermost surface layer are not, indicating that the latter has a more prohibitive surface energy cost. Secondly, step edges are expected to host adsorption sites with low O coordination due to broken Ti-O bonds in two perpendicular planes. Such low coordination O environments should allow for stronger Na-O bonds without over-coordinating O compared to surface terraces. Step edges would also grant Na access to TiO_x units in two planes, allowing for greater TiO_x coordination and thus a stronger interaction by spreading the charge received by Na over a greater number of TiO_x units, which should further mitigate over-coordination. These effects make step edges likely preferential adsorption sites, which was also noted in the literature presented in Chapter 2.

The arguments above regarding initial hole formation by O over-coordination and preferential step edge adsorption due to favourable coordination environments find some

support in DFT calculations. The least favoured calculated adsorption site causes greater over-coordination of the most over-coordinated O, greater under-coordination of the most under-coordinated O, and increased under-coordination of Ti in the outmost surface layer. The most favoured site, on the other hand, decreased under-coordination of the most under-coordinated O while having a significantly lower impact on the most over-coordinated Ti and O. This effect is significant and produces an adsorption strength difference of 2.4 eV between the least and most preferred sites. Adsorption strength, in addition, increases with the number of TiO_x units coordinating Na, and with a reduction in the number of O that Na bonds from any individual TiO_x units. Calculations thus suggest that O over-coordination causes significantly less stable adsorption sites, which gives some support to the idea that initial hole formation is due to Na destabilising TiO_x units by causing over-coordination. Calculations give further support to step edges being preferential adsorption sites by indicating that Na adsorption strength should be enhanced at sites where O has low coordination and Na has high TiO_x unit coordination. Based on STM data supported by DFT calculations, it will thus be proposed that holes initially form by Na etching of the outermost TiO_2 surface layer, which then become nucleation sites for step edges that in turn are stabilised by Na decoration.

The $(\sqrt{5}\times\sqrt{5})-R26.6^o$ reconstruction has previously been reported to form in heavily reductive environments[113]. Its creation was then assigned to reduction through O vacancy formation in the surface region, which increases O chemical potential while TiO_2 stoichiometry is maintained in the top surface layer. This may be understood by considering the free energy difference ΔG between two reconstructions α and β as the chemical potential μ of species i changes at constant temperature and pressure. ΔG can under these conditions be expressed as $G_\alpha - G_\beta = \Delta G = \sum_i \mu_i \Delta n_i$, thus, changes in O chemical potential can alter which reconstruction has lower free energy. $(\sqrt{5}\times\sqrt{5})-R26.6^o$ formation in the case of alkali metal deposition should consequently be the result of a similar process where the large O affinity of alkali metals make O preferentially bond with them over Ti. This would deprive surface Ti atoms of O bonds, which increases the energetic penalty for further O removal from the surface and thereby increases O chemical potential. The affected Ti atoms then become under-coordinated, which together with the ionicity of the alkali metal-O bond should promote a electron transfer from alkali valence orbitals

to Ti 3d. This Ti reduction was not evidenced directly for the $(\sqrt{5}\times\sqrt{5}) - R26.6^o$ reconstruction, but was shown to occur in the $SrTiO_3(001)$ substrate by the XPS data in Figure 49 and the subsequent filling of Ti 3d states is indicated by the calculated DOS spectra in Figure 56. It is, furthermore, plausible that the O chemical potential gradient between the surface and the bulk promotes O migration to maintain TiO_2 stoichiometry in the surface, which could produce O vaccines and associated electron donor states in the surface region. In any case, the alkali metal reaction is highly likely to reduce the surface region and thus increases O chemical potential, which will be proposed as the driving force that produces the $(\sqrt{5}\times\sqrt{5}) - R26.6^o$ reconstruction.

The high-T surface produced by the second transformation contains four pieces of information that may give an indication of its character. Firstly, the depths of its holes and step edges appear to be circa 15-20 % greater than the $SrTiO_3$ unit cell. Secondly, the second transformation occurs at a 200 ^oC lower temperature for the $0.1 < 0.3$ ML coverage than for the $0 < 0.1$ ML coverage. Thirdly, XPS data indicate that the high-T surface contains reduced Ti. And fourthly, there is a notable decrease in the concentration of Na particles on this surface compared to those formed at lower annealing temperatures. One can thus postulate that this surface is associated with some mechanism by which Na is removed from the surface. This mechanism, furthermore, seems to be a function of Na coverage, since it is activated at lower annealing temperature for a higher Na coverage. The electropositive nature of Na makes it plausible that this mechanism is related to reduction, due to the arguments made in the paragraph above pertaining to surface structure free energy and reduction-dependent chemical potential. Since Na can only disappear from the surface in one of two directions, i.e. into the bulk or out in the vacuum, this mechanism must be either intercalation or desorption. A discussion of whether intercalation or desorption occurs will be made in Chapter 7, which includes XPS data for Na on (111) that allow for a more substantive analysis of which mechanism is more likely. Regardless of the outcome of that analysis, these XPS data, as well as those presented for Li on (111) in Chapter 8, establish that the mechanism that removes alkali metals from $SrTiO_3$ surfaces at elevated annealing temperatures also causes a dramatic increase in Ti reduction. It will, for this reason, be proposed that the high-T surface is stabilised by enhanced reduction in the surface region. This means that there should be a critical O chemical potential at

which the high-T surface becomes lower in free energy than $(\sqrt{5}\times\sqrt{5}) - R26.6^o$. Interestingly, the high-T surface will also appear after similar annealing temperatures for Li on $SrTiO_3(001) - c(4\times2)$, as shall be seen in Chapter 6. The discussion of this surface will therefore be concluded there.

At high Na coverage, STM data indicates that an overlayer likely has formed on the $SrTiO_3(001)$ substrate. This is suggested firstly by FFT data after annealing at 500 ^oC and 600 ^oC showing diffuse FFT points, which can be explained by short-range ordering inclined towards certain periodicities but with variation in the degree of local compliance due to lattice mismatch. Real space images support this idea, as periodic rows inclined between -14^o and $+14^o$ with respect to $SrTiO_3[100]$ are visible after 500 ^oC annealing. Secondly, the focus of the points increase from 500 ^oC to 600 ^oC, indicating an increase in the degree of ordering, which is expected for an overlayer as the greater thermal energy would allow for a greater degree of epitaxy. Thirdly, FFT points after 600 ^oC annealing have a rotational symmetry that is in good agreement with $n \cdot 30^o$, where n is an integer. This could be explained by the overlayer facing the substrate with its (111) termination, giving it $\langle 110 \rangle$ type surface unit vectors. If the overlayer then is driven to keep one of its $\langle 110 \rangle$ vectors commensurate with a $SrTiO_3\langle 100 \rangle$ vector, it must choose either $SrTiO_3[100]$ or $SrTiO_3[010]$. The two possible overlayer unit vector orientations would as such be related by a 90^o rotation, which together with their intrinsic 60^o rotational symmetry would make all possible unit vector directions related by $n \cdot 30^o$. This would explain the FFT pattern observed in Figure 52e. Overlayer formation at high coverage, moreover, finds some support in high coverage DFT results, since this would require weaker adsorbate-substrate and stronger adsorbate-adsorbate interactions than at low coverage, which calculations indicate is the case.

If an overlayer has indeed formed, it should have Na_xO chemistry, as should the nanoparticles observed at the lower coverage of Section 5.2. This can be motivated by Na having a melting point of 98^oC, thus, if particles were pure Na, there should be no reason why they would not form after 300 ^oC annealing. 500 ^oC is, in addition, likely a high enough temperature for significant O diffusion in $SrTiO_3$, meaning the bulk could provide an O source for Na. The UHV chamber should, moreover, contain O_2

and H_2O contaminants with which Na can react. A probably chemistry for the overlayer and nanoparticles is thus Na_2O. This overlayer chemistry is likely to yield an epitaxial relationship that fits the STM data if Na_2O has its usual anti-fluorite structure. The length of the $Na_2O[110]$ vector is $\sqrt{2} \cdot 0.55\,nm = 0.778\,nm$, only 0.4% from the 0.781 nm periodicity of 2× along $SrTiO_3[100]$. A proposition for the interface epitaxy of the overlayer could hence be $Na_2O(111)||SrTiO_3(001)$, $Na_2O\langle 01\bar{1}\rangle||SrTiO_3[100]$ or $Na_2O(111)||SrTiO_3(001)$, $Na_2O\langle 01\bar{1}\rangle||SrTiO_3[010]$, which together could reproduce symmetries similar to those observed in Figure 52. Lastly, annealing to 700 ^oC exposes the $SrTiO_3$ substrate again, indicated by holes of unit cell depth at the colder end of the sample and the presence of the high-T surface at the hotter end.

5.6 Conclusion

Na interacts so strongly with $SrTiO_3(001)$ that it transforms the entire surface at coverages as low as $0 < 0.1$ ML and to produce a wetting overlayer at $1.0 < 2.0$ ML. Two low coverage transformations were observed. The lower temperature transformation commences around 400 ^oC and is characterised by a $(\sqrt{5}\times\sqrt{5})-R26.6^o$ reconstruction and step edge holes. The $(\sqrt{5}\times\sqrt{5})-R26.6^o$ reconstruction is proposed to form due to increased O chemical potential as the surface region is reduced. Step edge holes are proposed to form by Na etching the surface, thus creating step edge nucleation sites, with step edges being stabilised via Na decoration once formed. Step edge decoration stabilising step edges finds some support in DFT calculations, which suggest that coordination environment features that are conducive to strong Na adsorption include low O coordination and high TiO_x coordination around Na, both of which are expected at step edges. The second transformation commences around 550 ^oC for $0 < 0.1$ ML coverage and 750 ^oC for $0.1 < 0.3$ ML coverage and generates the previously unreported high-T surface. This surface is suggested to be associated with enhanced Ti reduction in the surface region, which makes the high-T surface more stable than $(\sqrt{5}\times\sqrt{5})-R26.6^o$. It is, lastly, proposed that a Na_2O monolayer covers the $SrTiO_3(001)$ following $1.0 < 2.0$ ML deposition and 500 ^oC annealing. This overlayer seemingly increases its commensurability with the substrate as annealing temperature increases from 500 ^oC to 600 ^oC, where the latter annealing temperature produces symmetries that seem compatible with a $Na_2O(111)||SrTiO_3(001)$, $Na_2O\langle 01\bar{1}\rangle||SrTiO_3\langle 100\rangle$ epitaxial relationship.

6 Li on $SrTiO_3(001)$

6.1 Introduction

This chapter describes the interaction of Li with $SrTiO_3(001) - c(4\times2)$ based on STM data and DFT calculations. Three surfaces will be encountered in this chapter that were already introduced in Chapter 5, namely $c(4\times2)$, $(\sqrt{5}\times\sqrt{5}) - R26.6^o$, and the surface that was named the high-T surface. To avoid repetition, the reader is referred to Chapter 5 for details on the structure of these surfaces. STM data will be presented in order of deposition quantity, starting with $0 < 0.1$ ML, followed by $0.1 < 0.3$ ML and lastly $1.0 < 2.0$ ML.

6.2 Low Deposition

The $0 < 0.1$ ML Li deposition onto $SrTiO_3(001) - c(4\times2)$ as a function of annealing temperature is displayed in Figure 58. Following annealing at 400 ^oC, nanoparticles emerge with a diversity of morphologies and sizes, as can be seen in Figure 58a. The first notable change to the $SrTiO_3$ surface is visible after 600 ^oC and can be seen in Figure 58b, where indents with diameters smaller than 2 nm appear at a density of circa 0.1 nm^{-2}, which will henceforth be referred to as "cavities". Cavities appear together with protruding spots circa 0.1 nm in height, which could be Na-based particles, but considering their coincidence with the cavities, they may also be formed from the TiO_2 material removed by cavity formation. The surface, thereafter, transforms to one that is indistinguishable from the high-T surface that also forms after Na deposition on $c(4\times2)$, which was described in Chapter 5. This transformation is activated above 700 ^oC and displayed in Figure 58c, which shows an image captured at the colder side of a 800 ^oC annealed sample. The two signature structures of this surface, namely 2×1 ordered rows and $(\sqrt{5}\times\sqrt{5}) - R26.6^o$ ordered dots, are indicated by lines 1 and 2 in Figure 58c, respectively. Also similar to the case of Na on $c(4\times2)$, the original $c(4\times2)$ reconstruction returns at the hotter side of the 800 ^oC annealed sample, as can be seen in Figure 58d.

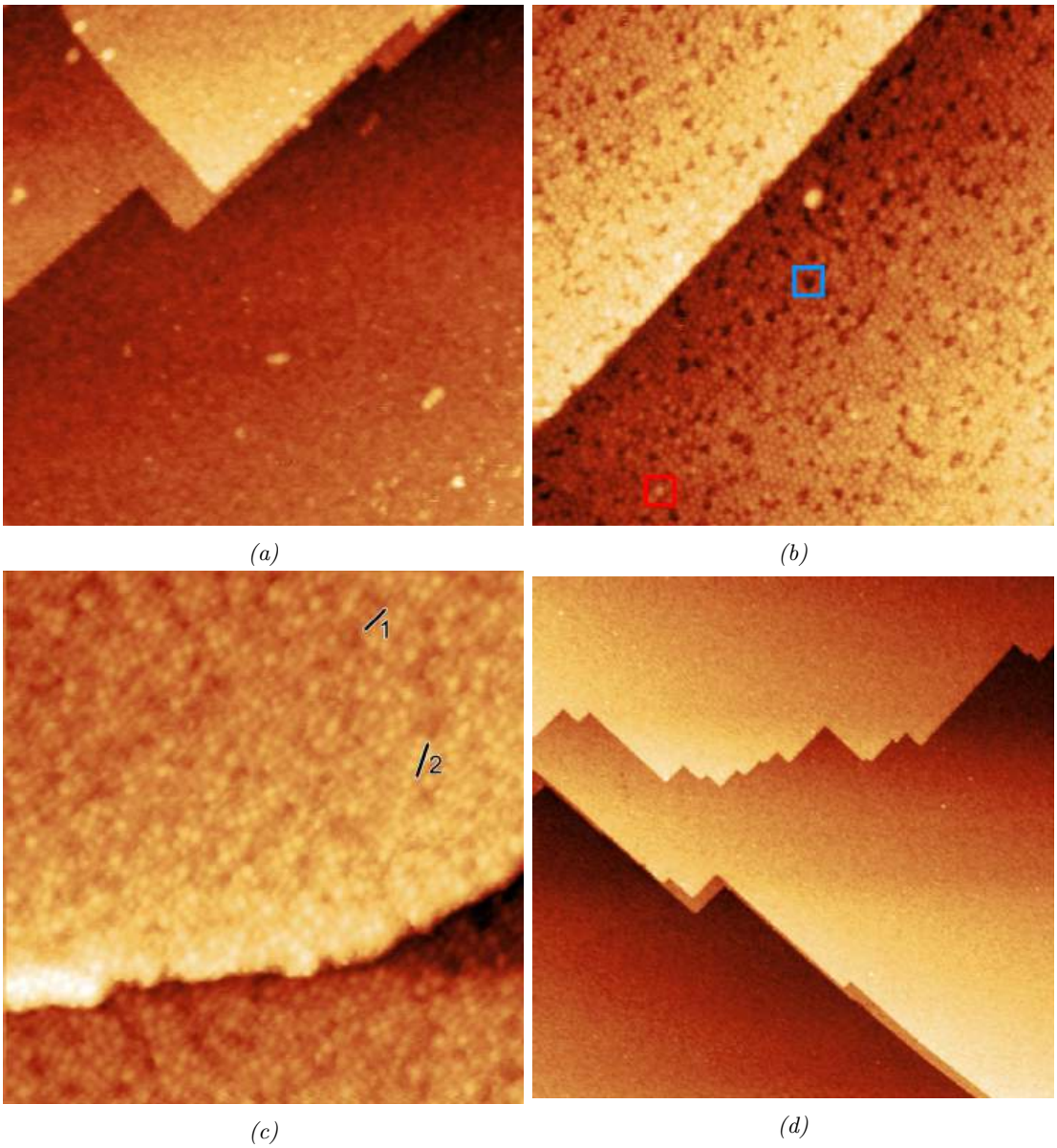

Figure 58: STM images of $0 < 0.1$ *ML Li deposited on* $SrTiO_3(001) - c(4\times2)$ *after 400-800 °C annealing, showing a) 400 °C (U=1.2 V, I=0.1 nA,* $80\times80\ nm^2$*), b) 600 °C (U=2.0 V, I=0.06 nA,* $50\times50\ nm^2$*), c) 800 °C at the colder side of sample (U=1.0 V, I=0.15 nA,* $40\times40\ nm^2$*) (averaged over two images in SmartAlign), and d) 800 °C at the hotter side of the sample (U=1.4 V, I=0.06 nA,* $200\times200\ nm^2$*). a) shows that nanoparticles have formed on the surface, where the eight largest ones have a mean height of* 0.31 ± 0.05 *nm and mean width of* 1.96 ± 0.76 *nm. b) shows the formation of cavities in the top surface layer, where a typical pit is marked by the blue rectangle. Measuring ten of the largest cavities yields a mean depth of* 0.13 ± 0.03 *nm and mean width of* 1.56 ± 0.47 *nm. The density of cavities is circa 0.1* nm^{-2}*. b) also displays small protruding spots, where a typical example is marked by the red rectangle and six of the largest spots have a mean height of* 0.11 ± 0.01 *nm. c) shows the formation of the high-T surface, where line 1 shows the* $2\times$ *periodicity in the* $[100]$ *direction for the* 2×1 *ordered rows, and line 2 shows the* $\sqrt{5}\times$ *periodicity along* $[210]$ *for the* $(\sqrt{5}\times\sqrt{5}) - R26.6^o$ *ordered dots. d) shows the return of the* $c(4\times2)$ *reconstruction at the hotter side of the 800 °C annealed sample. Step edges in all images were measured to have heights between 0.37 nm and 0.38 nm.*

6.3 Medium Deposition

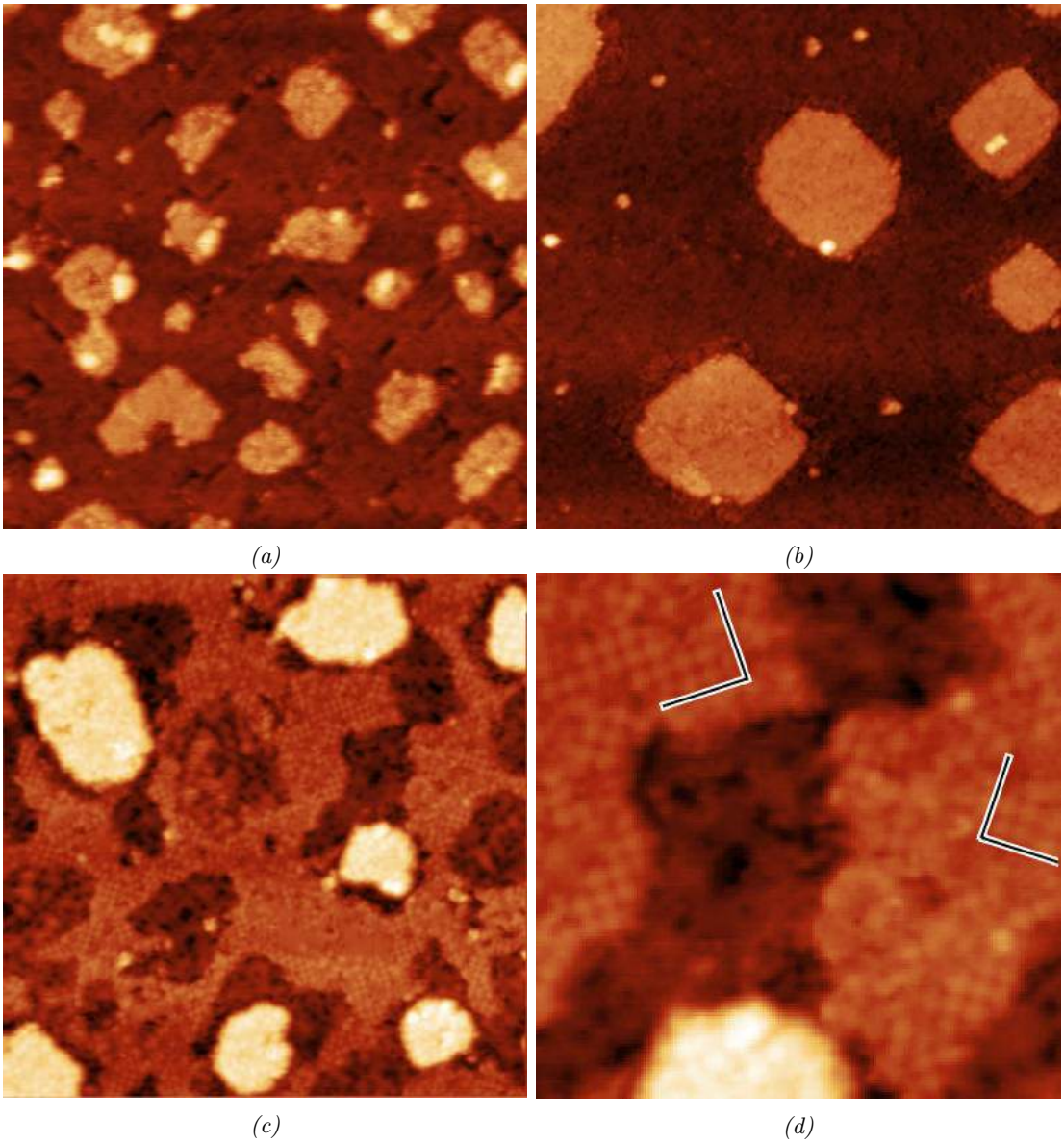

Figure 59: STM images of $0.1 < 0.3$ *ML Li deposited on* $SrTiO_3(001) - c(4\times2)$ *after 500-800* ^oC *annealing, showing a) 500* ^oC *(U=1.8 V, I=0.06 nA,* $60\times60\,nm^2$*), b) 700* ^oC *(U=1.4 V, I=0.08 nA,* $80\times80\,nm^2$*), c) 800* ^oC *at the colder end of sample (U=1.4 V, I=0.1 nA,* $60\times60\,nm^2$*) (averaged over six images in SmartAlign), and d) a crop of image c) showing the* $(\sqrt{5}\times\sqrt{5})-R26.6^o$ *reconstruction. Islands in a) have a mean height of* 0.40 ± 0.03 *nm and mean width of* 7.23 ± 1.95 *nm, and the mean depth of cavities is* 0.19 ± 0.04 *nm. Islands in b) have a mean height of* 0.39 ± 0.01 *nm and mean width of* 16.85 ± 4.65 *nm. In c), the mean height of islands above the pitted surface floor is* 0.60 ± 0.06 *nm, and their mean width is* 10.19 ± 3.07 *nm. The mean height of the top surface layer over the pitted surface floor is* 0.20 ± 0.03 *nm. Lines in d) are drawn along the unit vectors of* $(\sqrt{5}\times\sqrt{5})-R26.6^o$.

$0.1 < 0.3$ ML Li deposition and 500 ^oC annealing produce a surface that also contains cavities, as displayed in Figure 59a. Cavities have a similar depth of circa 0.2 nm, but now also show a preference for elongating in the $\langle100\rangle$ directions. This figure also shows a

feature not present in the lower deposition case, namely unit cell tall islands with diameters between 5 and 10 nm. These islands grow after 700 ^oC annealing, as can be seen in Figure 59b, now ranging from 10 nm to 20 nm in width while maintaining unit cell height. The growth of the islands, furthermore, coincides with a disappearance of the $\langle 100 \rangle$ aligned cavities. As annealing is increased to 800 ^oC, the surface commences a transformation that can be seen in Figure 59c, where it appears that it sheds its outmost layer(s), giving rise to the areas of darker contrast. The difference in height between these darker areas and the surface above is circa 0.20 nm and islands are circa 0.60 nm above the dark areas, indicating that they are produced by shedding of only the top surface layer. Islands are, at the same time, reduced in size, now having diameters between 5 nm and 10 nm. The non-shed areas display clear domains of $(\sqrt{5}\times\sqrt{5}) - R26.6^o$, as can be seen in the cropped image in Figure 59d.

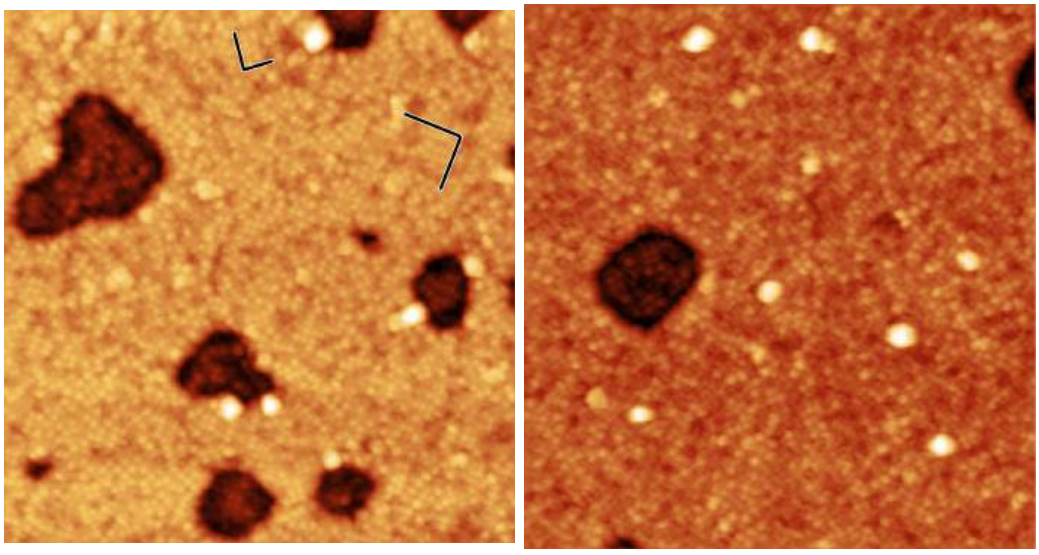

(a) *(b)*

Figure 60: STM images of $0.1 < 0.3$ *ML Li deposited on* $SrTiO_3(001) - c(4\times2)$ *after 800 ^oC annealing, showing a) the middle of the sample (U=1.0 V, I=0.2 nA,* $56.1\times58.6\ nm^2$*) (averaged over 7 images in SmartAlign) and b) the hotter end of the sample (U=1.4 V, I=0.06 nA,* $54\times57.5\ nm^2$*) (averaged over 8 images in SmartAlign). Lines in a) show the* $\langle 210 \rangle$ *directions of the* $(\sqrt{5}\times\sqrt{5}) - R26.6^o$ *unit vectors.*

Figure 59c was acquired at the colder side of the 800 ^oC annealed sample. In the centre of the sample, where temperature is up to 50 ^oC higher, the high-T surface seems to have formed, as displayed in Figure 60a. This particular high-T surface differs form the ones previously observed in that it has an unusually high density of $(\sqrt{5}\times\sqrt{5}) - R26.6^o$ ordering. Areas between $(\sqrt{5}\times\sqrt{5}) - R26.6^o$ do, however, contain the 2×1 ordered

rows, which together with the holes give this surface all the defining features of the high-T surface. One may speculate that holes have evolved from the shed areas shown in Figure 59c. The surface at the hotter side of the sample shows the high-T surface with lower $(\sqrt{5}\times\sqrt{5}) - R26.6^o$ ordering density that is more similar to the ones formed by Na deposition in Chapter 5, as can be seen in Figure 60b.

6.4 High Deposition

A coverage of $1.0 < 2.0$ ML Li and 500 ^oC annealing generate a surface that is dominated by nanoparticles and amorphous overlayer islands. Nanoparticles are 0.5 to 1.5 nm in height and 5 nm to 10 nm in diameter, and overlayer islands are 0.2-0.3 nm in height. This surface can be seen in Figure 61a, acquired at the colder side of the sample. The hotter side of the sample is displayed in Figure 61b and shows a surface that shares these two features but where the overlayer becomes more prevalent and where the underlying $SrTiO_3(001)$ substrate is now visible, as can be seen by the presence of the $(\sqrt{5}\times\sqrt{5}) - R26.6^o$ reconstructions in Figure 61c. After 600 ^oC annealing, the $SrTiO_3$ substrate becomes increasingly exposed, while overlayer islands maintain their 0.20 nm to 0.30 nm height, as can be seen in Figure 61d. The consistency and unit cell-like value of this height indicates that the overlayer most likely is a monolayer. Figure 62a shows an image acquired after 700 ^oC, displaying nanoparticles and holes with a mean depth of 0.44 ± 0.02 nm. This indicates that the $SrTiO_3(001)$ substrate now dominates the surface and that most Li has been evaporated or diffused into the bulk with the remaining Li forming surface nanoparticles. Nanoparticles seemingly display a preference for locating to step edges. After 800 ^oC annealing, the high-T surface can be seen to once more return in Figure 62b, meaning that this surface has appeared for every deposition of Li and Na onto $SrTiO_3(001)$.

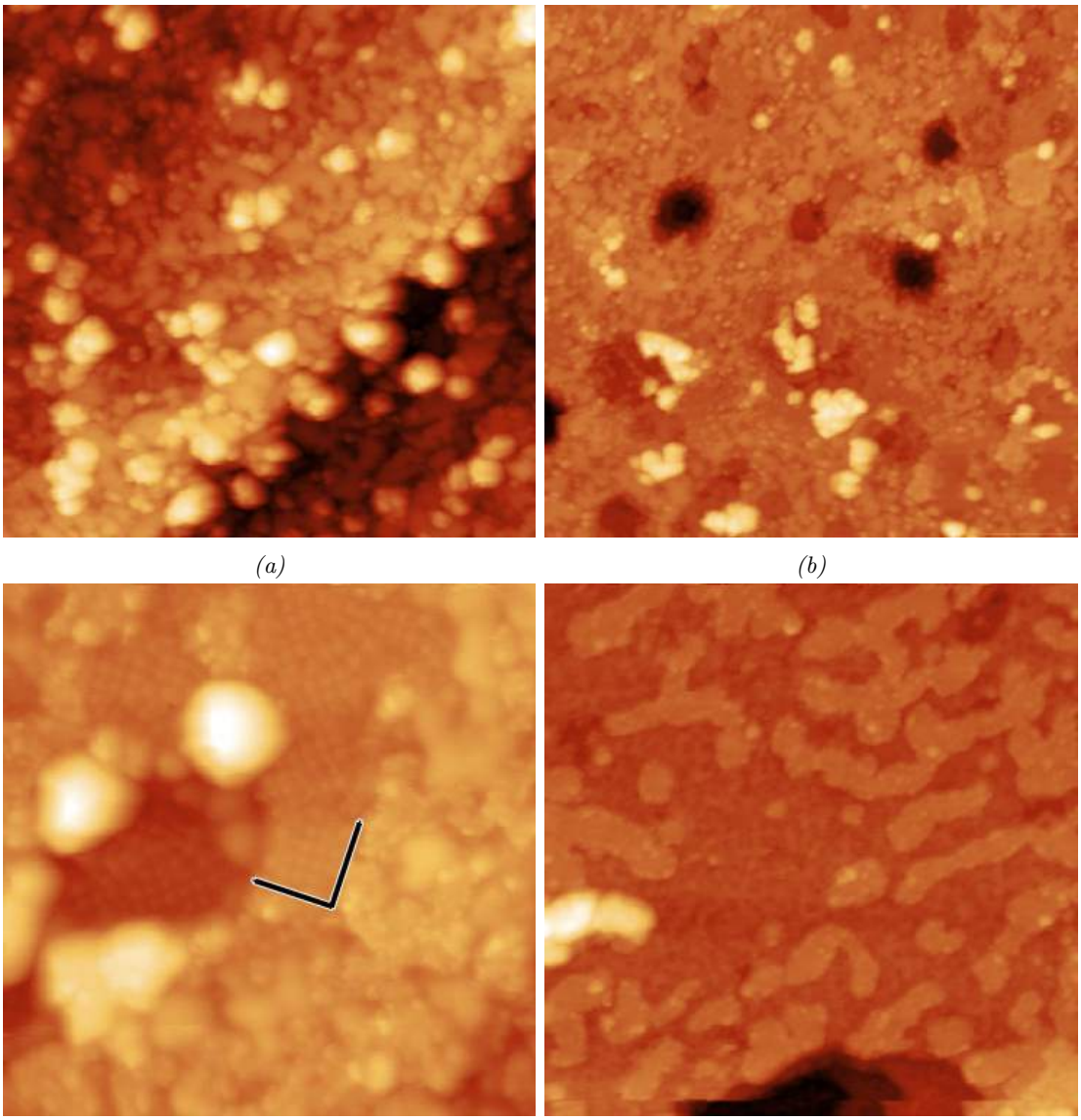

(a) *(b)*

(c) *(d)*

Figure 61: STM images of $1.0 < 2.0$ *ML Li deposited on* $SrTiO_3(001) - c(4\times2)$ *after 500 °C to 600 °C annealing, showing the surface produced by annealing temperatures of a) 500 °C (colder side of the sample) (U=1.8 V, I=0.04 nA,* $100\times100\,nm^2$*), and b) 500 °C (hotter side of the sample) (U=1.8 V, I=0.8 nA,* $120\times120\,nm^2$*, and c) 500 °C (the middle of the sample) (U=1.0 V, I=0.1 nA,* $30\times30\,nm^2$*), and d) 600 °C (U=1.2 V, I=0.12 nA,* $40\times40\,nm^2$*). a) shows an amorphous overlayer together with nanoparticles, where measurements of the ten largest nanoparticles yield a mean height of* 1.08 ± 0.3 *nm and mean diameter of* 7.0 ± 2.95 *nm. The overlayer is measured to have a mean height of* 0.26 ± 0.04 *nm in b). c) show areas between the overlayers and nanoparticles that form after 500 °C contain significant areas of* $(\sqrt{5}\times\sqrt{5}) - R26.6^o$ *reconstruction, with the unit vector directions of one* $(\sqrt{5}\times\sqrt{5}) - R26.6^o$ *orientation being indicated by the black lines. The overlayer in d) has a mean height of* 0.23 ± 0.03 *nm.*

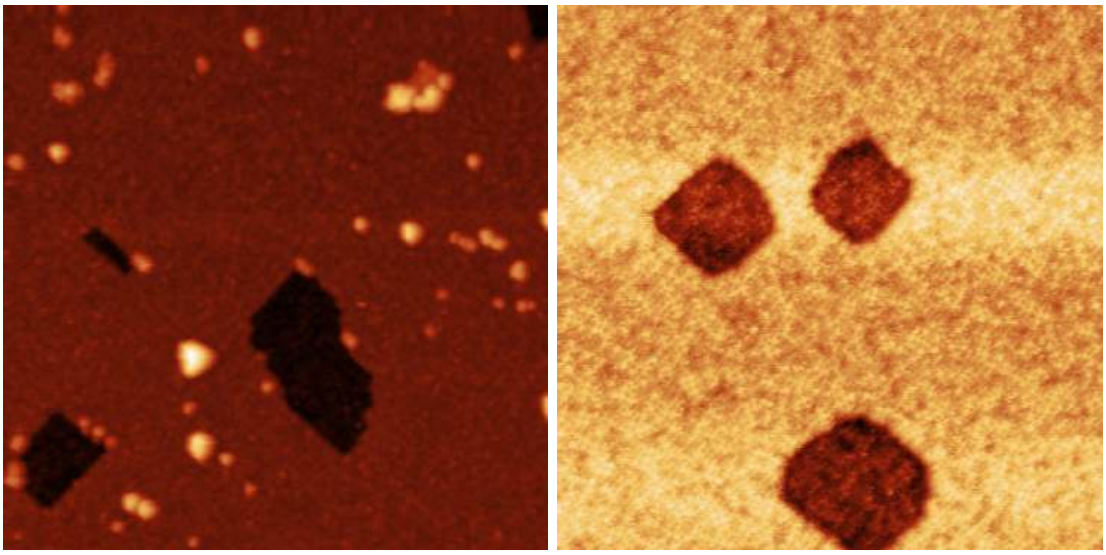

(a) *(b)*

Figure 62: STM images of $1.0 < 2.0$ *ML Li deposited on* $SrTiO_3(001) - c(4\times2)$ *after 700 °C to 800 °C annealing, showing the surfaces produced by a) 700 °C (U=1.2 V, I=0.1 nA,* $100\times100\,nm^2$*) and b) 800 °C (U=1.2 V, I=0.16 nA,* $60\times60\,nm^2$*). Holes in a) have a mean depth of* 0.44 ± 0.02 *nm, and holes in b) have a mean depth of* 0.46 ± 0.07 *nm and mean width of* 13.04 ± 5.26 *nm.*

6.5 Bonding Interactions

DFT calculations were conducted using the same methodology as for Na on $SrTiO_3(001) - c(4\times2)$ presented in Chapter 5, but with Na replaced by Li at the initial position in the vacuum above the surface. Li on $SrTiO_3(001) - c(4\times2)$ resulted in the same three adsorption sites, i.e. above, between-A, and between-B, displayed in Figures 63a-63f. The adsorption energies of the above, between-A and between-B sites are -3.49 eV, -6.18 eV, and -6.48 eV, respectively, meaning that the between-B site has the lowest energy and consequently strongest Li adsorption. As stated in Chapter 5, the most over-coordinated O atom on the $c(4\times2)$ surface is the one at the centre of the $TiO_5[]$ quartet, with a BVS value of -2.36. The above site significantly increases the over-coordination of this O atom to a BVS of -2.45, while between-A and between-B decrease its over-coordination to -2.33 and -2.34, respectively. The most under-coordinated Ti atom in the $TiO_5[]$ quartet has a BVS value of +3.80, which is decreased to +3.68 at the above site and +3.72 at the between-A site, while it is increased to +3.82 at the between-B site. The most favoured adsorption site, between-B, thus decreases the over-coordination of the most over-coordinated O atom, and is the only site to decrease the under-coordination of the most under-coordinated Ti atom in the top surface layer.

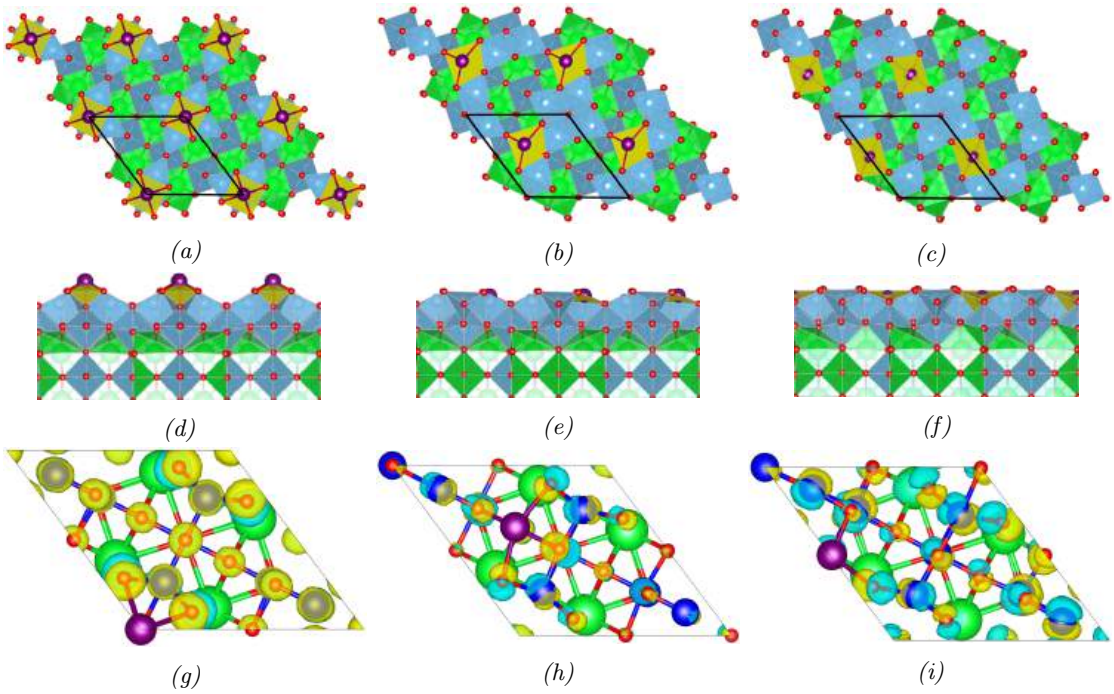

Figure 63: The three adsorption sites for Li on $SrTiO_3-c(4\times2)$, where green, blue, red, and purple balls are Sr, Ti, O and Li, respectively. Green, blue, and yellow polyhedra represent O coordination around Sr, Ti and Li, respectively. The above, between-A and between-B sites are seen from the top view parallel to the surface normal in a), b) and c) respectively, from the side view perpendicular to the surface normal in d), e) and f), respectively, and with charge density differences with respect to the clean surface overlaid in g), h) and i), respectively. In g)-i), gained charge density is indicated by yellow and lost charge density is indicated by blue.

Differences in bonding behaviour between adsorption sites are displayed in Figure 64. BVS values in Figures 64a-64d indicate that a narrow spread of BVS values close to the formal oxidation states of +4, -2 and +1 for Ti, O and Li, respectively, correlates with adsorption strength. The band centra positions of O 2p and Ti 3d move towards lower levels for stronger adsorption sites, while Li 2s+2p moves towards a higher level, as per Figure 64e. The Li 2s+2p band centrum is found at a notably low energy level, below -5.75 eV for all sites, compared to Ti 3d which is found at circa -5.25 eV. This puts Li 2s+2p close to the centre of the bonding region, which is found at -6.07 eV, as can be seen by the DOS in 64f. Many trends are largely similar to those for Na on $SrTiO_3$(001) discussed in Chapter 5, suggesting these two interactions are fundamentally similar. There is, however, one notable difference, which is that the Li 2s+2p band centrum is found at a lower level deep within the bonding region, indicating the Li-O bond is more covalent than the Na-O bond.

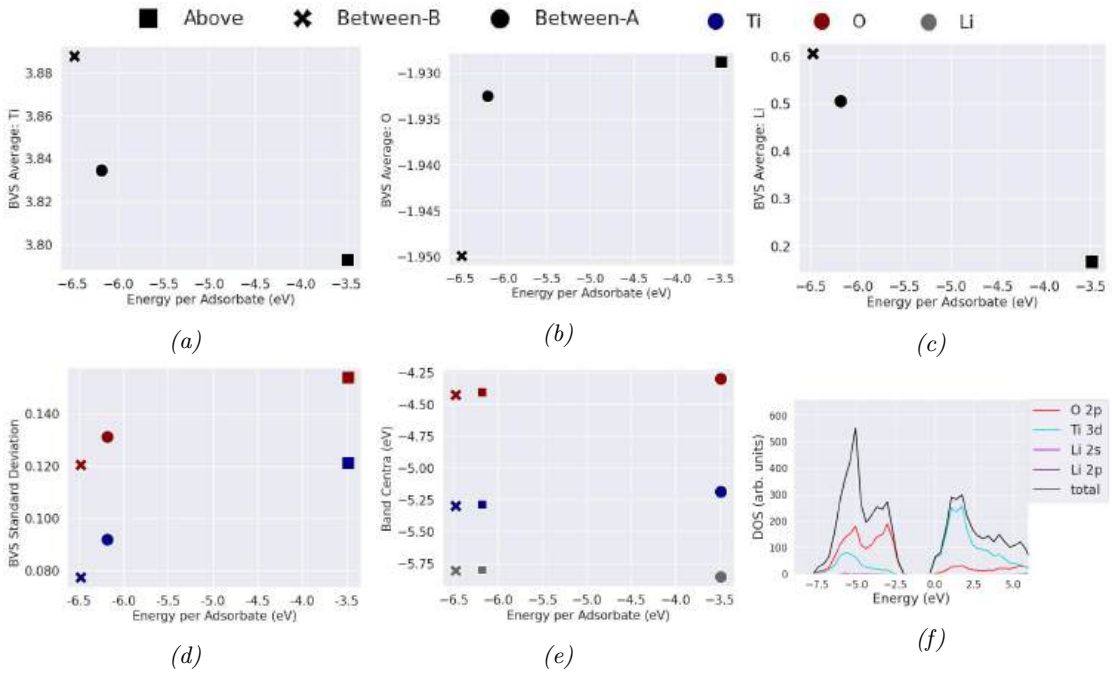

Figure 64: Key bonding data with respect to adsorption energy for the three Li adsorption sites on $SrTiO_3(001) - c(4\times2)$. The top row shows the average BVS for Ti, O and Li in a), b), and c), respectively. The bottom row shows d) the BVS standard deviation for Ti (blue) and O (red), e) the band centra of Ti 3d (blue), O 2p (red), and Li 2s+2p (grey), and f) DOS of the most strongly bonded adsorption sites, i.e. between-B. Ti and O BVS were calculated from surface atoms, defined as those above the outmost SrO layer. The centre of the valence band in f) is -4.71 eV, the centre of the bonding region is -6.07 eV, and the centre of the non-bonding region is -3.35 eV.

6.6 Discussion

At sub-monolayer coverage, Li induces three notable features to the structure of the $SrTiO_3(001) - c(4\times2)$ surface depending on coverage and temperature; namely cavities, islands and the $(\sqrt{5}\times\sqrt{5}) - R26.6^o$ reconstruction. The feature that forms at the lowest coverage and temperature is the cavities, which are observed both at coverages of $0 < 0.1$ ML and $0.1 < 0.3$ ML following annealing at 400-500 ^oC. This is the only structural change observed for $0 < 0.1$ ML coverage before the high-T surface ensues. At $0.1 < 0.3$ ML coverage, the cavities are coincidental with step edge islands after 500 ^oC annealing. Following 600-700 ^oC annealing, cavities are reduced in size while islands grow larger. As the annealing temperature approaches 800 ^oC, islands are consumed and replaced by a surface with large domains of $(\sqrt{5}\times\sqrt{5}) - R26.6^o$. The mechanism underlying the formation of $(\sqrt{5}\times\sqrt{5}) - R26.6^o$ was treated in Chapter 5 and will this not be further discussed here.

Since the topmost surface layer has TiO_2 stoichiometry, and since the cavities have a depth of circa half one $SrTiO_3(001)$ unit cell, they should result from removing $TiO_5[]$ units from the outmost TiO_2 layer. Examining Figure 58b, one may even find cavities that seemingly correspond to the lack of a single $TiO_5[]$ quartet (see the introduction of Chapter 5 for a model showing $TiO_5[]$ quartets). Figure 58b also shows spots protruding from the surface. A reasonable hypothesis would thus be that Li increases O over-coordination in the surface, which destabilises some $TiO_5[]$ quartets to cause their dissociation. The protruding spots could thus be the $TiO_5[]$ units of the destroyed $TiO_5[]$ quartets placed atop the surface. This would assign cavity formation to Li etching by similar mechanisms to those attributed to hole formation by Na etching in Chapter 5.

Islands also have similarities to structural features covered in Chapter 5, because they, like the holes observed in that chapter, are enclosures of step edge. As proposed for holes in the case of Na on $SrTiO_3(001)$, islands are likely the result of Li decoration stabilising step edges. The arguments for why this should be the case will therefore resemble those made for Na in Chapter 5, but the prevalence of step edge defect makes them worth covering from the perspective of Li as well. Step edges have two characteristics that should increase Li adsorption bond strength; firstly, they allow Li-O bonding in two perpendicular planes, which permits Li to coordinate a greater number of TiO_x units. This facilitates satisfying Li coordination while minimising the perturbation to any individual Ti or O atom. Secondly, step edges have reduced O coordination, thus allowing for stronger Li-O bonds by mitigating O over-coordination. This likely makes a configuration where Li decorates step edges preferred over one where step edges are bare and Li adorbs to flat surface terraces. If step edges then move across the surface at elevated temperatures, they may get pinned as Li preferentially bonds to them, creating a metastable surface with step edge islands. The energetic penalty of this high step edge density may then be reduced by increasing island size in a manner comparable to Oswald ripening, which explains the growth of islands as annealing temperature increases. As such, while Na was proposed to create holes that provided preferential nucleation sites for step edges, Li is instead proposed to pin step edges. The substantial increase in step edge density on $SrTiO_3(001)$ is in the case of both alkali metals proposed to be due to step edge stabilisation through

alkali metal decoration, driven by step edges providing preferential coordination sites.

Calculated correlations between adsorption energy and the coordination environments are effectively the same for Li as the ones presented for Na in Chapter 5, specifically with regard to over- and under-coordination and the number of $TiO_5[]$ units coordinating Li in the adsorption site. They will therefore not be explicitly stated here, but the conclusions to which they lead are worth reiterating; alkali metal adsorption sites are less stable when they cause greater O over-coordination, and step edges are likely preferential adsorption sites due to the low O coordination and increased accessibility of TiO_x units that may co-ordinate the alkali adsorbate. The former of these points indicates that Li may destabilise TiO_x units in the surface, thus supporting the arguments about cavity formation made above, and the latter supports Li preferentially decorating step edges. This chapter will instead analyse some correlations in the DFT results that were not discussed in Chapter 5. The correlations pertain to changes the character of bonding in the $c(4\times2)$ surface as Li adsorption strength increases. Stronger adsorption sites produced Ti and O BVS values closer to their formal oxidation states of +4 and -2, smaller spread in Ti and O BVS values, and lower energy levels for O 2p and Ti 3d band centra. This indicates that stronger adsorption sites on $c(4\times2)$ are associated with bonding becoming more bulk-like with electrons more closely bound to their atoms. This will become relevant for Chapter 8, where the $(111)-(2\times2)$ reconstruction is treated, which produces a distinctly different behaviour to which $(001)-c(4\times2)$ will be compared.

A remarkable difference in the effect Li has on the $SrTiO_3(001)$ surface compared to Na is the onset of the $(\sqrt{5}\times\sqrt{5})-R26.6^o$ reconstruction. Li did not induce the $(\sqrt{5}\times\sqrt{5})-R26.6^o$ until the $SrTiO_3$ sample was given a 300-400 ^oC higher annealing temperature than Na at the same coverage of $0<0.3$ ML. In addition, when $(\sqrt{5}\times\sqrt{5})-R26.6^o$ is induced by Li, it coincides with a significant fraction of the surface shedding its outermost layer. The lack of $(\sqrt{5}\times\sqrt{5})-R26.6^o$ prior to this shedding indicates that the surface was not notably reduced by either the cavities or the step edge islands. DFT may give an indication of why the two alkali metals differ in this manner, since DFT suggests that the Li-O bond is more covalent than the Na-O bond. The band centrum of Li 2s+2p is found firmly in the centre of the bonding region, whereas Na 3s+3p is found circa 1

eV closer to the non-bonding region, indicating greater Li-O hybridisation and therefore covalency. This greater tendency of Li than Na to form covalent bonds is, furthermore, known in the literature and was discussed in the literature review of Chapter 2. It may thus be that Li breaks up TiO_x units without transferring electrons to the surface to the same extent as Na, causing less reduction while breaking up TiO_x units to produce the observed cavities. Substantial reduction by Li may perhaps only occur at a high enough annealing temperature to activate some process unavailable at lower temperatures, such as Li intercalation into the surface region. If this happens, Li would presumably bond O at interstitial sites, which may force an electronic transfer from Li to Ti 3d and thus cause the reduction needed for $(\sqrt{5}\times\sqrt{5}) - R26.6^o$ formation. In any case, the difference in covalency between Li and Na will be suggested as the underlying reason for the onset of $(\sqrt{5}\times\sqrt{5}) - R26.6^o$ formation at a higher annealing temperature for Li.

Taking into account the high-T surface data acquired in Chapter 5, the following conditions for its formation are known. Firstly, it emerges after both Li and Na deposition on the $c(4\times2)$ reconstruction, meaning one can reasonably conclude that it is not based on a phase containing either alkali metal. If it were, this would result in two different chemistries, which would be unlikely to yield indistinguishable surfaces. This argument is, however, not conclusive, because Li and Na have similar atomic radii[212], meaning they could fit into the same surface site. However, as discussed in the paragraph above, Li and Na have been calculated to have a considerably different degree of covalency in their bond with O, meaning that they are expected to form bonding complexes with different geometries, which decreases the likelihood of them occupying the same surface site. Interestingly, Li and Na generate identical surface structures after annealing temperatures similar to those that yield the high-T surface also on (111), for which reason the analysis of the possibility of both alkalis occupying the same surface site will be continued in Chapter 7. Secondly, the high-T surface is coincident with the disappearance of alkali metals from the surface. As mentioned in Chapter 5, the intercalation versus desorption discussion will be given more detail in Chapter 7, where XPS data are available to assist the analysis. It is, however, appropriate for the purposes of finalising the assessment of the high-T surface to say that the conclusion from Chapter 7 will be that Li and Na are unlikely to occupy the same surface site, and that intercalation is more likely than desorption. Thirdly, it

was shown in Chapter 5 that the high-T surface region contains Ti^{3+} and Ti^{2+}, whereas these signals disappear when the $c(4\times2)$ surface returns. Ti^{3+} and Ti^{2+} should result from alkali metal valence electron transfer to Ti 3d orbitals. Chapters 7 and 8 will, furthermore, show that the mechanism associated with alkali metal disappearance from the surface is associated with substantially elevated reduction. Fourthly, the high-T surface has small domains of $(\sqrt{5}\times\sqrt{5})-R26.6^o$ ordering, and seems to have a higher density of this ordering at lower annealing temperatures, as displayed in Figure 60.

It will thus be proposed that the high-T surface forms at elevated annealing temperatures due to enhanced reduction, which increases O chemical potential to a point where the $(\sqrt{5}\times\sqrt{5})-R26.6^o$ becomes less stable than the high-T surface. When sufficient thermal energy is provided by annealing this reduction is undone, and the $c(4\times2)$ reconstruction can be re-established. Since intercalation is deemed more likely than desorption, the following model for the formation of the high-T surface may be proposed. The enhanced reduction that would ensue due to intercalation is motivated by the more restrictive coordination environments of the bulk compared to the surface, promoting electronic transfer from alkali interstitials to Ti. This reduction would subsequently cause the high-T surface to form as O chemical potential increases. When annealing temperature is further increased, alkali metals would be given sufficient thermal energy to diffuse deeper into the bulk and spread across the entire sample, making the concentration of alkali metals in the surface regions so low that the original $c(4\times2)$ reconstruction can re-emerge. It should, however, be noted that this is a speculative suggestion. Detailed arguments for the effects of intercalation, such as elevated reduction, will be given in Chapter 7.

At coverages of $1.0 < 2.0$ ML, Li produces nanoparticles and overlayer islands, where the overlayer islands becomes increasingly favoured at higher annealing temperature. After $500\ ^oC$ annealing, the hotter side of the sample is dominated by a 0.2-0.3 nm tall monolayer islands, with regions between monolayer islands being $(\sqrt{5}\times\sqrt{5})-R26.6^o$ reconstructions. This indicates that the surface region has been reduced at a lower temperature than for $0 < 0.3$ ML coverages, for which this reconstruction does not occur below $800\ ^oC$. Increased Li coverage thus drives $(\sqrt{5}\times\sqrt{5})-R26.6^o$ formation. This is compatible with the proposed mechanism for $(\sqrt{5}\times\sqrt{5})-R26.6^o$ formation, as the critical degree of reduction

that elevates O chemical potential to the point where $(\sqrt{5}\times\sqrt{5})-R26.6^o$ has the lower free energy than $c(4\times2)$ is likely to occur at lower temperature for a greater Li concentration at the surface. The association of $(\sqrt{5}\times\sqrt{5})-R26.6^o$ with reduction indicates that Li has reacted with O to form a lithium oxide, most likely Li_2O. Following 600 ^oC annealing, amorphous monolayer islands circa 30 nm in diameter cover circa 50% of the surface, indicating a high degree of Li adhesion.

6.7 Conclusion

Li on $SrTiO_3(001)-c(4\times2)$ displays three distinct structures by which Li is accommodated on the surface depending on coverage and annealing temperature; surface layer cavities, step edge islands, and the $(\sqrt{5}\times\sqrt{5})-R26.6^o$ reconstruction. It is hypothesised that cavities are formed by Li causing O atom over-coordination in $TiO_5[]$ quartets, leading to their dissolution. Step edge islands are hypothesised to form via preferential Li step edge decoration. The formation of the $(\sqrt{5}\times\sqrt{5})-R26.6^o$ reconstruction is attributed to Li reducing the surface, thus elevating O chemical potential to a point where this reconstruction has lower free energy than $c(4\times2)$. The high-T surface, which was introduced in Chapter 5, is suggested to form due to the enhanced reduction that ensues at elevated annealing temperatures, which increases O chemical potential to a point where $(\sqrt{5}\times\sqrt{5})-R26.6^o$ is unstable. It was, furthermore, suggested that this elevated reduction is driven by Li intercalation as a substantial number of Li atoms migrate into interstitial sites in the surface region. At 1.0 $<$ 2.0 ML coverage, Li forms wetting monolayer islands, which dominate the surface at 500-600 ^oC.

7 Na on $SrTiO_3(111)$

7.1 Introduction

This chapter describes the interaction of Na with $SrTiO_3(111)$ as indicated by STM, DFT and XPS. Four $SrTiO_3(111)$ reconstructions were consistently observed in STM during the course of this project, namely (4×4), (5×5), $(6\times6)A$, and $(6\times6)B$, as displayed in Figure 65. These reconstructions often appear together as neighbouring domains in the same area. Typically, (5×5) was found alone, (6×6)A and (4×4) were together, and (6×6)B was found forming domains in regions dominated by (5×5) or (6×6)A. All reconstructions were studied at three Na coverages; $0 < 0.1$ ML, $0.1 < 0.3$ ML, and $1.0 < 2.0$ ML. The two lower coverages produced the same surface structures, but with features being more accentuated at $0.1 < 0.3$ ML coverage. The $0 < 0.1$ ML deposition is thus redundant and will be excluded from this presentation. The XPS data presented in Section 7.5 pertains to samples that were prepared in the STM treatment chamber but were exposed to the atmosphere during transfer to the XPS instrument.

The DFT calculations presented in Section 7.4 consider Na on the $SrTiO_3(111) - (2\times2)$ and (3×3) reconstructions. These two reconstructions were used for calculations of (111) surfaces since they are sufficiently small to make adsorption behaviour calculations practicable. The atomic structures of these two reconstructions are displayed in Figure 66. (2×2) and (3×3) differ in their surface structure in one important respect; (2×2) is not a TiO_2 double-layer reconstruction, while (3×3) is. As discussed in Chapter 2, this means that (2×2) faces the environment with $TiO_5[]$ units, whereas the outmost polyhedral units of (3×3) are TiO_4.

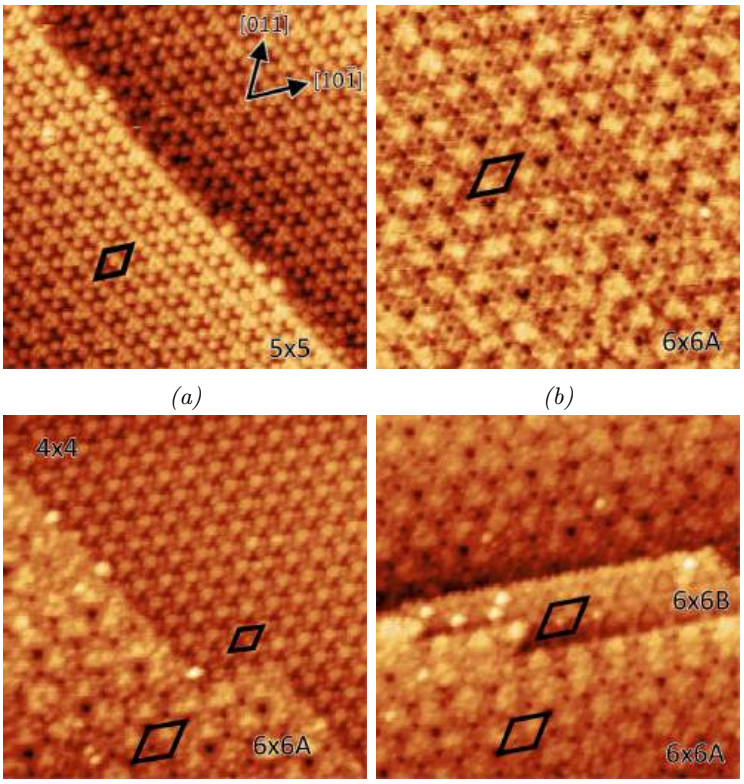

Figure 65: Reconstructions of $SrTiO_3$(111), showing a) (5×5) (1.6 V, 0.08 nA, $30\times30nm^2$), b) $(6\times6)A$ (1.5 V, 0.1 nA, $30\times30nm^2$), c) $(6\times6)A+(4\times4)$ (2.0 V, 0.1 nA, $30\times30nm^2$), and d) $(6\times6)A+(6\times6)B$ (1.5 V, 0.1 nA, $30\times30nm^2$). Black diamonds mark surface units cells. $(6\times6)A$ and $(6\times6)B$ are found together in d), demonstrating that they are indeed distinct reconstructions.

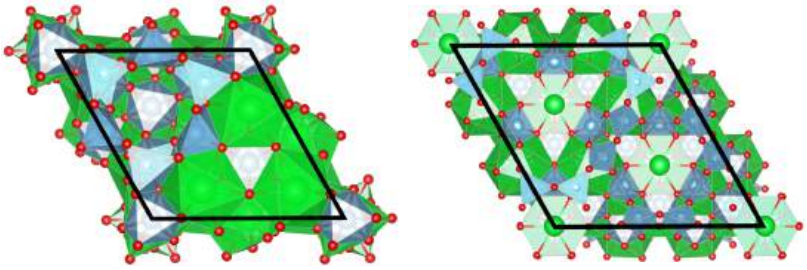

Figure 66: Surface unit cells of the (2×2) and (3×3) reconstructions used in calculations of $SrTiO_3$(111) surfaces, where green, blue, and red balls are Sr, Ti, and O respectively. Green and blue polyhedra represent O coordination around Sr and Ti, respectively. Surface unit cells are marked by black diamonds. A notable difference between (2×2) and (3×3) is that the former does not contain TiO_4 units, whereas the latter does, indicated by the lighter blue TiO_x polyhedra in b).

7.2 Medium Deposition

A coverage of $0.1 < 0.3$ ML Na on $SrTiO_3$(111) does not cause significant structural modifications, such as induced defects or reconstructions. The most noteworthy Na behaviour on this termination is a remarkably strong preferential adsorption to the $(6\times6)B$

reconstruction. The other three reconstructions are displayed in Figure 67, where the top row shows the (5×5) surface and the bottom row shows the $(6\times6)A + (4\times4)$ surface. The images displayed in this figure show bright spots scattered across the surface, which most likely correspond to Na nanoparticles. An indication that spots are indeed nanoparticles is that they tend to grow larger on the $(6\times6)A$ and (4×4) than (5×5). They furthermore seemingly have a preference for locating to step edges on $(6\times6)A$ and (4×4), which they did not demonstrate on (5×5).

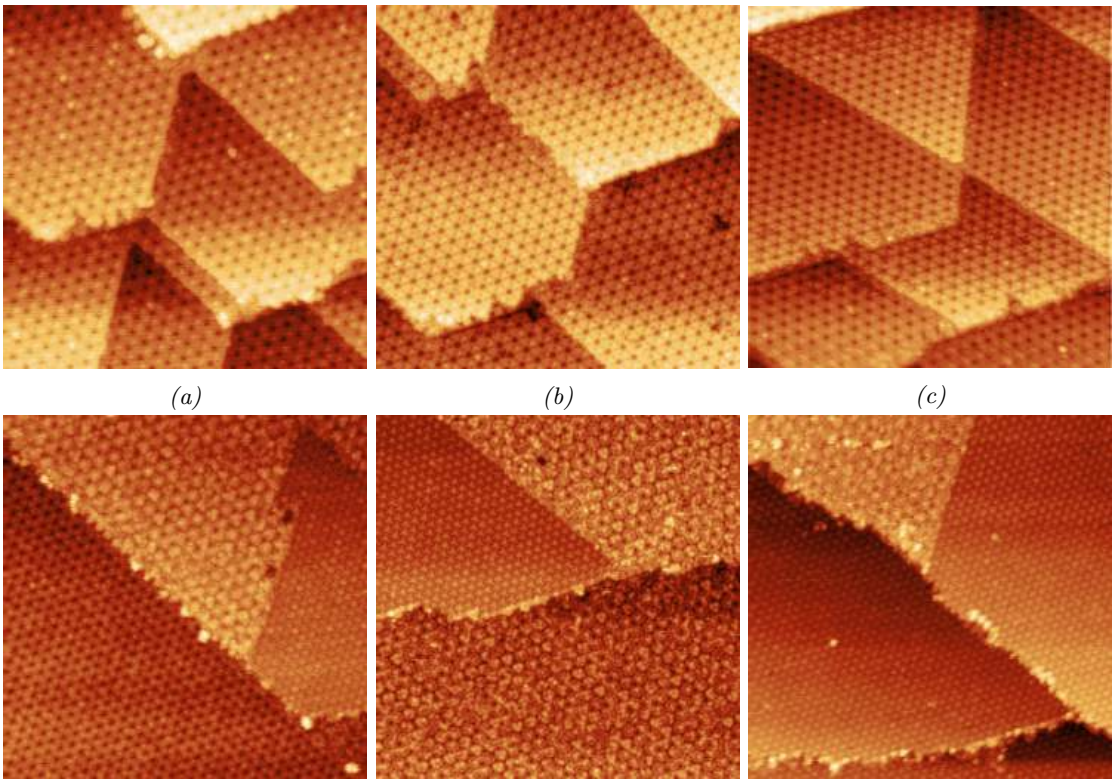

Figure 67: $0.1 < 0.3$ *ML Na deposition on* $SrTiO_3(111)$. *The top row shows* (5×5) *areas after annealing temperatures of a) 500 °C (U=1.5 V, I=0.1 nA,* $60\times60\,nm^2$*), b) 700 °C (U=1.5 V, I=0.1 nA,* $60\times60\,nm^2$*), and c) 800 °C (U=2.0 V, I=0.1 nA,* $60\times60\,nm^2$*). Nanoparticles have a mean height and width of* 0.22 ± 0.02 *nm and* 1.12 ± 0.23 *nm in a), as well as* 0.22 ± 0.04 *nm and* 1.00 ± 0.43 *nm in c). The bottom row shows* $(6\times6)A + (4\times4)$ *areas after annealing temperatures of d) 400 °C (U=1.1 V, I=0.1 nA,* $80\times80\,nm^2$*), e) 700 °C (U=1.5 V, I=0.1 nA,* $80\times80\,nm^2$*), and f) 800 °C (U=2.0 V, I=0.1 nA,* $80\times80\,nm^2$*). Nanoparticles have a mean height and width of* 0.43 ± 0.07 *nm and* 1.98 ± 0.24 *nm in d), as well as* 0.29 ± 0.03 *nm and* 1.95 ± 0.39 *nm in f). Nanoparticles on* $(6\times6)A + (4\times4)$ *show a tendency to preferentially locate to step edges.*

The Na interaction with $(6\times6)B$ is very different, as can be seen in Figure 68. Na seemingly gathers on this reconstruction to form nanoparticles circa 0.4-0.5 nm in height and 2-4 nm in width. Surfaces where $(6\times6)B$ coexists with $(6\times6)A$ is shown in Figure

68a, with $(6\times6)A$ and (4×4) in Figure 68b, and with (5×5) in Figure 67b, where no reconstruction except $(6\times6)B$ has a notable presence of nanoparticles. Moreover, it seems that Na has a high degree of mobility on $(6\times6)B$, as displayed in Figure 69. Figures 69a and 69b constitute two adjacent STM scans of the same area, showing five locations where bright spots have disappeared from one image to the next. These spots are likely Na atoms or Na-based clusters of a few atoms, which readily diffuse across the surface.

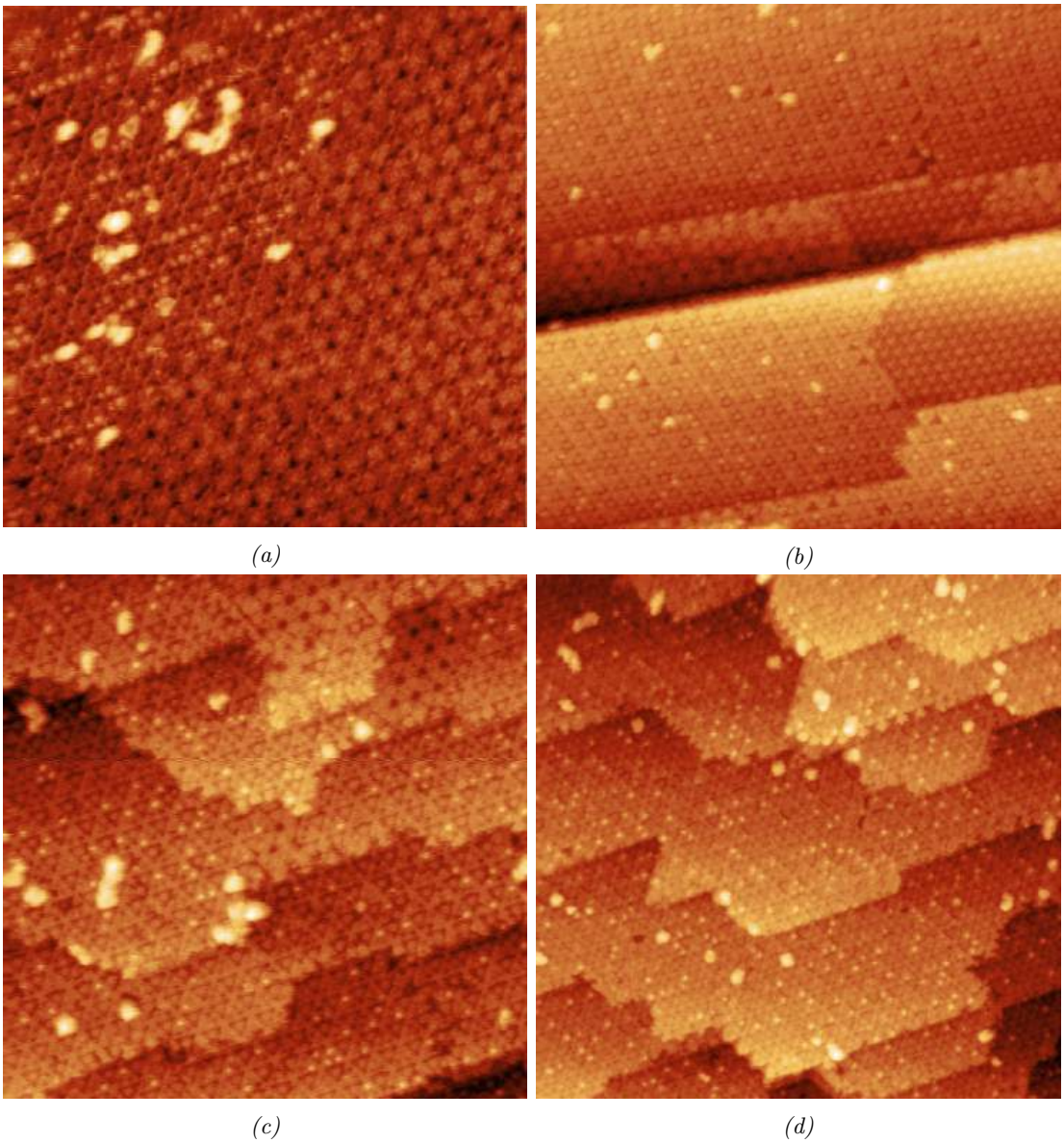

(a) *(b)* *(c)* *(d)*

Figure 68: $0.1 < 0.3$ *ML Na deposition on* $SrTiO_3(111) - (6\times6)B$ *after annealing temperatures a) 500 °C (U=2.0 V, I=0.1 nA,* $60\times60\,nm^2$*), b) 500 °C (U=1.0 V, I=0.1 nA,* $80\times80\,nm^2$*), c) 700 °C (U=1.0 V, I=.1 nA,* $60\times60\,nm^2$*), and d) 800 °C (U=1.5 V, I=0.1 nA,* $80\times80\,nm^2$*). a) Nanoparticles have a mean height of a)* 0.38 ± 0.02 *nm, b)* 0.40 ± 0.04 *nm, c)* 0.49 ± 0.05 *nm, and d)* 0.42 ± 0.05 *nm. Nanoparticles have a mean width of a)* 2.74 ± 0.85 *nm, b)* 2.14 ± 0.43 *nm, c)* 3.94 ± 0.20 *nm, and d)* 4.03 ± 0.21 *nm. Step edges have a mean height of c)* 0.25 ± 0.03 *nm and d)* 0.23 ± 0.02 *nm.*

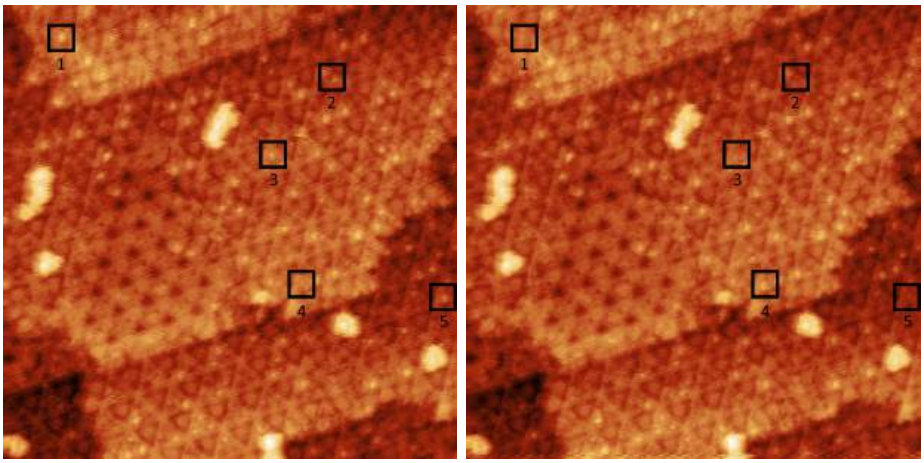

(a) *(b)*

Figure 69: $0.1 < 0.3$ *ML Na deposited on* $SrTiO_3(111)-(6\times6)B$ *after 700* ^oC *annealing (U=1.0 V, I=0.1 nA,* $40\times40\,nm^2$*), showing movement of particles on the surface between images captured of the same area in adjacent STM scans displayed in a) and b). Each black box labelled 1-5 indicates a position where a particle has moved between a) and b). The other reconstruction in these images, defined by its dark triangular indents, is the* (5×5)*, on which no Na particle movement can be seen.*

7.3 High Deposition

$1.0 < 2.0$ ML Na deposition on $SrTiO_3(111)$ was conducted on two surfaces, one dominated by (5×5) and the other by $(6\times6)A + (4\times4)$, displayed in Figures 70a and 70b, respectively. The original reconstruction plays a significant role in determining the structures that form on these surfaces after Na deposition and annealing. Figure 71 shows the evolution of the originally (5×5) surface between 500 ^oC and 700 ^oC annealing. After 500 ^oC annealing, the surface is covered in amorphous Na nanoparticles and films, but with the underlying $SrTiO_3(111)$ substrate visible, as can be seen in Figure 71a. There seems to be short-range ordering in the $SrTiO_3(111)$ substrate beneath, which is transformed to long-range ordering after 600 ^0C annealing, as can be seen in Figure 71b. The periodicity of this order is in good agreement with (5×5), which is maintained also after 700 ^oC annealing, as can be seen in Figure 71c.

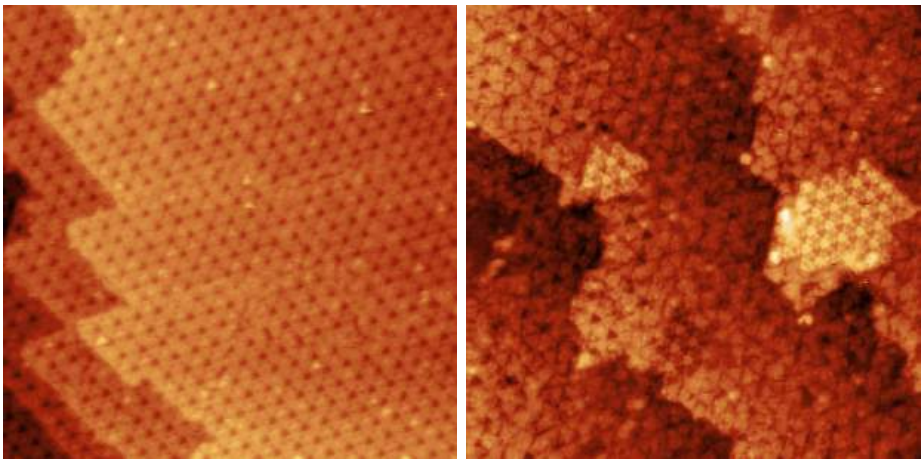

(a) *(b)*

Figure 70: Surfaces used for $1.0 < 2.0$ *ML Na deposition, showing a)* (5×5) *(U=1.0 V, I=0.1 nA,* $60\times60\,nm^2$*) and b)* $(6\times6)+(4\times4)$*, (U=1.5 V, I=0.1 nA,* $50\times50\,nm^2$*).*

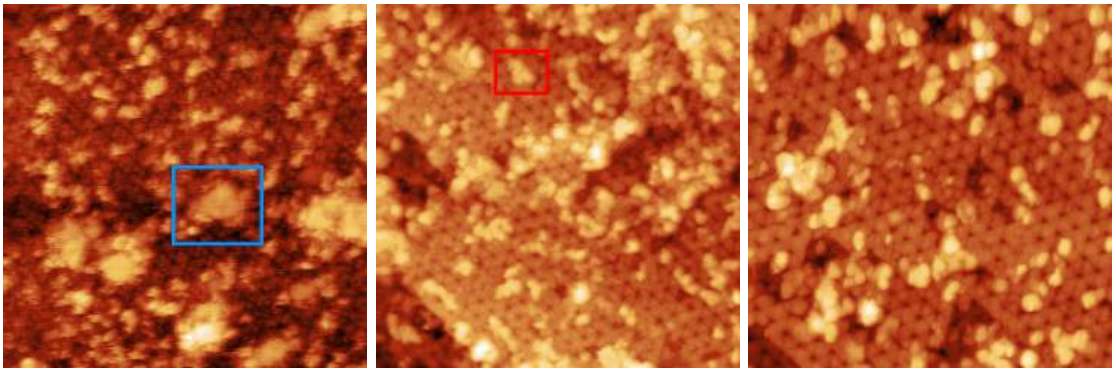

(a) *(b)* *(c)*

Figure 71: $1.0 < 2.0$ *ML Na deposition on* $SrTiO_3(111)-(5\times5)$ *after annealing temperatures of a) 500* ^oC *(U=1.0 V, I=0.1 nA,* $50\times50\,nm^2$*), b) 600* ^oC *(U=1.5 V, I=0.1 nA,* $60\times60\,nm^2$*), and c) 700* ^oC *(U=1.0 V, I=0.1 nA,* $50\times50\,nm^2$*). An example of a Na film is marked by the blue rectangle in a), and an example of a Na nanoparticle is marked by the red rectangle in b). Films in a) have a mean height of* 0.85 ± 0.07 *nm, nanoparticles in b) have a mean height of* 0.43 ± 0.04 *nm, and nanoparticles in c) have a mean height of* 0.40 ± 0.03 *nm and mean width of* 2.40 ± 0.51 *nm. The periodicity in the underlying* $SrTiO_3(111)$ *surface was measured to be within 1% of* $5\times$ *in b) and within 7% of* $5\times$ *in c).*

Figure 72 shows the evolution of the originally $(6\times6)+(4\times4)$ surface between 500 ^oC and 700 ^oC annealing. The underlying substrate is not clearly visible after 500 ^oC annealing and the surface is dominated by amorphous Na films, as can be seen in Figure 72a. After annealing to 600 ^oC and 700 ^oC, the surface is dominated by Na nanoparticles, but with the underlying substrate now exposed, as can be seen in Figures 72b and 72c, respectively. The periodicity of the underlying substrate is in good agreement with (5×5).

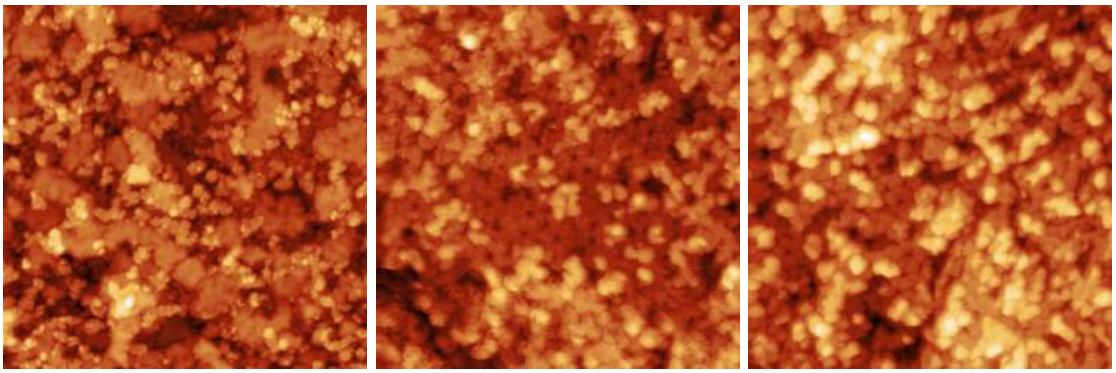

(a) *(b)* *(c)*

Figure 72: $1.0 < 2.0$ *ML Na deposition on* $SrTiO_3(111)-(6\times6)+(4\times4)$ *after annealing temperatures of a) 500 °C (U=1.5 V, I=0.1 nA,* $60\times60\,nm^2$*), b) 600 °C (U=1.0 V, I=0.1 nA,* $50\times50\,nm^2$*), and c) 700 °C (U=0.75 V, I=0.1 nA,* $50\times50\,nm^2$*). Nanoparticles in b) have a mean height of* 0.45 ± 0.06 *nm. Isolated nanoparticles in c) have a mean height of* 0.42 ± 0.05 *nm and mean width of* 2.49 ± 0.43 *nm. The periodicity in the underlying* $SrTi0_3(111)$ *surface in b) is within 5% of* $5\times$.

Following 800 ^oC annealing, both surfaces become dominated by the substrate, with Na seemingly only present in the form of small nanoparticles. The top row of the Figure 73 shows the surface that was originally the (5×5) reconstruction, which has once more returned. There are, however, three notable features of this surface that distinguishes it from the original (5×5) pre-Na exposure; firstly, there are now holes present on the surface, circa 0.20-0.25 nm in depth, which is consistent with the interplanar spacing of (111) planes in $SrTiO_3$. Secondly, there are triangular indentations, which are morphologically homogenous and cover an area equal to circa half a (5×5) unit cell. These indentations thus indicate the lack of a few TiO_x units, making them similar to the cavities reported on $SrTiO_3(001)$ in Chapter 6, for which reason they too will be referred to as cavities. Thirdly, the surface now contains amorphous domains, typically in close proximity to holes. A clear example of an amorphous domain can be found in the centre of Figure 73b. The bottom row of Figure 73 shows the surface that was originally $(6\times6)+(4\times4)$ and displays the coexistence of two reconstructions, the familiar $(6\times6)B$, as well as a new reconstruction with (5×5) ordering, which will be called $(5\times5)\gamma$. $(6\times6)B$ and $(5\times5)\gamma$ are marked by the blue and red rectangles, respectively, in Figure 73c. $(5\times5)\gamma$ is given a characterisation in Figure 74, which asserts that this reconstructions first of all has 5× periodicity, and second of all is different from the previously encountered (5×5). $(5\times5)\gamma$ is also generated following the Li deposition on $SrTiO_3(111)$ treated in Chapter 8, where it will be further discussed.

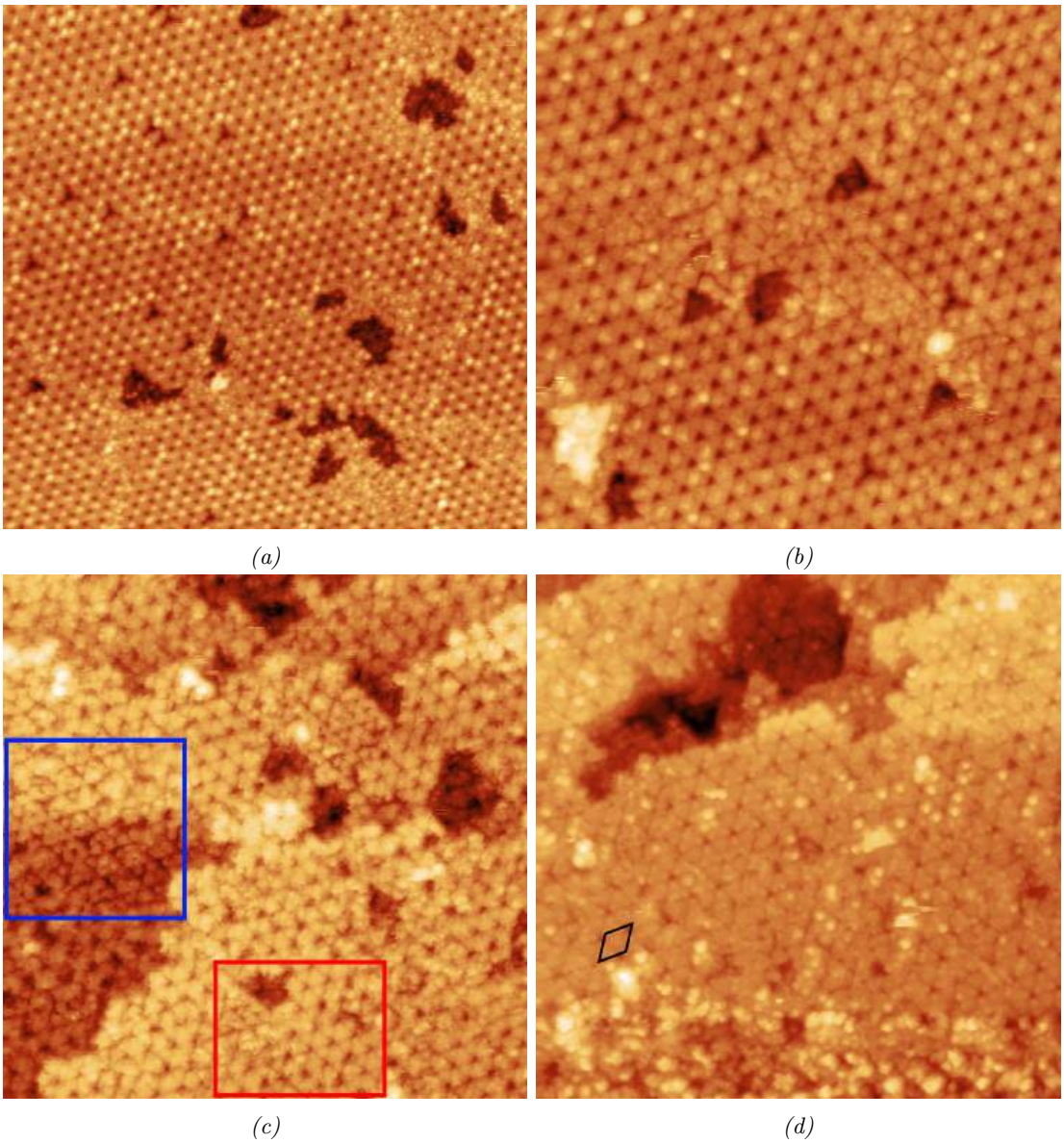

Figure 73: $1.0 < 2.0$ *ML Na deposition on* $SrTiO_3(111)$ *after 800 °C annealing, showing areas where the original reconstruction was* (5×5) *in the top row and* $(6\times6)A+(4\times4)$ *in the bottom row.* (5×5) *has returned to the area where it dominated the surface prior to Na exposure, but with a significantly higher defect density. Holes in this surface have a mean depth of* 0.23 ± 0.03 *nm in a) (U=1.0 V, I=0.1 nA,* $80\times80\,nm^2$*) and* 0.24 ± 0.03 *nm in b) (U=0.75 V, I=0.1 nA,* $50\times50\,nm^2$*). Both a) and b), furthermore, show triangularly indented cavities corresponding to circa half one* (5×5) *unit cell. The* $(6\times6)A+(4\times4)$ *area has generated notable domains of* $(6\times6)B$*, but is dominated by the new reconstruction* $(5\times5)\gamma$*, where the former is indicated by the blue rectangle and the latter by the red rectangle in c) (U=1.0 V, I=0.1 nA). The unit cell of* $(5\times5)\gamma$ *is displayed in d) (U=1.5 V, I=0.1 nA,* $50\times50\,nm^2$*).*

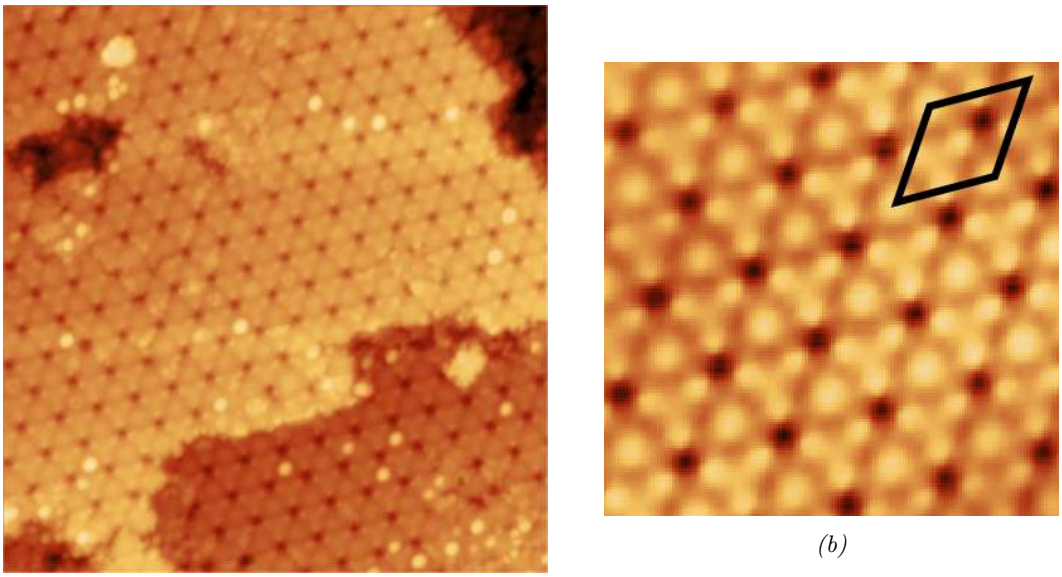

(a) *(b)*

Figure 74: Characterisation of $SrTiO_3(111) - (5\times5)\gamma$. a) shows the original image (U=1.6 V, I=0.06 nA, $40\times40\ nm^2$) (averaged over eight images in SmartAlign), where the periodicity is measured to be within 2% of 5× with respect to $\langle110\rangle$ of $SrTiO_3$. b) shows a crop where the surface unit cell is marked by the black diamond. Comparing b) and Figure 65a, where the normal (5×5) is displayed, it is clear that their geometries are fundamentally different, e.g. the triangular indents in (5×5) are not present in (5×5)γ, and the triangle of dots in (5×5)γ are not present in (5×5). N.B. This image was acquired after 0 < 0.1 Li deposition on $SrTiO_3(001) - (5\times5)$ and 700 °C annealing, but is displayed here due to its higher quality than (5×5)γ images acquired in the Na-on-$SrTiO_3(111)$ experiment.

7.4 Bonding Interactions

DFT calculations were used to identify features that allow for strong bonding interactions between Na and $SrTiO_3(111)$ surfaces, which would help explaining the preferential bonding to $(6\times6)B$ observed in Section 7.2. As mentioned in Section 7.1, two $SrTiO_3(111)$ reconstructions were used for this propose, namely (2×2) and (3×3). Adsorption sites for (2×2) and (3×3) are displayed in Figures 75 and 76, respectively. On both reconstructions, a greater number of TiO_x units coordinating Na correlates with lower adsorption energy. The lowest energy site on (2×2) is the between site with an adsorption energy of -5.54 eV, followed by the above site at -4.30 eV and lastly the floor site at -3.91 eV. On the (3×3) surface, the lowest energy adsorption site is the between site with an adsorption energy of -3.83 eV, while the atop site has an adsorption energy of -2.58 eV. Na adsorption is thus significantly stronger on the (2×2) surface than (3×3).

There are significant differences in the thermodynamic, electronic, and structural properties of the (2×2) and (3×3) surfaces which indicate why Na adsorption is stronger on

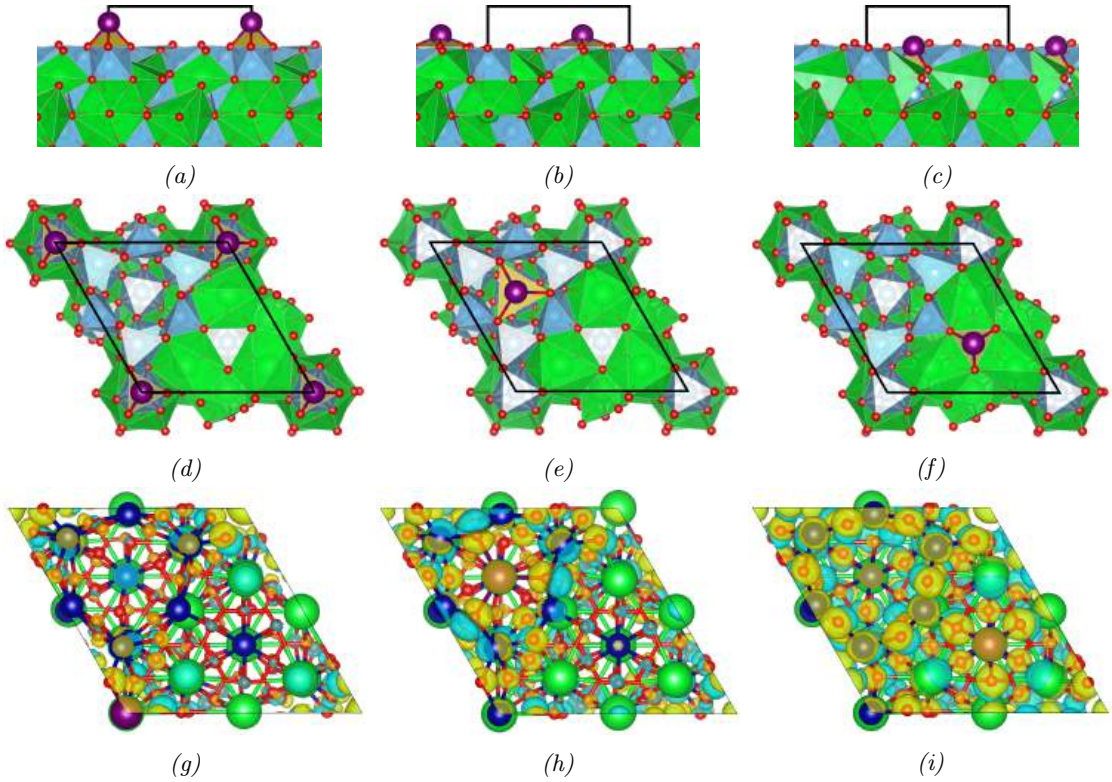

Figure 75: Na adsorption sites on $SrTiO_3(001) - (2\times2)$, where the above, between, and floor sites are shown from the top view i a), b) and c), respectively, form the side view in d), e), and f), respectively, and with electron density changes overlaid in g), h), and i), respectively. Green, blue, red, and purple balls are Sr, Ti, O and Na, respectively. Green, blue, and yellow polyhedra represent O coordination around Sr, Ti and Na, respectively. Black lines mark the surface unit cell. Na is coordinated by three O in all sites. Na is coordinated by four $TiO_5[]$ in the above site, six $TiO_5[]$ in the between site, three $TiO_5[]$ in the floor site.

(2×2). Firstly, the surface energy of (2×2) is 0.050 eV/Å^2 while that of (3×3) is 0.035 eV/Å^2, suggesting that a greater surface energy reduction should be possible on (2×2). Secondly, these two surfaces differ in the nature of their Ti-O bonding. The (2×2) surface has a O 2p-Ti 3d band separation of -1.32 eV, while that of the (3×3) surface is -1.61 eV, indicating greater Ti-O covalency in the (2×2) surface. (2×2), furthermore, has effective oxidation states that differ more from the formal Ti and O values, as the average Ti and O BVS for (3×3) are +3.83 and -1.89, respectively, whereas those for (2×2) are +3.61 and -1.77, respectively. All these effects are likely the result of (2×2) being a single TiO_2 layer reconstruction whereas (3×3) has an outmost layer composed of TiO_4 units, which will be further discussed in Section 7.6.

Figure 77 shows the influence of Na adsorption on the surface energies and band centra of the (2×2) and (3×3) surfaces. As expected, the strength of adsorption sites strongly correlates with surface energy reduction, as can be seen in Figure 77a. The change

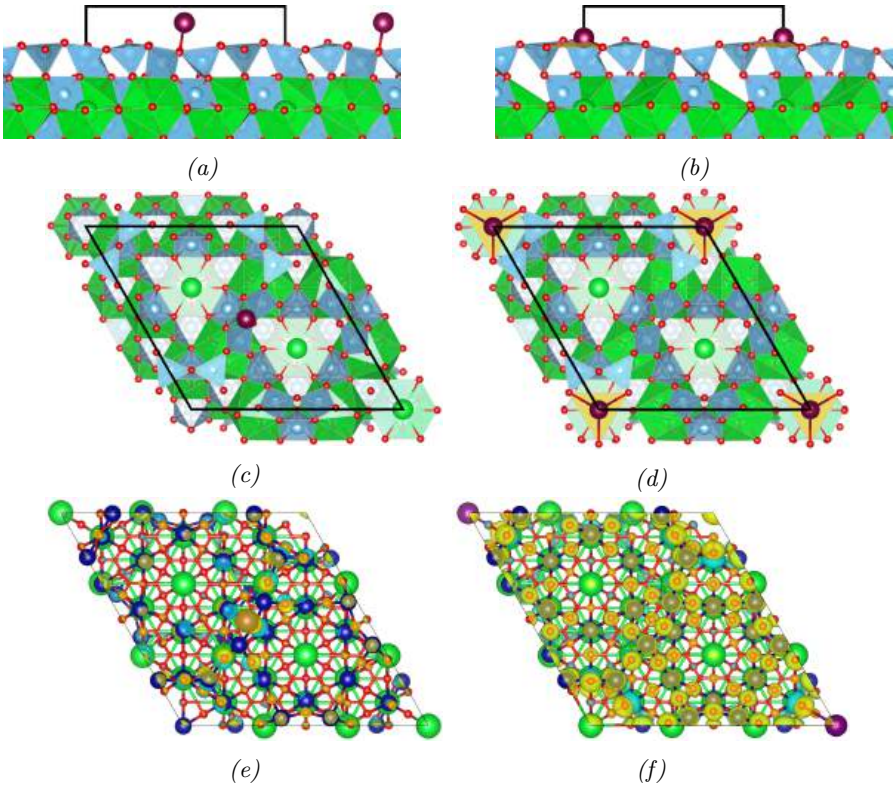

Figure 76: Na adsorption sites on $SrTiO_3(001) - (3\times3)$, where the atop and between sites are shown from the top view i a) and b) respectively, from the side view in c) and d), respectively, and with electron density changes overlaid in e) and f). Black lines mark the surface unit cell. Na is coordinated by one O in the atop site and three O in the between site, as well as two TiO_4 in the atop site and six TiO_4 in the between site. The same colour scheme as in Figure 75 was used.

in surface energy with respect to the clean surface of the reconstruction in question is significantly greater for (2×2), as can be seen in Figure 77b. This lowering in surface energy for (2×2) is accompanied by both Ti 3d and O 2p moving to lower energy levels with respect to the clean surface, as can be seen in Figures 77c and 77d, with both orbitals reducing their energies significantly more in the case of the (2×2) surface. The reason for this is suggested by the DOS spectra of the clean reconstructions in Figures 77e and 77f, which indicate that a greater fraction of both O 2p and Ti 3d valence DOS are found in the bonding region for (3×3) than (2×2). This suggests that the coordination environments of (2×2) produce a greater concentration of unsaturated valence orbitals, leading to a greater energetic gain when Na adsorbates bond to the surface.

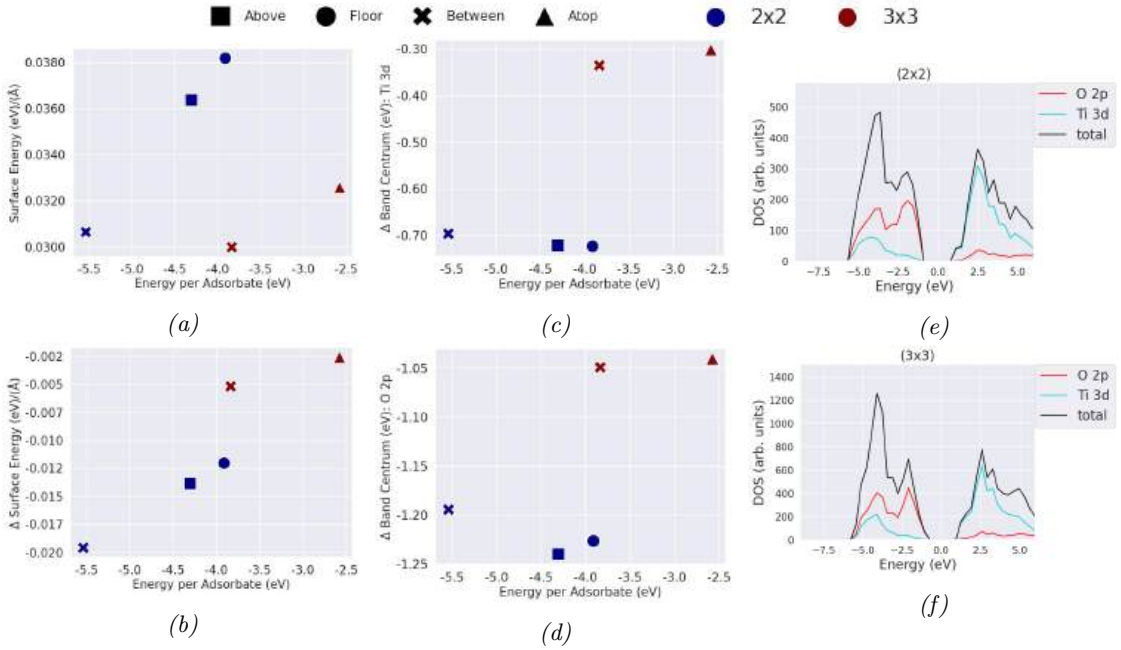

Figure 77: Calculated bonding data for Na adsorption sites on $SrTiO_3(001) - (2\times2)$ and (3×3), as well as the DOS of the clean surfaces. With respect to adsorption energy, a) and b) show absolute surface energy and change in surface energy, respectively. c) and d) show Ti 3d and O 2p band centra movement with respect to the clean surface, respectively. e) and f) show the DOS for the clean (2×2) and (3×3) reconstructions, respectively. Using the same definition of bonding and non-bonding regions as explained in Chapter 5, the O 2p bonding/non-bonding ratios are 0.75 for (2×2) and 1.03 for (3×3), and Ti 3d bonding/non-bonding ratios are 2.56 for (2×2) and 4.56 for (3×3). Thus, a greater fraction of both O 2p and Ti 3d valence DOS are found in the non-bonding region for (2×2) than for (3×3).

7.5 Chemical Environments

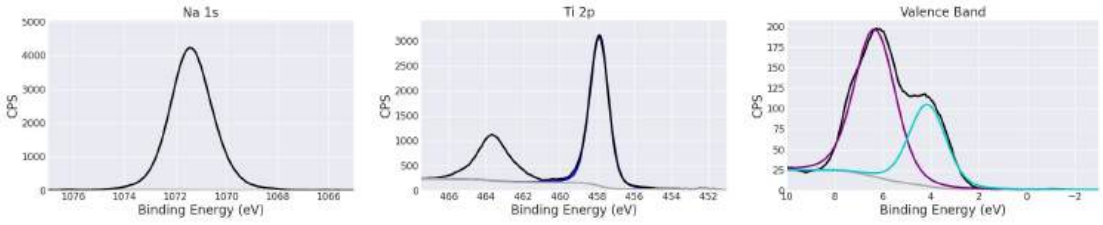

(a) Na-on-$SrTiO_3$(111) *(b) Na-on-$SrTiO_3$(111)* *(c) Cleaved $SrTiO_3$*

Figure 78: Foundational XPS data to which samples will be compared to demonstrate the influence of Na on $SrTiO_3$. a), and b) show the Na 1s and Ti 2p peaks acquired from a sample where $2.0 < 4.0$ ML Na was deposited on a $SrTiO_3$(111) substrate without subsequent annealing, The Ti 2p spectrum thus shows that Na does not notably reduce Ti without annealing. c) shows the valence band of a $SrTiO_3$ sample that was cleaved in the introduction chamber of the XPS instrument, where the purple and turquoise lines are bonding and non-bonding regions, respectively. The percentage of the valence band consisting of bonding and non-bonding peaks are 71% and 29%, respectively.

The bonding environments of the surface region and its evolution with annealing temperature may be gauged by the XPS data displayed in Figures 78 and 79. The Na 1s region

following 2.0 < 4.0 ML deposition without annealing is displayed in Figure 78a, and the Ti 2p and valence band regions of an in situ cleaved sample are shown in Figures 78b and 78c, respectively. The Na 1s, Ti 2p and valence band regions following 1.0 < 2.0 ML Na deposition and 600 ^oC annealing are displayed in Figure 79.

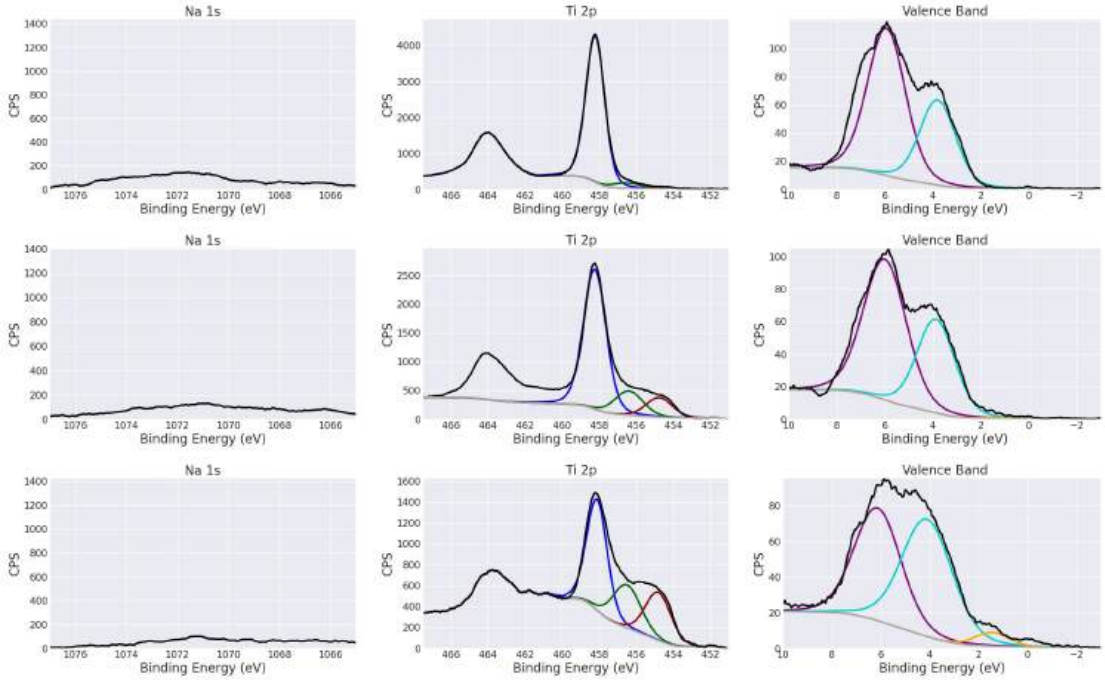

Figure 79: XPS spectra for 2.0 < 4.0 *ML Na deposited on* $SrTiO_3(111)$ *and 600* ^oC *annealing. Deposition and annealing were conducted in the UHV treatment chamber of the STM instrument. The x axis shows binding energy in eV and y axis shows counts per second (CPS). The black, and gray lines are the total signal and Shirley background, respectively, the blue, green, and red lines are* Ti^{4+}, Ti^{3+}, *and* Ti^{2+}, *respectively, and the purple, turquoise, and orange lines are bonding, non-bonding, and band gap states, respectively. The top row shows data from the colder side of the sample, the middle row the middle of the sample, and the bottom row shows data from the hotter end of the sample. The leftmost column shows the Na 1s region, the middle column the Ti 2p region, and the rightmost column the valence band region. No significant Na signal is visible, despite the sample receiving the same amount of Na as in Figure 78a and these two samples being measured in the same XPS experiment. As the temperature increases from the colder side to the middle of the sample, the percentages of the Ti 2p signal belonging* Ti^{4+}, Ti^{3+}, *and* Ti^{2+} *change from 94%, 5%, and 1% to 72%, 16%, 12%, respectively, indicating a significant increase in reduced Ti. At the hotter side of the sample, Ti has been further reduced to gain* Ti^{4+}, Ti^{3+}, *and* Ti^{2+} *percentages of 48%, 26%, and 26%, respectively. The cold side of the sample has a valence band consisting of 65% bonding and 35% non-bonding states, which sees a small change to 62.6% bonding and 37% non-bonding states in the middle of the sample. The middle of the sample, furthermore, seemingly sees the emergence of some states in the band gap, producing a peak that constitutes 0.4% of the total valence band. At the hotter side of the sample, the percentages of non-bonding and band gap states increase to 51% and 4%, respectively, while the bonding state peak decreases to 45%. Ti reduction hence seems to correlate with an increase in non-bonding states, as well as a band gap state. As explained in Chapter 3, the difference in effective annealing temperature between the centre of the sample and one of its ends is expected to be up to 50* ^oC, *meaning the hot and cold side of the sample should differ by no more than 100* ^oC.

The Na 1s signal is clearly present in Figure 78a is gone in Figure 79, despite the

two samples being part of the same experiment and prepared in the same manner, only differing by 600 ^oC annealing. It thus seems that this annealing temperature is sufficient to remove enough Na from the surface as to make it undetectable in XPS. Notably, in the centre and hotter end of the sample, the percentages of the Ti 2p signal originating from Ti^{3+} and Ti^{2+} compared to Ti^{4+} increase. Similarly, hotter annealing temperature seemingly increases the contribution of non-bonding states to the valence band signal, and states in the band gap have emerged. The presence of Ti^{3+} and Ti^{2+} of the XPS spectra in Figure 79, together with filled states in the band gap of the clean $SrTiO_3(111)$ substrate, suggest that occupied band gap states are due to filling of Ti 3d orbitals. DFT calculations support this idea, as can be seen in Figures 80a and 80b, which show the DOS around Fermi level for 1.5 ML Na on (2×2) and 0.67 ML Na on (3×3), respectively. Both these calculations yield conduction band states below the Fermi level that are dominated by Ti 3d.

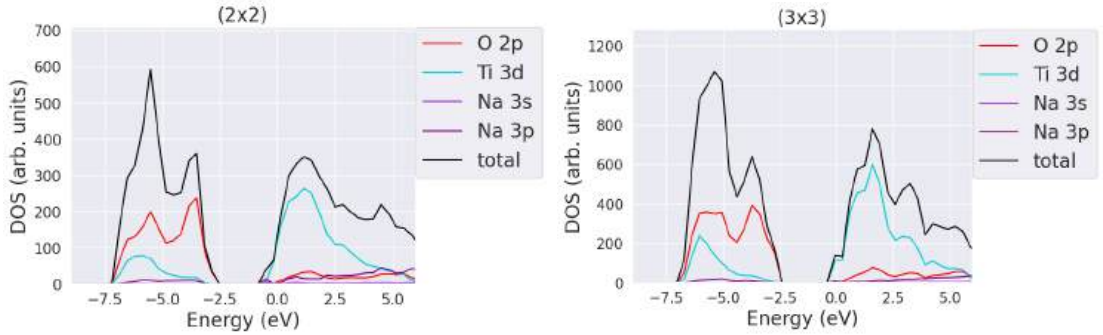

(a) *(b)*

Figure 80: DOS around the Fermi level for a) 1.5 ML Na on (2×2) *and b) 0.67 ML Na on* (3×3)*. Conduction band states are present below the Fermi level, the total composition of which for* (2×2) *is 75% Ti 3d, 3% O, 6% Na 3s and 16 % Na 3p, and for* (3×3) *is 90% Ti 3d, 2% O 2p, 1% Na 3s and 7% Na 3p.*

7.6 Discussion

At coverages below 0.3 ML, Na was not observed to induce any structural changes to the (4×4), (5×5), $(6\times6)A$, nor $(6\times6)B$ reconstructions of $SrTiO_3(111)$. The most notable Na behaviour at this coverage is the clear difference in Na interactions between reconstructions. Na-based nanoparticles on (6×6)A and (4×4) grow circa two times larger than their counterparts on (5×5) in height as well as width. Nanoparticles, furthermore, show a tendency to locate to $(6\times6)A$ and (4×4) step edges, whereas no such inclination was demonstrated for the (5×5) surface. It thus seems that Na has a slight preference

for $(6\times6)A$ and (4×4) over (5×5). Na does, however, overwhelmingly prefer adsorption to $(6\times6)B$ over any other reconstruction. In any area where $(6\times6)B$ coexists with other reconstructions, nanoparticles are only found on $(6\times6)B$, where they acquire a rather homogenous height of circa 0.4 nm with widths of 2.0-4.0 nm. It also seems that Na has a substantial degree of mobility on the $(6\times6)B$ surface, as sub-nanometre particles were observed to appear and disappear between STM scans.

DFT was used to predict what features of $SrTiO_3(111)$ surfaces are conducive to strong Na interactions by comparing calculations of the (2×2) and (3×3) reconstructions. These calculations demonstrated that adsorption strength is greater when Na is coordinated by a larger number of TiO_x units, and that coordination by $TiO_5[]$ units produces stronger adsorption than TiO_4 units. The reason seems to be that an outermost layer of TiO_4 units on $SrTiO_3(111)$ allows the surface to acquire more bulk like oxidation states and bonding, which takes the expression of Ti and O BVS values closer to +4 and -2, as well as lower Ti 3d and O 2p energy levels. The lack of TiO_4 units for the single-layer (2×2) reconstruction hence seems to yield more reactive O 2p orbitals that interact more strongly with Na. This many be understood firstly by the more bulk-like coordination environments TiO_4 units provide for the layer beneath, and secondly by the inert nature of TiO_4 units themselves. TiO_4 should namely have more rigid Ti-O bonds than $TiO_5[]$ due to the dependence of bond strength on bond length and the lower number of Ti-O bonds. TiO_4 units should thus be less prone than $TiO_5[]$ to redistribute charge as to adapt a lower energy configuration in response to Na bonding. One may thus hypothesise that the very clear Na preference for the $(6\times6)B$ surface could be due to this surface having a high density of unsaturated O valence orbitals resulting from a low density of TiO_4 units, which produces a high surface energy that may be lowered by Na adsorption. The reason why (5×5) is the least preferred reconstructions for Na adsorption should, similarly, be due to a lower surface energy than $(6\times6)A$, $(6\times6)B$, and (4×4), perhaps due to a high density of TiO_4 units that allows for more bulk-like bonding than other reconstructions.

Unlike the $0 < 0.1$ ML Na coverage, $1.0 < 2.0$ ML Na transforms the structure of the $SrTiO_3$ substrate following annealing. The result of this transformation is dependent on the reconstruction prior to Na exposure. In the case of Na on (5×5), the original

reconstruction returns after annealing to 800 ^oC, albeit with a significant presence of three types of defects; unit cell deep holes, triangular cavities where half a (5×5) unit cell is missing, and amorphous domains. Holes and cavities were observed also for Na and Li on $SrTiO_3(001) - c(4\times2)$ in Chapter 5 and 6, respectively, where holes are equivalent to small enclosures of step edge and the cavities are equivalent to the removal of a few TiO_x units. It is reasonable to assume that holes and cavities are produced by a similar process on (111) and (001), which were already been treated in Chapters 5 and 6, and will for this reason only be summarised in brief here. Cavities are proposed to result from a group of TiO_x units being destabilised and thus dissolved by Na causing O over-coordination. One may thus say that Na etches the surface to create the cavities, which in turn produces sites with low O coordination and thus strong Na adsorption. Holes are proposed to result from step edges constituting preferential adsorption sites for Na due to lower O coordination, which allows them to be stabilised by Na step edge decoration. It is, furthermore, a reasonable suggestion that holes are initially produced from cavities, because the smallest holes are comparable to cavities in size, which is most evident in Figure 73b. This indicates that holes may evolve from cavities, which could occur by additional Na attachment to already existing cavities, leading to further TiO_x unit group dissolution and growth into a hole, perhaps with the excess TiO_x material rejected onto the surface to produce the amorphous regions. This hole formation process would be fundamentally equivalent to the one proposed for Na on $SrTiO_3(001)$ in Chapter 5, where it was postulated that Na etches away areas of the outermost TiO_2 layer, which then grow into step edge holes.

XPS data for 2.0 $<$ 4.0 ML Na on $SrTiO_3(111)$ annealed to 600 ^oC demonstrate the influence of annealing temperature on the chemical environments in the surface region. Importantly, the Na 1s signal is absent in the annealed sample, which should be related to the disappearance of Na from the surface at elevated annealing temperatures observed in STM. This absence is proposed to be due to either intercalation or desorption, as mentioned in Chapters 5 and 6. For the purpose of analysing surface structure transformations, such as the formation of $(5\times5)\gamma$, the exact nature of the mechanism behind the enhanced reduction at elevated temperatures is less important than the confirmation that such a mechanism exists at all. It is, nonetheless, appropriate to conduct an analysis aimed at identifying what mechanism most likely underlies the enhanced reduction. In this

analysis, intercalation and desorption will be considered and compared using the available XPS data. These data show that the colder side of this sample has little Ti reduction, with circa 94% of the Ti 2p signal stemming from Ti^{4+}. This percentage decreases to 72% in the middle and 48% at the hotter side of the sample as the Ti^{3+} and Ti^{2+} signals become more prevalent with increased effective annealing temperature. As the degree of Ti reduction increases, the valence band sees an increasing portion of non-bonding states and the growth of a band gap state, which DFT indicates is of Ti 3d character. This increased degree of Ti reduction with annealing temperature cannot simply be due to the elevated temperature, because $SrTiO_3$(111) samples prepared by annealing to 1100 ^oC showed no detectable reduced Ti signal prior to Na exposure, as can be seen in Figure 78. The observed reduction of $SrTiO_3$(111) is thus causally dependent on Na exposure.

Intercalation readily offers an explanation for these XPS observations since an increase in reduction is expected from intercalation, mainly for two reasons. Firstly, bulk O atoms do not suffer from under-coordination like surface O atoms do, which makes them less prone to accepting electrons from Na. Secondly, bulk atoms are more electronically rigid than surface atoms, as they are less free to change bond lengths, angles, degree of covalency, et cetera, meaning they have fewer mechanisms by which they can accommodate electron density from Na. Intercalated Na atoms, which are expected to bond to O atoms at interstitial sites, would consequently be more likely to transfer electrons to Ti 3d than surface Na atoms. This charge transfer would reduce Ti atoms and decrease the amount of Ti-O bonding, thus also increasing the fraction of non-bonding states in the valence band. When assessing the likelihood of desorption being the mechanism behind the elevated reduction, one must remember that this phenomenon entails not only single Na atoms desorbing from adsorption sites, as would be the case if they were to decorate step edges as proposed, but also sublimation of Na-based nanoparticles. It can be known within reasonable doubt that if desorption takes place, it cannot take the form of pure Na atoms. This is because reduction is caused interaction with Na atoms, as discussed above, so the loss of Na atoms would contradict the enhanced reduction observed. An enhancement in reduction is, on the other hand, consistent with desorption in the form of NaO_x sublimation. If Na leaves the sample, e.g. via Na_2O sublimation[213], this could drive Ti reduction because O atoms in some Na_2O units would also bond Ti atoms. The surface would thus

be deprived of O, which at the 600 ^oC annealing temperature in question would be likely to drive O vacancy formation in the surface region to lower surface energy and equilibrate O chemical potential. Both Na intercalation and Na_2O sublimation may thus qualitatively explain enhanced reduction at elevated annealing temperature. The available data do not allow for a conclusive statement of what mechanism is at work, however, by comparing the physics of intercalation and sublimation, one may propose the more likely candidate. This mechanism would, in particular, have greater explanatory power from a quantitative perspective, meaning that it could account for the evolution of XPS peak areas as effective annealing temperature increases from the colder side of the sample to the hotter.

The Na 1s peak signal will be considered first, which is so weak across the entire the sample that it cannot be used to confidently demonstrate the presence of Na at all. This is somewhat puzzling since the degree of Ti reduction is an order of magnitude greater on the hotter side than the colder side of the sample. If Na is truly absent, this difference in Ti reduction is extremely difficult to explain, meaning that Na most likely is present but in such low quantity that its peak area is comparable to fluctuations in the background noise. One might, at first glance, expect this lack of a discernible Na signal to support sublimation, because a discernible Na signal is expected in the case of intercalation, especially at the hotter side where reduction-inducing intercalated Na would be protected from the environment. If sublimation occurs, however, then the stark increase in Ti reduction would be concurrent with a decrease in the Na signal, meaning that Na is expected to still be present in the middle and especially colder side of the sample where less reduction has occurred. The consequence of this line of reasoning for the intercalation versus sublimation discussion is that neither mechanism is supported by the absent Na signal. Considering next the Ti 2p signal, which experiences a dramatic increase in reduced Ti from 6% at the colder side of the sample to 48% at the hotter side. A crucial difference in the physics of intercalation compared to sublimation is that reduction by sublimation is caused by O vacancies, whereas reduction by intercalation is not. This fact works against sublimation, because O chemical potential equilibration will work to distribute O vacancies evenly throughout the substrate. It is thus difficult to explain how as much as 48% of Ti atoms in the XPS signal could be reduced by sublimation, because this would require a high concentration of O vacancies in the surface region within a few

nm of the surface (as discussed in Chapter 3). The underlying bulk has an effectively inexhaustible supply of O atoms from the perspective of the surface, meaning that O chemical potential equilibration is expected to fill those vacancies until a steady state is achieved. Intercalation, on the other hand, offers a mechanism by which reduction can be anchored to the surface region if alkali metal insertion is surface limited, which it could be e.g. due to the strain associated with interstitial alkali atoms restricting their migration into the bulk. Lastly, a brief comment on the O 1s peak is in order. Since the sample was atmospherically exposed prior to the XPS experiment, the O peak carries a high degree of uncertainty and must be used with greater caution in a stoichiometric analysis. However, it should be mentioned that O/Ti raw peak area ratios show no notable decrease from the colder side of the sample to the middle and hotter side. Instead, the O/Ti raw peak area ratios increase by 1% and 10% at the middle and hotter side of the sample with respect to the colder side. This increase coincides with a small increase in the C 1s signal by 4% and 13%, respectively, which could explain the increase in O by a higher concentration of C- and O-containing contaminants. If surface region O vacancies were responsible for the enhanced Ti reduction, one may reasonably expect at least a decrease in the O/Ti peak area ratios, despite the contamination-related uncertainties introduced by atmospheric exposure. Summa summarum, this quantitative analysis concludes that with respect to the intercalation versus sublimation discussion, the Na 1s peak is indifferent, the Ti 2p peak has a weak preference for intercalation, and the O 1s peak does not favour sublimation. This analysis thus proposes that intercalation is more likely than sublimation to be the mechanism responsible for the increased Ti reduction at elevated annealing temperatures.

In the case of $1.0 < 2.0$ ML Na on $(6\times6)+(4\times4)$, annealing transforms the surface to the reconstruction named $(5\times5)\gamma$. This reconstruction is not present on any $SrTiO_3(111)$ surface prior to Na exposure and thus likely forms in reductive conditions. A reasonable hypothesis is therefore that as the degree of reduction increases, there is a critical O chemical potential μ_O^* where the $(5\times5)\gamma$ attains a lower free energy G_γ than the original $(6\times6)+(4\times4)$ reconstructions, G_0, i.e. $\Delta G = G_\gamma(\mu_O^*) - G_0(\mu_O^*) < 0$. The absence of $(5\times5)\gamma$ on the surface that originally was (5×5) may additionally constitute another argument for (5×5) having a particularly low surface energy, as this surface induces energetically costly defects instead of transforming. As revealed in Figure 74 and as shall be further explored

in Chapter 8, $(5\times5)\gamma$ is also produced by Li exposure at elevated annealing temperatures. This necessitates a discussion about whether this reconstruction incorporates alkali metals into its surface unit cell. Two different chemistries producing structurally indistinguishable surfaces may seem unlikely, but this possibility cannot be dismissed. Since the ionic radii of Na^+ and Li^+ are similar, 0.1-0.14 nm and 0.06-0.09 nm, respectively[212], they may be able to fit into the same site in the $(5\times5)\gamma$ surface unit cell. There are, however, two arguments for why the alkali metals are unlikely to partake in the $(5\times5)\gamma$ surface unit cell. Firstly, as discussed in Chapter 6, DFT calculations show that Li forms substantially more covalent O bonds on $SrTiO_3$ surfaces than Na, so even if both alkali ions could fit the same surface site, their bonding symmetries and electron density distributions would likely be too different to stabilise the same exact surface unit cell. Secondly, it was observed also on $SrTiO_3(001)$ that both Na and Li produce the same high-T surface at similar temperatures to $(5\times5)\gamma$. This indicates that rather than the special case of different surface chemistries producing the same surface structure manifesting on both (001) and (111), there is likely a more general underlying phenomenon, such as intercalation driven reduction. It will consequently be proposed that alkali metals are not incorporated into either $(5\times5)\gamma$ or the high-T surface, but rather, these surfaces form due to the enhanced surface region reduction that ensues at elevated annealing temperature.

7.7 Conclusion

Na does not change the structure of the $SrTiO_3(111)$ reconstructions (4×4), (5×5), $(6\times6)A$, or $(6\times6)B$ at coverages below 0.3 ML and preferentially adsorbs on $(6\times6)B$. DFT calculations indicate that this may be due to $(6\times6)B$ lacking TiO_4 units, which makes O 2p orbitals more reactive with Na and thus allows for a greater surface energy decrease through Na adsorption. At a coverage of $1.0 < 2.0$ ML, Na does not wet the surface, but forms nanoparticles and films with the $SrTiO_3(111)$ substrate being visible after annealing to 500 ^oC. Following 800 ^oC annealing, the pre-Na deposition reconstruction is restored in areas that were dominated by (5×5), but with a significantly elevated defect density. Defects are predominantly half-unit cell sized triangular cavities and step edge holes, which are proposed to form by Na etching and to be stabilised by producing preferential Na bonding sites. In areas dominated by $(6\times6)+(4\times4)$, the surface is transformed to a new reconstruction referred to as $(5\times5)\gamma$. It is proposed that $(5\times5)\gamma$ is

stabilised by the increased O chemical potential that results from a mechanism that drives enhanced reduction at annealing temperatures above 600 ^oC, as evidenced by XPS data. It was, furthermore, proposed that this mechanism specifically is intercalation, which is suggested to enhance reduction as the more restrictive coordination environments of the bulk compared to the surface make electronic states in the bulk more rigid, thus forcing charge transfer from Na to Ti. The enhanced reduction mechanism could alternatively be Na_2O sublimation, but it was deemed less probable than intercalation based on a quantitative analysis of the XPS data. XPS data, furthermore, demonstrate the presence of band gap states that DFT calculations indicate are of Ti 3d character.

8 Li on $SrTiO_3(111)$

8.1 Introduction

This chapter treats the response of $SrTiO_3(111)$ to Li deposition. The reconstructions used for this investigation were introduced in Chapter 7, to which the reader is referred for details on their structure. The STM data of this chapter includes $0 < 0.1$ ML and $1.0 < 2.0$ ML Li coverages, thus omitting the $0.1 < 0.3$ ML deposition present in previous chapters. This is because the $0 < 0.1$ ML deposition produced a sufficiently rich data set to be considered representative of Li on $SrTiO_3(001)$ at the low deposition limit. Three new reconstructions were observed during the course of the Li-on-$SrTiO_3$ experiments, one for each of the (4×4), (5×5), and (6×6)A reconstructions. As shall be seen in Section 8.2.1, these new reconstructions maintain the periodicity of the original reconstructions from which they transformed, and will for this reason be called (4×4)δ, (5×5)δ, and (6×6)δ, collectively referred to as the δ reconstructions. The δ reconstructions play a prominent role throughout Section 8.2, and will for the sake of minimising nomenclature be referred to by these names also before their periodicities have been characterised.

8.2 Low Deposition

Three surfaces were used to study the $SrTiO_3(111)$ response to $0 < 0.1$ ML Li, namely (5×5), $(6\times6)A$ coexisting with (5×5), and $(6\times6)A$ coexisting with (4×4), all displayed in Figure 81.

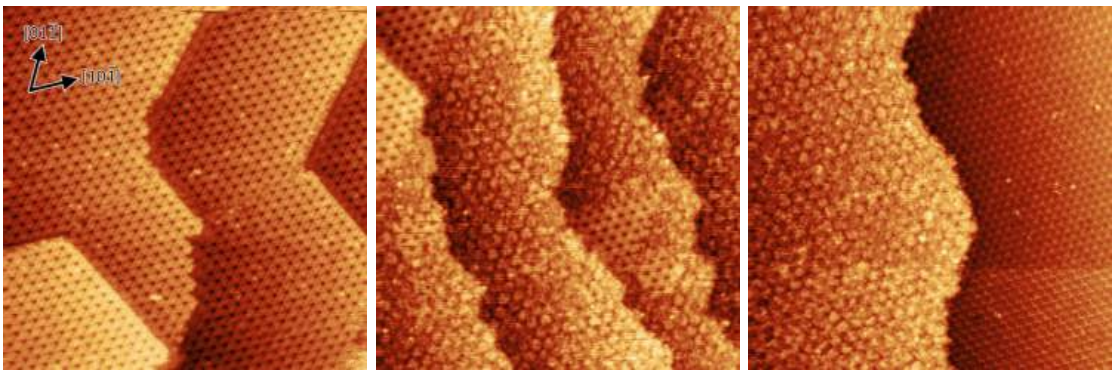

(a) *(b)* *(c)*

Figure 81: $SrTiO_3(111)$ surfaces onto which $0 < 0.1$ ML Li was deposited, showing a) (5×5) (U=1.6 V, I=0.08 nA, $80\times80\,nm^2$), b) $(6\times6)A + (5\times5)$ (U=1.6 V, I=0.08 nA, $80\times80\,nm^2$), and c) $(6\times6)A + (4\times4)$ (U=1.6 V, I=0.08 nA, $80\times80\,nm^2$). The step edge height in a) is 0.23 ± 0.03 nm and in b) 0.24 ± 0.02 nm.

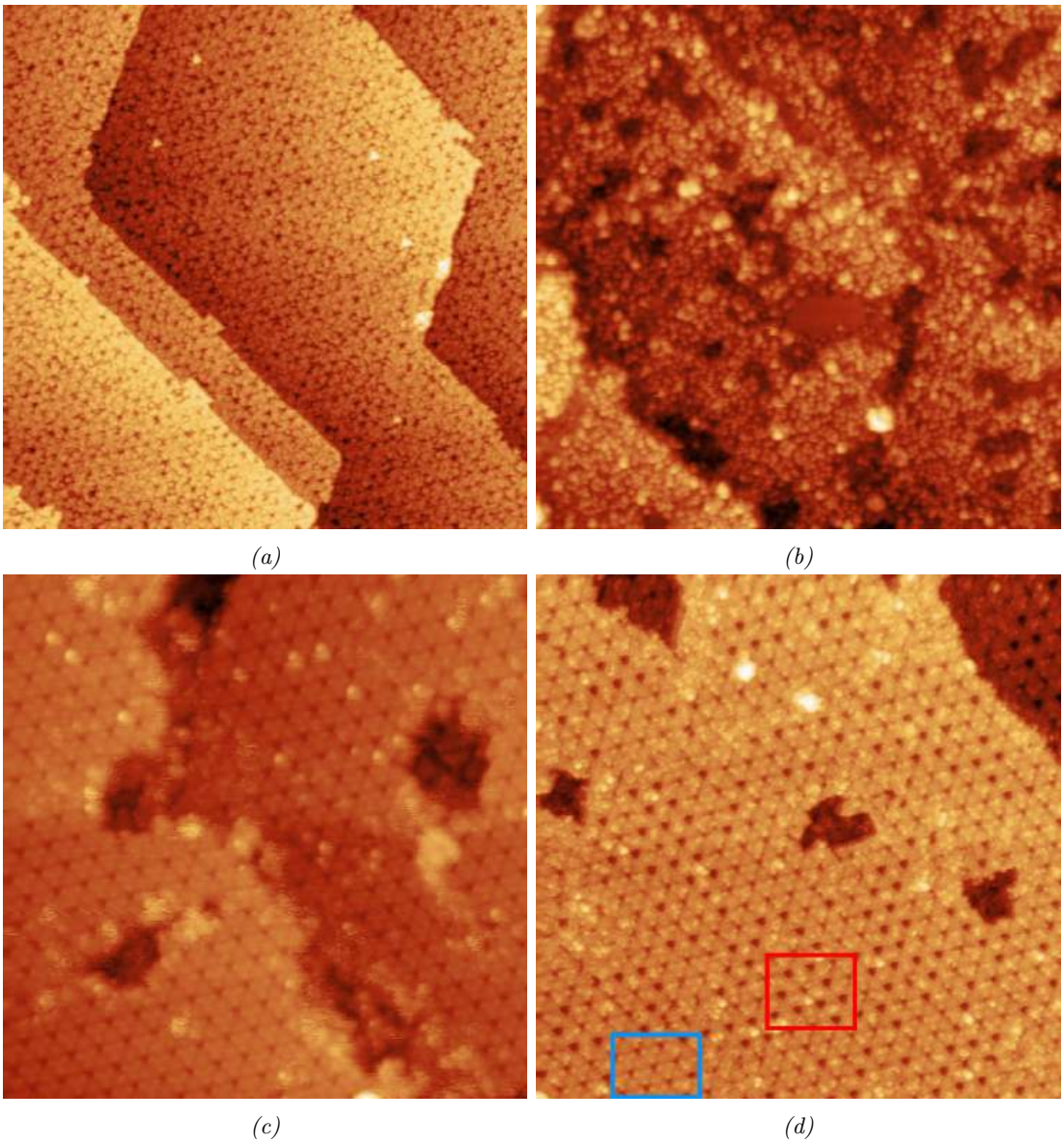

Figure 82: Surfaces produced by $0 < 0.1$ *ML Li deposition onto* $SrTiO_3(111)-(5\times5)$ *after annealing temperatures of a) 400 °C (U=1.5 V, I=0.1 nA,* $100\times100\,nm^2$*), b) 600 °C (U=1.6 V, I=0.08 nA,* $100\times100\,nm^2$*), c) 700 °C (U=1.2 V, I=0.1 nA,* $50\times50\,nm^2$*), and d) 800 °C (U=1.6 V, I=0.12 nA,* $60\times60\,nm^2$*). a) shows the* $(5\times5)\delta$ *surface, b) shows a region containing a so-called flat lake, and c) shows the* $(5\times5)\gamma$ *surface, and d) shows a mixed* $(5\times5)+(5\times5)\gamma$ *surface. The holes in d) have a mean depth of* 0.25 ± 0.02 *nm, and the* (5×5) *and* $(5\times5)\gamma$ *reconstructions are marked by the red and blue rectangles, respectively. The presence of these two reconstructions in the same image confirms that they are indeed structurally different and not the same reconstruction under different imaging conditions.*

The response of the originally (5×5) surface to $0 < 0.1$ ML Li and 400-800 ^oC annealing can be seen in Figure 82. After 400 ^oC the entire surface has been transformed to $(5\times5)\delta$, which is presented in Figure 82a and will be treated in greater detail in Figure 83b. 600 ^oC annealing produces the surface shown in Figure 82b, with no apparent order and severe unevenness. This surface does, however, contain one significant feature, namely the flat

region in the middle of the image. This feature will be referred to as a "flat lake" and has a greater presence in the originally $(6\times6)+(5\times5)$ surface displayed in Figure 83d. Following 700 ^oC annealing, the $(5\times5)\gamma$ surface characterised in Chapter 7 dominates the surface, as can be seen in Figure 82c. This reconstruction is still present after 800 ^oC annealing, but now shares the surface with the original (5×5), as can be seen in Figure 82d.

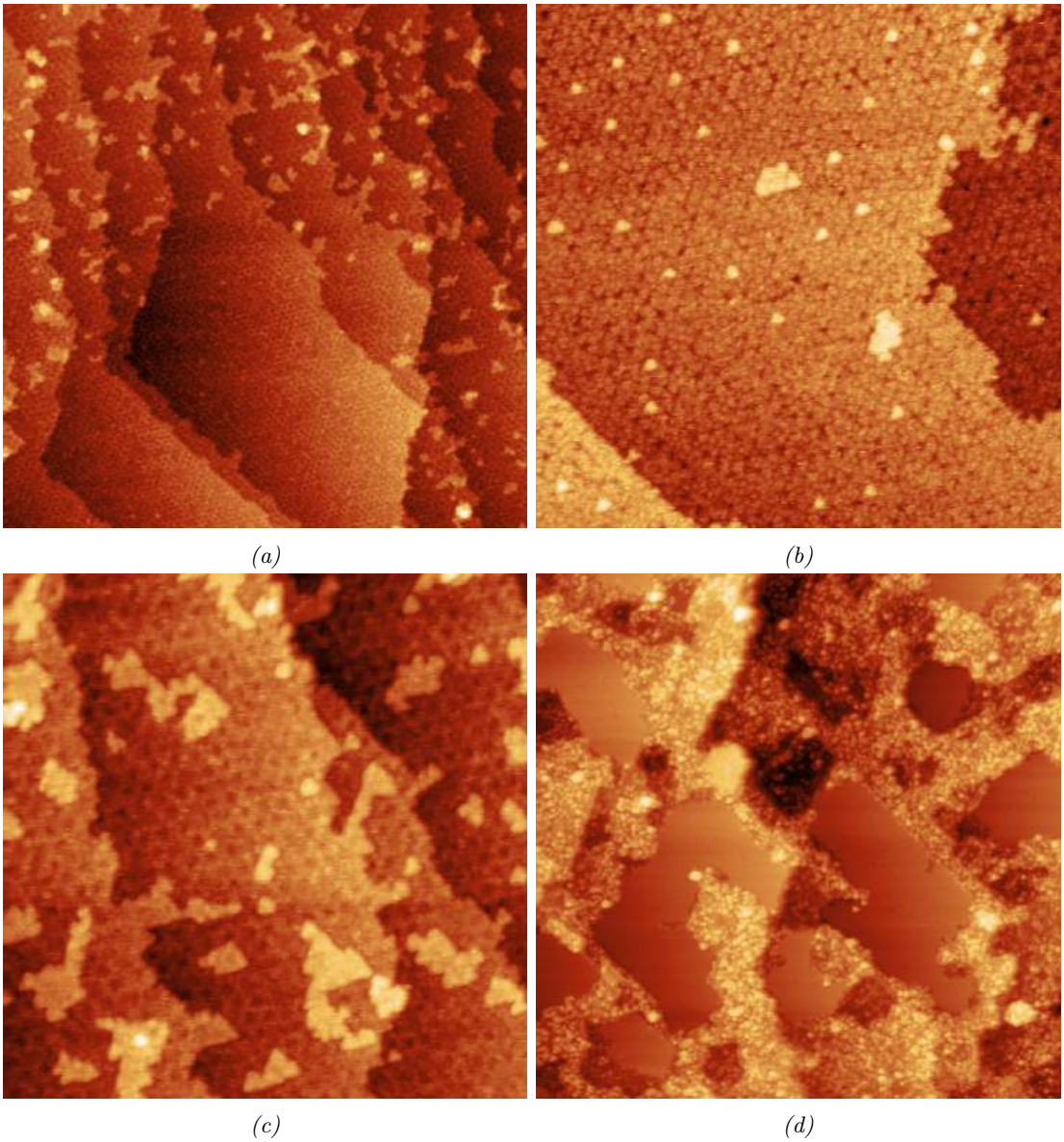

Figure 83: Surfaces produced by $0 < 0.1$ *ML Li deposition onto* $SrTiO_3(111)-(6\times6)+(5\times5)$ *after annealing temperatures of a) 400 °C (U=1.8 V, I=0.1 nA,* $200\times200\,nm^2$*), b) 500 °C (U=1.6 V, I=0.06 nA,* $80\times80\,nm^2$*), c) 400 °C (U=1.6 V, I=0.06 nA,* $80\times80\,nm^2$*), d) 600 °C (U=1.6 V, I=0.06 nA,* $150\times150\,nm^2$*). a) shows domains of both* $(5\times5)\delta$ *and* $(6\times6)\delta$ *surfaces, with higher resolution images of* $(5\times5)\delta$ *displayed in b) and of* $(6\times6)\delta$ *displayed in c). The smaller variation of nanoparticles in b) have a height of* 0.27 ± 0.04 *nm and mean width of* 1.71 ± 0.18 *nm, and the islands in c) have mean height of* 0.24 ± 0.05 *nm. d) shows a region where the flat lakes occupy circa half the surface.*

The originally $(6\times6)+(5\times5)$ surface acquires two distinct domains, one with a high density of amorphous nanoislands up to 20 nm in diameter and one without, as per Figure 83a. The one without nanoislands is the already introduced $(5\times5)\delta$ surface. Figure 83b shows that $(5\times5)\delta$ hosts small triangular nanoparticles 1.5-2.0 nm in diameter, seemingly lacks long-range order and can be distinguished from other reconstructions by the presence of black spots scattered across the surface. The surface containing nanoislands is $(6\times6)\delta$, which is also shown in Figure 83c. This surface does have long-range order, which is generated by a lattice of troughs. Nanoparticles in 83b and nanoislands in 83c both have a height of circa 0.25 nm, indicating monolayer height. Notably, $(5\times5)\delta$ is present after Li deposition and annealing for both the originally (5×5) and (6×6)+(5×5) surfaces, whereas $(6\times6)\delta$ is not. One may thus reasonably deduce that $(5\times5)\delta$ should be generated from the reconstruction that is common to both these initial surfaces, i.e. (5×5). Similarly, $(6\times6)\delta$ should be generated from the reconstruction that the initial surfaces do not have in common, i.e. (6×6). This implies that the new reconstructions have conserved the periodicities of the ones from which they transformed.

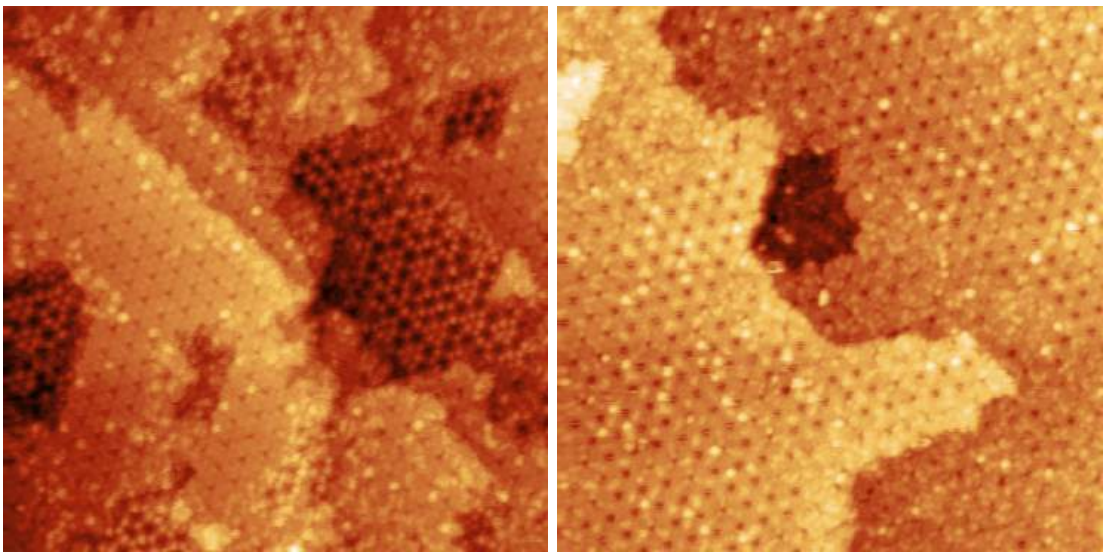

(a) *(b)*

Figure 84: Surfaces produced by $0 < 0.1$ *ML Li deposition onto* $SrTiO_3(111)-(6\times6)+(5\times5)$ *after an annealing temperatures of a) 700 °C (U=1.2 V, I=0.15 nA,* $60\times60\,nm^2$*) and b) 800 °C (U=1.6 V, I=0.06 nA,* $60\times60\,nm^2$*).*

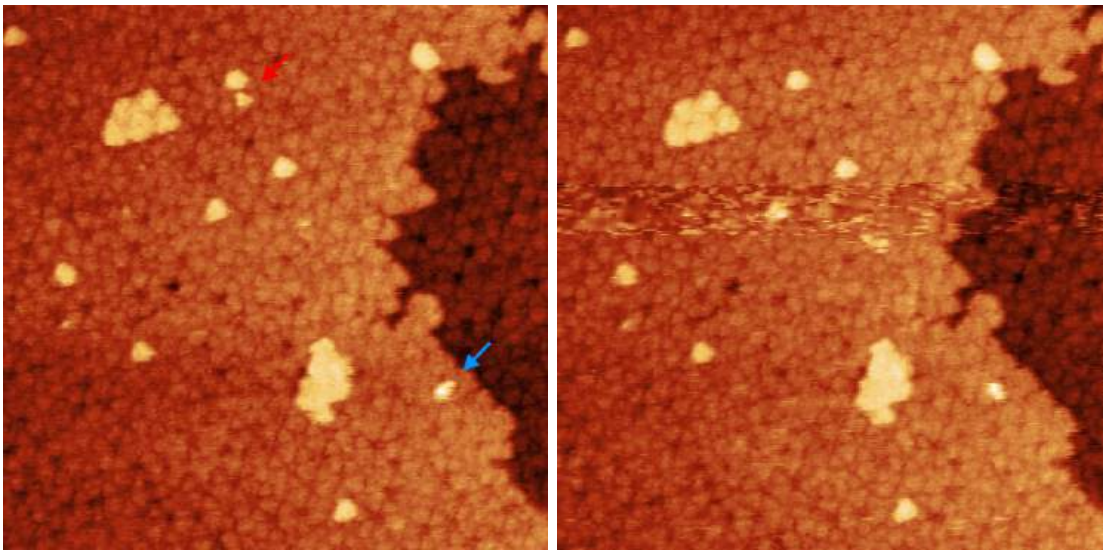

(a) *(b)*

Figure 85: Nanoparticle movement on $(5\times5)\delta$ *between two adjacent STM scans after 400* ^oC *annealing (U=1.6 V, I=0.06 nA,* $50\times50\,nm^2$*). The blue arrow in a) indicates a nanoparticle that rotates from alignment with* $[10\bar{1}]$ *to* $[\bar{1}10]$*, and the red arrow in a) indicates a nanoparticle that departs.*

600 ^oC annealing induces a radical transformation of the surface the result of which is shown in Figure 83d. This surface is similar to the one produced after 600 ^oC annealing of the originally (5×5) reconstructions shown in Figure 82b, however, the flat lake regions now cover a considerably larger fraction of the surface. These flat lakes will be given a thorough discussion and attempted characterisation in Section 8.2.2. Figure 84a shows the result of 700 ^oC annealing, where the $(5\times5)\gamma$ reconstruction is once more generated, this time accompanied by domains of a short-range quasi-periodic (2×2) ordering, characterised by dots with a strong tendency to form linear and triangular arrangements. 800 ^oC annealing transforms this surface to the one in Figure 84b, where the original (5×5) and $(5\times5)\gamma$ seem to coexist, as they did for the surface that was originally (5×5) after this annealing temperature. A notable aspect of Li on $SrTiO_3(111)$ is a high degree of Li mobility, which is evidenced in Figure 85. Figures 85a and 85b display two images acquired in adjacent STM scans, between which nanoparticles have moved considerably. The nanoparticle indicated by the blue arrow rotates to change its epitaxially alignment with the substrate, and the one indicated by the red arrow is absent in the next scan.

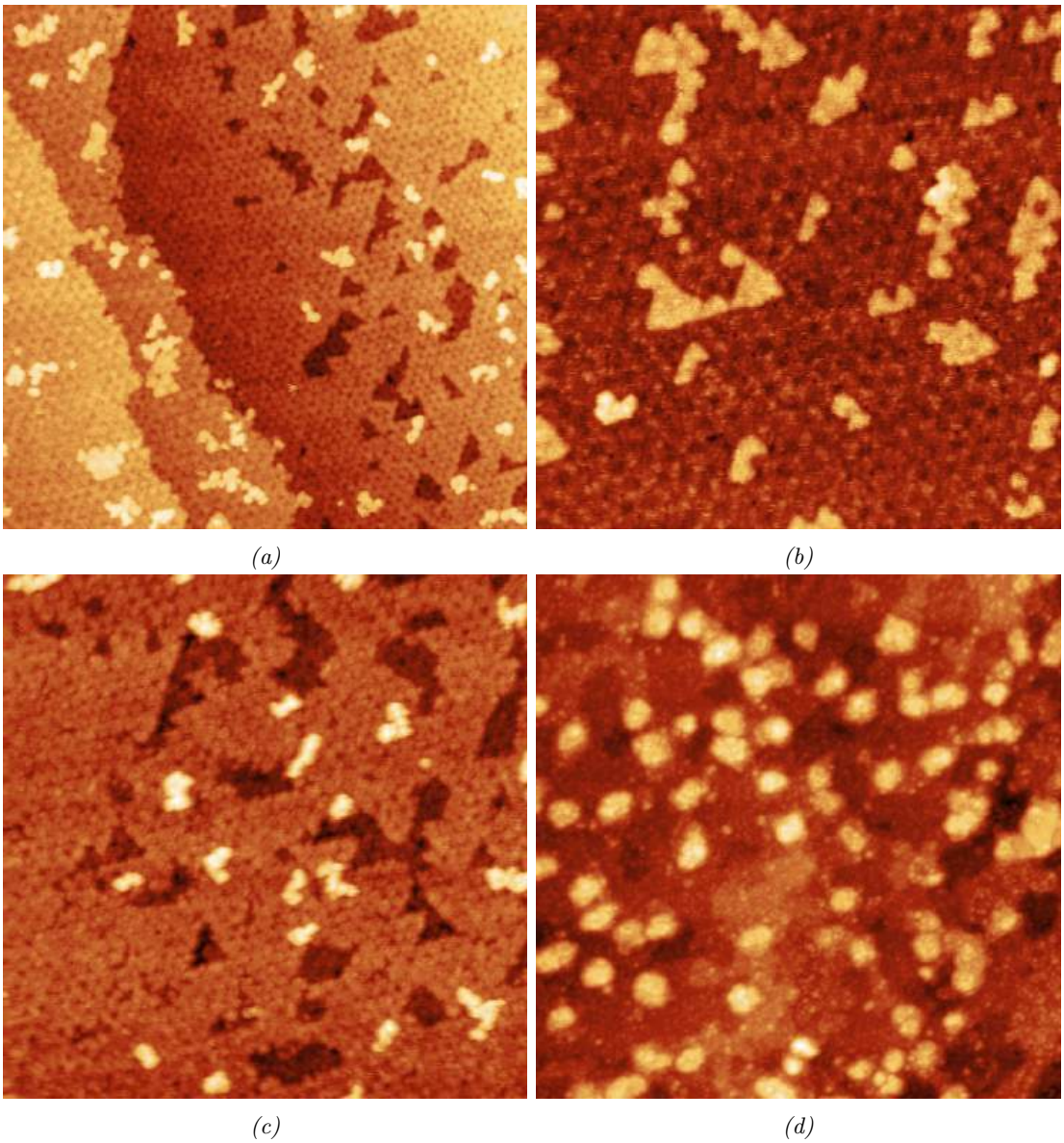

Figure 86: Surfaces produced by $0 < 0.1$ *ML Li deposition onto* $SrTiO_3(111) - (6\times6) + (4\times4)$ *after annealing temperatures of a) 500 °C (U=1.8 V, I=0.08 nA,* $120\times120\,nm^2$*), b) 500 °C (U=1.2 V, I=0.1 nA,* $60\times60\,nm^2$*), c) 400 °C (U=1.2 V, I=0.08 nA,* $80\times80\,nm^2$*), and d) 600 °C (U=1.4 V, I=0.1 nA,* $150\times150\,nm^2$*). Nanoparticles in b) have a mean height of* 0.26 ± 0.03 *nm, whereas nanoparticles in c) have a mean height of* 0.51 ± 0.07 *nm. Holes in c) have a mean depth of* 0.29 ± 0.03 *nm.*

The surface that was originally $(6\times6)+(4\times4)$ generates the surfaces displayed in Figure 86a following $0 < 0.1$ ML Li deposition and 400-500 ^oC annealing. This surface contains two domains; the $(6\times6)\delta$ reconstructions treated above, as well as one characterised by holes, which is the $(4\times4)\delta$ reconstruction. Close-up images of $(6\times6)\delta$ and $(4\times4)\delta$ are displayed in Figures 86b and 86c, respectively. Nanoparticles on $(4\times4)\delta$ have a mean height of circa 0.50 nm and holes have a mean depth of circa 0.25 nm, indicating that

the former likely consists of a double layer and the latter has a depth of one $SrTiO_3(111)$ interplanar spacing. The holes in $(4\times4)\delta$ are hence unit cell deep, making them similar to the holes observed in Chapters 5 and 7. The presence of $(6\times6)\delta$ after Li deposition and annealing for both the originally $(6\times6)A+(5\times5)$ and $(6\times6)A+(4\times4)$ surfaces provides further evidence that it was specifically the $(6\times6)A$ reconstruction that transformed into $(6\times6)\delta$. One may similarly deduce that (4×4) most probably gave rise to $(4\times4)\delta$. As for the originally (5×5) and $(6\times6)A+(5\times5)$ surfaces, 600 ^oC annealing causes a radical transformation to produce a disordered surface, which is shown in Figure 86d. This time, no flat lakes are present. 700 ^oC annealing introduces some order to the surface in the form of areas of the quasi-periodic (2×2) ordering displayed in Figure 87a. 800 ^oC annealing once more reproduces a reconstruction that was present prior to Li deposition, this time (4×4), as can be seen in Figure 87b.

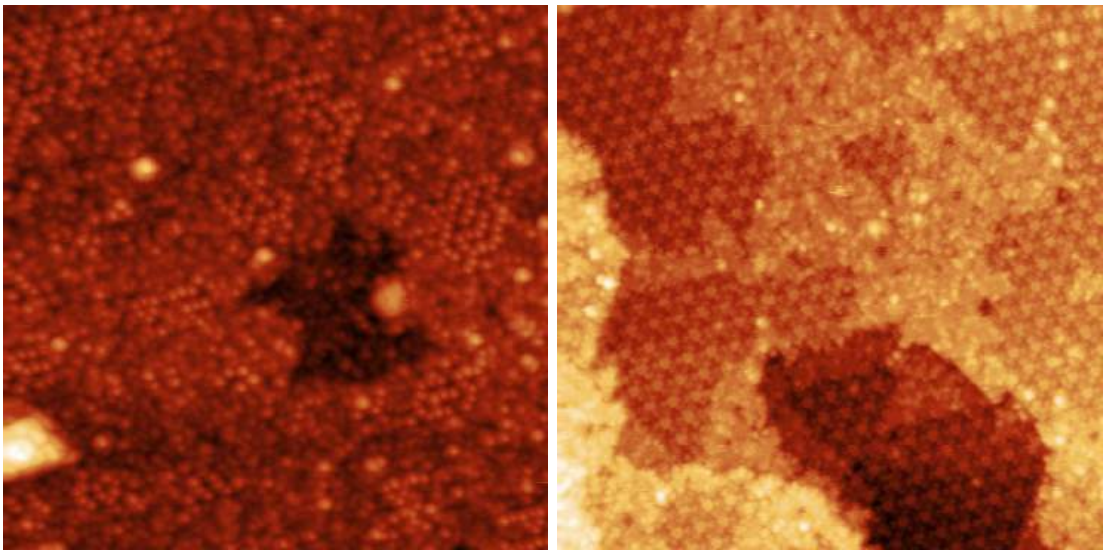

(a) *(b)*

Figure 87: Surfaces produced by $0<0.1$ *ML Li deposition onto* $SrTiO_3(111)-(6\times6)+(4\times4)$ *after annealing temperatures of a) 700 ^oC (U=1.2 V, I=0.06 nA,* $60\times60\,nm^2$*) and b) 800 ^oC (U=1.6 V, I=0.08 nA,* $50\times50\,nm^2$*).*

There are notable differences in the density and morphology of the nano-sized structures that form on the $(4\times4)\delta$, $(5\times5)\delta$, and $(6\times6)\delta$ reconstructions. It is, first of all, worth noting that these structures most likely are Li-based nanoparticles as opposed to protruding $SrTiO_3$ islands. This is clear for small nanoparticles, as evidenced by their mobility on $(5\times5)\delta$ in Figure 85. Larger nanoparticles, furthermore, have surface structures different from the $SrTiO_3(111)$ substrate beneath, and have distinctly different mean heights on

$(6\times6)\delta$ and $(4\times4)\delta$, which indicates that they too are Li-based nanoparticles. There is also reason to believe that Li decorates step edges, which is evidenced by the holes in the $(4\times4)\delta$ reconstructions for the same reason as discussed in Chapters 5 and 7 with regard to step edge decoration and its stabilisation of unit cell deep holes.

8.2.1 Reconstruction Characterisation

Figures 88 and 89 display the four new surface structures induced by $0 < 0.1$ ML Li coverage and annealing, where black lines indicate directions along which periodicities were measured. $(6\times6)\delta$ and $(4\times4)\delta$, shown in Figures 88a and 88b, respectively, have long-range order and therefore easily identified periods. The $(5\times5)\delta$ of Figure 89a, on the other hand, only has short-range order, which is most clearly expressed by rows of triangles with indented boarders, for which reason this feature was measured to discern 5× periodicity. The quasi-periodic (2×2) ordering is shown in Figure 89b, which shows a tendency to arrange its constituent dots into lines as well as equilateral triangles with sides the length of one (4×) period along $SrTiO_3\langle01\bar{1}\rangle$, as indicated by the blue triangle in this image.

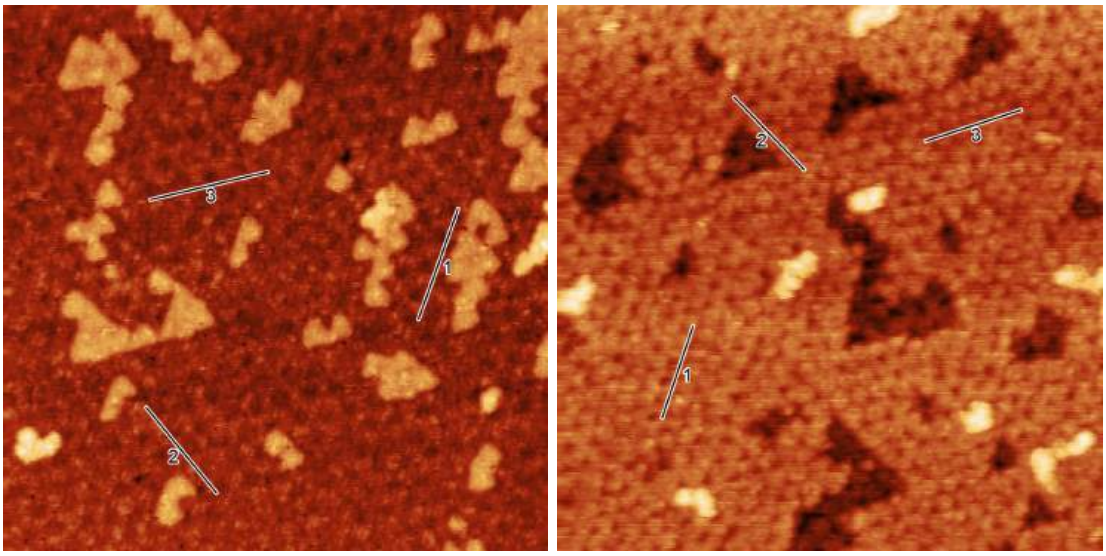

(a) *(b)*

Figure 88: Characterisation of a) (6×6)δ *(500 °C, U=1.6 V, I=0.08 nA,* $60\times60nm^2$*) and b)* (4×4)δ *(500 °C U=1.6 V, I=0.1 nA,* $60\times60\,nm^2$*). The periodicities along the* $SrTiO_3\langle01\bar{1}\rangle$ *directions as indicated by the black lines are a)* 5.78 ± 0.04 *and b)* 3.95 ± 0.10*, i.e. within 3% and 2% of* 6× *and* 4× *periodicities, respectively.*

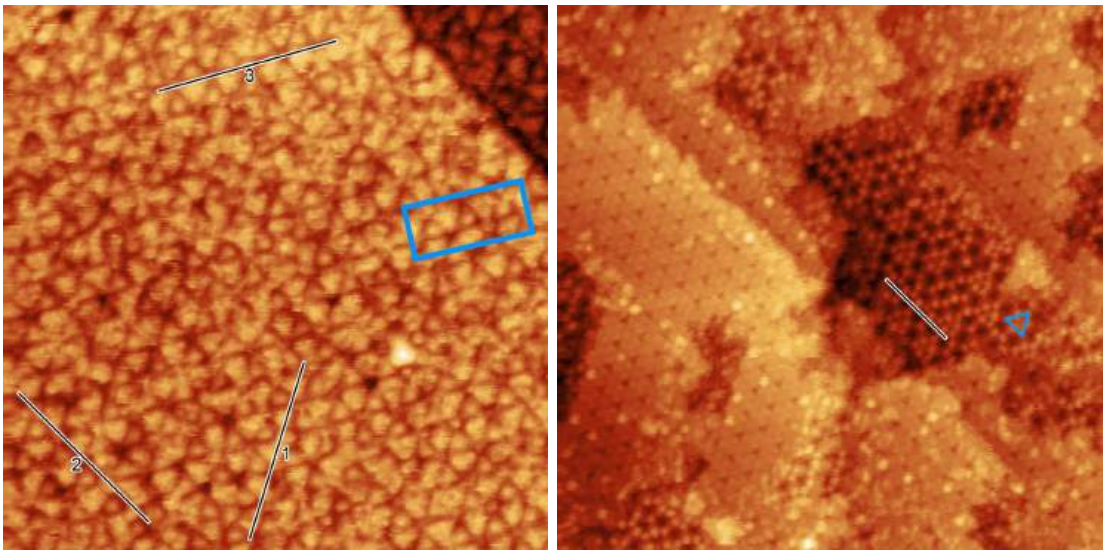

(a) *(b)*

Figure 89: Characterisation of a) $(5\times5)\delta$ *(400 °C, U=1.0 V, I=0.1 nA,* $40\times40\ nm^2$*) and b) the quasi-periodic* (2×2) *ordering. The image in b) was already presented in Figure 84a. The blue rectangle in a) marks an example of indented triangles aligning to create short-range order, which is the feature that was used to identify the periodicity of* $(5\times5)\delta$*. The periodicities along the* $SrTiO_3\langle01\bar{1}\rangle$ *directions as indicated by the black lines are in a)* 4.87 ± 0.05 *and b) 1.10 nm, i.e. within 4% and 1% of* $5\times$ *and* $2\times$ *periodicities, respectively. The blue triangle in b) marks an example of the dots of the quasi-periodic* (2×2) *ordering producing a triangular arrangement, which has sides the length of one* $(4\times)$ *period along* $SrTiO_3\langle01\bar{1}\rangle$*.*

8.2.2 Flat Lake Characterisation

Height profiles of the flat lakes confirm that they are indeed remarkably flat, as can be seen in Figure 90. Two areas of flat lakes are displayed in Figures 90a and 90b, where the lines indicate where the height profiles displayed in Figures 90c and 90d were measured. None of these height profiles deviate from the mean by more than 0.02 nm at any point, and none yields a standard deviation of more than 0.01 nm. The height distribution on the flat lakes thus seems to be within even the 0.06-0.09 nm[212] ionic radius of Li^+.

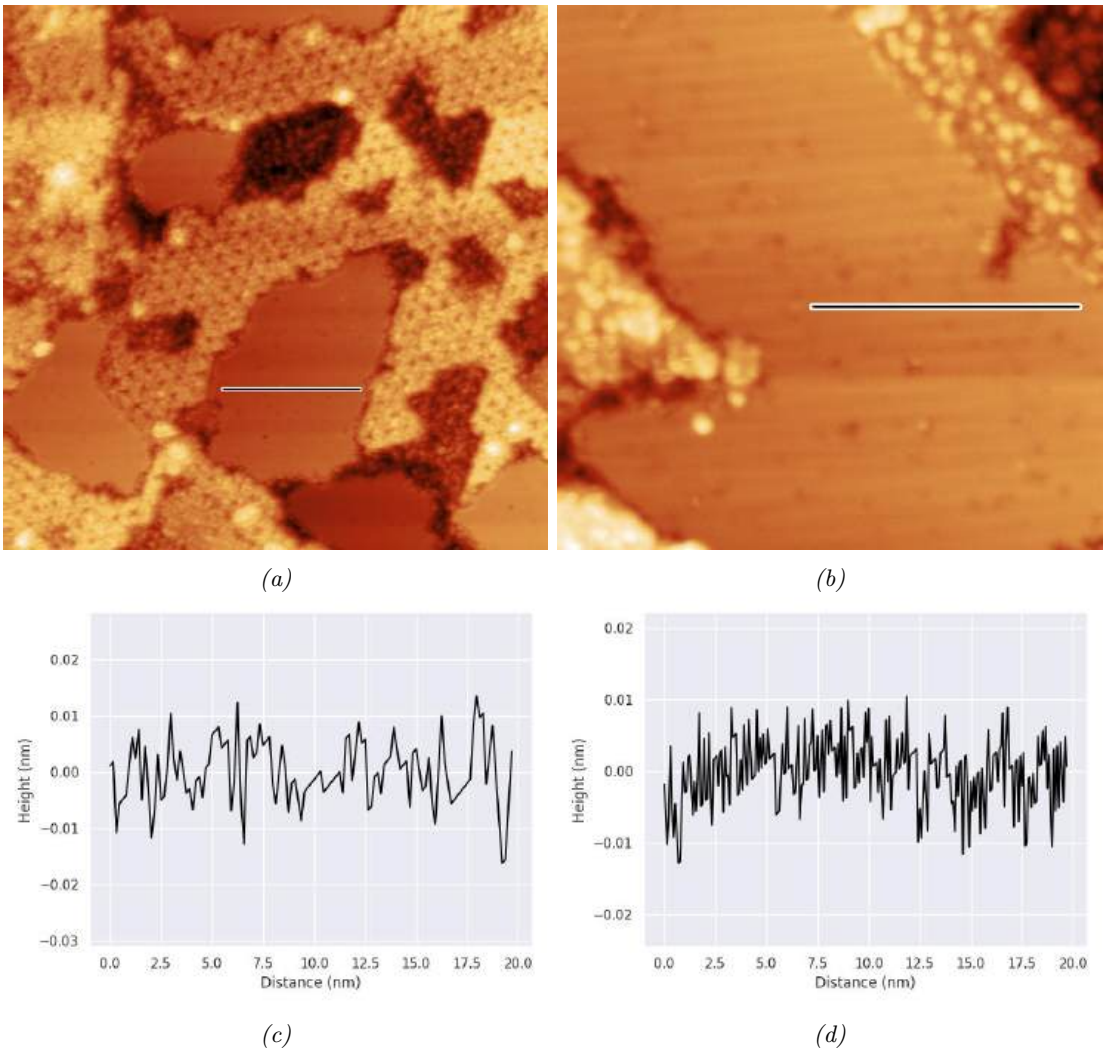

Figure 90: Characterisation of the flat lakes emerging in the $(6\times6)+(5\times5)$ *region after 600 °C annealing. a) (U=1.0 V, I=0.2 A,* $80\times80\,nm^2$*) and b) (U=0.8 V, I=0.1 A,* $40\times40\,nm^2$*) show two flat lake areas, where the black lines indicate the height profile shown in c) and d), respectively. The profile in c) has a minimum of -0.016 nm, maximum of 0.013 nm, and standard deviation of 0.006 nm, and the one in c) has a minimum of -0.016 nm, maximum of 0.013 nm, and standard deviation of 0.005 nm.*

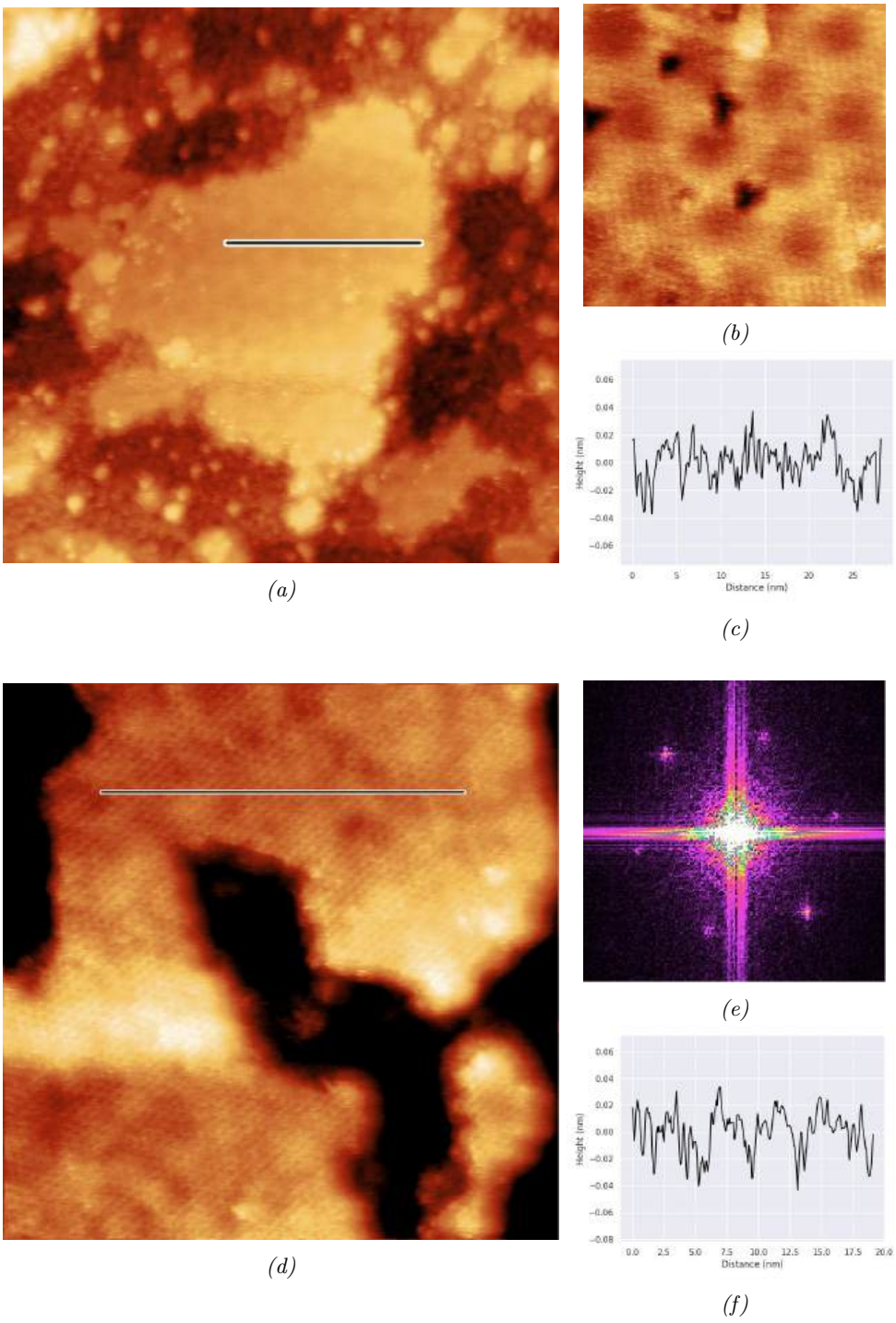

Figure 91: Data from the experiment reproducing the flat lakes by depositing $0 < 0.1$ *ML Li on* $SrTiO_3(111) - (5 \times 5)$ *and annealing to 600 °C. a) shows what appears to be a moiré pattern, indicated by the periodic and diffuse spots (U=2.0 V, I=0.075 nA,* $80 \times 80\ nm^2$*). b) shows the moiré pattern at greater resolution (U=0.6 V, I=0.3 nA,* $15 \times 15\ nm^2$*) (averaged over two images in SmartAlign). Dark spots in b) are aligned within* 5^o *of the* $\langle 11\bar{2} \rangle$ *direction of* $SrTiO_3(111)$ *and have a period of* 4.0 ± 0.04*. Considering the 0.96 nm length of a* $\langle 11\bar{2} \rangle$ *vector, the moiré pattern is within 5% of* $4\times$ *periodicity along* $\langle 11\bar{2} \rangle$*. It thus seem that this pattern has a surface unit cell equivalent to* $SrTiO_3(111) - (4 \cdot \sqrt{3} \times 4 \cdot \sqrt{3}) - R30^o$*. c) shows the height profile of the line in a), which has a minimum of -0.037 nm, maximum of 0.037 nm and standard deviation of 0.014 nm. d) shows an image indicating the presence of* (1×1) *periodicity by its FFT image in e) (U=0.5 V, I=0.3 nA,* $30 \times 30\ nm^2$*) (averaged over 6 images in SmartAlign). FFT points in e) are found at angles* $2.9^0 \pm 2.1^o$ *to* $\langle 01\bar{1} \rangle$ *and have a periodicity of* 0.50 ± 0.02 *nm, thus circa 10% smaller than the periodicity of* $\langle 01\bar{1} \rangle$*. f) shows the height profile associated with the line in d), which has a minimum of -0.043 nm, maximum of 0.034 nm and standard deviation of 0.015 nm.*

The extraordinary topography of the flat lakes prompted an experiment to reproduce them, the key results of which are displayed in Figure 91. The flatness of the previously observed lakes was reproduced, as can be seen in Figures 91a and 91d and their associated height profiles in Figures 91c and 91f. The height distributions measured in these images are within a span of 0.04 nm and have standard deviations of 0.02 nm. There are two more important flat lake features that were revealed in these experiments, namely what appears to be a moiré pattern and (1×1) periodicity. The apparent moiré pattern is visible in Figure 91a and emphasised in Figure 91b. The spots producing the pattern are aligned in the $\langle 11\bar{2}\rangle$ direction and were measured to have a 4× periodicity in this direction. This symmetry, together with the contrast continuously varying in the periodic directions to produce sinusoidal contrast profiles, is indicative of the formation of an overlayer with varying degrees of epitaxial compliance. The contrast maxima and minima between spots would on this view correspond to maxima and minima in overlayer epitaxial compliance with the underlying substrate, or vice versa. If an epitaxial overlayer is indeed present on the surface, its periodicity appears to be (1×1), which is evidenced by Figure 91d and its associated FFT in Figure 91e. There are six FFT points with a 6-fold symmetry, which all are within 3% of the $\langle 01\bar{1}\rangle$ directions and have a mean periodicity within 10% of $SrTiO_3\langle 01\bar{1}\rangle$.

The flat lakes consequently seem to be associated with an Li-based overlayer on a $SrTiO_3(111) - (1 \times 1)$ bulk termination, where the periodicities of the two coincide to generate a moiré pattern. If one follows Ockham's razor to suggest the simplest possible overlayer that could produce (1×1) periodicity and balance the dipole associated with the polar $SrTiO_3(111)$ termination, one finds two options; either a SrO_3^{4-} bulk termination, which has a net unbalanced charge of -2 and could be stabilised by a Li overlayer via $2Li^+$ per $SrTiO_3(111)$ surface unit cell, or a Ti^{4+} bulk termination, which has a net unbalanced charge of $+2$ and could similarly be stabilised by $Li_2O_2^{2-}$. The Li overlayer option was deemed the more likely candidate due to the strength of the Li-O bond and the small size of Li, which together should allow Li to find suitable adsorption sites on the termination SrO_3 that minimizes protrusions and hence maximises flatness. A calculation was made of this proposed SrO_3/Li structure, with the result displayed in Figure 92. The two Li that

are required for dipole cancellation find suitable 3-fold O coordinated adsorption sites in the SrO_3-terminated surface unit cell, as can be seen in Figure 92b. An STM simulation of this calculated structure yields an apparent height profile where no two points on the surface differ by more than 0.004 nm, as per Figure 92c. This calculation thus produces a structure compatible with the extreme flatness observed in the real STM experiment. The moiré pattern will be further discussed in Section 8.6.

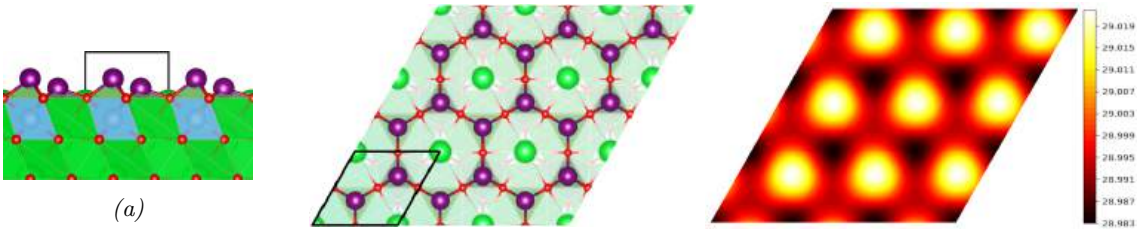

(a) *(b)* *(c)*

Figure 92: DFT simulation of a Li overlayer on SrO_3 bulk-terminated $SrTiO_3(111) - (1\times1)$. a) shows the surface from the side view, b) from the top view, and c) shows an STM simulation. Green, blue, red, and purple balls are Sr, Ti, O and Li, respectively, and green, blue, and purple polyhedra are O coordination around Sr, Ti, and Li, respectively. Black lines in a) and the black diamond in b) shows the (1×1) surface unit cell. The STM simulation in c) was generated with a potential of 0.65 V and a tip-surface separation of 6.1 Å. The bright contrast in the STM simulation is primarily due to the most superficial Li atoms that can be seen in a). The scale bar in c) has units Å, indicating a simulated height difference between the darkest and brightest points of 0.0036 nm.

8.3 High Deposition

Two original surfaces were used for deposition of $1.0 < 2.0$ ML Li; one homogenous surface dominated by (5×5), and one mixed surface where $(6\times6)A$, $(6\times6)B$, (4×4) coexist, displayed in 93a and 93b, respectively. Figures 93c and 93d display the responses of the homogenous and mixed surfaces, respectively, to $1.0 < 2.0$ ML Li deposition and 600 ^oC annealing. The surface in 93c shows the formation of irregular and amorphous islands up to 100 nm in diameter with no visibility of the $SrTiO_3(111)$ substrate. Figure 93d, on the other hand, shows the $SrTiO_3(111)$ substrate exposed, which likely is a consequence of the mixed surface being found in a hotter region of the sample than the homogenous one.

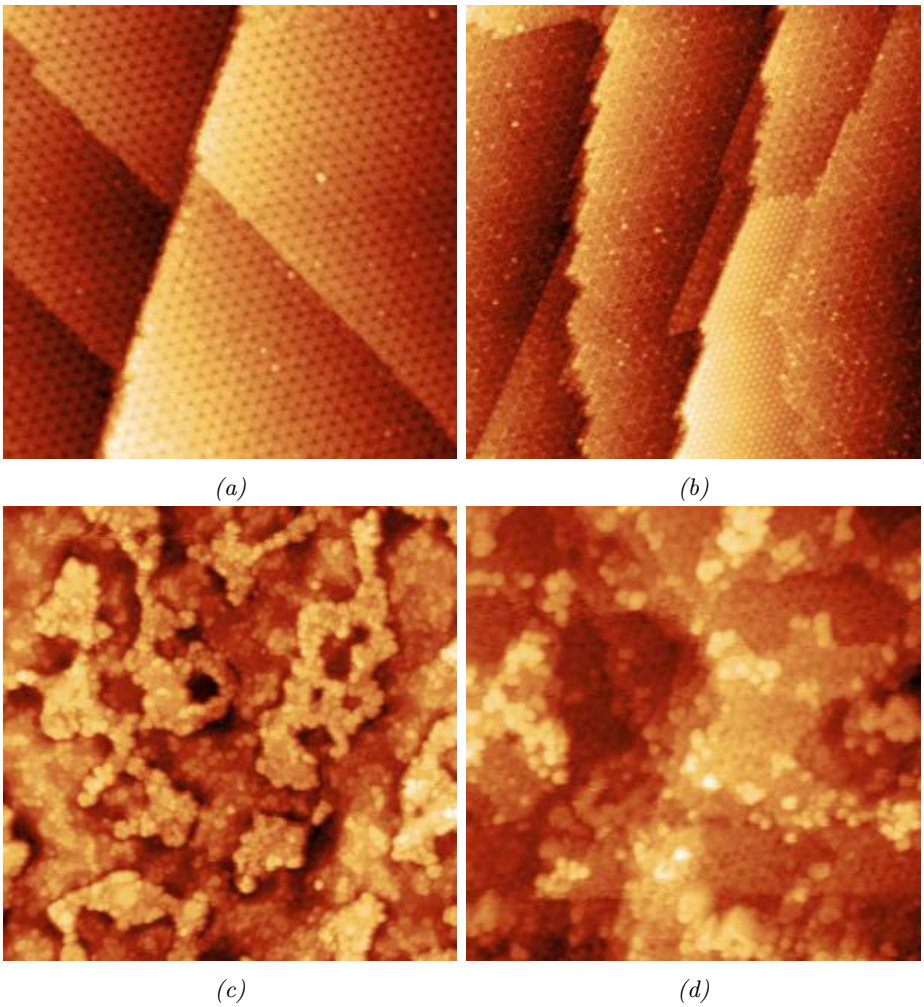

Figure 93: The original reconstructions used for $1.0 < 2.0$ *ML Li coverage experiments on* $SrTiO_3(111)$ *prior to deposition in the top row and the same surfaces after deposition and annealing to 600* ^oC *in the bottom row. a) shows a surface dominated by the* (5×5) *reconstruction (U=1.5 V, I=0.1 nA,* $80\times80\,nm^2$*), b) shows a surface with* $(6\times6)A$*,* $(6\times6)B$ *and* (4×4) *coexisting (U=1.5 V, I=0.1 nA,* $120\times120\,nm^2$*). c) shows the surface in a) after deposition and annealing (U=1.5 V, I=0.075 nA,* $150\times150\,nm^2$*) and d) shows the surface in b) after deposition and annealing (U=1.2 V, I=0.1 nA,* $80\times80\,nm^2$*).*

After 700 ^oC the homogenous and mixed surfaces converge on the same structure, as can be seen in Figures 94a and 94b. This surface does not have long-range order and contains indented triangles as well as dark spots, which are features indicative of the $(5\times5)\delta$ surface. After 800 ^oC, the surface is transformed to attain a long range $5\times$ periodicity, as can be seen in Figures 94c and 94d. The imaging conditions of this experiment were during the acquisition of the images in Figures 94c and 94d not quite good enough to confidently discern the reconstruction of these surfaces, however, considering the annealing temperature at which they form and their long-range ordered $5\times$ periodicity, it would be reasonable to suspect it to be the $(5\times5)\gamma$. The region around the black line in Figure 94d

also contain patterns similar to those seen on the (5×5) surface, namely small triangular indents, which increases the likelihood that it is indeed $(5\times5)\gamma$ that has formed.

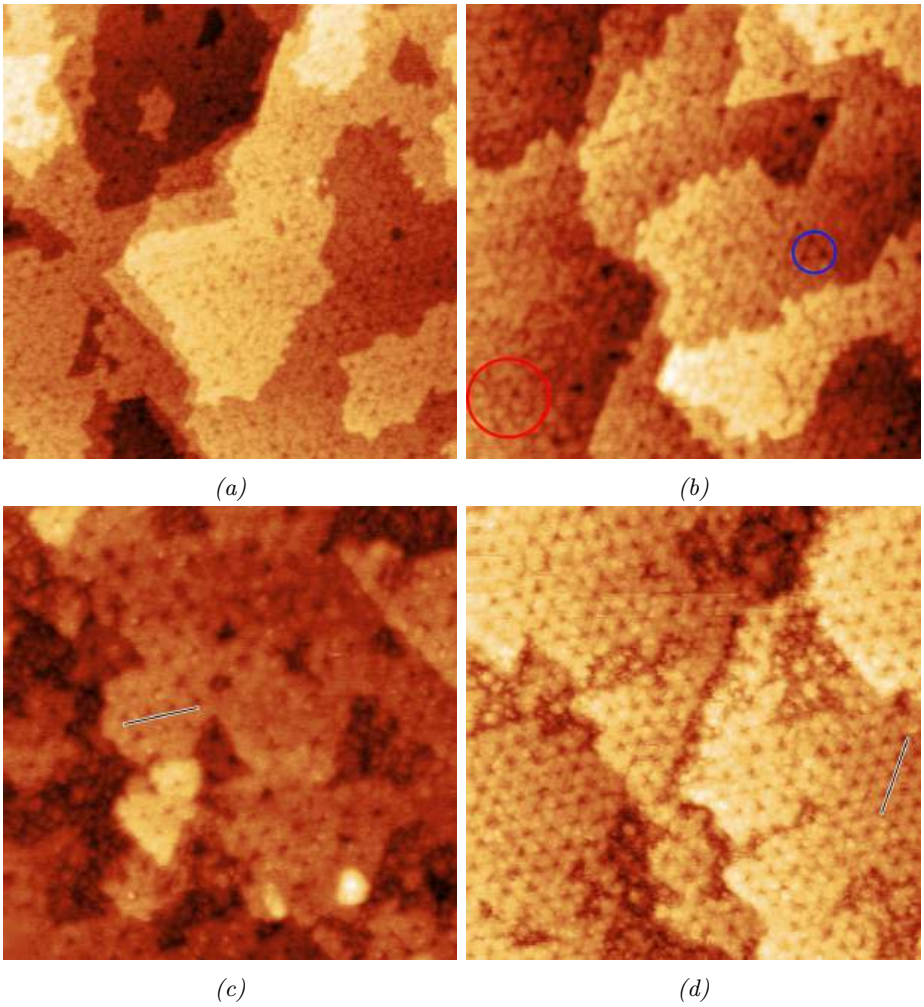

Figure 94: Surfaces produced by $1.0 < 2.0$ *ML Li deposition onto* $SrTiO_3(111)$ *after an annealing to 700 °C and 800 °C. The left column shows surfaces that originally were the* (5×5) *surface of Figure 93a, and the right column shows surfaces that originally were* $(6\times6)A+(6\times6)B+(4\times4)$ *surface of Figure 93b. 700 °C annealing produces the surfaces in a) (U=1.2 V, I=0.1 nA,* $80\times80\,nm^2$*) and b) (U=1.25 V, I=0.1 nA,* $60\times60\,nm^2$*), which have a similar character where both lack discernible long-range periodicity, contain the indented triangles and dark spots. Indented triangles and dark spots are indicated by the red and blue circles in b), respectively. These two features are both found on the* $(5\times5)\delta$ *surface, which suggests that this surface has been produced. After 800 °C, both the surface in c) (U=0.8 V, I=0.2 nA,* $50\times50\,nm^2$*) and d) (U=1.2 V, I=0.1 nA,* $60\times60\,nm^2$*) have developed long-range order. The periodicity of this long-range order is indicated by the black lines, which are within c) 1% and d) 6% of* $5\times$ *periodicity, respectively. The dark, indented triangles make these surfaces visually similar to* $(5\times5)\gamma$*, which forms at the same annealing temperature for* $0 < 0.1$ *ML Li deposition, making this a probable candidate for the surface structure after 800 °C.*

8.4 Bonding Interactions

The adsorption sites produced by Li on (2×2) and (3×3) are displayed in Figures 95 and 96, respectively. Li on (2×2) finds one additional site compared to the Na calculations presented in Chapter 7, which will be called the "side" site and is similar to the between

site but displaced away from the centre of the $TiO_5[]$ hexagon towards one of its sides. As in the case of Na adsorption, Li on the (2×2) reconstructions produces considerably lower energy adsorption sites than on (3×3), with the most preferred (3×3) site being 1.9 eV higher in energy than the least preferred (2×2) site. The order of site preference on (2×2) from most to least preferred is between, side, above and floor. As with Na on (2×2), sites that are coordinated by a greater number of $TiO_5[]$ units are lower in energy, yet there is a 0.7 eV gap between the side and above sites, despite both being coordinated by four $TiO_5[]$. This is likely due to Li bonding O atoms that are all part of the same single $TiO_5[]$ unit in the above site. This should reduce the degree to which Ti-O bonding in this unit can be adjusted to accommodate Li to a greater extent than in the $TiO_5[]$ hexagon of the side site, where Li bonds at most two O from the same unit. This line of argumentation can also explain the between site being lowest in energy of all, as Li is coordinated by 6 $TiO_5[]$ and bonds only one O from each $TiO_5[]$ unit.

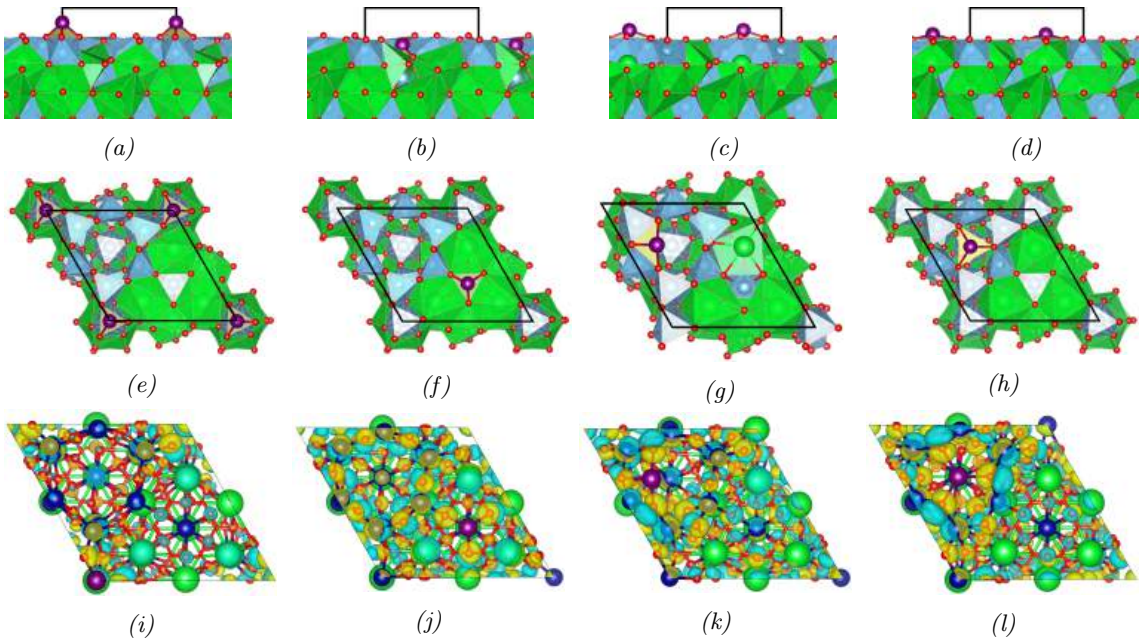

Figure 95: Li adsorption sites on $SrTiO_3(001) - (2\times2)$, where the above, floor, side, and between sites are shown from the top view in a), b), c), and d), respectively, from the side view in e), f), g), and h), respectively, and with electron density changes overlaid in i), j), k), and l), respectively. Li is coordinated by three O in all sites. Li is coordinated by four $TiO_5[]$ in the above site, three $TiO_5[]$ in the floor site, four $TiO_5[]$ in the side site, and six $TiO_5[]$ in the between site. The same colour scheme was used as in Figure 92.

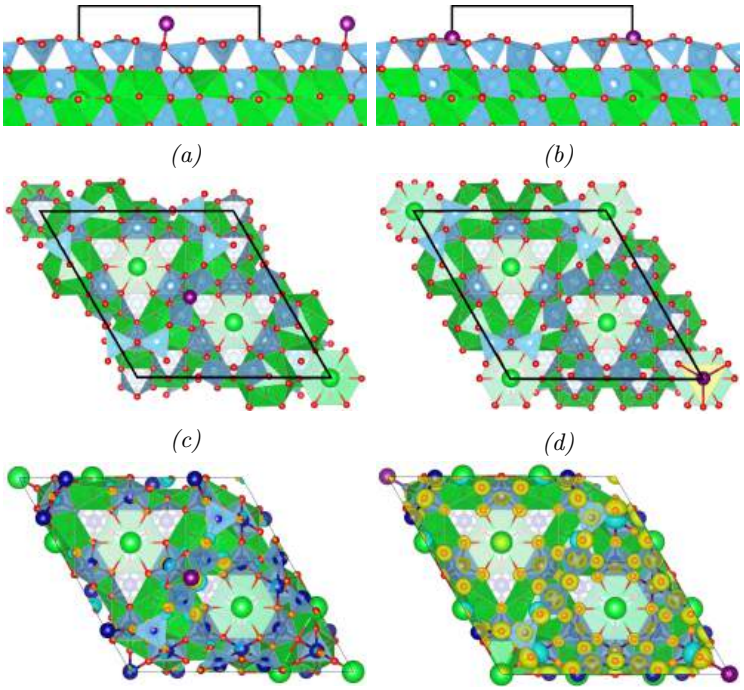

Figure 96: Li adsorption sites on $SrTiO_3(001) - (3\times3)$, where the atop and between sites are shown from the top view i a) and b) respectively, from the side view in c) and d), respectively, and with electron density changes overlaid in e) and f), respectively. Li is coordinated by one O in the atop site and three O in the between site, as well as two TiO_4 in the atop site and six TiO_4 in the between site. The same colour scheme was used as in Figure 92.

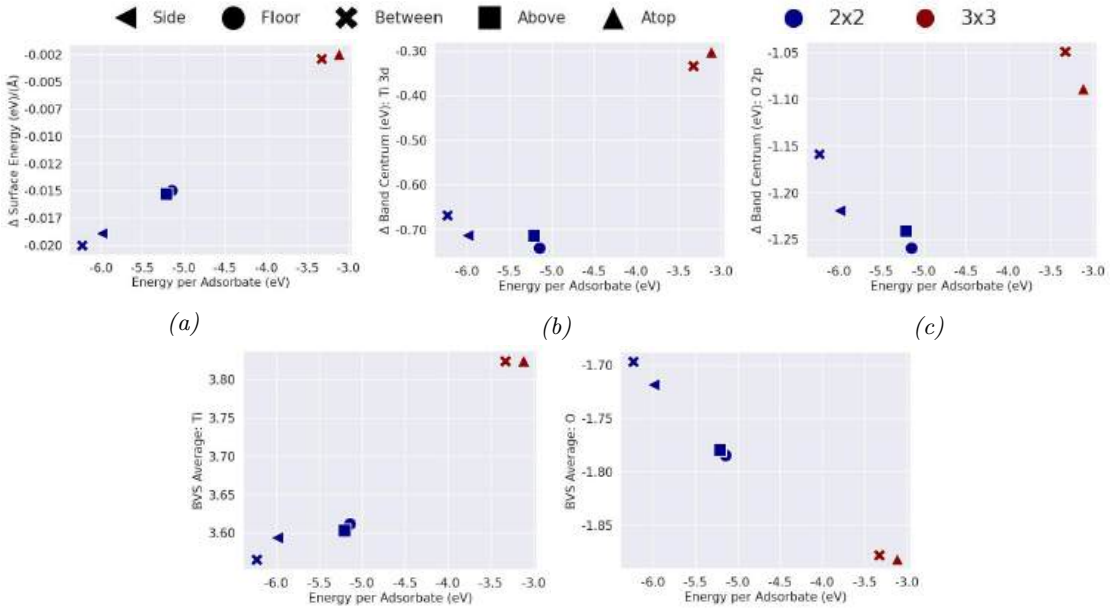

Figure 97: Bonding data for all Li adsorption sites on $SrTiO_3(001) - (2\times2)$ and (3×3). With respect to adsorption energy, the graphs show a) change in surface energy with respect to the clean surface, the change in band centrum energy with respect to the clean surface for b) Ti 3d and c) O 2p, and the average BVS of surface atoms for d) Ti and e) O.

Similar to the case of Na adsorption on $SrTiO_3(111)$ covered in Chapter 7, the greater Li adsorption strength on (2×2) compared to (3×3) is explicable by TiO_4 units in the outermost (3×3) layer being more inert than $TiO_5[]$ and producing overall more bulk-like bonding in the surface, thus making orbitals in (3×3) less reactive than in (2×2). This allows Li adsorption to reduce (2×2) surface energy to a greater extent, thus producing stronger adsorption, as can be seen in Figure 97a. The reasoning behind this proposition was explained in Chapter 7 and will hence not be further discussed here. The bonding data obtained for calculations of Li adsorption on $SrTiO_3(111)$ will instead be used to examine correlations between adsorption strength and the character of bonding in the (2×2) surface in greater detail. It is namely the case that this surface displays behaviours not seen in any other surface calculated for this thesis. Specifically, a greater adsorption strength on (2×2) correlates with Ti 3d and O 2p band centra moving towards higher energy levels (Figures 97b and 97c) and with Ti and O BVS departing from the formal oxidation states to approach +3 and -1, respectively (Figures 97d and 97e). These trends are all direct opposites of those calculated for Li on $SrTiO_3(001)-c(4\times2)$. The movement of Ti 3d, O 2p, and Li 2s+2p band centra with respect to the positions of the non-bonding and bonding regions are displayed in Figure 98, where Li 2s+2p is shown to move by more than 1.0 eV between the floor and between sites from a position deep within the bonding region to move close to the non-bonding region. The electronic structure implications of this (2×2) behaviour will be further discussed in Section 8.6.

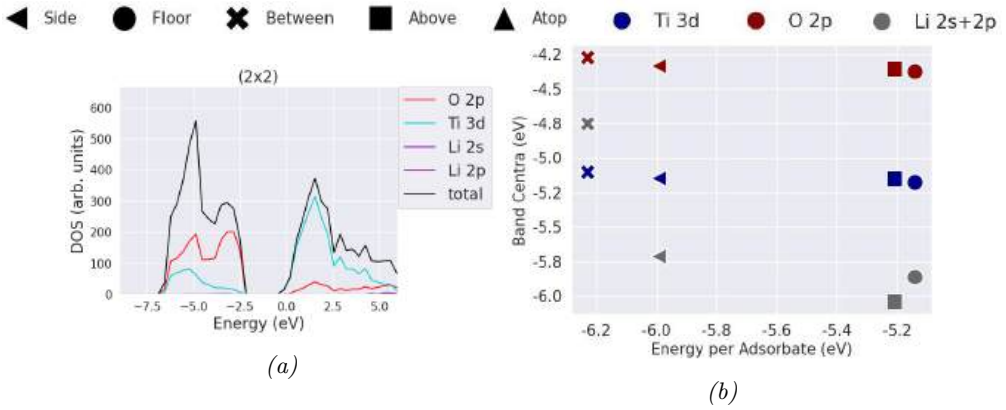

Figure 98: DOS data for (2×2), where a) shows the DOS spectrum of the between site around the Fermi level and b) shows band centra position for Ti 3d, O 2p, and Li 2s+2p. The centre of the valence band in a) is -4.54 eV, the centre of the bonding region is -5.56 eV, and the centre of the non-bonding region is -3.527 eV. The Li 2s+2p band centrum moves circa 1.1 eV form the weakest adsorption site to the strongest, which constitutes a shift from circa 0.3 eV beneath the bonding region centre to circa 0.3 eV beneath the non-bonding region. The band centrum moves upwards in energy from the weakest adsorption site to the strongest also for Ti 3d and O 2p, by circa 0.1-0.2 eV in both cases.

8.5 Chemical Environments

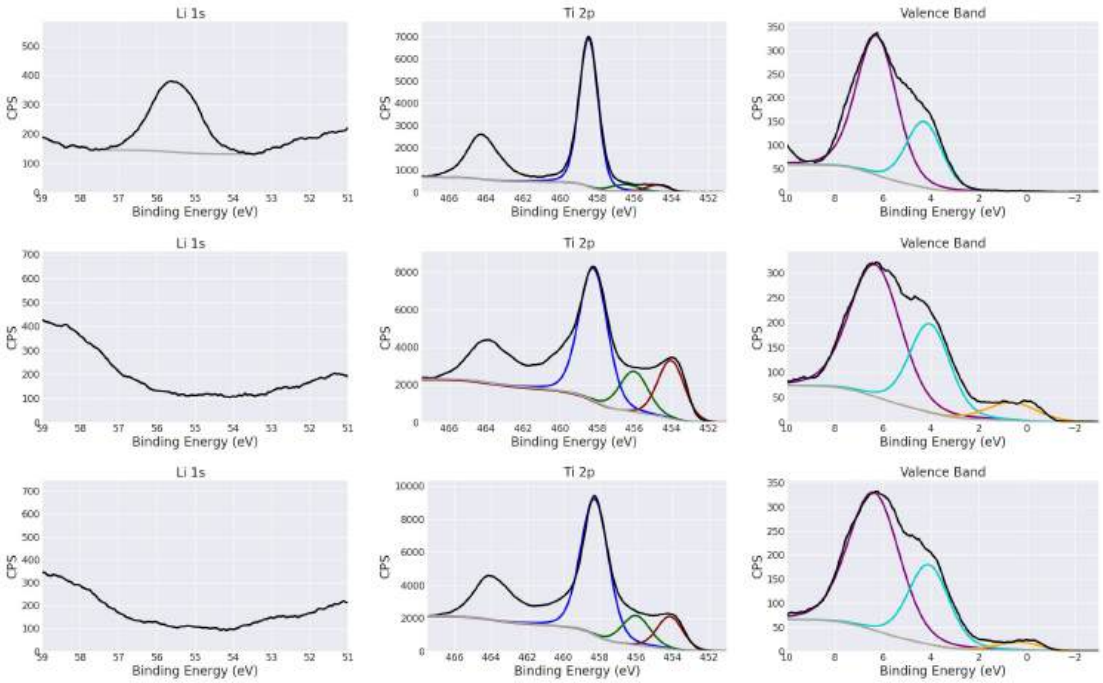

Figure 99: XPS spectra acquired following $1.0 < 2.0$ *ML Li deposition on* $SrTiO_3(111)$ *and 600* ^oC *annealing. Deposition and annealing were conducted in the UHV treatment chamber of the STM instrument. The x axis shows binding energy in eV and the y axis shows counts per second (CPS). The black, and gray lines are the total signal and Shirley background, respectively, the blue, green, and red lines are* Ti^{4+}, Ti^{3+}, *and* Ti^{2+}, *respectively, and the purple, turquoise, and orange lines are bonding, non-bonding, and band gap states, respectively. The top, middle, and bottom rows show data from the colder end, middle, and hotter end of the sample, respectively. The leftmost column shows the Li 1s region, the middle column the Ti 2p region, and the rightmost column the valence band region. As the temperature increases from the colder side to the middle of the sample, the Li signal disappears, the percentages of* Ti^{4+}, Ti^{3+}, *and* Ti^{2+} *change from 89%, 6%, and 5% to 58%, 18%, and 24%, respectively, indicating a significant increase in fraction of reduced Ti in the surface region. This Ti reduction coincides with the valence band developing states in the band gap. As temperature increases from the middle to the hot side of the sample, the percentages of* Ti^{4+}, Ti^{3+}, *and* Ti^{2+} *change to 70%, 15%, and 15%, respectively. The band gap state similarly decreases from 8% to 3% of the total valence band signal. The percentage of the valence band associated with the bonding and non-bonding peaks is 70% and 30% at the cold side of the sample, 60%, 32% at the middle of the sample, and 66% and 30% at the hot end of the sample. It thus seems that Ti reduction correlates with an increase in non-bonding Ti-O states, as well as a band gap state. As explained in Chapter 3, the difference in effective annealing temperature between the centre of the sample and one of its ends is expected to be up to 50* ^oC, *meaning the hot and cold side of the sample should differ by no more than 100* ^oC.

XPS spectra of the chemical environments present after $1.0 < 2.0$ ML Li deposition on $SrTiO_3(111)$ and 600 ^oC annealing are displayed in Figure 99. A Li 1s peak is visible at the colder side of the sample, where 89% of the Ti 2p signal stems from Ti^{4+} and the valence band is similar to that of the cleaved sample presented in Chapter 7. In the middle of the sample, where the effective annealing temperature is up to 50 ^oC higher, no Li 1s

signal was detected, 42% of the Ti 2p signal has become $Ti^{3+}+Ti^{2+}$, and the valence band shows states in the band gap together with an increased fraction of non-bonding states. At the hotter side of the sample, both the fraction of Ti 2p signal stemming from $Ti^{3+}+Ti^{2+}$ and the fraction of valence band signal stemming from the band gap state have seemingly decreased with respect to the centre of the sample, possibly indicating partial re-oxidation. Based on the same arguments as those of the XPS analysis presented in Chapter 7, it thus seems that $SrTiO_3$ has been reduced by Li, which fills Ti states and produces states in the band gap. DFT again suggests that band gap states are predominantly of Ti 3d character, as per Figure 100 and as anticipated by the literature in Chapter 2.

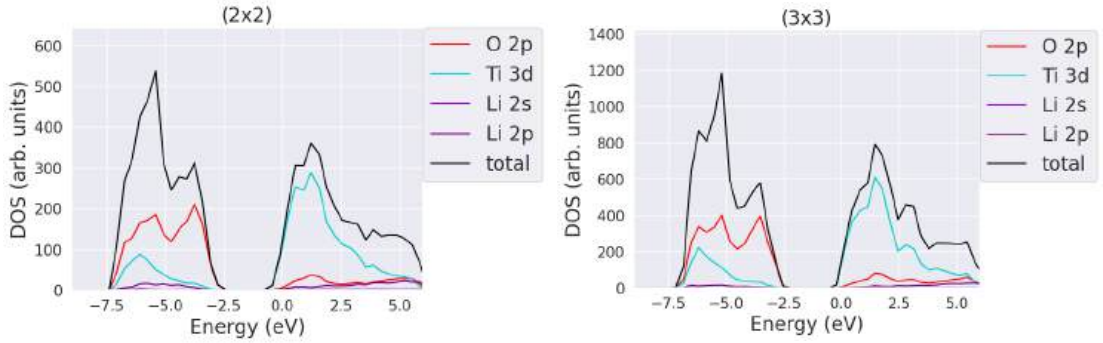

Figure 100: DOS around the Fermi level for a) 1.5 ML Li on (2×2) *and b) 0.67 ML Li on* (3×3). *Conduction band states are present below the Fermi level, the total composition of which for* (2×2) *is 95% Ti 3d, 4% O, and 1% Li 2p, and for* (3×3) *is 99% Ti 3d and 1% O 2p.*

8.6 Discussion

$SrTiO_3$(111) exposed to $0 < 0.1$ ML Li is transformed in three stages as a function of annealing temperature; a first reconstruction induction, a disordered intermediate state, and a second reconstruction induction. The first reconstruction induction occurs following 400 ^oC annealing, where the symmetry of the new reconstruction is dependent on the original. The periodicities of the initial (4×4), (5×5), and $(6\times6)A$ reconstructions are maintained as they are transformed to $(4\times4)\delta$, $(5\times5)\delta$, $(6\times6)\delta$, respectively. At 600 ^oC, $SrTiO_3$(111) undergoes a dramatic transformation where the surface becomes dominated by disordered and uneven areas, lacking any semblance of symmetry and order. These disordered areas are, however, broken up areas of the so called flat lakes, which will be treated in the next paragraph. Following 700 ^oC, the second set of new reconstructions and surface orderings are induced, with the character of the new surface again depending on the original reconstruction prior to Li exposure. Where the original reconstruction was (5×5),

the $(5\times5)\gamma$ reconstruction, which was characterised in Chapter 7, dominates the surface after 700 ^oC, which is joined by the regular (5×5) following 800 ^oC annealing. The surface that originally was $(6\times6)+(5\times5)$ similarly produces $(5\times5)\gamma$ following 700 ^oC annealing, but coexisting with a short-range quasi-periodic (2×2) ordering. This surface too becomes dominated by regular (5×5) after 800 ^0C annealing. Where the original reconstruction was $(6\times6)+(4\times4)$, 700 ^oC annealing produces no symmetric feature except the quasi-periodic (2×2) ordering, and 800 ^oC annealing transforms the surface to one dominated by (4×4). It has thus been shown that there is an inertia to the symmetries of a reconstruction, which can be preserved even if its structure changes. This inertia is so strong that the periodicity of a reconstruction may survive through multiple transformations with the original reconstruction returning when the chemistry of the surface region is restored to its original state.

The flat lakes are perhaps the most striking structure observed during the course of this project. They have three features which provide information about their fundamental nature. Firstly, they are extremely flat, so flat that their height profiles measured across 30 nm show no feature that diverges from their mean height by more than 0.04 nm. Secondly, what seems to be a moiré pattern has been observed on the lakes, appearing as diffuse spots aligned with the $SrTiO_3\langle11\overline{2}\rangle$ directions, along which they 4× periodicity. If this pattern of diffuse spots is indeed a moiré pattern, this would indicate that an epitaxial overlayer has formed. Thirdly, the surface structure of the flat lakes appears to have (1×1) ordering. These three features, i.e. atomic flatness, moiré pattern and bulk unit cell ordering, lead to the suspicion that they are an Li-based monolayer covering a $SrTiO_3(111)$ bulk termination. Due to the strength of the Li-O bond and the small size of Li, it was proposed that the most likely structure of this overlayer is a Li monolayer on a SrO_3 termination. This proposed structure was calculated in DFT and yields STM simulations which indicate an apparent topographic profile compatible with the extreme flatness observed in real STM.

The periodicity of the moiré pattern allows for an attempt to determine the epitaxial relationship from which it stems. It should be made clear that the result of this attempt is speculative due to the limited information about the exact character of the overlayer.

It will for the purposes of this analysis be assumed that the proposition above is correct, namely that the moiré pattern is produced by an Li overlayer on a $SrTiO_3-(1\times1)$ surface with SrO_3 bulk termination. To start, a set of 2D basis vectors $\{\mathbf{s}_1, \mathbf{s}_2\}$ is chosen in the $SrTiO_3$ surface against which the periodicity M and direction ϕ of the moiré pattern are measured. The natural choice for $\mathbf{s}_1$ is one of the $SrTiO_3(111)$ surface unit cell vectors and for $\mathbf{s}_2$ an adjacent surface unit cell vector at an angle 60^o to $\mathbf{s}_1$. If the length of a surface unit cell vector is s, then $\mathbf{s}_1$ and $\mathbf{s}_2$ may be set to $\mathbf{s}_1 = s[1, 0]$ and $\mathbf{s}_2 = s[1/2, \sqrt{3}/2]$. The periodicity of the observed moiré pattern must be equal to the magnitude of a vector formed by the sum of some integer numbers h of $\mathbf{s}_1$ and k of $\mathbf{s}_2$. A similar set of unit vectors $\{\mathbf{a}_1, \mathbf{a}_2\}$ can be defined for a hexagonal overlayer with a surface unit cell length of a such that $\mathbf{a}_1 = a[1, 0]$ and $\mathbf{a}_2 = a[1/2, \sqrt{3}/2]$, where an integer number m of $\mathbf{a}_1$ and n of $\mathbf{a}_2$ also must coincide with the moiré pattern periodicity. The overlayer is potentially rotated with respect to the $SrTiO_3(111)$ surface, for which reason the angle θ between them must be considered. These conditions for the coincidence of the surface and overlayer lattices with the moiré pattern can be expressed by the following equality[214–216]:

$$\begin{bmatrix} s & \frac{1}{2}s \\ 0 & \frac{\sqrt{3}}{2}s \end{bmatrix} \begin{bmatrix} h \\ k \end{bmatrix} = \begin{bmatrix} cos(\theta) & -sin(\theta) \\ sin(\theta) & cos(\theta) \end{bmatrix} \begin{bmatrix} a & \frac{1}{2}a \\ 0 & \frac{\sqrt{3}}{2}a \end{bmatrix} \begin{bmatrix} m \\ n \end{bmatrix}. \tag{22}$$

The values for M and ϕ can be taken from the STM images in Figure 91, where they were measured to be 4.0 nm and 30^o, respectively. This length is within 5% of a $4\times$ periodicity along $\langle 11\overline{2}\rangle$, which is the expected direction given the value of ϕ. The values for both h and k may thus be set to 4. The values pertaining to the overlayer are more elusive, because if the overlayer is indeed an Li monolayer on SrO_3-terminated $SrTiO_3(111)$, then this environment is too unusual to credibly estimate a based on bulk of any known Li compound, such as cubic Li_2O. This complicates the determination of m and n. It is known, however, that an Li overlayer would stabilise the SrO_3 termination by cancelling its dipole, which opens up an angle d'attaque by considering the number of Li needed to cancel the dipole of the SrO_3^{-2} layer within one moiré pattern surface unit cell.

The length of the moiré pattern surface unit cell vector length is $4\sqrt{3}|SrTiO_3\langle 01\overline{1}\rangle|$, meaning there are $4\sqrt{3} \approx 7$ $SrTiO_3(111)$ unit cells along the moiré pattern vector. This requires 14 Li^+ for surface dipole moment cancellation, which can be achieved by two

possible overlayer unit cells; either, the overlayer has universally uniform Li spacing, giving 14 Li unit cells per moiré pattern length with one Li per unit cell. Alternatively, the Li overlayer has two non-degenerate adsorption sites per $SrTiO_3(111)$ unit cell, producing 7 Li unit cells per moiré pattern length with two Li per unit cell. The latter option seems more plausible considering that the SrO_3 surface has a considerable amount of structure in its potential landscape. Both Sr and O have strong electrostatic interactions with Li, and the two adsorption sites calculated in Figure 92 are not degenerate due to the proximity of a Ti atom in the layer beneath to one of them. It is, for this reason, unlikely that there should be two equivalent Li unit cells per SrO_3 unit cell across the entire flat lake, and more likely that there is one Li unit cell per SrO_3 unit cell which hosts two distinct Li sites. The overlayer is as such proposed to be Li_2. Li-Li repulsion and surface dipole minimisation will, furthermore, work to spread Li evenly over all SrO_3 unit cells, which since $h = k$ means that $m = n$. The Li_2 cell length along the moiré pattern vector would according to this model be $4\sqrt{3}|SrTiO_3\langle 01\bar{1}\rangle|/7 = 0.547$ nm, which for a hexagonal Li_2 monolayer with $\langle 01\bar{1}\rangle$ aligned with the moiré pattern vector would correspond to a unit cell parameter $a = 0.386$ nm. This is circa 1% from the 0.39 nm unit cell parameter of $SrTiO_3$. Such a close lattice match is reasonable for this surface system since this is required for the charge balancing that cancels the dipole moment.

Determining the epitaxial relationship of the Li_2 overlayer is then a question of finding the vector $\mathbf{v}$, along which the Li_2 surface unit cell periodicity c along the moiré pattern is such that $mc = 7$. This is complete analogy to the $SrTiO_3(111)$ surface, where the equivalent of $\mathbf{v}$ is $\langle 11\bar{2}\rangle$ and the equivalent of c is $\sqrt{3}$. This follows from the magnitude of $\langle 11\bar{2}\rangle$ being $\sqrt{6}$ and the $SrTiO_3(111)$ surface unit cell vector magnitude being $|\langle 01\bar{1}\rangle|$, hence $\sqrt{3} = \sqrt{6}/\sqrt{2}$. Given the 6-fold rotation of the pattern, it is known that the Li_2 overlayer is hexagonal, meaning its surface unit vectors too are of $\langle 01\bar{1}\rangle$ type, thus $c = |\mathbf{v}|/\sqrt{2}$. It is then known that $m|\mathbf{v}|/\sqrt{2} = 7$. It is now possible to survey possible values for $\mathbf{v}$ which satisfies this relationship. $\mathbf{v}$ must itself be given by some integer numbers x and y of $\langle 01\bar{1}\rangle$, hence:

$$\mathbf{v} = x \begin{bmatrix} 0 \\ 1 \\ -1 \end{bmatrix} + y \begin{bmatrix} 1 \\ 0 \\ -1 \end{bmatrix} \therefore |\mathbf{v}| = \sqrt{y^2 + x^2 + (-x - y)^2}, \tag{23}$$

.

Finding the Li_2 overlayer epitaxy that corresponds to the moiré pattern is thus a matter of finding allowed solutions for x, y, and m that satisfy $m|\mathbf{v}|/\sqrt{2} = 7$. Only two such solutions are possible, which with respect to $SrTiO_3(111)$ can be described as $Li_2(111)-(7\times7)-R30^o$ and $Li_2(111)-(7\times7)-R38.2^o$, both of which are displayed in Figure 101. The $(7\times7)-R38.2^o$ solution produces a visually superior similarity to the pattern observed in STM, as can be seen by comparing Figures 101a and 101b. In particularity, it seems that the $(7\times7)-R30^o$ solution produces a number of equally valid coincidence epitaxial points outside the corners of the moiré pattern unit cell, whereas the $(7\times7)-R38.2^o$ solution only produces coincidence epitaxy at the moiré pattern corners. The $(7\times7)-R38.2^o$ solution, furthermore, produces rows in between moiré pattern corners where the SrO_3 and Li_2 unit cells seem to align in one of the $\langle 01\bar{1}\rangle$ directions but with minimal epitaxy. This solution thus produces an epitaxial relationship that is more compatible with the contrast maxima of minima observed in STM. The $(7\times7)-R38.2^o$ solution of Figure 101b will thus tentatively be proposed as the solution to the moiré pattern. This solution yields an epitaxial relationship that can be expressed as $Li_2(111)||SrTiO_3(111)$, $Li_2[53\bar{8}]||SrTiO_3[11\bar{2}]$. This relationship would generate a moiré pattern from coincidence between $Li_2(111)-(7\times7)-R38.2^o$ and SrO_3-terminated $SrTiO_3(111)-(4\sqrt{3}\times4\sqrt{3})-R30^o$.

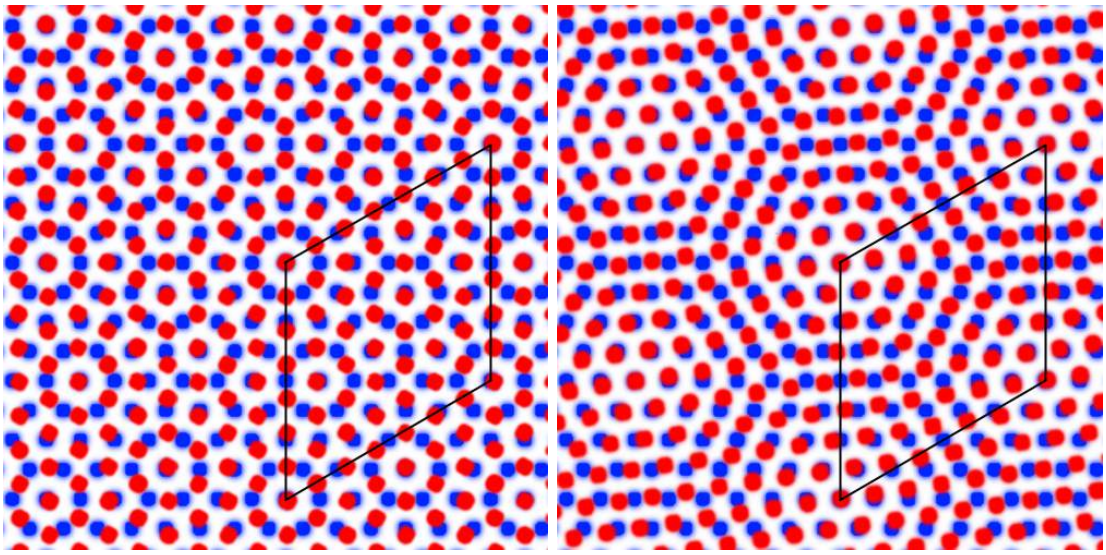

(a) (b)

Figure 101: Models for the proposed moiré pattern structure, which is suggest to be a Li_2 monolayer on the SrO_3 bulk termination of $SrTiO_3(111)-(1\times1)$. Blue and red balls are the centre of $SrTiO_3(111)-(1\times1)$ and Li_2 unit cells, respectively. The black diamond marks one moiré pattern unit cell. Two solutions exist that satisfy $m|\boldsymbol{v}|/\sqrt{2}=7$. The first has $m=7$ and $x=y=1$ with $\boldsymbol{v}=\langle01\bar{1}\rangle$ aligned with the moiré pattern, which is displayed in a). The Li_2 overlayer periodicity with respect to $SrTiO_3(111)$ would according to this solution be $Li_2(111)-(7\times7)-R30^o$. The second solution has $m=1$, $x=5$, and $y=3$ with $\boldsymbol{v}=\langle53\bar{8}\rangle$ aligned with the moiré pattern, which is displayed in b). The Li_2 overlayer periodicity with respect to $SrTiO_3(111)$ would according to this solution be $Li_2(111)-(7\times7)-R38.2^o$. The pattern in b) is proposed as the solution.

1.0 < 2.0 ML Li coverage on $SrTiO_3(111)$ does not produce a wetting monolayer, but rather nanoparticles and films with the substrate exposed following 600 ^oC annealing. After 700 ^oC annealing, what seems to be the $SrTiO_3(111)-(5\times5)\delta$ reconstruction completely dominates the surface with little sign of Li-based nanoparticles. Following 800 ^oC annealing, the surface appears to transform into $(5\times5)\gamma$. The disappearance of Li from the surface at 600-700 ^oC is also observed in XPS and coincides with a stark increase in Ti reduction. At the colder end of the sample, the Li signal is still present and 11% of the Ti signal originates from reduced Ti atoms. In the middle of the sample, there is a simultaneous disappearance of the Li signal and increase in Ti reduction to 42%. This enhanced reduction is interpreted as the effect of the mechanism that removes alkali metal from the surface, as observed in STM. That mechanism is proposed to most likely be Li intercalation, as per the argumentation in Chapter 7. As such, the Ti reduction observed prior to the Li signal disappearing is likely due to Li bonding to surface O, while the increase in Ti reduction as the Li signal disappears is interpreted as Li migrating into the bulk to occupy interstitial sites. In both cases, Ti reduction should occur adjacent to O

atoms that acquire Li bonds, resulting in the transfer of an electron from Li to Ti 3d to mitigate O over-coordination. This two-step reduction process, where a lower annealing temperature causes reduction of the surface layer only and a higher annealing temperature reduces the entire surface region, may also explain the reconstruction transformations observed in STM. The δ-reconstructions would thus be the result of surface layer reduction, whereas $(5\times5)\gamma$ would be produced as reduction is enhanced at elevated annealing temperature, probably due to intercalation. If the sample has indeed been partially reoxidised at its hotter end, this could, on the view that the enhanced reduction was driven by Li intercalation, be explained by a decrease in Li concentration in the surface region because increased thermal energy allows Li to migrate deeper into the substrate.

DFT calculations of Li on (2×2) and (3×3) produce results pertaining to coordination environments similar to those for Na on the (2×2) and (3×3) (Chapter 7), as well as Na and Li on $SrTiO_3(001)-c(4\times2)$ (Chapters 5 and 6). Calculations indicate that alkali adsorption strength on $SrTiO_3$ surfaces increases when adsorbates maximise the number of TiO_x units they coordinate while minimising the number of O they bond from any single TiO_x unit. This is true for $TiO_x = TiO_4$ as well as $TiO_x = TiO_5[]$. This seemingly general behaviour allows for some hypothesising as to why a greater number of TiO_x units coordinating the alkali adsorbate produces stronger adsorption. Firstly, it should be the case that when a TiO_x unit is freer to alter its Ti-O bonds, more charge can be redistributed within this TiO_x unit. Such Ti-O bond alterations include e.g. degree of covalency, bond length, and bond angle; the key point is that the TiO_x unit has a greater ability to redistribute electron density, thus increasing its contribution to the adsorbate-surface interaction strength. A greater number of coordinating TiO_x units should increase this freedom to redistribute charge, because fewer O per TiO_x unit are constrained by bonding Li, thus increasing the electronic degrees of freedom of the average TiO_x unit. Secondly, a greater number of coordinating TiO_x units means that more Ti-O bonds participate in the charge redistribution. This is because Ti-O bond alterations mainly occur in those TiO_x units that have an adsorbate-O bond, as this additional bond produces a driving force to change the bonds of the unit so as to acquire bond valences that are as conducive as possible to the stability of the unit. Thus, a greater TiO_x coordination should both increase the degree to which individual Ti-O bonds can

be adjusted and the number of Ti-O bonds that are adjusted. This in turn should yield greater charge distribution and hence a stronger interaction, which consequently reduces surface energy to a greater extent. This will be proposed as the reason for the correlation between TiO_x unit coordination maximisation and adsorption strength.

The way in which bonds are adjusted to achieve greater adsorption strength may, however, differ significantly between reconstructions. This is evidenced by comparing the bonding data for Li on (2×2) with that of Li on $c(4\times2)$ discussed in Chapter 6. These reconstructions have similar surface energies (0.050 eV/Å for (2×2) and 0.046 eV/Å for $c(4\times2)$) and maximum Li adsorption strengths (-6.23 eV for (2×2) and -6.48 eV for $c(4\times2)$). Yet, the character of bonding in these two reconstructions changes in diametrically opposite ways with increasing Li adsorption strength. The stronger the Li adsorption site on the (2×2) surface, the more Ti 3d and O 2p band centra move towards higher energy levels, indicating that non-bonding states are being filled. The O 2p band centrum, in particular, moves strongly towards the non-bonding region of the valence band. The separation between O 2p and Ti 3d band centra also increase, indicating a decrease in covalency. Stronger adsorption lastly correlates with Ti and O BVS values approaching +3 and -1, respectively, which suggests a decrease in the absolute value of Ti and O effective oxidation states. All these trends are reversed for Li on $c(4\times2)$, as covered in Chapter 6. One may interpret this difference as (2×2) and $c(4\times2)$ having energetically opposite responses to electron delocalisation. More delocalised valence electrons should have band centra at higher energy levels closer to the Fermi level. They should also yield oxidation states deviating more from the formal values of +4 for Ti and -2 for O, because electrons would be more evenly distributed between Ti and O. It thus seems like (2×2) energetically benefits from electron delocalisation, while $c(4\times2)$ energetically benefits from electron localisation. This suggests that the physics of how $SrTiO_3$ surfaces respond to alkali metals may drastically differ between reconstructions, despite similar adsorption energies.

8.7 Conclusion

Li induces a number of reconstructions in the $SrTiO_3(111)$ surface at a coverage of $0 < 0.1$ ML. After annealing temperatures of 400-500 ^oC, each of the (4×4), (5×5), and $(6\times6)A$

reconstructions are transformed into a new reconstructions that maintains the periodicity of the old. After 700 ^0C, the $(5\times5)\gamma$ reconstruction familiar from Chapter 7 is observed. Following 800 ^oC annealing, the original reconstructions return in areas that were initially (4×4) or (5×5). At intermediate temperatures between these transformations, the surface is largely dominated by uneven and disordered regions, but also contains extremely flat areas, which across 30 nm have height profiles where no feature diverges more than 0.04 nm from the mean height. This atomic flatness is attributed to an Li overlayer stabilising a SrO_3 bulk termination, which is evidenced by the presence of a moiré pattern and (1×1) ordering in the flat areas. This moiré pattern was measured to have a periodicity of $SrTiO_3(111) - (4\sqrt{3}\times4\sqrt{3}) - R30^o$. A model was tentatively proposed where this moiré pattern periodicity is the product of coincidence epitaxy between SrO_3-terminated $SrTiO_3(111) - (1\times1)$ and a Li_2 overlayer. DFT calculations yield correlations between Li adsorption strength on $(111) - (2\times2)$ and Ti 3d and O 2p band centra, as well as Ti and O BVS values, that are the opposite of those obtained for Li on $(001) - c(4\times2)$. This difference is proposed to be due to (2×2) favouring increased electron delocalisation in the surface, while $c(4\times2)$ favours increased electron localisation.

9 Conclusions

9.1 Overview

This thesis has described the interaction of Li and Na with $SrTiO_3$ surfaces, primarily using STM but with support from DFT and XPS. Na on (001), Li on (001), Na on (111), and Li on (111) were presented in Chapters 5, 6, 7, and 8, respectively. It was established in these chapters that the structure of a $SrTiO_3$ surface, including its termination and reconstruction, has a significant influence on the nature of its interaction with alkali metals. This influence effects properties such as alkali metal adhesion, reconstruction stability, and defect formation, and also determines whether unusual phenomena such as bulk termination stabilisation are possible.

The present chapter serves primarily as a summary of the key findings from Chapters 5-8. Some information will be included from Appendix II pertaining to DFT calculations of Li and Na on $SrTiO_3(110) - (4\times1)$; firstly, this reconstruction has a low surface energy and bulk-like surface bonding compared to other reconstructions. This is most likely related to its ultimate surface layer being composed of TiO_4 units, making it similar to $(111) - (3\times3)$ in this regard, as discussed in Chapter 7. Secondly, $(110) - (4\times1)$ follows the trend of increasing adsorption strength with increasing TiO_x unit coordination around the alkali adsorbate. At the end of this chapter, a brief note on potential future work will be given, where some insights that may be useful for solid-state battery research will be discussed.

9.2 Key Findings

9.2.1 Adhesion

Alkali metal adhesion to $SrTiO_3$ surfaces has been shown to differ significantly between terminations and between reconstructions of the same termination. It seems that alkali metal adhesion to (001) is notably stronger than to (111), which is evidenced by the $1.0 < 2.0$ ML coverage experiments. For this coverage on (001), both alkali metals form wetting monolayers following annealing up to 700 ^oC (Chapters 5 and 6). On (111), however, both alkali metals form nanoparticles and films at annealing temperatures in

this range with the $SrTiO_3$ substrate still exposed, indicating weaker interface bonding (Chapters 7 and 8). The influence of reconstruction on adhesion is best demonstrated by the $0 < 0.3$ ML Na deposition experiment on (111) (Chapter 7). On this surface, Na displays a clear preference for, and thus stronger adhesion to, the $(6\times6)B$ reconstructions over (4×4), (5×5), and $(6\times6)A$. Such variations in alkali metal adhesion are likely related to $SrTiO_3$ surfaces having different coordination environments and consequently different surface energies. This should, in turn, result in differences in degree to which surface energy can be lowered by alkali metal adsorption. The $(6\times6)B$ reconstruction should according to this line of argumentation have higher surface energy due coordination environment effects that can be mitigated by Na adsorption, hence allowing for greater surface energy reduction via Na adsorption and thus greater adhesion.

DFT was used to support the coordination-based arguments above by grounding them in bonding. Calculations in Chapters 5-8, as well as Appendix II, show that two aspects of the bonding environment at the adsorption site strongly influence alkali metal adsorption strength, namely the number and type of TiO_x units. The greater the number of TiO_x units coordinating the alkali adsorbate, the stronger the adsorption, which was explained by the increased flexibility granted to Ti-O bonds. This is because fewer O per TiO_x unit are constrained by bonding alkali adsorbates, which in turn leads to a greater number of positional and electronic degrees of freedom in the TiO_x units, thus allowing for a lower energy bonding configuration to be attained. It also seems that surfaces with outmost layers composed of $TiO_5[]$ units produce stronger adsorption than those composed of TiO_4 units. This was proposed in Chapter 7 to be because TiO_4 units firstly are unreactive, and secondly make bonding in the layer beneath more bulk-like, thus passivating the surface. An outermost surface layer of $TiO_5[]$ units, on the other hand, produces less bulk-like bonding, thus yielding effects like increases Ti-O covalency and higher surface energy. It was therefore suggested that the $(6\times6)B$ reconstruction may have a lower density of TiO_4 units, hence a high concentration of unsaturated O 2p orbitals compared to other reconstructions, producing higher surface energy and consequently greater Na adhesion.

DFT calculations also indicate that there are subtleties to surface bonding that are not readily explained by the simple TiO_x unit based considerations above. This is evidenced

by the unique behaviour of the $(111)-(2\times2)$ reconstruction (Chapters 7 and 8). The other (111) reconstruction, namely (3×3), exhibits the same behaviour as $(001)-c(4\times2)$ (Chapters 5 and 6) and $(110)-(4\times1)$ (Appendix II), where surface energy is reduced by bonding that is more bulk-like. This is expressed by lower surfaces energies resulting from Ti and O BVS closer to formal oxidation states and O 2p and Ti 3d orbitals at the lowest possible energies. For $(111)-(2\times2)$, on the other hand, the stronger the adsorption of a given site, the closer Ti and O BVS values are to +3 and -1 respectively, and the higher the energy level of Ti 3d and O 2p orbitals. This suggests that $(111)-(2\times2)$ attains lower surface energy by delocalising electrons in the surface, and vice versa for $(001)-c(4\times2)$, $(110)-(4\times1)$, and $(111)-(3\times3)$. Different $SrTiO_3$ reconstructions hence appear to lower their surface energies by altering bonding in diametrically opposite ways, which illustrates that subtle structural differences may produce signifiant consequences for electronic structure that dramatically alter the interaction between oxide surfaces and alkali adsorbates.

9.2.2 Surface Structure Alterations

Two mechanisms by which alkali metals alter the structure of $SrTiO_3$ surfaces were observed: reconstruction induction and defect formation, where the latter entails step edges and surface layer cavities. Both mechanisms are active on (001) as well as (111) surfaces, but the prevalence of one mechanism compared to the other differs between terminations. Each mechanism will be given a separate treatment before a comparison is made at the end of this subsection.

9.2.2.1 Reconstruction Induction

Among the various $SrTiO_3$ reconstructions observed during the course of this project, some are previously undiscovered. All newly observed reconstructions are revealed in the experiment investigating $0 < 0.1$ ML Li on (111) and are specifically those named $(4\times4)\delta$, $(5\times5)\delta$, $(6\times6)\delta$, and $(5\times5)\gamma$ (Chapter 8). The δ reconstructions form after annealing temperatures between 400 ^oC and 600 ^oC and have two noteworthy aspects; firstly, they all transform from different original reconstructions, and secondly, they maintain the periodicity of the original. Thus (4×4), (5×5), and (6×6) produce $(4\times4)\delta$, $(5\times5)\delta$, and $(6\times6)\delta$, respectively. $(5\times5)\gamma$ is generated at annealing temperatures above 700 ^oC, which was also

observed for 1.0 < 2.0 ML Na coverage on (111) after 800 ^oC annealing (Chapter 7). New information has, in addition, been acquired about the character and formation of already known $SrTiO_3$ reconstructions. $(\sqrt{5}\times\sqrt{5})R26.6^o$ had already been reported, however, this project shows that its formation is due to surface region reduction in general, and not dependent on O vacancy formation specifically. New information was also gained regarding a $SrTiO_3$(111) reconstructions that is not alkali reduction induced, namely (6×6). It was confirmed that (111) has two distinct reconstructions with this periodicity, which were named $(6\times6)A$ and $(6\times6)B$. This distinction was, to the best knowledge of the author, not previously established.

Induced reconstructions should form as the highly reductive environment created by Li and Na increases O chemical potential to a point where the induced reconstruction becomes more stable than the original. Reduction increases O chemical potential due to alkali metals bonding to O, which deprives Ti atoms of O bonds and thus increases the energetic penalty for further O removal. The ensuing transformation may in simple terms be understood by the relationship $G_\alpha - G_\beta = \Delta G = V\Delta p - S\Delta T + \sum_i \mu_i \Delta n_i$, where G, V, p, S, T, and μ, are the usual quantities free energy, volume, pressure, entropy, and temperature, respectively, n is the number of the chemical species i, and α and β are two distinct reconstructions. Changes in O chemical potential may consequently alter which reconstruction yields the lower free energy, which explains the observed transformations.

STM and XPS data of the (111) termination in combination, furthermore, indicate that the lower annealing temperature transformation that produces the δ reconstructions ensues at a lower degree of reduction, while the higher annealing temperature transformation that produces $(5\times5)\gamma$ ensues at a higher degree of reduction. XPS data from Chapters 7 and 8 show that for both Li and Na samples annealed to 600 ^oC, the total amount of reduced Ti at the colder end of the sample is no greater than $10\% \pm 5\%$ for either alkali metal, while in hotter regions, the reduced Ti signal may be as strong as $40\% \pm 10\%$. This increased Ti reduction is accompanied by an increased fraction of the valence band being due to non-bonding states and the emergence of band gap states. The mechanism behind this enhanced reduction at elevated annealing temperatures was proposed to be alkali metal intercalation, although it was recognised that this assessment is not conclusive, and that

Li_2O and Na_2O sublimation is an alternative. If intercalation is at play, then alkali metals bonding to O atoms from interstitial sites would likely force charge transfer to Ti 3d due to the bulk atoms having more restrictive coordination environments than surface atoms. Based on the annealing temperatures after which the δ reconstructions were observed in STM versus those that produced $(5 \times 5)\gamma$, it would seem that the enhanced reduction drives the transformation from δ reconstructions to (5×5)γ. This would mean that (5×5)γ forms at a higher O chemical potential than the δ reconstructions. In addition, the fact that $(5 \times 5)\gamma$ is created by both Li and Na exposure constitutes evidence that it is a pure $SrTiO_3$ reconstruction that does not incorporate either alkali metal into its atomic structure. These two reconstruction transformations on (111) have an interesting (001) parallel, which also sees two distinct transformations. First, $(001) - c(4\times2)$ is transformed to $(\sqrt{5} \times \sqrt{5}) - R26.6$ after annealing temperature similar to those that produce the δ reconstructions on (111). Then, the surface that was called the high-T surface (Chapters 5 and 6) is produced after annealing temperatures similar to those that generate (5×5)γ on (111). It thus seems that both (001) and (111) terminations undergo two distinct surface transformations, which could be explained by the lower temperature one being caused by reduction of only the outermost surface layers as alkali metals bond to the surface, while the latter ensues when the entire surface region is reduced, which most likely is a consequence of alkali metal insertion into the bulk.

9.2.2.2 Defect Formation

The defects formed due to alkali metal exposure include cavities, which are created by the removal of less than a dozen TiO_x units from the surface layer, and step edge holes or islands less than 10 nm in diameter. Both these defects were proposed to result primarily from O coordination effects. As alkali metals bond O in the surface, they increase O coordination, which may cause O over-coordination and thus destabilise TiO_x units to a point where they dissolve. Cavities were observed primarily for $0 < 0.1$ ML Li on $(001) - c(4 \times 2)$ after 400 ^oC to 600 ^oC annealing (Chapter 6), but are also observed for $1.0 < 2.0$ ML Na on $(111) - (5 \times 5)$ after 800 ^oC annealing (Chapter 7). Cavities are, furthermore, proposed to be stabilised by alkali metal decoration, because they are suspected to host coordination environments where O has lower coordination than on surface terraces due to a lack of Ti bonds in two directions. This lower O coordination

should produce preferential alkali metal adsorption sites by allowing alkali metals access to O in two planes, as well as to O with lower coordination with which they can produce stronger bonds without causing over-coordination. This O under-coordination argument is also proposed to explain step edge holes and islands, as they should be stabilised by alkali metal decoration. Step edge islands were observed for $0 < 0.3$ ML Li on $(001) - c(4\times2)$ up to 700 ^oC annealing (Chapter 6), and step edge holes were observed for $0 < 0.3$ ML Na on $(001) - c(4\times2)$ up to 700 ^oC annealing (Chapter 5), for $1.0 < 2.0$ ML Na on $(111) - (5\times5)$ after 800 ^oC annealing (Chapter 7), as well as for $0 < 0.1$ ML Li on $(111) - (4\times4)\delta$ after 500 ^oC annealing (Chapter 8).

9.2.2.3 Reconstruction Induction versus Defect Formation

The extent to which alkali metals cause reconstruction induction versus defect formation in $SrTiO_3$ surfaces seems to depend primarily on termination. The (001) termination appears to have a much greater proclivity towards defect formation, whereas (111) seemingly favours reconstruction induction. As displayed in Chapters 5 and 6, both Li and Na on $SrTiO_3(001)$ substantially increase the step edge density, with Li additionally causing the formation of cavities. These defects are, however, often accompanied by the $(\sqrt{5}\times\sqrt{5}) - R26.6^o$ reconstruction. Chapters 7 and 8 show that this situation is reversed for Li and Na on $SrTiO_3(111)$, with reconstruction induction being significantly more prominent. This is primarily displayed by Li, which induces four new reconstructions, all completely dominating the region where they form. Defect formation is, however, still observed on some (111) surfaces, most notably in the form of holes caused by $0 < 0.1$ ML Li on $(111) - (4\times4)\delta$ after 400 ^oC annealing and $1.0 < 2.0$ ML Na on $(111) - (5\times5)$ after 800 ^oC annealing. The greater proclivity of (001) than (111) to form step edges can be explained by considering surface energy. On (001), the planes perpendicular to the surface normal that become exposed by step edge formation are, like the surface plane, of the $\{001\}$ type. On (111), however, the exposed planes are of the $\{01\overline{1}\}$ type, which may have higher surface energy. This would mean that step edge formation on (111) incurs a greater energetic penalty relative to (001), impeding this mechanism to a greater extent. The greater tendency of the (111) termination to induce reconstructions is likely related to its greater complexity compared to (001)[104]. The larger number of symmetries in the hexagonal 2D Bravais lattice of (111) grants it a larger number of possible surface struc-

tures[10]. (111) is consequently likely to host a greater number of reconstructions within a given surface energy range than (001), which is exemplified by its clean surface exhibiting the coexistence of multiple reconstructions whereas (001) does not. (111) should thus be able to more readily form a metastable reconstruction with lower surface energy as a response to changes in O chemical potential, making this mechanism more active than on (001). It should be noted that the arguments presented here regarding lower step edge formation energy on (001) and greater reconstruction variety on (111) are not specific to $SrTiO_3$ and should hold for oxide surfaces in general.

9.2.3 Bulk Termination Stabilisation

Among all structures observed during the course of this project, the flat lakes from Chapter 8 are uniquely peculiar. They have three features that can be known with a high degree of confidence; firstly, they are so flat that across tens of nanometres, no point diverges from the mean height by more than 0.04 nm. Secondly, they have $SrTiO_3(111) - (1\times1)$ ordering. Thirdly, they produce a moiré pattern with a periodicity equivalent to $SrTiO_3(111) - (4\sqrt{3}\times4\sqrt{3}) - R30^o$. The extreme flatness, together with the (1×1) ordering, indicate that the lakes are produced by a bulk termination. $SrTiO_3(111)$ bulk terminations are, however, highly unstable due to polarity in the bulk crystal along the [111] direction producing a uncompensated surface dipole moment. (1×1) ordering should, as a consequence, only be possible if a mechanism cancelling this dipole is present, which could be provided by a Li overlayer. The presence of an overlayer is, furthermore, reasonably established by the moiré pattern, which can only form by coincidence epitaxy between two superimposed lattices. It was thus proposed than an Li-based overlayer stabilises a $SrTiO_3(111) - (1\times1)$ bulk termination and consequently yields a moiré pattern. This conclusion can be made with a high degree of certainty as it stands on clear data and an analysis based in well-established concepts. Furthermore, the simplest overlayer by which a $SrTiO_3(111) - (1\times1)$ may be stabilised is one composed of two Li adsorbates per unit cell on a SrO_3 bulk layer, which DFT calculations predict to be stable and to produce a STM height profile compatible with the extreme flatness experimentally observed. The overlayer was thus proposed to be Li_2.

The exact nature of the moiré pattern is, however, much less certain, and it should

be made clear that the favoured solution is only a tentative suggestion. The proposed solution was derived from the following ansatz; firstly, the density of Li along the moiré pattern vector is two per $SrTiO_3(111)$ unit cell, which must be the case for dipole moment cancellation. Secondly, there is an integer number of Li overlayer unit cells along the moiré pattern vector, which must be the case for coincidence epitaxy. This ansatz yields two candidate epitaxial relationships, where the preferred one was selected based on a qualitative, visual analysis. This final reliance on a visual judgement is why the proposed epitaxial relationship should be seen as a tentative hypothesis rather than a confident conclusion. Regardless of the exact character of the epitaxial relationship, the identity of the flat lakes as a polar bulk termination being stabilised by an alkali metal overlayer could be reasonably established, which constitutes a striking example of the variety of structures that can be produced when oxide surfaces interact with alkali metals.

9.3 Future Work

The research presented in this thesis was largely motivated by a desire to better understand the interface between alkali metal anodes and electrolytes in solid-state batteries. The direct applicability of its findings to battery research should not be overstated, as experiments were conducted under conditions more controlled than one could never hope to achieve in the operation of a battery cell. This being said, some findings do have relevance to key interface properties and could motivate further investigations. These properties are primarily chemical stability and adhesion, both of which have been shown to vary significantly depending on surface structure.

It has been shown that different $SrTiO_3$ surfaces have different stabilities against reaction with alkali metals. Na on $SrTiO_3(001)$ versus $SrTiO_3(111)$ provides the clearest example of this, as a coverage of $0 < 0.3$ ML Na on the former induces a new reconstructions and causes a high defect density, while on the latter, Na causes no notable structural modifications. The first recommendation for future work in the context of solid-state battery interfaces would thus be to investigate whether oxide crystal termination must be taken into account when assessing the chemical stability of an interface. It may be that reactivity is so dependent on oxide termination that one essentially must consider different terminations of the same electrolyte as different materials, with their own distinctive

reactivities and interphase formations.

It was, furthermore, demonstrated that different $SrTiO_3$ surfaces have different adhesion strengths to alkali metals. This is expressed, for example, by the higher adhesion of Li and Na to (001) than (111) at $1.0 < 2.0$ ML coverage. A second recommendation for future battery work would thus be an investigation into adhesion differences between different crystal terminations of the same oxide electrolyte, similar to the chemical stability study suggested above. If different crystal termination produce significantly different adhesion strengths to alkali metals, this could cause variations in ionic conductivity and morphological stability across the interface, which would enhance the likelihood of dendrite formation. Adhesion was, moreover, shown to be dependent also on reconstruction, which is most clearly displayed by Na having an overwhelming preference for the $(6\times6)B$ surface among $SrTiO_3(111)$ reconstructions. Based on DFT calculations, it was suggested variations in alkali metal adhesion between reconstruction may be due to the type and density of cation coordination polyhedra in the surface. Those surfaces that lack low-coordination cation polyhedra, such as TiO_4, in their outmost surface layers and instead have a high density of high-coordination polyhedra, such as $TiO_5[]$, are predicted to produce stronger alkali metal adhesion. Because low-coordination polyhedra are generated due to a low transition metal density in the surface[10], it may be possible that surface preparation conditions that enhance transition metal richness produce surface structures with higher alkali metal adhesion. A third and least recommendation would thus be to investigate whether transition metal enriched oxide electrolyte surfaces produce stronger alkali metal adhesion and hence improved battery performance.

The strongest recommendation for future work directly pertaining to surface science would focus on the potential of Li to stabilise bulk terminations. If this can be done for $SrTiO_3(111)$ via the mechanism proposed in Section 9.2.3, it is likely possible also for other polar oxide terminations. If Li can reliably stabilise bulk terminations of polar surfaces, it may be interesting to investigate the electronic and chemical properties of such systems. A second recommendation would be a systematic study of redox induced reconstruction transformations. This is inspired by the fact that sub-monolayer Li coverages have proven a potent method by which reconstruction transformations can be studied. If

one, for example, had a UHV chamber where both Li deposition and exposure to some extremely oxidising agent were possible, then one may be able to systematically investigate reconstruction transformations as a function of redox environment and annealing temperature. Such a study could extend the $SrTiO_3$ work of this thesis to also include heavily oxidising environments, and also include other well-known oxide surfaces, such as $TiO_2(110)$. This may be useful, as there currently is little in terms of a unified framework that explains the formation of oxide surface structures. This situation may be redeemed to some extent by a more extensive data set of reconstructions transformations.

I Formulas for Calculated Quantities

This appendix provides definitions of the central quantities used to compare the surfaces calculated in DFT. These quantities are adsorption energy, surface energy, bond valence sum, and band centra. Band centra refers to the centre of mass of the DOS of a given orbital. The following variables will be used:

E	Energy
E_a	Adsorption energy per adsorbate
E_s	Energy of the relaxed, clean $SrTiO_3$ surface slab
E_{alk}	Energy of a single alkali metal atom
N_A	Number of alkali metal adsorbates
E_{s+alk}	Energy of alkali metal adsorbed surface
γ	Surface energy
E_{STO}	Energy of one $SrTiO_3$ bulk unit cell
E_{TO}	Energy of one rutile TiO_2 unit cell
N_{STO}	Number of $SrTiO_3$ bulk unit cells
N_{TO}	Surface excess of TiO_2
$N_{1\times1}$	Number of (1×1) surface unit cells in the surface
N_B	Number of bonds around a given atom
BVS	Bond valence sum
BV	Bond valence
R	Calculated bond distance
R_0	Standard bond distance taken from the database in reference [217]
b	An empirical constant equal to 0.37, as is common in the literature[35]
DOS	Density of states
BC	Band centrum

A large, negative E_a value thus indicates a strong adsorption bond. E_{alk} was calculated by dividing the relaxed energy of a BCC alkali metal unit cell by the number of atoms in the unit cell. $N_{1\times1}$ is modified by a factor of 2 because the surface slab used in the calculation has two sides.

Adsorption energy[40,61]

$$E_a = \frac{E_{s+alk} - (E_s + N_A E_{alk})}{N_A} \tag{24}$$

Surface energy[51]

$$\gamma = \frac{E_s - E_{STO}N_{STO} - E_{TO}N_{TO}}{2N_{1\times1}} \tag{25}$$

BVS[35]

$$BVS = \sum_{i}^{N_B} BV_i \tag{26}$$

$$BV = exp\Big(\frac{R_0 - R}{b}\Big) \tag{27}$$

Band centrum

$$BC = \frac{\int DOS(E)E\,dE}{\int DOS(E)\,dE} \tag{28}$$

II Overview of DFT Calculations

II.i Introduction

This appendix serves two purposes; firstly, it presents DFT results excluded from Chapters 5-8 as they pertain to the (110) termination, which was not studied in STM, and secondly, it provides an overview of all $SrTiO_3$ calculations results. All reconstructions on which Li and Na adsorption was calculated are listed in Table 3, together with the publications from which their surface structures were taken. The $(110) - (4\times1)$ reconstruction will be given special attention in this appendix due to its similar size to $(001) - c(4\times2)$ and $(111) - (2\times2)$, making these three surface suitable for comparisons. $(110) - (4\times1)$ is thus given a adsorption site presentation similar to those provided for $(001) - c(4\times2)$, $(111) - (2\times2)$, and $(111) - (3\times3)$ in Chapters 5-8.

II.ii Overview of Reconstructions

Termination	Reconstruction	Source Publication
(001)	$c(4\times2)$	[109]
(110)	(3×1)	[12]
(110)	(4×1)	[12]
(110)	(5×1)	[12]
(111)	(2×2)	[103]
(111)	(3×3)	[103]

Table 3: Calculated reconstructions and their source publications.

Reconstruction	γ (eV/Å^2)	$\Delta_{O2p,Ti3d}$ (eV)	Ti_{BVS}	O_{BVS}	E_{Na}^{max} (eV)	E_{Li}^{max} (eV)
$(001) - c(4\times2)$	0.046	1.31	3.86	1.95	-5.17	-6.48
$(110) - (3\times1)$	0.027	1.52	3.89	1.95	-4.50	-4.86
$(110) - (4\times1)$	0.023	1.51	3.87	1.94	-3.86	-5.12
$(110) - (5\times1)$	0.026	1.49	3.80	1.90	-3.89	-4.98
$(111) - (2\times2)$	0.050	1.32	3.61	1.77	-5.54	-6.23
$(111) - (3\times3)$	0.035	1.61	3.83	1.90	-3.83	-3.32

Table 4: Overview of key data for calculated reconstructions on the (001), (110), and (111) terminations of $SrTiO_3$. γ is surface energy, $\Delta_{O2p,Ti3d}$ is O 2p and Ti 3d band centra separation, Ti_{BVS} is average Ti BVS, and O_{BVS} is average O BVS. E_{Na}^{max} and E_{Li}^{max} are the maximum adsorption strengths achieved by any adsorption site for Na and Li, respectively, among all calculations conducted of the surface in question. Six initial positions were tested for $c(4\times2)$, five for (3×1), six for (4×1), five for (5×1), seven for (2×2), and five for (3×3).

Table 4 shows an overview of key data from adsorption calculations of six $SrTiO_3$ reconstructions. One notable feature is that O 2p-Ti 3d separation generally decreases

as surface energy increases, indicating that O 2p-Ti 3d hybridisation and thus covalency is enhanced by increased surface energy. This is most notable for $(001) - c(4\times2)$ and $(111) - (2\times2)$, which have the greatest surface energies as well as degree of covalency according to O 2p-Ti 3d separation, and also yield the greatest adsorption strengths for both Na and Li. (2×2) stand out by having significantly lower effective oxidation state magnitudes, as indicated by Ti and O BVS values, which will be further investigated in Section II.iv. The (110) reconstructions have the lowest surface energies, which may produce the expectation that they should have weakest Na and Li adsorption strengths. This is however not the case as $(111) - (3\times3)$ yields a clearly lower adsorption strength for Li. Despite the higher surface energy of $(111) - (3\times3)$ compared to (110) reconstructions, it seemingly has the highest degree of ionicity and most bulk-like O 2p-Ti 3d bond, which may reduce its driving force to bond with alkali adsorbates if surface energy reduction is driven by producing more bulk-like bonding.

II.iii Li and Na Adsorption Sites on $SrTiO_3(110) - (4\times1)$

Reconstructions on $SrTiO_3(110)$ are exemplified by the $(n\times1)$ homologous series reconstructions, which were described in Chapter 2. They consist of units of TiO_4 arranged on an outermost bulk-like layer of $SrTiO$, where TiO_4 is organised into two rings; one small consisting of six TiO_4 units, and one large, the size of which varies with the value of n. The $SrTiO_3(110) - (4\times1)$ reconstruction will be used to represent the interactions between alkali metals and this class of surfaces. Four types of adsorption sites were identified on this surface, which following the same naming convention as in Chapters 5-8 are referred to as atop, floor, side, and between. These adsorption sites are displayed in Figure 102.

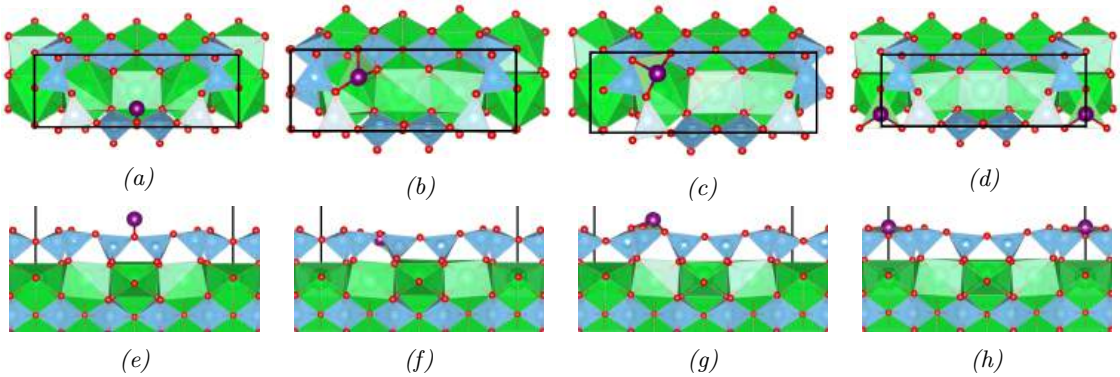

Figure 102: Adsorption sites on $SrTiO_3(110)-(4\times1)$ for Li and Na, showing the atop, floor, side and between sites from the top view in a), b), c), and d), respectively, and form the side view in e), f), g), and h), respectively. Green, blue, red, and purple balls are Sr, Ti, O and alkali adsorbate, respectively. Green, blue, and yellow polyhedra represent O coordination around Sr, Ti and alkali adsorbate, respectively. The $SrTiO_3(110)-c(4\times1)$ surface unit cell is marked by the black diamond. The atop site is coordinated by one O and all other sites by three O. The number of coordinating TiO_4 units for the atop, floor, side and between sites is two, four, four, and six, respectively. In the floor site, the alkali adsorbate bonds one O in the SrTiO layer surface, while adsorbates in all other sites only bond TiO_4 units in the outermost surface layer. The side site was only obtained for Li as Na from the same initial position relaxed into the floor site.

II.iv Adsorption Site Comparison

Figures 103 and 104 show key bonding data for Na and Li on $c(4\times2)$, (2×2), and (4×1). For each reconstruction, the most preferred adsorption site is the between site, where alkali adsorbates are coordinated by six TiO_x units. The second most preferred site for Li is the side site, which are similar to between sites, but lack coordinating TiO_x units in one direction, producing a total TiO_4 coordination of four. This site was not observed for Na. The third most preferred site is either the floor or above sites. These two sites attain a high TiO_x coordination, as high as five at the above site on $c(4\times2)$, however, above sites bond at least three O from the same TiO_x unit, which should impede Ti-O bond adjustment to accommodate the alkali adsorbate. The floor sites bonds alkali adsorbates to O that are shared with Sr atoms, which have rigid positions and effective charges. This is likely the cause for their lower adsorption energy. The least preferred sites are the atop sites, which bond a single O and are coordinated by two TiO_4 units. It thus seems that maximising coordination of TiO_x units, minimising the number of O the alkali adsorbate shares with any single TiO_x unit, and minimising Sr screening leads to the greatest adsorption energies.

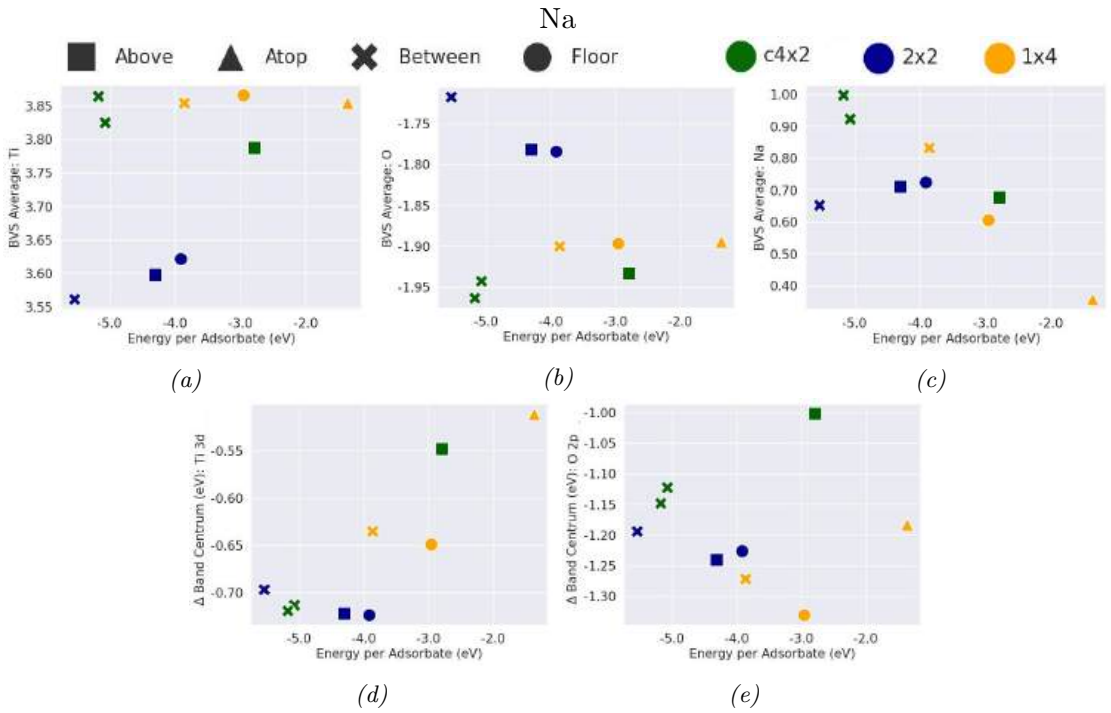

Figure 103: Bonding data for Na adsorption on c(4×2), (2×2), and (4×1), showing a) surface Ti BVS, b) surface O BVS, c) Na BVS, d) change in Ti 3d band centrum versus the clean surface, and e) change in O 2p band centrum versus the clean surface.

Alkali adsorbates, furthermore, seem to form stronger adsorption bonds neighbouring TiO_5[] units than TiO_4 units, which was already noted in Chapters 7 and 8 when comparing adsorption energies on (2×2) to (3×3). This behaviour seems to hold for (4×1) as well, as this reconstruction produced consistently lower adsorption energies than $c(4\times2)$ and (2×2). This behaviour can be discerned from the BVS data, in particular the O BVS data in Figures 103b and 104b. O BVS values for (4×1) do not diverge by more than ±0.01 between sites that differ up to 3.0 eV in adsorption energy, whereas O BVS values for (2×2) diverge up up to 0.1. This indicates that O in TiO_4 units are more constrained in their ability to change bond lengths. This is, furthermore, also likely the reason why the (4×1) surface consistently shows weaker adsorption strength at increasing alkali metal coverage, as per Figure 105, since it seems that TiO_4 units make the (4×1) surface more inert than $c(4\times2)$ and (2×2).

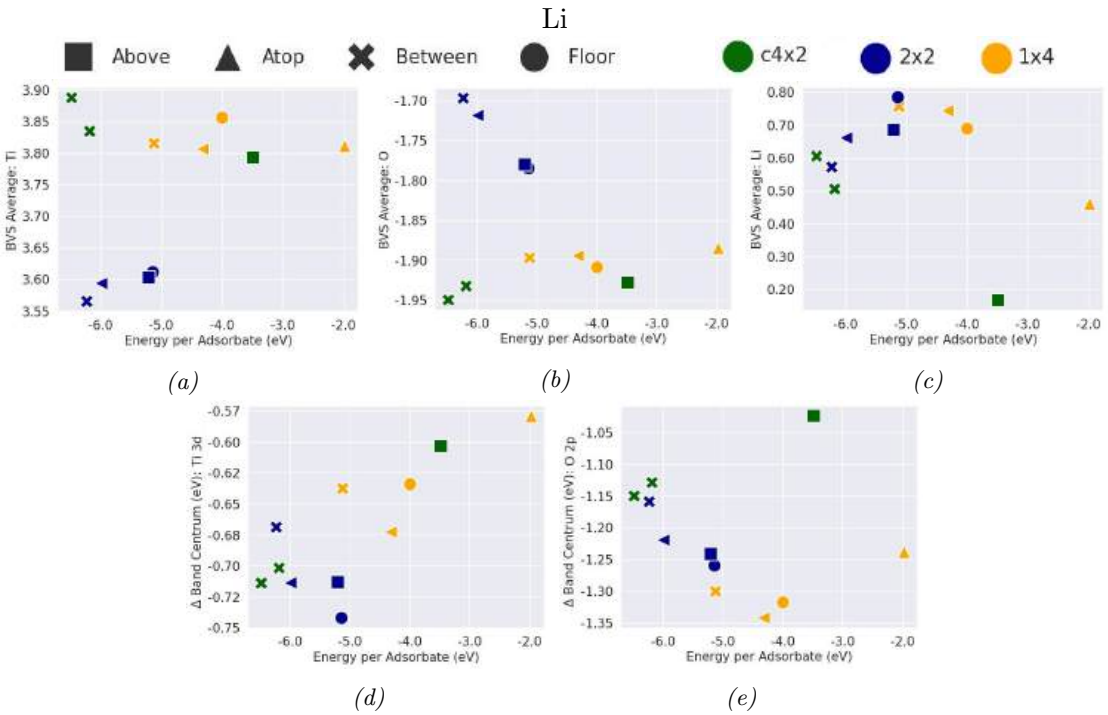

Figure 104: Bonding data for Li adsorption on $c(4\times2)$, (2×2), and (4×1), showing a) surface Ti BVS, b) surface O BVS, c) Li BVS, d) change in Ti 3d band centrum versus the clean surface, and e) change in O 2p band centrum versus the clean surface.

The difference in response of Ti and O bonding between reconstructions is most evident when comparing $c(4\times2)$ and (2×2), which display opposite trends both in band centrum movement and BVS, as displayed in Figures 103a-103e and 104a-104e. For both Li and Na, the Ti and O BVS values for more preferred sites approach +4 and -2 in the case of $c(4\times2)$, respectively, and +3 and -1 in the case of (2×2), respectively. Similarly, the BVS values of Na and Li move aggressively towards +1 as adsorption strength increases for both $c(4\times2)$ and (4×1), but decreases towards 0 for (2×2). Simultaneously, both Ti 3d and O 2p band centra for more preferred adsorption sites move to lower energy levels for $c(4\times2)$, whereas they move towards higher energy values for (2×2). It thus seems that the $c(4\times2)$ surface is stabilised by increasing the Ti, O, and Li oxidation state magnitude towards their formal oxidation states, which leads to more strongly bound Ti 3d and O 2p orbitals that acquire lower lying energy levels. (2×2), on the other hand, decreases Ti, O, and Li oxidation state magnitudes, which causes Ti 3d and O 2p orbitals to become less bound to their atoms and acquiring higher energy levels. This is indicative of electrons becoming more delocalised for stronger adsorption on (2×2), while they become more localised for stronger adsorption on $c(4\times2)$.

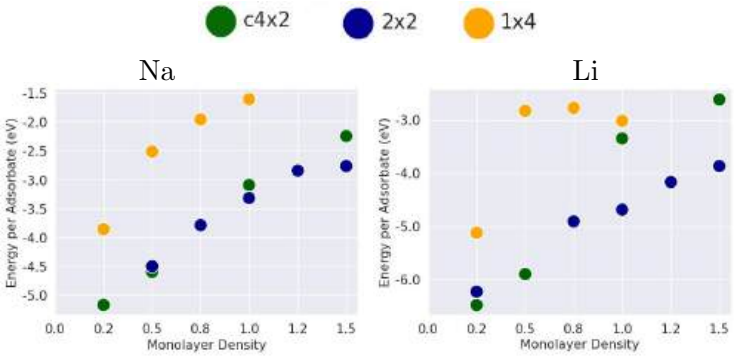

Figure 105: Li and Na at coverages of up to 1.5 ML on c(4×2)*,* (2×2)*, and* (4×1)*. Adsorption energy decreases with each increase in coverage, wiht the exception of 1.0 ML Li on* (4×1)*.* (2×2) *produces the greatest adhesion at coverages above 0.8 ML both in the case of Li and Na.*

References

1. Klauber, C & Smart, R. C. S. in *Surface Analysis Methods in Materials Science* 3–69 (Springer, 2003).

2. Alvarez, J & Asensio, M. C. in *Studies in Surface Science and Catalysis* A79–A159 (Elsevier, 1990).

3. Desjonqueres, M. & Spanjaard, D. in *Concepts in Surface Physics* 1–3 (Springer, 1998).

4. Lin, X. *et al.* Quantum Well States in Two-dimensional Gold Clusters on MgO Thin Films. *Physical Review Letters* **102,** 206801 (2009).

5. Silly, F. & Castell, M. R. Bimodal Growth of Au on $SrTiO_3$(001). *Physical Review Letters* **96,** 086104 (2006).

6. Chen, P., Silly, F., Zhao, Y. & Castell, M. R. Transition Volumes from Multiply Twinned Particles to Single Crystals of Supported Ag and Au Nanoparticles. *Applied Physics Letters* **121,** 061604 (2022).

7. Lee, K. D., Kim, C. Y. & Chung, J. W. Evidence of Substrate Metallization by Li Adsorption on the Si(001) Surface. *Surface Science* **366,** 709–714 (1996).

8. Shaltaf, R., Mete, E. & Ellialtioglu, S. Cs Adsorption on Si(001) Surface: an Ab Initio Study. *Physical Review B* **72,** 205415 (2005).

9. Eriksson, P. E., Sakamoto, K. & Uhrberg, R. I. Lithium-induced Dimer Reconstructions on Si(001) Studied by Photoelectron Spectroscopy and Band-structure Calculations. *Physical Review B* **75,** 205416 (2007).

10. Andersen, T. K., Fong, D. D. & Marks, L. D. Pauling's Rules for Oxide Surfaces. *Surface Science Reports* **73,** 213–232 (2018).

11. Diebold, U. The Surface Science of Titanium Dioxide. *Surface Science Reports* **48,** 53–229 (2003).

12. Enterkin, J. A. *et al.* A Homologous Series of Structures on the Surface of $SrTiO_3$(110). *Nature Materials* **9,** 245–248 (2010).

13. Henrich, V. E. & Cox, P. A. in *The Surface Science of Metal Oxides* 14–74 (Cambridge University Press, 1994).

14. Kittel, C. in *Introduction to Solid State Physics* 487–514 (Wiley, 2004).

15. Sutton, A. P. & Balluffi, R. W. in *Interfaces in Crystalline Materials* 396–409 (Clarendon Press, 1995).

16. Tabor, D. Solid Surfaces: Their Atomic, Electronic and Macroscopic Properties. *Contemporary Physics* **22,** 215–234 (1981).

17. Tsukada, M & Adachi, H. Theory of Electronic Structure of Oxide Surfaces. *Progress in Surface Science* **14,** 113–174 (1983).

18. Ashcroft, N. & Mermin, N. D. in *Solid State Physics* 353–371 (Saunders College Publishing, 1976).

19. Michaelides, A. & Scheffler, M. in *Surface and Interface Science* 13–72 (Wiley-VCH, 2012).

20. Janek, J. & Zeier, W. G. A Solid Future for Battery Development. *Nature Energy* **1,** 16141 (2016).

21. Famprikis, T., Canepa, P., Dawson, J. A., Islam, M. S. & Masquelier, C. Fundamentals of Inorganic Solid-state Electrolytes for Batteries. *Nature Materials* **18,** 1278–1291 (2019).

22. Luntz, A. C., Voss, J. & Reuter, K. Interfacial Challenges in Solid-State Li Ion Batteries. *Journal of Physical Chemistry Letters* **6,** 4599–4604 (2015).

23. Wang, Y. *et al.* Design Principles for Solid-state Lithium Superionic Conductors. *Nature Materials* **14,** 1026–1031 (2015).

24. Boulineau, S., Tarascon, J. M., Leriche, J. B. & Viallet, V. Electrochemical Properties of All-solid-state Lithium Secondary Batteries Using Li-argyrodite Li_6PS_5Cl as Solid Electrolyte. *Solid State Ionics* **242,** 45–48 (2013).

25. Li, J., Ma, C., Chi, M., Liang, C. & Dudney, N. J. Solid Electrolyte: The Key for High-voltage Lithium Batteries. *Advanced Energy Materials* **5,** 1401408 (2015).

26. Xiao, Y. *et al.* Understanding Interface Stability in Solid-state Batteries. *Nature Reviews Materials* **5,** 105–126 (2020).

27. Dai, J., Yang, C., Wang, C., Pastel, G. & Hu, L. Interface Engineering for Garnet-Based Solid-State Lithium-Metal Batteries: Materials, Structures, and Characterization. *Advanced Materials* **30,** 1802068 (2018).

28. Wood, K. N., Noked, M. & Dasgupta, N. P. Lithium Metal Anodes: Toward an Improved Understanding of Coupled Morphological, Electrochemical, and Mechanical Behavior. *ACS Energy Letters* **2,** 664–672 (2017).

29. Zhang, W. *et al.* (Electro)chemical Expansion during Cycling: Monitoring the Pressure Changes in Operating Solid-state Lithium Batteries. *Journal of Materials Chemistry A* **5,** 9929–9936 (2017).

30. Krauskopf, T., Richter, F. H., Zeier, W. G. & Janek, J. Physicochemical Concepts of the Lithium Metal Anode in Solid-State Batteries. *Chemical Reviews* **120,** 7745–7794 (2020).

31. Wang, M., Wolfenstine, J. B. & Sakamoto, J. Temperature Dependent Flux Balance of the Li/$Li_7La_3Zr_2O_{12}$ Interface. *Electrochimica Acta* **296,** 842–847 (2019).

32. Kasemchainan, J. *et al.* Critical Stripping Current Leads to Dendrite Formation on Plating in Lithium Anode Solid Electrolyte Cells. *Nature Materials* **18,** 1105–1111 (2019).

33. Lou, J. *et al.* Achieving Efficient and Stable Interface between Metallic Lithium and Garnet-type Solid Electrolyte through a Thin Indium Tin Oxide Interlayer. *Journal of Power Sources* **448,** 227440 (2019).

34. Tsai, C. L. *et al.* $Li_7La_3Zr_2O_{12}$ Interface Modification for Li Dendrite Prevention. *ACS Applied Materials and Interfaces* **8,** 10617–10626 (2016).

35. Enterkin, J. A., Becerra-Toledo, A. E., Poeppelmeier, K. R. & Marks, L. D. A Chemical Approach to Understanding Oxide Surfaces. *Surface Science* **606,** 344–355 (2012).

36. Erdman, N. *et al.* The Structure and Chemistry of the TiO_2-rich Surface of $SrTiO_3$(001). *Nature* **419,** 55–58 (2002).

37. Marks, L. D., Chiaramonti, A. N., Tran, F. & Blaha, P. The Small Unit Cell Reconstructions of $SrTiO_3$(111). *Surface Science* **603,** 2179–2187 (2009).

38. Noguera, C. Polar Oxide Surfaces. *J. Phys.: Condens. Matter* **12,** 367–410 (2000).

39. Goniakowski, J., Finocchi, F. & Noguera, C. Polarity of Oxide Surfaces and Nanostructures. *Reports on Progress in Physics* **71,** 016501 (2008).

40. Asthagiri, A. & Sholl, D. S. DFT Study of Pt Adsorption on Low Index $SrTiO_3$ Surfaces: $SrTiO_3$(100), $SrTiO_3$(111) and $SrTiO_3$(110). *Surface Science* **581,** 66–87 (2005).

41. Russell, B. C. & Castell, M. R. $(\sqrt{13} \times \sqrt{13})$R13.9^o and $(\sqrt{7} \times \sqrt{7})$R19.1^o Reconstructions of the Polar $SrTiO_3$(111) Surface. *Physical Review B* **75,** 155433 (2007).

42. Russell, B. C. & Castell, M. R. Surface of Sputtered and Annealed Polar $SrTiO_3$(111): TiO_x-Rich (n×n) Reconstructions. *Journal of Physical Chemistry C* **112,** 6538–6545 (2008).

43. Chiaramonti, A. N., Lanier, C. H., Marks, L. D. & Stair, P. C. Time, Temperature, and Oxygen Partial Pressure-dependent Surface Reconstructions on $SrTiO_3$(111): A Systematic Study of Oxygen-rich Conditions. *Surface Science* **602,** 3018–3025 (2008).

44. Radin, M. D., Rodriguez, J. F., Tian, F. & Siegel, D. J. Lithium Peroxide Surfaces Are Metallic, while Lithium Oxide Surfaces Are Not. *Journal of the American Chemical Society* **134,** 1093–1103 (2012).

45. Kaxiras, E. in *Atomic and Electronic Structure of Solids* 385–429 (Cambridge University Press, 2010).

46. Hamers, R. J. in *Materials Interfaces: Atomic-level Structure and Properties* 300–314 (Springer Netherlands, 1993).

47. Davison, S. G. & Steslicka, M. in *Basic Theory Of Surface States* 150–194 (Oxford Clarendon Press, 1992).

48. Winfried, M. in *Semiconductor Surfaces and Interfaces* 283–324 (Springer, 1993).

49. Pauling, L. The Principles Determining the Structure of Complex Ionic Crystals. *Journal of the American Chemical Society* **51,** 1010–1026 (1929).

50. Plato. in *Timaeus, Section I* (Project Gutenberg, 1998).

51. Cook, S. & Marks, L. D. Ab Initio Predictions of Double-Layer TiO_2-Terminated $SrTiO_3$(001) Surface Reconstructions. *Journal of Physical Chemistry C* **122,** 21991–21997 (2018).

52. Henrich, V. E. & Cox, P. A. in *The Surface Science of Metal Oxides* 102–156 (Cambridge University Press, 1994).

53. Wang, Z. *et al.* Transition from Reconstruction toward Thin Film on the (110) Surface of Strontium Titanate. *Nano Letters* **16,** 2407–2412 (2016).

54. Zangwill, A. in *Physics at Surfaces* 204–232 (Cambridge University Press, 1988).

55. Continenza, A., Li, C. & Freeman, A. J. in *Materials Interfaces: Atomic-level Structure and Properties* 275–299 (Springer, 1993).

56. Albaret, T., Finocchi, F., Noguera, C. & Vita, A. D. First-principles Study of the TiO_2(110) Surface Reduction upon Na Adsorption. *Physical Review B* **65,** 035402 (2002).

57. Marikutsa, A., Rumyantseva, M., Konstantinova, E. A. & Gaskov, A. The Key Role of Active Sites in the Development of Selective Metal Oxide Sensor Materials. *Sensors* **21,** 2554 (2021).

58. Woodruff, D. P. in *Chemical Bonding at Surfaces and Interfaces* 1–56 (Elsevier, 2008).

59. Osterwalder, J. in *Surface and Interface Science* 151–214 (Wiley-VCH, 2012).

60. Zangwill, A. in *Physics at Surfaces* 232–257 (Cambridge University Press, 1988).

61. Buchwald, J. & Hennes, M. Adsorption and Diffusion of Au, Pt, and Co Adatoms on $SrTiO_3$(001) Surfaces: A Density Functional Theory Study. *Surface Science* **701,** 121683 (2020).

62. Benedetti, S. *et al.* Growth and Morphology of Metal Particles on MgO/Mo(001): A Comparative STM and Diffraction Study. *Physical Review B* **83,** 125423 (2011).

63. Fu, Q. & Wagner, T. Metal/oxide Interfacial Reactions: Oxidation of Metals on $SrTiO_3$(100) and TiO_2(110). *Journal of Physical Chemistry B* **109,** 11697–11705 (2005).

64. Sutton, A. P. & Balluffi, R. W. in *Interfaces in Crystalline Materials* 350–393 (Clarendon Press, 1995).

65. Zhang, J., Yang, H. B., Zhou, D. & Liu, B. Adsorption Energy in Oxygen Electrocatalysis. *Chemical Reviews* **122,** 17028–17072 (2022).

66. Chen, P., Murugappan, K. & Castell, M. R. Shapes of Epitaxial Gold Nanocrystals on $SrTiO_3$ Substrates. *Physical Chemistry Chemical Physics* **22,** 4416–4428 (2020).

67. Winterbottom. Equilibrium Shape of a Small Particle in Contact with a Foreign Substrate. *Acta Metallurgica* **15,** 303–310 (1967).

68. Lai, F. *et al.* Surface Energy Prediction and Winterbottom Morphology Evolution Analysis in Winterbottom Construction on Various Crystal Orientations Using Machine Learning. *Materials Science and Engineering: B* **302,** 117240 (2024).

69. Packham, D. E. Work of Adhesion: Contact Angles and Contact Mechanics. *International Journal of Adhesion and Adhesives* **16,** 121–128 (1996).

70. Trampert, A., Ernst, F., Flynn, C. P., Fischmeister, H. F. & Rühle, M. High Resolution Transmission Electron Microscopy Studies of the Ag/MgO Interface. *Acta Metallurgica Et Materialia* **40,** 227–236 (1992).

71. Clarke, D. R & Gee, M. I. in *Materials Interfaces: Atomic-level Structure and Properties* 255–270 (Springer Netherlands, 1993).

72. Wang, J. *et al.* Fundamental Study on the Wetting Property of Liquid Lithium. *Energy Storage Materials* **14,** 345–350 (2018).

73. Sun, J. *et al.* Controlled Growth of Ni Nanocrystals on $SrTiO_3$ and Their Application in the Catalytic Synthesis of Carbon Nanotubes. *Chemical Communications* **49,** 3748–3750 (2013).

74. Chen, P., Gao, Y. & Castell, M. R. Experimental Determination of the {111}/{001} Surface Energy Ratio for Pd Crystals. *Applied Physics Letters* **117,** 5–8 (2020).

75. Souza, R. A. D., Metlenko, V., Park, D. & Weirich, T. E. Behavior of Oxygen Vacancies in Single-crystal $SrTiO_3$: Equilibrium Distribution and Diffusion Kinetics. *Physical Review B* **85,** 174109 (2012).

76. Silly, F., Powell, A. C., Martin, M. G. & Castell, M. R. Growth Shapes of Supported Pd Nanocrystals on $SrTiO_3$(001). *Physical Review B* **72,** 165403 (2005).

77. Myrach, P. *et al.* Temperature-Dependent Morphology, Magnetic and Optical Properties of Li-Doped MgO. *ChemCatChem* **2,** 854–862 (2010).

78. Sutton, A. P. & Balluffi, R. W. in *Interfaces in Crystalline Materials* 243–349 (Clarendon Press, 1995).

79. Silly, F. & Castell, M. R. Fe Nanocrystal Growth on $SrTiO_3$(001). *Applied Physics Letters* **87,** 9–11 (2005).

80. Silly, F. & Castell, M. R. Self-assembled Supported Co Nanocrystals: The Adhesion Energy of Face-centered-cubic Co on $SrTiO_3$(001)-(2×2). *Applied Physics Letters* **87,** 053106 (2005).

81. Egdell, R. G. in *Oxide Surfaces* 550–607 (Elsevier, 2001).

82. Henrich, V. E. & Cox, P. A. in *The Surface Science of Metal Oxides* 158–254 (Cambridge University Press, 1994).

83. Greiner, M. T., Chai, L., Helander, M. G., Tang, W. M. & Lu, Z. H. Transition Metal Oxide Work Functions: the Influence of Cation Oxidation State and Oxygen Vacancies. *Advanced Functional Materials* **22,** 4557–4568 (2012).

84. Evans, R. C. in *An Introduction to Crystal Chemistry* 136–177 (Cambridge University Press, 1965).

85. Wang, J. & Lefebvre, I. Germanium Adsorption and Initial Growth on $SrTiO_3$(001) Surface: A First-principles Investigation. *Journal of Physical Chemistry C* **115,** 22893–22900 (2011).

86. Bube, R. H. in *Electrons in Solids* 212–244 (Elsevier, 1992).

87. Ren, S. Y. in *Electronic States in Crystals of Finite Size* 51–67 (Springer, 2017).

88. Cahen, D. & Kahn, A. Electron Energetics at Surfaces and Interfaces: Concepts and Experiments. *Advanced Materials* **15,** 271–277 (2003).

89. Kahn, A. Fermi level, Work function and Vacuum level. *Materials Horizons* **3,** 7–10 (2016).

90. Kittel, C. in *Introduction to Solid State Physics* 47–88 (Wiley, 2004).

91. Tian, H. K., Liu, Z., Ji, Y., Chen, L. Q. & Qi, Y. Interfacial Electronic Properties Dictate Li Dendrite Growth in Solid Electrolytes. *Chemistry of Materials* **31,** 7351–7359 (2019).

92. Henrich, V. E. The Nature of Transition-metal-oxide Surfaces. *Progress in Surface Science* **14,** 175–200 (1983).

93. Kneedler, E, Skelton, D, Smith, K. E. & Kevan, S. D. Surface-State-Surface-Resonance Transition on Ta(011). *Physical Review Letters* **64,** 26 (1990).

94. Ehlen, N. *et al.* Direct Observation of a Surface Resonance State and Surface Band Inversion Control in Black Phosphorus. *Physical Review B* **97,** 045143 (2018).

95. Martinez, U., Giordano, L. & Pacchioni, G. Tuning the Work Function of Ultrathin Oxide Films on Metals by Adsorption of Alkali Atoms. *Journal of Chemical Physics* **128,** 164707 (2008).

96. Olson, C. L., Nelson, J. & Islam, M. S. Defect Chemistry, Surface Structures, and Lithium Insertion in Anatase TiO_2. *Journal of Physical Chemistry B* **110,** 9995–10001 (2006).

97. Tian, H. K., Xu, B. & Qi, Y. Computational Study of Lithium Nucleation Tendency in $Li_7La_3Zr_2O_{12}$ (LLZO) and Rational Design of Interlayer Materials to Prevent Lithium Dendrites. *Journal of Power Sources* **392,** 79–86 (2018).

98. Sutton, A. P. & Balluffi, R. W. in *Interfaces in Crystalline Materials* 657–673 (Clarendon Press, 1995).

99. Zangwill, A. in *Physics at Surfaces* 183–204 (Cambridge University Press, 1988).

100. Yu, C. *et al.* Accessing the Bottleneck in All-solid State Batteries, Lithium-ion Transport over the Solid-electrolyte-electrode Interface. *Nature Communications* **8,** 1086 (2017).

101. Castell, M. R. Nanostructures on the $SrTiO_3(001)$ Surface Studied by STM. *Surface Science* **516,** 33–42 (2002).

102. Deak, D. S., Silly, F., Newell, D. T. & Castell, M. R. Ordering of TiO_2-based Nanostructures on $SrTiO_3(001)$ Surfaces. *Journal of Physical Chemistry B* **110,** 9246–9251 (2006).

103. Marks, L. D., Chiaramonti, A. N., Rahman, S. U. & Castell, M. R. Transition from Order to Configurational Disorder for Surface Reconstructions on $SrTiO_3(111)$. *Physical Review Letters* **114,** 226101 (2015).

104. Andersen, T. K., Wang, S., Castell, M. R., Fong, D. D. & Marks, L. D. Single-layer TiO_x Reconstructions on $SrTiO_3(111)$: $(\sqrt{7} \times \sqrt{7})R19.1^o$ $(\sqrt{13} \times \sqrt{13})R13.9^o$ and Related Structures. *Surface Science* **675,** 36–41 (2018).

105. Becerra-Toledo, A. E., Enterkin, J. A., Kienzle, D. M. & Marks, L. D. Water Adsorption on $SrTiO_3(001)$: II. Water, Water, Everywhere. *Surface Science* **606,** 791–802 (2012).

106. Castell, M & Silly, F. Growth of Ag Icosahedral Nanocrystals on a $SrTiO_3(001)$ Support. *Applied Physics Letters* **87,** 213107 (2005).

107. Lin, Y. *et al.* The (2×2) Reconstructions on the $SrTiO_3(001)$ Surface: A Combined Scanning Tunneling Microscopy and Density Functional Theory Study. *Surface Science* **605,** L51–L55 (2011).

108. Gerhold, S., Wang, Z., Schmid, M. & Diebold, U. Stoichiometry-driven Switching between Surface Reconstructions on $SrTiO_3(001)$. *Surface Science* **621,** L1–L4 (2014).

109. Erdman, N. *et al.* Surface Structures of $SrTiO_3(001)$: A TiO_2-rich Reconstruction with a c(4×2) Unit Cell. *Journal of the American Chemical Society* **125,** 10050–10056 (2003).

110. Zhu, G. Z., Radtke, G. & Botton, G. A. Bonding and Structure of a Reconstructed (001) Surface of $SrTiO_3$ from TEM. *Nature* **490,** 384–387 (2012).

111. Kubo, T. & Nozoye, H. Surface Structure of $SrTiO_3(100)$. *Surface Science* **542,** 177–191 (2003).

112. Silly, F., Newell, D. T. & Castell, M. R. $SrTiO_3(001)$ Reconstructions: the (2×2) to c(4×4) Transition. *Surface Science* **600,** 219–223 (2006).

113. Newell, D. T., Harrison, A., Silly, F. & Castell, M. R. $SrTiO_3(001)$-(5×5)-R26.6^o Reconstruction: A Surface Resulting from Phase Separation in a Reducing Environment. *Physical Review B* **75,** 205429 (2007).

114. Kubo, T. & Nozoye, H. Surface Structure of $SrTiO_3(100)$-$(\sqrt{5}\times\sqrt{5})$R26.6^o. *Physical Review Letters* **86,** 1801–1804 (2001).

115. Kienzle, D. M., Becerra-Toledo, A. E. & Marks, L. D. Vacant-site Octahedral Tilings on $SrTiO_3(001)$, the $(\sqrt{13}\times\sqrt{13})$R33.7^o Surface, and Related Structures. *Physical Review Letters* **106,** 176102 (2011).

116. Becerra-Toledo, A. E., Castell, M. R. & Marks, L. D. Water Adsorption on $SrTiO_3(001)$: I. Experimental and Simulated STM. *Surface Science* **606,** 762–765 (2012).

117. Marsh, H. L., Deak, D. S., Silly, F., Kirkland, A. I. & Castell, M. R. Hot STM of Nanostructure Dynamics on $SrTiO_3(001)$. *Nanotechnology* **17,** 3543–3548 (2006).

118. Russell, B. C. & Castell, M. R. Reconstructions on the Polar $SrTiO_3$(110) Surface: Analysis Using STM, LEED, and AES. *Physical Review B* **77,** 245414 (2008).

119. Li, F. *et al.* Reversible Transition between Thermodynamically Stable Phases with Low Density of Oxygen Vacancies on the $SrTiO_3$(110) Surface. *Physical Review Letters* **107,** 036103 (2011).

120. Bando, H., Aiura, Y., Haruyama, Y., Shimizu, T. & Nishihara, Y. Structure and Electronic States on Reduced $SrTiO_3$(110) Surface Observed by Scanning Tunneling Microscopy and Spectroscopy. *Journal of Vacuum Science and Technology B: Microelectronics and Nanometer Structures* **13,** 1150–1154 (1995).

121. Brunen, J. & Zegenhagen, J. Investigation of the $SrTiO_3$(110) Surface by Means of LEED, Scanning Tunneling Microscopy and Auger Spectroscopy. *Surface Science* **389,** 349–365 (1997).

122. Benthem, K. V., Elsässer, C. & French, R. H. Bulk Electronic Structure of $SrTiO_3$: Experiment and Theory. *Journal of Applied Physics* **90,** 6156–6164 (2001).

123. Wei, W., Dai, Y., Guo, M., Zhu, Y. & Huang, B. Density Functional Theory Study of Ag Adsorption on $SrTiO_3$(001) Surface. *Journal of Physical Chemistry C* **114,** 10917–10921 (2010).

124. Silly, F. & Castell, M. R. Temperature-dependent Stability of Supported Five-fold Twinned Copper Nanocrystals. *ACS Nano* **3,** 901–906 (2009).

125. Nerlov, J., Christensen, S. V., Weichel, S., Pedersen, E. H. & Moiler, P. J. A Photoemission Study of the Coadsorption of CO_2 and Na on TiO_2(110)-(1×1) and-(1×2) Surfaces: Adsorption Geometry and Reactivity. *Surface Science* **371,** 321–336 (1997).

126. Lagarde, P., Flank, A. M., Prado, R. J., Bourgeois, S. & Jupille, J. The Defined Adsorption Site of Sodium on the TiO_2(110)-(1×1) Surface. *Surface Science* **553,** 115–125 (2004).

127. Suchorski, Y. & Rupprechter, G. Surface Science Studies of the Diffusion of Adsorbed and Intercalated Lithium. *Solid State Ionics* **316,** 143–152 (2018).

128. Vlachos, D., Giotopoulou, E., Foulias, S. D. & Kamaratos, M. Cesium Growth on the $SrTiO_3$(100) Surface. *Materials Research Express* **2,** 116501 (2015).

129. Somaratne, R. M. S. & Whitten, J. E. Metallization of TiO_2(110) with Gold and Lithium. *Journal of Physical Chemistry C* **125,** 26744–26754 (2021).

130. Mcgrath, R & Diehl, R. D. Current Progress in Understanding Alkali Metal Adsorption on Metal Surfaces. *J. Phys.: Condens. Matter* **9,** 951–968 (1997).

131. Evans, R. C. in *An Introduction to Crystal Chemistry* 79–110 (Cambridge University Press, 1965).

132. Moullet, I., Andreoni, W. & Parrinello, M. Alkali Adsorption on Si(111) Surfaces: Ab Initio Molecular Dynamics Studies. *Surface Science* **269-270,** 1000–1004 (1992).

133. Calzado, C. J., Miguel, M. A. S. & Sanz, J. F. Theoretical Analysis of K Adsorption on TiO_2(110) Rutile Surface. *Journal of Physical Chemistry* **103,** 480–486 (1999).

134. Shi, H. Q., Radny, M. W. & Smith, P. V. Atomic and Electronic Structure of the Si(001)2×1-Li Chemisorption System at 1.0 Monolayer Coverage. *Surface Science* **574,** 233–243 (2005).

135. Fiori, S. *et al.* Li-intercalated Graphene on SiC(0001): An STM Study. *Physical Review B* **96,** 1–8 (2017).

136. Lang, N. D. Theory of Work-Function Changes Induced by Alkali Adsorption. *Physical Review B* **4,** 4234–4243 (1971).

137. Hasegawa, Y. *et al.* Cluster Formation of Li on the Si(111)7×7 Surface. *Journal of Vacuum Science and Technology A: Vacuum, Surfaces, and Films* **8,** 238–240 (1990).

138. Strasser, P. & Ogasawara, H. in *Chemical Bonding at Surfaces and Interfaces* 397–448 (Elsevier, 2008).

139. Sakamoto, K. *et al.* Photoemission Study of the Si(111)3×1-K Surface. *Physical Review B* **50,** 1725–1732 (1994).

140. Fukuda, T. Determination of Silver Coverage on Si(111) 3×1(6×1)-Ag Surfaces. *Physical Review B* **50,** 1969–1972 (1994).

141. Hasegawa, S., Maruyama, M., Hirata, Y., Abe, D. & Nakashima, H. New Model for Si(111)-(3×1)Li through Determination of its Surface Si Atom Density with the Use of Scanning Tunneling Microscopy. *Surface Science* **405,** 503–508 (1998).

142. Hird, B & Armstrong, R. A. Determination of the Site of Na on TiO_2 Rutile (110)-(1×1) by Ion Shadowing/Blocking Measurements. *Surface Science* **431,** 570–576 (1999).

143. Miguel, M. A. S., Calzado, C. J. & Sanz, J. F. Modeling Alkali Atoms Deposition on TiO_2(110) Surface. *Journal of Physical Chemistry B* **105,** 1794–1798 (2001).

144. Bredow, T, Aprà, E, Catti, M & Pacchioni, G. Cluster and Periodic Ab-initio Calculations on K/TiO_2(110). *Surface Science* **418,** 150–165 (1998).

145. Tatsumi, H., Sasahara, A. & Tomitori, M. Lateral Distribution of Li Atoms at the Initial Stage of Adsorption on TiO_2(110) Surface. *Journal of Physical Chemistry C* **116,** 13688–13692 (2012).

146. Krischok, S., Schaefer, J. A., Höfft, O. & Kempter, V. Lithium Adsorption on TiO_2: Studies with Electron Spectroscopies (MIES and UPS). *Surface and Interface Analysis* **37,** 83–89 (2005).

147. Juan, J. *et al.* Theoretical Study of Li Intercalation in TiO_2(B) Surfaces. *Applied Surface Science* **526,** 146460 (2020).

148. Ding, K., Li, J., Zhang, Y. & Wang, W. A DFT Study for the Coadsorption of Na and NO on TiO_2(110) Surface. *Chemical Physics Letters* **389,** 255–260 (2004).

149. Uhl, B., Hekmatfar, M., Buchner, F. & Behm, R. J. Interaction of the Ionic Liquid [BMP][TFSA] with Rutile TiO_2(110) and Coadsorbed Lithium. *Physical Chemistry Chemical Physics* **18,** 6618–6636 (2016).

150. Stashans, A., Lunell, S., Bergström, R., Hagfeldt, A. & Lindquist, S.-E. Theoretical Study of Lithium Intercalation in Rutile and Anatase. *Physical Review B* **53,** 159–170 (1996).

151. Onishi, H., Aruga, T. & Egawa, C. Modification of Surface Electronic Structure on TiO_2(110) and TiO_2(441) by Na Deposition. *Surface Science* **199,** 54–66 (1988).

152. Mori, E. E. & Kamaratos, M. Adsorbtion Kinetics of Potassium on $SrTiO_3$(100). *Surface Review and Letters* **13,** 681–686.

153. Connell, J. G. *et al.* Crystal Orientation-Dependent Reactivity of Oxide Surfaces in Contact with Lithium Metal. *ACS Applied Materials and Interfaces* **10,** 17471–17479 (2018).

154. Wang, J., Li, Z. & Zou, Z. Na Adsorption on $SrTiO_3$(001) Surface and its Interaction with Water: A DFT Calculation. *Applied Surface Science* **270,** 359–363 (2013).

155. Mori, E. E. & Kamaratos, M. Lithium Adsorption on the $SrTiO_3$(100) Surface. *Journal of Physics Condensed Matter* **19,** 356001 (2007).

156. Ageev, V. N. & Solov'ev, S. M. Study of Lithium Adsorption on the TiO_2 Surface by Electron-Stimulated Desorption. *Low-Dimensional Systems and Surface Physics* **42,** 2159–2163 (2000).

157. Vlachos, D, Giotopoulou, E & Kamaratos, M. Adsorption of Water on a Cesium Covered $SrTiO_3$(100) Surface. *Proceedings of the International Conference on Nanomaterials* **3,** 15 (2014).

158. Onishi, H. & Iwasawa, Y. Atom-resolved Observation of Na Ensembles Activating CO_2 Adsorption on a TiO_2(110)-(1×1) Surface as the Genesis of Basic Sites. *Catalysis Letters* **38,** 89–94 (1996).

159. Grant, A. W. & Campbell, C. T. Cesium Adsorption on TiO_2(110). *Physical Review B* **55,** 1844–1851 (1997).

160. Kamaratos, M., Giotopoulou, E. & Vlachos, D. The Interaction Mechanism of Cesium with Water on the $SrTiO_3$(100) Surface at Room Temperature. *Reaction Kinetics, Mechanisms and Catalysis* **135,** 3257–3274 (2022).

161. Sanz, J. F. & Zicovich-Wilson, C. M. A Periodic Hartree-Fock Study of Na Adsorption on the TiO_2(110) Rutile Surface. *Chemical Physics Letters* **303,** 111–116 (1999).

162. Lopez, A, Heller, T, Bitzer, T, Chen, Q & Richardson, N. V. The Influence of Sodium on the Adsorption of Water on $SrTiO_3$(100)-1×1 Surfaces. *Surface Science* **494,** 811–814 (2001).

163. Miguel, M. A. S., Calzado, C. J. & Sanz, J. F. First Principles Study of Na Adsorption on TiO_2(110) Surface. *International Journal of Quantum Chemistry* **70,** 351–357 (1998).

164. Murray, P. W., Condon, N. G. & Thornton, G. Na Adsorption Sites on TiO_2(110)-1×2 and its 2×2 Superlattice. *Surface Science* **323,** 281–286 (1995).

165. Vickerman, J. C. & Gilmore, I. S. in *Surface Analysis: The Principal Techniques* 479–511 (Wiley, 2009).

166. Chen, J. in *Introduction to Scanning Tunneling Microscopy* 45–76 (Oxford University Press, 1993).

167. Castell, M. in *Nanocharacterisation* 80–107 (The Royal Society of Chemistry, 2015).

168. Gottlieb, A. D. & Wesoloski, L. Bardeen's Tunnelling Theory as Applied to Scanning Tunnelling Microscopy: A Technical Guide to the Traditional Interpretation. *Nanotechnology* **17,** R57–R65 (2006).

169. Giustino, F. in *Materials Modelling Using Density Functional Theory: Properties and Predictions* 66–86 (Oxford University Press, 2014).

170. Tersoff, J & Hamann, D. R. Theory of the Scanning Tunneling Microscope. *Physical Review B* **31,** 805–813 (1985).

171. Chen, P. *Synthesis and Characterisation of Epitaxial 2D Nanocrystals* PhD thesis (University of Oxford, 2019), 42–60.

172. Ibe, J. P. *et al.* On the Electrochemical Etching of Tips for Scanning Tunneling Microscopy. *Journal of Vacuum Science and Technology A: Vacuum, Surfaces, and Films* **8,** 3570–3575 (1990).

173. Nečas, D. & Klapetek, P. Gwyddion: An Open-source Software for SPM Data Analysis. *Central European Journal of Physics* **10,** 181–188 (2012).

174. Jones, L. *et al.* Smart Align - a New Tool for Robust Non-rigid Registration of Scanning Microscope Data. *Advanced Structural and Chemical Imaging* **1,** 8 (2015).

175. Aziz, M. & Ismail, A. F. in *Membrane Characterization* 81–93 (Elsevier, 2017).

176. Wren, A., Laffir, F., Mellot, N. & Towler, M. in *X-ray Photoelectron Spectroscop* 1–30 (Nova Science Publishers, 2011).

177. Stevie, F. A. & Donley, C. L. Introduction to X-ray Photoelectron Spectroscopy. *Journal of Vacuum Science and Technology A: Vacuum, Surfaces, and Films* **38,** 063204 (2020).

178. Watts, J. & Wolstenholme, J. in *An Introduction to Surface Analysis by XPS and AES* 59–76 (Wiley, 2003).

179. Zangwill, A. in *Physics at Surfaces* 20–27 (Cambridge University Press, 1988).

180. Greczynski, G. & Hultman, L. A Step-by-step Guide to Perform X-ray Photoelectron Xpectroscopy. *Journal of Applied Physics* **132,** 011101 (2022).

181. Shchukarev, A. & Korolkov, D. XPS Study of Group IA Carbonates. *Central European Journal of Chemistry* **2,** 347–362 (2004).

182. *ThermoFisher Scientific, Carbon X-ray photoelectron spectra* `https://www.thermofisher.com/uk/en/home/materials-science/learning-center/periodic-table/non-metal/carbon.html`. 2024-09-04.

183. Martin, R. in *Electronic Structure* 119–134 (Cambridge University Press, 2012).

184. Hohenberg, P. & Hohn, W. Inhomogeneous Electron Gas. *Physical Review* **136,** 864–871 (1964).

185. Kohn, W & Sham, L. J. Self-Consistent Equations Including Exchange and Correlation Effects. *Physical Review* **140,** 1133–1138 (1965).

186. Giustino, F. in *Materials Modelling Using Density Functional Theory: Properties and Predictions* 19–35 (Oxford University Press, 2014).

187. Kaxiras, E. in *Atomic and Electronic Structure of Solids* 42–81 (Cambridge University Press, 2010).

188. Martin, R. in *Electronic Structure* 171–187 (Cambridge University Press, 2012).

189. Kratzer, P. & Neugebauer, J. The Basics of Electronic Structure Theory for Periodic Systems. *Frontiers in Chemistry* **7,** 106 (2019).

190. Ashcroft, N. & Mermin, N. D. in *Solid State Physics* 132–150 (Saunders College Publishing, 1976).

191. Kaxiras, E. in *Atomic and Electronic Structure of Solids* 82–120 (Cambridge University Press, 2010).

192. Kaxiras, E. in *Atomic and Electronic Structure of Solids* 121–157 (Cambridge University Press, 2010).

193. Martin, R. M. in *Electronic Structure* 262–282 (Cambridge University Press, 2012).

194. Mortensen, J. J. *et al.* GPAW: An Open Python Package for Electronic-structure Calculations. *Journal of Chemical Physics* **160,** 9 (2023).

195. Martin, R. M. in *Electronic Structure* 81–108 (Cambridge University Press, 2012).

196. Larsen, A. H. *et al.* The Atomic Simulation Environment - A Python Library for Working with Atoms. *Journal of Physics Condensed Matter* **29,** 273002 (2017).

197. Blochl, P. E. Projector Augmented-Wave Method. *Physical Review B* **50,** 954–979 (1994).

198. Giustino, F. in *Materials Modelling Using Density Functional Theory: Properties and Predictions* 36–50 (Oxford University Press, 2014).

199. Becerra-Toledo, A. E., Marshall, M. S., Castell, M. R. & Marks, L. D. c(4x2) and Related Structural Units on the $SrTiO_3$(001) Surface: Scanning Tunneling Microscopy, Density Functional Theory, and Atomic Structure. *Journal of Chemical Physics* **136,** 214701 (2012).

200. Lin, Y. *et al.* The (2x2) Reconstructions on the $SrTiO_3$(001) Surface: A Combined Scanning Tunneling Microscopy and Density Functional Theory Study. *Surface Science* **605,** L51–L55 (2011).

201. Hennes, M. *et al.* Growth of Vertically Aligned Nanowires in Metal-oxide Nanocomposites: Kinetic Monte-Carlo Modeling Versus Experiments. *Nanoscale* **10,** 7666–7675 (2018).

202. Rappoport, D., Crawford, N. R. M., Furche, F. & Burke, K. in *Computational Inorganic and Bioinorganic Chemistry* (Wiley, 2008).

203. Hammer, B, Hansen, L. B. & No, J. K. Improved Adsorption Energetics within Density-functional Theory Using Revised Perdew-Burke-Ernzerhof Functionals. *Physical Review B* **59,** 7413–7421 (1999).

204. Wellendorff, J. *et al.* A Benchmark Database for Adsorption Bond Energies to Transition Metal Surfaces and Comparison to Selected DFT Functionals. *Surface Science* **640,** 36–44 (2015).

205. Dorado, B., Freyss, M. & Martin, G. GGA+U Study of the Incorporation of Iodine in Uranium Dioxide. *European Physical Journal B* **69,** 203–209 (2009).

206. Hatch, R. C. *et al.* Surface Electronic Structure for Various Surface Preparations of Nb-doped $SrTiO_3$(001). *Journal of Applied Physics* **114,** 103710 (2013).

207. Wagner, C. D. *et al.* Empirical Atomic Sensitivity Factors for Quantitative Analysis by Electron Spectroscopy for Chemical Analysis. *Surface and Interface Analysis* **3,** 211–225 (1981).

208. Seah, M. P. Simple Universal Curve for the Energy-dependent Electron Attenuation Length for all Materials. *Surface and Interface Analysis* **44,** 1353–1359 (2012).

209. Golyk, V. A., Krueger, M. & Kardar, M. Heat Radiation from Long Cylindrical Objects. *Physical Review E* **85,** 046603 (2012).

210. Saidi, M. & Hosseini, R. Air Pressure Dependence of Natural-Convection Heat Transfer. *Proceedings of the World Congress on Engineering* **2,** 1665 (2010).

211. Kim, C. Y., Shin, K. S., Lee, K. D. & Chung, J. W. Lithium-induced Reconstructions of the Si(001) Surface. *Surface Science* **324,** 8–16 (1995).

212. Shannon, R. D. Revised Effective Ionic Radii and Systematic Studies of Interatomic Distances in Halides and Chaleogenides. *Acta Cryst* **32,** 751 (1976).

213. Brewer, L. & Margrave, J. The Vapor Pressures of Lithium and Sodium Oxides. *J. Phys. Chem.* **59,** 421–425 (1955).

214. Silly, F. & Castell, M. R. Encapsulated Pd Nanocrystals Supported by Nanoline-structured $SrTiO_3$(001). *Journal of Physical Chemistry B* **109,** 12316–12319 (2005).

215. Hommrich, J., Hümann, S. & Wandelt, K. Cadmium Underpotential Deposition on Cu(111): In Situ Scanning Tunneling Microscopy. *Faraday Discussions* **121,** 129–138 (2002).

216. Günther, S., Zeller, P., Böller, B. & Wintterlin, J. Method for the Manual Analysis of Moiré Structures in STM images. *ChemPhysChem* **22,** 870–884 (2021).

217. Brown, I. D. & Altermatt, D. Bond-valence Parameters Obtained from a Systematic Analysis of the Inorganic Crystal Structure Database. *Acta Crystallographica Section B* **41,** 244–247 (1985).